Modelling of long-term controls on volcanic eruption processes

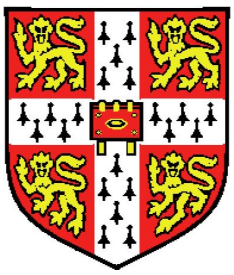

Rachel Berkowitz

BP Institute, Department of Earth Sciences

Hughes Hall College, University of Cambridge

A thesis submitted for the degree of

Doctor of Philosophy

17 January, 2013

This dissertation is the result of my own work and includes nothing which is the outcome of work done in collaboration except where specifically indicated in the text.

This thesis contains less than 275 pages as required by the Department of Earth Sciences.

Rachel Berkowitz

17 January 2013, Cambridge

Acknowledgements

First and foremost I am very grateful to Andy Woods for his ongoing support and wealth of ideas throughout my PhD. This project would not have been possible without the financial support from the BP Institute, BP, and the Nuclear Decommissioning Authority. I would also like to thank the rest of the BPI students and staff for their help and kindness, in particular Andrew Pluck and Chris Richardson who made the lab and computer parts of my PhD possible.

Many thanks for the support and encouragement over the years also go to my landlords (Peter and Pat Glazebrook), family (Mom, Dad, Grandma, Uncle), friends (too many to name here), and the Cambridge University Mountaineering Club.

Finally, I would like to thank Charles Day, John Travis, and Lucas Laursen for their mentorship and advice in other writing pursuits.

Abstract

In this thesis, we analyse the long-term evolution of historical volcanic eruptions and identify different patterns of behaviour at the volcanoes. In some cases the volumetric flux, or eruption rate, decays exponentially over years. In other cases, the eruption involves periods of ground inflation and deflation. In still other cases, the eruption rate first wanes at one rate and then changes to a different rate.

Historically, long-term eruptive trends have beeen interpreted in terms of a closed or open magma plumbing system. A closed system leads to simple exponential decay as magma leaves a storage reservoir or chamber. An open system, in which a storage reservoir is recharged with magma, allows for more complexity.

In this thesis we develop a series of models that allow for the possibility of more than one magma chamber. We build a generalised picture to allow for multiple chambers at different depths in the earth's crust. We illustrate how combining multiple chambers with a critical chamber overpressure at which an eruption starts and stops can lead to rich dynamics in which the timescale of eruption can be initially controlled by a shallow reservoir and later by a deeper reservoir. We use our model to interpret historical eruption data.

Additionally, we develop laboratory experiments to model the effects of recharge to a chamber. These illustrate how an eruption may converge to steady state following a period of relatively intense or mild eruption activity, as controlled by resistance in the conduit and the critical pressure at which eruptions are initiated.

We consider the implications of our models for monitoring the long-term evolution of volcanic events.

Contents

List of Figures

Chapter 1

Introduction

1.1 Abstract

In this chapter, we describe our motivation for studying the magma plumbing system of a volcano and present a series of observations of the time evolution of volcanic eruptions. We review models in the literature that explain features including processes that drive explosive and effusive eruptions, and present literature that explains the controls of a magma chamber on eruptions. This motivates the main topic of the thesis, in which a more detailed model of a magma plumbing system, allowing for two or more magma reservoirs which may be open or closed, is developed and compared with historical data. We conclude the chapter by presenting the structure of the thesis and the topics that will be included in each chapter. Our hypothesis is that one or more magma chambers, in which a critical overpressure is required to start and stop an eruption, can explain some of the trends observed in volcanic eruptions.

1.2 Motivation

The study of volcanoes is important both in terms of forecasting and managing hazards associated with eruptions, and in terms of general scientific interest.

Two examples of hazards associated with recent eruptions include Iceland's Eyjafjallajokull eruption in 2010, where ash released to the atmosphere halted air traffic for weeks; and the Soufriere Hills Volcano eruption beginning in 1995, during which the southern half of Montserrat had to be evacuated due to pyroclastic flows. Gaining a better understanding of how eruptions proceed is important for better informing hazard management.

Items that are important to understand regarding volcanic hazards include the timing, duration, intensity, and style of eruptive events. Ability to forecast is important for planning how the hazards will be managed. Cities and countries can try to minimise volcanic eruptions' impacts by responding appropriately to predicted hazards, and by managing their existence within a volcanic environment in which ongoing eruptions may cause effects for years to decades.

Providing a fundamental understanding of volcanoes and adding to the body of scientific knowledge is another reason to study volcanoes. It is interesting to understand why and how volcanoes erupt, how long they erupt, in what style they erupt, and the controls on all of these items. Many different factors control eruptions, and there have been many studies on the processes that occur following the injection of magma into the Earth's crust which ultimately leads to an eruption.

In this thesis, an analysis of observations at volcanoes around the world leads us to focus on the importance of understanding of how magma chambers interact.

1.2.1 Observations

Much can be learned about eruptions from observations of emitted magma and gases, eruption style and duration, and ground deformation. There is enormous variability in all of these properties and the data is extremely complex. One of the most interesting things to observe is how eruptive episodes unfold.

Over the last few decades, volcanic eruptions around the world have been monitored in great detail, enabling a new understanding of the range of phenomena that occur and of the different possible styles of an eruption. The data suggest complex transitions in eruption styles.

Understanding and quantifying the behaviour of eruptions relies on data gathered in many forms. Lava domes - both areal extent and gas emission - are monitored via satellite imaging. Ground surface deformation in the vicinity of a volcano is measured by GPS units. Some volcanoes have seismic monitoring networks which record activity below the surface in addition to seismic tremor associated with lava dome collapse. Observations of magma petrology and crystal content provide constraints on the depth of magma reservoirs that feed eruptions and on possible magma mixing in these reservoirs.

Some volcanic eruptions seem to wane with time, while others show complex behaviour, such as waning and then stopping or waning and then increasing in rate again. However, the long-term eruption may wane overall regardless of the shorter term patterns. Three historic eruptions for which the long-term eruption rate was monitored show simple waning eruptions with time, as shown in plots of erupted volume for Mexico's Paricutin volcano in 1943-1952; Chile's Lonquimay volcano in 1988-1990; and the Windward Islands' La Soufriere de St Vincent volcano in 1979 in Figure 1.1 Stasiuk et al. [1993]. Stasiuk showed that these eruptions might be explained by exponential decay. We will revisit these eruptions later in this chapter as well as in Chapters 3 and 4 where we show how they demonstrate certain behaviours and compare them to a model which we develop.

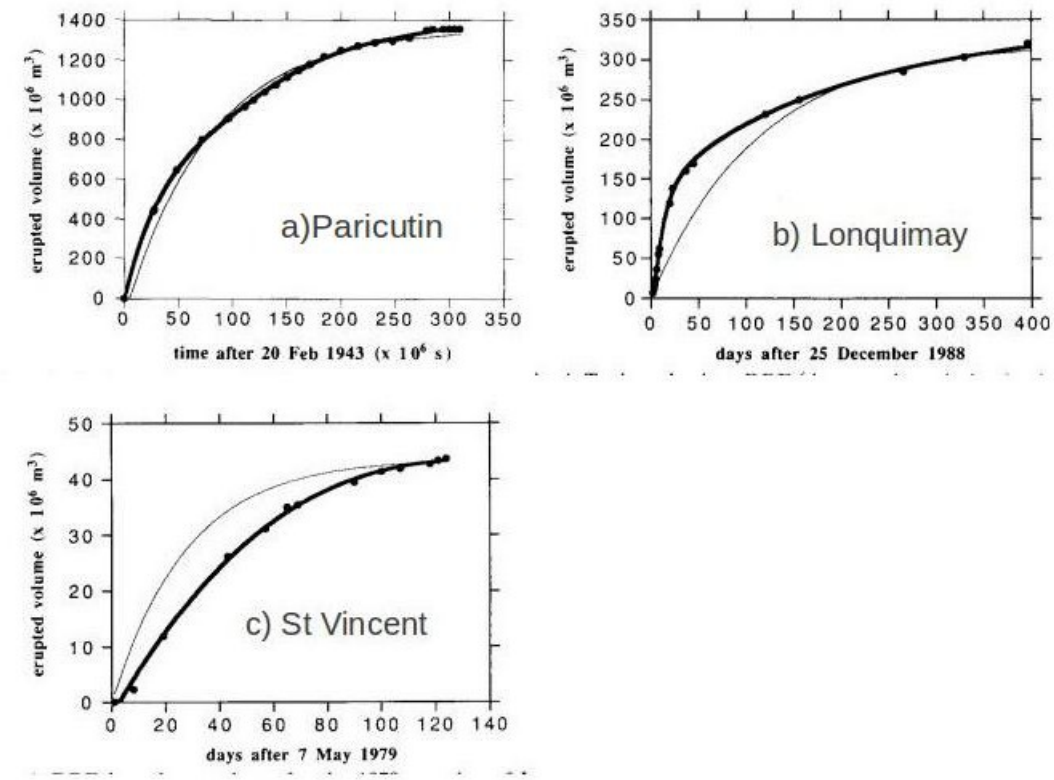

Figure 1.1: a) Paricutin 1943-1952 , b) Lonquimay 1988-1990, and c) La Soufriere de St Vincent 1979 erupted volume. Light curves show exponential eruption rate and dark curves show best-fit to the data Stasiuk et al. [1993].

Other eruptions show cyclic behaviour with periods of eruption separated by pauses during which no magma is produced, as we demonstrate with data from the Soufriere Hills Volcano at Montserrat in the West Indies from 1995-2007. The Soufriere Hills Volcano is one of the best monitored volcanoes in the world. This volcano gradually formed a lava dome, but also had intermittent dome collapse events that led to pyroclastic flows. Additionally, explosive eruptions of ash, gas, and pumice occurred over the course of the eruption. Day-to-day observations show complex behvaiour, but the behaviour shows different patterns over the longer term.

Figure 1.2 shows the multi-year pattern of erupted volume from the lava dome-building eruption at the Soufriere Hills Volcano. This shows that the eruption proceeded for two years and then paused for two years; then proceeded for over three years and paused for another two years; and the third phase of eruption lasted for only one year. We refer to these periods during which an eruption proceeds as eruptive episodes or events, and the periods between eruptions are refered to as pauses. A period of dormancy would refer to years or decades over which no sign of activity occurred.

Geophysical measurements of seismic activity and surface deformation at the Soufriere Hills Volcano show that cycles in seismic and surface deformation data correlate with these eruptive episodes, and we will present this data and discuss it in more detail in Chapter 2. As a result of such observations, we have evidence that the whole volcano inflated and deflated as the eruption evolved.

Even though the long-term phases of eruption are apparent at the Soufriere Hills Volcano, data from day-to-day monitoring of the volcano reveals more intricate patterns of activity associated with dome collapse events. For example, in Figure 1.3, seismic and ground deformation data from 6 days during the summer of 1997 reveal changes that occur on a timescale of hours. All the activity in this diagram occurs at the point marked by the red arrow on Figure 1.2, during the first eruptive event. It seems that a series of ground inflation and deflation events, each associated with a small collapse of the growing lava dome, generated small pyroclastic flows along the flanks of the volcano Wylie et al. [1999].

This illustrates that although time-averaged data captures a long-term trend, detailed activity is more complex. The day-to-day trends are more important for

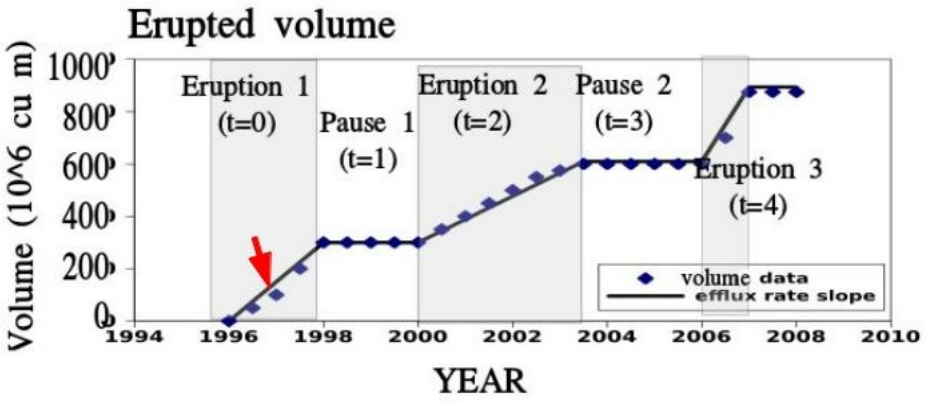

Figure 1.2: The erupted volume data from the Soufriere Hills Volcano shows cycles of eruptions that occur over a timescale of years. The eruptive episodes depicted by grey shading, during which the volume increases, last for different amounts of time; while the pauses, during which no volume is erupted, last for equal lengths of time. Detail of the eruption at the time marked by the red arrow is presented in Figure 1.3.

hazard management and predicting when volcanic activity might be imminent, but the overall trend is important for long-term monitoring.

We will revisit the Soufriere Hills Volcano data in Chapter 2, along with data from Mt Fugen of Japan's Unzen volcano complex (1990-1995), Washington State's Mt St Helens (1980-1986), and Mt Etna (1865-present) which also show how eruptive episodes persist from years to centuries. We will analyse these eruptions in detail and study the history of eruption rate with time to provide an understanding of ways in which volcanoes evolve.

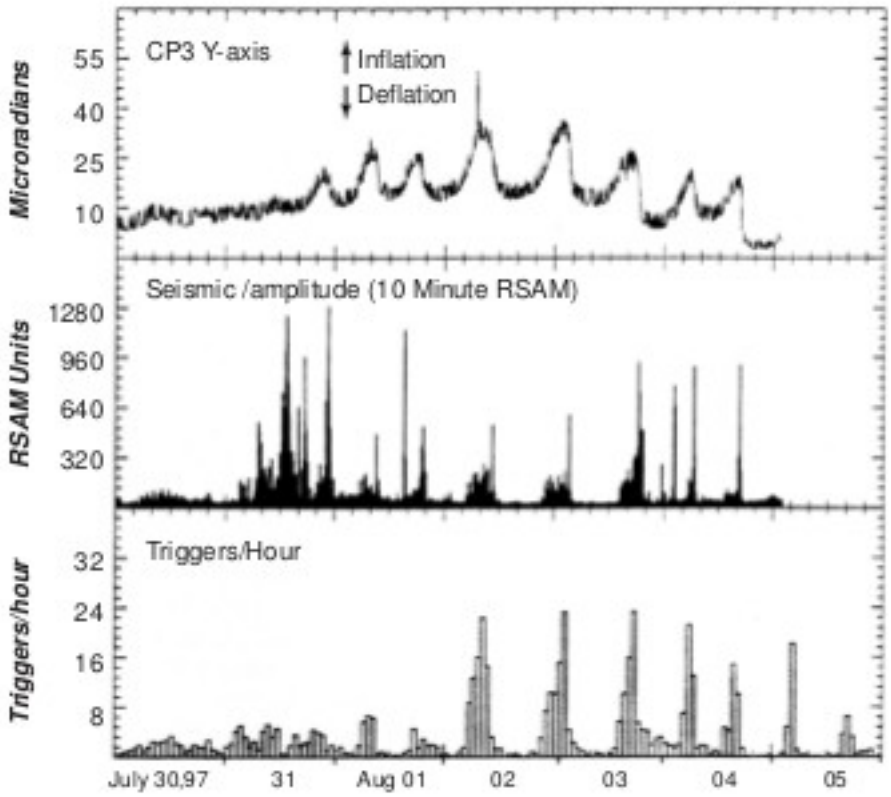

Figure 1.3: Surface deformation (top), pulsed seismic amplitude (middle), and triggered earthquakes (bottom) at the Soufriere Hills Volcano from 30 July to 5 August 1997 Wylie et al. [1999]. This shows the complexity of short-term fluctuations that occur during eruptions. All the activity in this diagram occurs at the point marked by the red arrow on Figure 1.2

1.3 Conduit models and explosive eruptions

Effort has been made to model aspects of volcanic eruptions, which are often categorised into two groups: explosive eruptions, in which gas-rich magma fragments and erupts as a cloud of ash and gas, and lava dome eruptions, in which viscous degassed magma erupts slowly from the crater and forms a lava dome. In this thesis we refer to the lava dome eruption as an effusive eruption; however, it is worth noting that effusive eruptions also comprise the outpouring of lava onto the ground, such as basaltic lava flowing from Mauna Loa in Hawaii in 1984.

One set of models focuses on the dynamics of magma flow in a conduit. This is of interest because during an explosive eruption, viscous magma becomes fragmented, meaning that it erupts as a gas continuum with dispersed particles. In an effusive eruption, magma releases volatiles and erupts as a viscous plug. We will review models of conduit processes, and then investigate how the role of a magma chamber couples to these models.

In these models, the conduit is a cylindrical tube. This is not representative of a real conduit, which would likely come in a range of geometries; however, for the sake of modeling, a cylindrical approximation is often adopted. Aspects of an eruption have been studied in various levels of detail. Wilson and Head carried out some of the original work exploring explosive eruption dynamics Wilson and Head III [1981].

Magma contains dissolved volatiles, mostly water, CO_2, and SO_2, when it is in a subsurface magma chamber. Gas bubbles in the magma nucleate at some depth, and volatiles continue to exsolve and bubbles grow as magma ascends the conduit Sparks [1997]. As magma ascends the conduit, pressure drop causes volatiles to exsolve and bubbles to expand, and bubbles may be released from the melt Wilson and Head III [1981]. Since the magma is very viscous, the bubbles remain locked with the liquid melt and the mixture becomes progressively more foamy as it rises to the surface. The liquid films around the bubbles eventually fracture and the gas changes to a continuous phase with suspended fragments of liquid Chassignet et al. [2012]. This leads to the explosive eruption.

Figure 1.4 provides a schematic of some of the subsurface processes involved in explosive eruptions Sparks [1978, 1997].

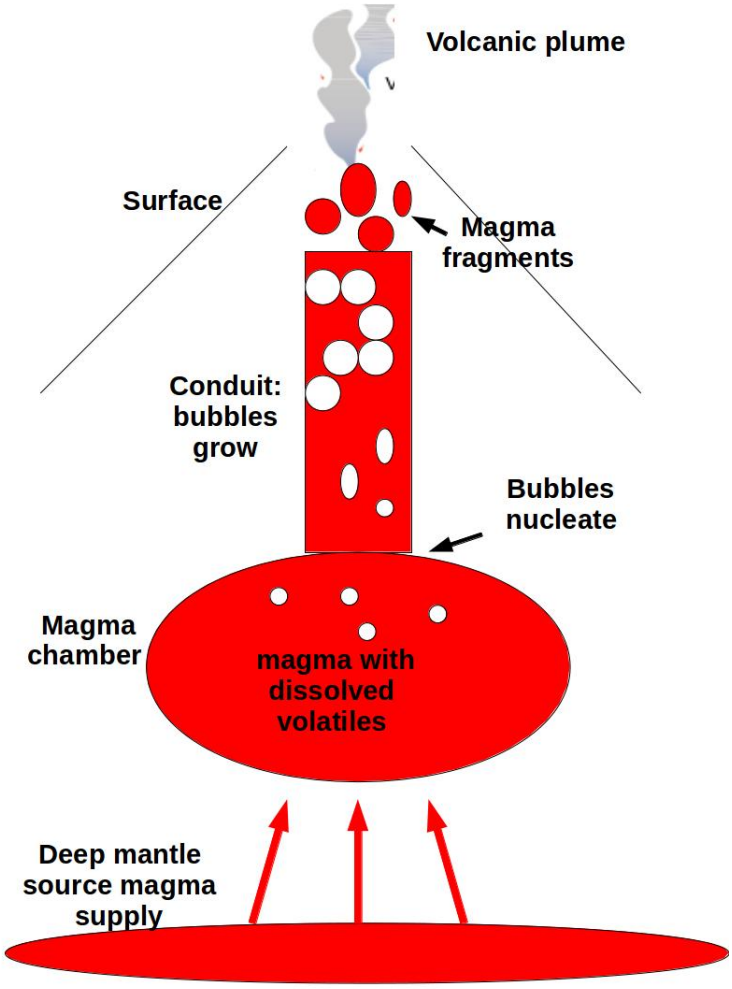

Figure 1.4: Schematic illustration of some of the basic subsurface processes in a volcano Sparks [1978].

The detailed dynamics of fragmentation, in which magma undergoes transformation from bubbly liquid to gas, has been a rich area of research. It is thought that in the region of the conduit, liquid and gas may become a continuous phase. This can have an important impact on the development of permeability, which allows the gas to separate from the melt, and can impact the size distribution of fragments produced Blower [2001]; Blower et al. [2001]. This is not the dominant control on long-term dynamics but is mostly relevant to explosive events.

1.4 Degassing and effusive eruptions

Magma can also erupt effusively as viscous, degassed magma which piles over the eruption vent as a lava dome. It has been observed that the same sort of magma erupts both explosively and effusively, because it can reduce its gas content and erupt at the surface more slowly as a viscous, dense phase.

Jaupart originally demonstrated that if gas can escape from the magma, the eruption can proceed effusively Jaupart and Allègre [1991]. The literature looks at controls on cycles between explosive and effusive events.

Woods and Koyaguchi developed models that look at conduit flow and an effusion rate that depends on the ability of the magma to degas Woods and Koyaguchi [1994]. Transition from explosive to effusive events is due to gas loss through permeable conduit walls or through the magma itself (or, in some cases, emanating through groundwater heated by volcanic action), at a rate inversely proportional to eruption rate Jaupart and Allègre [1991]. If the magma degasses on a timescale faster than the time of its ascent through the conduit, it erupts as a degassed magma that has lost its buoyancy force. Melnik and Sparks demonstrated that crystallised magma increases its viscosity as well, and the association of viscosity with crystallisation is an additional mechanism for transition of explosive to effusive eruptions when coupled with permeable flow Melnik and Sparks [1999]; Sparks [1978]. Figure 1.5 shows some of these explosive-effusion transition processes.

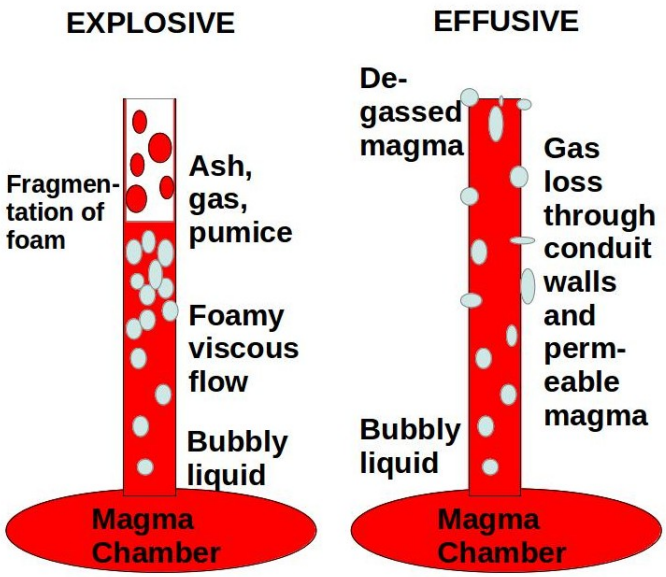

Figure 1.5: Transition from explosive to effusive events is due to gas loss through permeable conduit walls or gas diffusing through permeable magma itself. If the magma has not had time to degas, it fragments and erupts explosively. If it has degassed, it erupts effusively.

1.5 Reservoir models

Several models explore how the pressure in a magma reservoir evolves with recharge and eruption and drives the magma through the conduit during an eruption.

One of the basic concepts involves a single magma chamber in which magma erupts at a rate proportional to chamber pressure, and shows exponential decay of eruption rate Wadge [1977]. Sparks and Druitt add to the concept by modeling the Earth's crust, in which the magma chamber resides, as an elastic medium so that the chamber has an elastic response to pressurisation Druitt and Sparks [1984]. Stasiuk looked at data from different volcanoes and proposed that a theory of exponential decay of eruption rate is overly simplified Stasiuk et al. [1993]. He plotted eruption data to indicate a more complex evolution of eruption rate with time, and interpreted the complexity as arising from erosion of the conduit and changes in magma rheology. Stasiuk argued that an exponential eruption rate provides a good fit to the eruption of Mexico's Paricutin volcano in 1943-1952 as shown in Figure 1.1a, but does not fully describe Chile's Lonquimay volcano in 1988-1990 or the Windward Islands' La Soufriere de St Vincent volcano in 1979 eruptions as shown in Figure 1.1 b and c. Light curves show exponential eruption rate and dark curves show best-fit to the data Stasiuk et al. [1993].

Since this work, it has been shown that magma evolves as it ascends the conduit. Initial models assumed different steady state eruptions, but more recent numerical models allow flow to evolve in time depending on magma properties Melnik and Sparks [2005]. By including time constants for crystallisation, gas exsolution, and permeability of flow, the travel time of magma compared to the timescale of these other processes means that different timescales of eruption are possible.

Barmin illustrated a range of non-periodic cycles which develop as a result of evolution of chamber pressure when the ability of magma to flow depends on the rate of crystallisation Barmin et al. [2002]. Melnik and Sparks showed that as magma degasses, it can produce crystals which lead to an increase in viscosity and a slower flow Melnik and Sparks [2005]. Denlinger showed that there is a critical level of resistance reached in the conduit after which magma will not flow

and proceeds by stick/slip boundary conditions, rather than as a cylindrical pipe flow Denlinger and Hoblitt [1999]. Bower and Woods added that the decay rate of the eruption depends on the magma composition: a more compressible magma makes an eruption last longer, while magma compressibility varies due to volatile content Bower and Woods [1997, 1998]; Huppert and Woods [2002].

The key feature of these processes is that they lead to the prediction of eruption rate. A critical chamber overpressure may be required to start and stop a 'fast' rate of effusive eruption, as shown in Figure 1.6 with red and blue lines delineating the transitions. This transition in rate can be associated with the magma's ability to release gas, crystallise, or stick and slip along the conduit wall. The common feature is the prediction of a critical overpressure at which a relatively fast eruption slows, and a relatively slow eruption speeds up.

In this thesis, we build this critical chamber overpressure into a model. We use a simple parametric model for the transition between fast and slow eruption rates, assuming a critical overpressure. As a simplification, we assume that the slow phase is significantly slow such that no material erupts (other models in the literature assume slow effusion rates with small amounts of material output e.g. Melnik and Sparks [2005]; however we look at the extreme case of 'slow' phases in which no material is produced). Then we re-interpret data from historical eruptions in the context of this model.

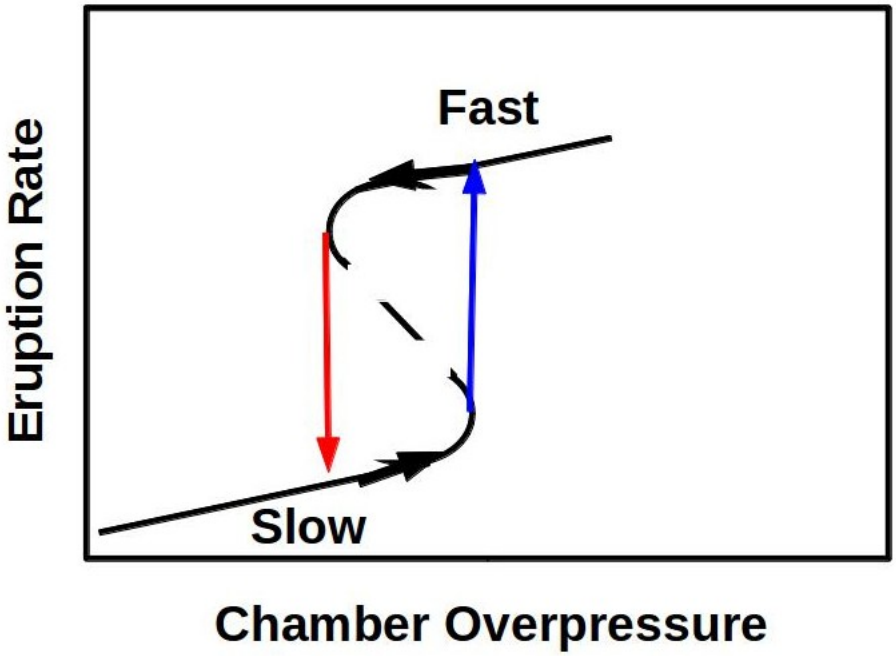

Figure 1.6: Eruption rate depends on chamber overpressure: there may be a critical overpressure at which a 'Fast' eruption drops to a 'Slow' regime (red), and another critical overpressure at which a 'Slow' eruption increases to a 'Fast' regime (blue). A basic description follows: During the 'slow' regime, chamber pressure increases because influx into the chamber from a deep source is higher than outflux Barmin et al. [2002], possibly because magma degasses and crystallises thus forming a crystalline plug. The chamber overpressure builds until further increase is impossible, or is sufficient to remove the crystalline plug, and the eruption rate transitions to the 'fast' regime (blue). Then the magma begins to cool, becoming more viscous and losing momentum, and the chamber overpressure drops as magma is removed. Eruption rate begins to slow, eventually transitioning to the 'slow' regime (red) and allowing overpressure to rebuild again, leading to periodic behaviour of eruption rate and chamber pressure. The dashed line that suggests a third possible eruption rate associated with a given chamber overpressure is mathematically but not physically possible Barmin et al. [2002].

1.6 Different magma petrology and multiple chambers

Another area of the literature shows that while the same type of magma can erupt both effusively and explosively depending on its gas content, a huge variety of rocks and magma chemistry in eruption products suggest that magma is likely to have spent time at different depths in the Earth's crust Annen and Sparks [2002]; Barclay et al. [1998]; Blundy and Cashman [2001, 2005]; Sparks [1997].

Petrological studies support a picture of multiple dykes and sills which inject magma during the formation of volcanic centers Gudmundsson [2006]. Magma rising into the crust interacts with a complex geometry of dykes and sills distributed through the crust. This suggests a plumbing system more complex than a single chamber.

Seismic data from the 2010 eruption of Eyjafjallajokull in Iceland shows multiple chambers at different depths which have been interpreted as erupting in series, as different types of magma are erupted at different times Tarasewicz et al. [2012].

Different magma types have been observed to erupt simultaneously as enclaves of basalt and andesite at the Unzen volcanic complex Nakada et al. [1999]. If new magma from depth recharges a chamber that already contains evolved magma, the incoming heated magma may generate sufficient overpressure to trigger a slow effusive eruption of the overlying evolved magma, with components of both magmas apparent in the eruption products Woods and Huppert [2003]. A sketch of this situation is included in Figure 1.7.

This introduces the concept of an 'open' magma system, which allows for more complexity by allowing recharge of magma from a deep mantle source to the chamber. The recharge also allows the chamber overpressure to persist over time as illustrated in Figure 1.8 Blake [1984]. New magma may pond in the chamber, while magma that already resides in the chamber erupts to the surface.

But describing a system as closed or open may be too simplistic because petrology indicates magma that has spent time at different depths. This leads to the hypothesis that an eruption may involve two or more chambers, which affects the overall eruption in complex ways. We provide a framework for a magma plumbing system that shows the impact of magma spending time at different

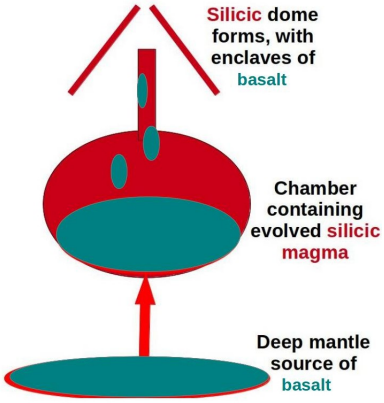

Figure 1.7: Enclaves such as those found at Unzen may occur when basaltic magma from a deep mantle source recharges a chamber that already contains evolved silicic magma Woods and Huppert [2003].

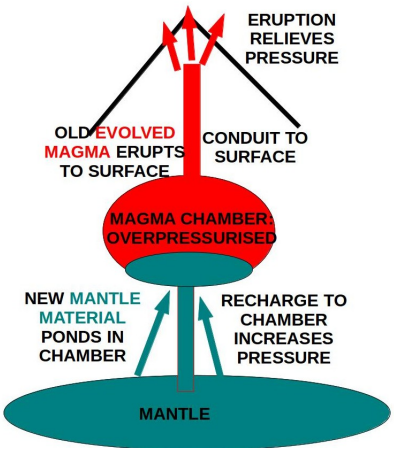

Figure 1.8: Recharge from a deeper source such as the mantle to a magma chamber drives an overpressure in the chamber. New magma may pond in the chamber, while magma that already resides in the chamber erupts to the surface. A sustained overpressure means that an eruption may persist.

depths.

In this thesis, we review data from volcanoes to interpret the evolution of an eruption by combining a model of one or more magma chambers operating as an open or closed system, together with a model of critical overpressure at which an eruption starts and stops, to rationalise the complex patterns observed at volcanoes around the world.

1.7 Structure of thesis

The general picture of how we structure this thesis is to analyse data from various volcanoes; then to build a model of a single chamber system; then to extend the model to a double chamber system. We explore how the single and double chamber models affect surface deformation predictions, and show how these models lead to understanding of trends at certain volcanoes

In Chapter 2, we present data from volcanoes which have interesting features illustrating the long-term evolution of an eruption. In particular, the Soufriere Hills Volcano reveals multiple ground inflation and deflation events, and we argue that these patterns show that it behaves as an open system with magma supply from depth. We also describe the 2010 eruption of Eyjafjallajokull in Iceland, where high resolution seismic data reveal the presence of multiple sills interacting below the volcano and informs the model we develop of effusive systems at other volcanoes.

In Chapter 3, we review a model of a single chamber erupting to the surface, and describe the character of the eruption for both closed and open systems. As the magma chamber pressure drops over months to years, the eruption rate falls to zero. The detailed mechanism for this decreasing pressure is not understood but may be associated with the flow rate of magma slowing sufficiently to form a crystalline plug that can no longer be displaced Barmin et al. [2002]; Melnik and Sparks [2005].

We assume that the eruption stops at a critical pressure which is no longer sufficient to drive magma to the surface. After an eruption, the chamber is recharged with magma up to a pressure sufficient to start the eruption again. In this way, we develop a model of an eruption that predicts nonlinear cycles of chamber inflation and deflation. The timescale for degassing and crystallisation is assumed to be shorter than the timescale for the magma to ascend to the surface, so the focus of our model is effusive eruptions. This corresponds to magma eruption on the order of 1 m^3/s, which is an effusive eruption rate.

Using the closed system model, we interpret the long-term eruption trends at Unzen and Mount St Helens. We review the data from Stasiuk on Paricutin volcano and La Soufriere de St Vincent, as they also are consistent with the

picture of a closed system. However, the Soufriere Hills Volcano eruption stops and then resumes in several cycles, which we rationalise by positing an open system in which a chamber is recharged as it erupts. We also observe that the 1979 eruption of Lonquimay volcano in Chile erupts on two different timescales.

Petrological data suggests that magma ponds at 12 km and 6 km depth beneath the Soufriere Hills Volcano Barclay et al. [1998]; Devine et al. [2003]; Edmonds et al. [2001]. Evolving surface deformation in the vicinity of this volcano also suggests a complex system of chambers. This leads us to look at how a closed two-chamber system works and may lead to two timescales of eruption such as occurred at Lonquimay.

In Chapter 4, we develop a model of a two-chamber system. This provides a mechanism for an eruption that proceeds on two different timescales, as well as for a source of recharge to a shallow chamber. We use this to rationalise the Lonquimay eruption, which erupts rapidly at first and then slowly: this could be controlled by a shallow chamber that drains rapidly, then a slowly draining deep chamber becomes the dominant control on the eruption rate. We show how a recharge to the deeper of two chambers can lead to steady state cycles of eruption. We use a closed two chamber system to re-interpret the discrete episodes of lava dome growth at Mount St Helens, where a shallow chamber provides a nonlinear control on the flow while the deep chamber wanes in time.

In Chapter 5, we predict the evolving shape of ground surface deformation near a volcano owing to two magma chambers whose pressures evolve differently over time. If the chamber pressures are not linearly proportional to each other at all times, the shape of the surface deformation due to subsurface pressurisation changes in time. A detailed data set of surface deformation exists for the Soufriere Hills Volcano, and shows different surface deformation in time. This may be rationalised by the deformation due to two unequally pressurised chambers.

Finally, in Chapter 6, we test the model of a two-chamber system with an experimental system. The experiment models recharge of the second chamber from a deep source at a constant pressure. We model the transient evolution of a weak and a strong plug in the conduit, or whether an eruption proceeds rapidly and then slowly or vice versa. This is one way to rationalise the fast then slow eruption at Lonquimay volcano.

Chapter 2

Observing patterns at volcanoes around the world

2.1 Abstract

In this chapter, we discuss the activity from five volcanoes which have received much attention in the literature due to the broad range of information which is available regarding their eruptions. We identify features in the eruption style, magma composition, and seismic activity at these volcanoes. Features include years of activity that cycle between periods of lava extrusion; ground deformation in the vicinity of the volcanoes that parallels periods of extrusion; seismic activity that reaches to a range of depths; and magma composition that contains both basaltic and andesitic elements. Key differences from one volcano to the next that interest us include the duration, rate, and frequency of periods of lava extrusion. We discuss how these principles motivate new insights into a model of a magma plumbing system, which is the main contribution of this thesis as discussed in the introductory chapter.

We discuss eruptions at Mount Etna, Italy; Mount St Helens, Washington state; the Soufriere Hills Volcano at Montserrat, West Indies; Mount Fugen of the Unzen complex, Japan; and Eyjafjallajokull, Iceland.

2.2 Introduction

There is a range of styles and patterns that arise in effusive eruptions. Historical data from Paricutin, Lonquimay, and La Soufriere de St Vincent presented in Chapter 1 seem to indicate a waning eruption with time. More recently monitored volcanoes show richer trends in eruption patterns. We will describe these in detail to help motivate the models developed later in the thesis.

2.3 Mount Etna

2.3.1 Abstract

Mount Etna is a stratovolcano in Sicily, Italy, as shown in Figure 2.1 and pictured in Figure 2.2, and has been used in one of the early examples of a single chamber magma plumbing system model. It is of interest to us because its long-term history since the 19th century shows a complex series of eruptions that last for years, starting and stopping by a mechanism that is not fully understood. A single flank eruption within this series, in 1950-51, has provided the framework for a model of a magma plumbing system comprised of a single depressurising chamber Wadge [1977]. We present a timeline for Mount Etna's activity from 1863 until the present day, as well as erupted volume data from these events, to show the cycles of eruption and an overall increase in erupted volume over the decades. We then focus on the 1950-51 eruption and show how it appears to behave as simple exponential decay. We present Wadge's model and other literature regarding Mount Etna petrological data, which shows multiple magma types erupted in the volcano's history, and seismic data that covers a range of depths Behncke and Neri [2003]; GVP. Our main purpose for discussing Mount Etna is to provide context for the Wadge model and a background for the thesis.

Figure 2.1: Location of Mount Etna in Sicily, Italy

Figure 2.2: Mount Etna volcano

2.3.2 Background and timeline

The stratovolcano lies above the subduction zone where the African and Eurasian plates collide, near the boundary between two regions that exhibit different types of volcanism: to the north, the Aeolian islands are thought to be related to subduction. However, no chemical or seismological evidence exist on Sicily itself for subduction related volcanism, and activity at Etna is thought to stem from upwelling of mantle material Schiano et al. [2001].

Mount Etna provides an opportunity to investigate long-term controls because the history of eruptions is sufficiently documented that extremely long-term trends can be observed. It also provides the opportunity to focus on a single event in the long-term series that has been studied in detail and supplies a framework for magma plumbing models

Eruptions at Mount Etna have been recorded in detail since 1865, and records continue to the present day. The years since 1865 show five cycles of eruption and involve summit and flank eruptions. One period of eruption from 1950 to 1951 involved lava dome growth whose volume was recorded in detail over time, and provides an example of an effusive eruption whose output rate wanes with time. Wadge proposed a model based on this period, comprising a pressurised magma chamber that decompresses over time, extruding magma until there is no longer sufficient pressure or volume to continue the eruption Wadge [1977]. Mount Etna provides an important example of one of the earlier models of a deflating magma chamber.

Next we present a timeline of the Mount Etna eruptive events in four episodes from 1865 to the present day. After the timeline, we present eruption data from the longterm history of Mount Etna, followed by data from the 1950-51 event.

2.3.2.1 Timeline of events 1865 - 2001 Behncke and Neri [2003]

- Cycle I (1865 - 1892)
  - Summit eruption followed by 5 flank eruptions, mean interval between flank eruptions 3.6 years.
- Cycle II (1892 - 1928)
  - Summit eruption followed by 6 flank eruptions. Lower mean output rate than in previous cycle.
- Cycle III (1928 - 1951)
  - Summit eruption followed by 4 flank eruptions. Higher mean output rate than in previous cycles.
- Cycle IV (1951 - 1993)
  - Summit eruption followed by 12 flank eruptions, mean interval between flank eruptions 1.5 years. Higher mean output rate than previous cycles.
- Cycle V (1993 - ?)
  - Summit eruption followed by 2+ flank eruptions (ongoing). Flank eruptions occur much earlier after summit eruption than in previous cycles. Summit activity more varied and more vigorous, including 120 brief episodes of violent explosions accompanied by lava flows. Higher mean output rate than in previous cycles.

2.3.3 Eruption data

Figure 2.3 shows the cumulative magma volume output of Etna from 1866 to 2003. Notable features of these cycles are discussed in the timeline in the previous section. There are five noted cycles of activity, delineated by dashed red lines Behncke and Neri [2003]. Each cycle consists of a period of inactivity, followed by a period of summit activity (explosive events), followed by a series of flank eruptions.

For the overall history of Etna from the 16th century to the 1970s, Wadge proposed that magma reaches the surface at a rate that is uniform over tens to hundreds of years, although eruptive activity is not continuous Wadge and Walker [1975]. This background uniform rate is evident from the dashed black line in Figure 2.3, suggesting a mean rate of 0.39 m^3/s for the 1865 - present period Behncke and Neri [2003].

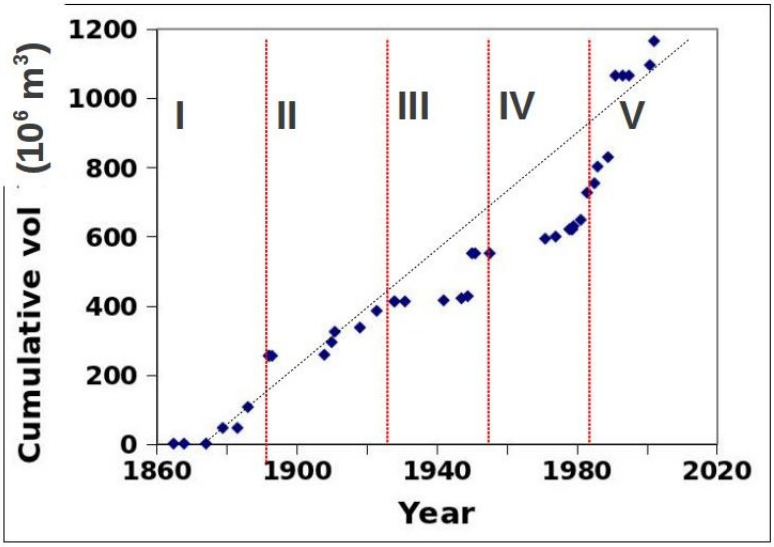

Figure 2.3: Mount Etna erupted volume, including tephra and lava from summit and flank eruptions, since 1866 Behncke and Neri [2003]. Five cycles of contrasted outputs are denoted by dashed red lines. A uniform rate is suggested over the entire history of eruption for these years (black line), but output rate within each cycle varies.

Having presented the long-term picture of Mount Etna, we now focus on a single flank eruption in 1950-51 for which detailed erupted volume data exist. The incremental erupted volume is shown in Figure 2.4 Cumin [1954]. This includes both lava efflux, plus a small amount of tephra from an explosive event in November 1950. The individual data points are not separate extrusive events, but rather measurements of the overall extrusion from the flank eruptions. The total efflux of lava is of order 100×10^6 m^3, while the total tephra from the explosion is of order less than 1×10^6 m^3. We suggest that this magma output behaves as simple exponential decay (Figure 2.5).

The exponential decay of the 1950-51 eruption provides the basis for a model of a simple elastic magma chamber that we will discuss in the next chapter Wadge [1977].

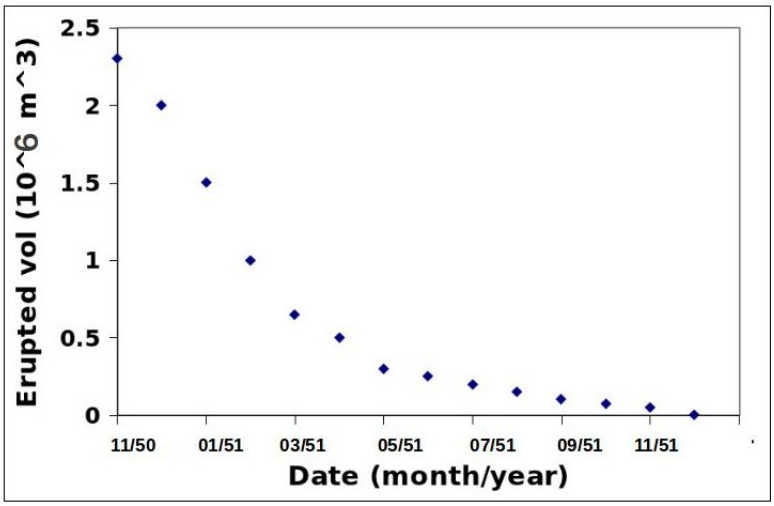

Figure 2.4: Incremental erupted volume (extruded lava) measured during flank eruptions from 1950-51 Cumin [1954]; Wadge [1977]. The explosive activity was during the first month and is included in the total volume shown in the figure.

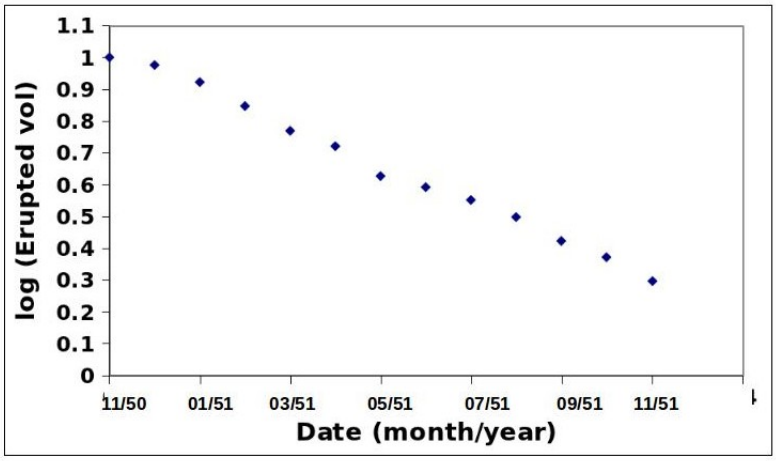

Figure 2.5: Log plot of incremental erupted volume (extruded lava) measured during flank eruptions from 1950-51 Cumin [1954]; Wadge [1977]. The data in Figure 2.4 suggest an exponential decay.

2.3.4 Additional data and interpretation

Mount Etna provides motivation for one of the classic models of a single magma chamber system. The model comprises a system into which magma rises from the mantle into a broad conduit or 'chasm' that extends beneath the surface and acts as a magma reservoir for eruptions on the flanks Wadge [1977]. When the reservoir has been filled by magma and is in a critical state, failure may result in an eruption and the reservoir is drained. The large volumes in historic eruptions require a source in addition to the reservoir, and this is thought to be either new magma from depth or from some other reservoir Wadge [1977]. Theoretical behaviour of the magma is modeled by calculating the magmatic pressure, which is a balance between lithostatic pressure and hydrostatic pressure and the pressure of the enclosing rocks. This provides the groundwork for further models of a magma chamber that sits in bedrock, where tensile and elastic properties of the rock may affect the draining and filling rate of the chamber. We discuss this model in more detail in later chapters.

The complex cycles described in the timeline and in Figure 2.3 need a more detailed explanation, however, and we look to other data for more information.

Seismic data exist from various events in the 20th century. In a 1987 eruption, seismic activity was detected from 4-15 km depth in the pre-eruptive months, which extended to 20 km depth accompanying the opening of a fissure [GVP]. From 1993-2005, eruptions are preceded by seismic activity ranging from 3 to 20 km depth; additionally, ground deformation measured by GPS systems accompanied periods of eruption and inflation accompanied periods between eruptions Allard [1997]. These could indicate movement of magma at various depths and times throughout an eruption.

Magma erupted from Mount Etna has become more mafic since 1974, and recent eruptions of Mount Etna in the 21st century were the first to produce two types of magma simultaneously: one is more mafic than most other magmas erupted from Etna since 1669 Behncke and Neri [2003]. SO_2 gas output during the summit activity also indicates that not all of the magma from a mantle source is erupted Allard [1997]; Tanguy [1978]. Differentiation of magma types implies crystal fractionation - that is, when a mineral precipitates from a melt to form

crystals, changing the composition of the melt - at varying levels in the crust Tanguy [1978]. Changes in magma composition suggest that magma may pool in sills or chambers in the crust, indicating deep migration of basalt which mix with more evolved magmas Annen and Sparks [2002].

2.3.5 Key characteristics

Mount Etna undergoes cycles of activity which change in rate and intensity but exhibit a relatively constant long-term output rate, while individual cycles comprise summit activity followed by ongoing flank activity over a period of months to years. The erupted material becomes more mafic over time and in recent eruptions has included two different types of magma. Seismic activity and GPS ground deformation data suggest ongoing activity. A single eruption in 1950-51 provides an example of an eruption whose rate wanes with time. These traits combine to imply further complexity in Mount Etna's magma plumbing system.

The next three volcanoes that we discuss share the characteristic of erupting evolved andesitic magma as well as more primitive magma.

2.4 Soufriere Hills Volcano at Montserrat, West Indies

2.4.1 Abstract

The Soufriere Hills Volcano occupies the southern half of Montserrat, an island in the Lesser Antilles chain of islands in the West Indies in the Caribbean Sea as shown in Figure 2.6. After several years of seismic unrest, phreatic activity began at the volcano in July 1995 for the first time since the 17th century, and was later accompanied by lava extrusion and pyroclastic flows. On 18 July, the central vent eruption shown on the left in Figure 2.7 produced pyroclastic flows, and lava dome extrusion led to mudflows and land and property damage. Until 2007, the volcano experienced 3 episodes of lava extrusion, each lasting two to three years and separated by two-year pauses. Since then, there have been incidents of dome collapse and shorter and vigorous episodes of lava extrusions and bursts of ash Wadge et al. [2010].

Since 1995, Soufriere Hills Volcano has been one of the most closely monitored volcanoes in the world. Monitoring of the volcano has included details of short term cycles, including shallow earthquake swarms, surface deformation changes over periods of hours, and variation in SO_2 emission rates over the course of a month. The former has been explained in the literature by models including a conduit whose elastic walls allow oscillatory magma flow for a steady flow input Wylie et al. [1999]. The latter has been explained by gas emission rate increasing during pressure buildup but varying as gas is relesed via cracks in the conduit wall or dome Watson et al. [2000]. But the long-term output and cycles are controlled by the deep magma plumbing system, which is what interests us.

We present data showing phases of eruption from 1996 to 2006, and illustrate how these phases are correlated to dome growth and collapse as well as ground surface deformation in the vicinity of the volcano Wadge et al. [2010]. Then we present more information regarding other characteristics of the Soufriere Hills Volcano eruption including seismic activity preceding eruption; ground deformation correlated to eruptions; and crystal-rich andesitic magma that suggests magma that has evolved between 5 and 10 km depths Barclay et al. [1998]; Devine et al.

[2003]; Mattioli et al. [1998, 2010]; Wadge et al. [2010]. The periods of extrusion exhibit different rates, but the overall eruption for 10 years exhibits a constant rate. The magma plumbing system at the Soufriere Hills Volcano is thought to comprise a chamber and a deep source of magma recharge in order to sustain this constant background rate Elsworth et al. [2008]; Sparks et al. [1998]; Wadge et al. [2010].

Figure 2.6: Location of Soufriere Hills Volcano at Montserrat, West Indies.

.

2.4.2 Background and timeline

The lava dome at the Soufriere Hills volcano has been growing slowly at a steady rate since 1995. A recent lava dome is shown on the right in Figure 2.7. The volcano's eruption exhibits a pattern comprised of a several year extrusive event, then a several year pause, then another several-year eruption. The growth rate is different from one cycle to the next.

We present a timeline of eruptive events from 1995 to 2008. In the next section, we present the erupted volume and some surface deformation data from these events.

Figure 2.7: Soufriere Hills Volcano erupting in 1995 (left) and the lava dome in 2006 (right)

2.4.2.1 Timeline of events 1995 - 2008 Wadge et al. [2010]

- Pre-eruption: 18 July 1995
  - Phreatic activity (explosions of steam, water, ash, and rock) begins at Soufriere Hills volcano, accompanied by swarms of hybrid earthquakes Miller et al. [1998]
- Eruption 1: 15 Nov 1995 - 10 March 1998
  - Andesite lava dome begins to grow (846 days, $331M\ m^3$, extrusion rate 4.5 m^3/s), accompanied by initial phreatic explosions. The lava dome collapses on 26 December 1997
  - Swarms of earthquakes precede an explosive event on 17 Sept 2006, and earthquakes increase in frequency and accompany surface deformation until dome collapses Luckett et al. [2007]
- Pause 1: 10 March 1998 - Nov 1998
  - Pause in growth (627 days), and lava dome collapses with minor explosive activity after 3 July 1998
- Eruption 2: 27 Nov 1999 - 28 July 2003
  - Lava dome growth (1339 days, $336M\ m^3$, extrusion rate: 2.9 m^3/s). This is the slowest rate of eruption, and the largest dome built after 2 major collapses. Dome collapses three times during this eruption.
- Pause 2: July 2003 - Oct 2005
  - Pause in growth (735 days), minimal residual activity
- Eruption 3: 1 Aug 2005 - 20 April 2007
  - Lava dome growth (627 days, $282M\ m^3$, extrusion rate 5.3 m^3/s). Dome collapses but episode ends with largest dome in place. This is the fastest extrusion rate so far.
- Pause 3: April 2007 - July 2008

- Pause in dome growth (465 days)

- After Pause 3 (not included in Figure 2.8): 28 July 2008 - 2011
  - Slow extrusion of $39M\ m^3$ at 2.9 m^3/s on western flank of dome until 3 January 2009. Pause in dome growth for 10 months until 1 Nov 2010, when a new lava dome began to grow in conjunction with a swarm of earthquakes. Further rapid growth ocurred in early February 2010 and followed by dome collapse. Vigorous explosions occurred five times in Jan - Feb 2010. There was been no observed dome growth as of 30 April 2011 Cole et al. [2011], but surface deformation returned and gas measurements indicate that the system remains active [GVP].

2.4.3 Eruption and surface deformation data

Figure 2.8 shows the lava dome (efflux) volumes and durations of pauses and extrusions at the eruption of the Soufriere Hills Volcano Wadge et al. [2010]. The extrusion beginning in 1996 lasted around 2 years; the second extrusive phase was longer at 3.5 years and had the slowest eruption rate; and the extrusion beginning in 2006 lasted 1 year and had the fastest eruption rate. But the volume (dense rock equivalent) produced in each episode is roughly equal at about 300 million cubic meters per event. The pauses between eruptions were fairly consistant at about two years each. It is not obvious why the extrusions should last different times yet produce the same amount of material, while the pauses are similar durations. The periods of dome growth activity up until 2007 are apparent but the overall trend could be described as a linear increase in volume over time (shown by the red line) Elsworth et al. [2008].

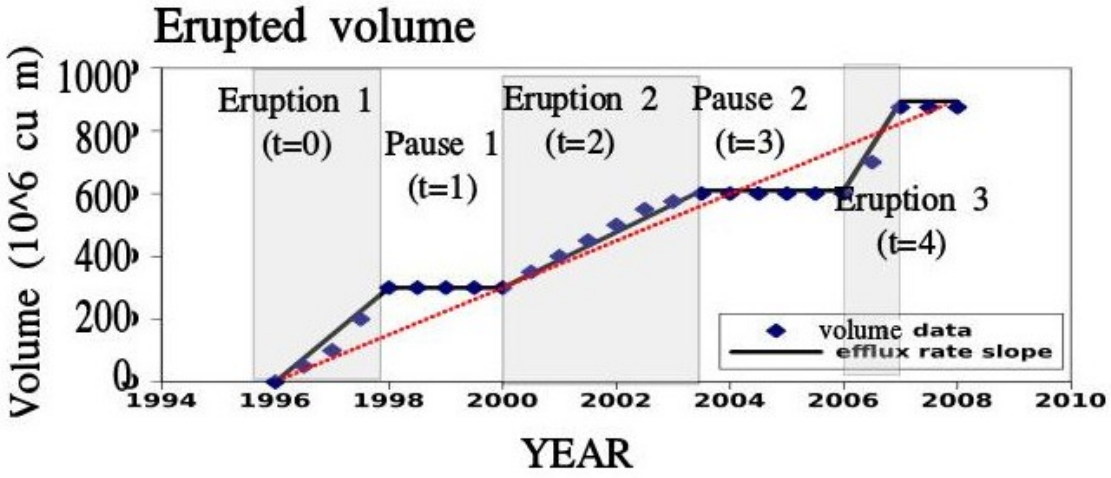

Figure 2.8: Soufriere Hills Volcano volume efflux data, and time labels for each eruptive event (gray shaded) and pause. The average rate is constant over 12 years (red dashed straight line fit), with multi-year cycles of eruption and pauses Elsworth et al. [2008]; Wadge et al. [2010].

Not only does the Soufriere Hills volcano lava dome grow in phases, but ground surface deformation around the volcano accompanies each phase of growth and repose. Global Positioning System (GPS) geodesy enables measurement of surface deformation, which has become common in volcano monitoring because of its high precision, relatively low cost, and ease of use. This provides vertical site residuals for all of ten sites on the volcano, and attempts have been made to define the geometry of the magma chamber system beneath the volcano by inverting the data. During each phase of extrusion at Soufriere Hills Volcano, the surface deformation decreased. During each pause, the surface deformation increased. This indicates magma movement beneath the volcano.

Figure 2.9 gives an example of data from GPS station labeled HARR, located 3.7 km almost due north of the central volcano vent Mattioli et al. [2010]. Each red dot represents a 24 hour average absolute point position estimate relative to the Earth's centre of mass. Three dome growth periods are represented by grey shading (subsidence), while unshaded periods (uplift) are periods with minimal surface lava efflux. The sites are continuous GPS sites, meaning that deformation of these sites is monitored in near real-time. Such data exist for 10 different stations with varying degrees of completeness, and we will address these data in more detail in later chapters.

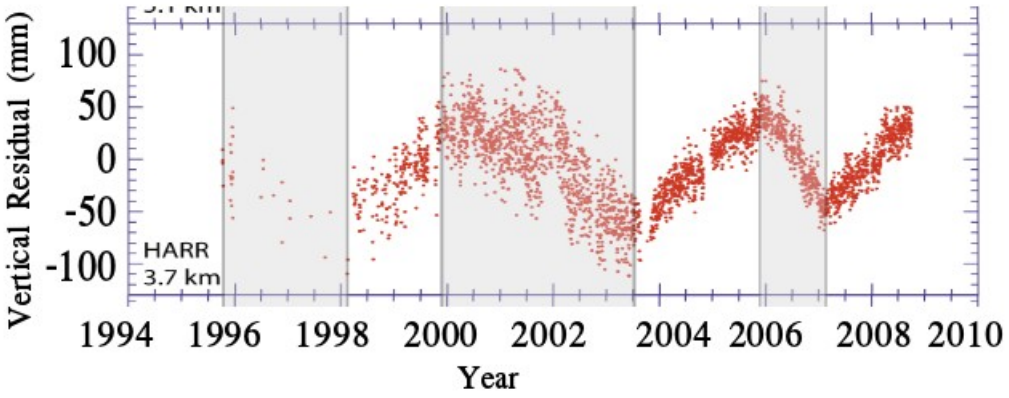

Figure 2.9: GPS data from station 'HARR' Mattioli et al. [2010]. Three dome growth periods are represented by grey shading (subsidence), while unshaded periods (uplift) are periods with minimal surface lava efflux.

2.4.4 Additional data and interpretation

The Monserrat Volcano Observatory "provides impartial advice to the authorities on the volcanic activity and its associated hazards and risks." A dilatometer, seismometer, tiltmeter, and surface GPS station recorded surface deformation and seismic activity during the eruptions. Inversion of surface deformation data and modeling of multi-chamber systems provides insights to some features of the Soufriere Hills magma supply system, but the size, depth, orientation, and other properties of any chambers are not well understood Elsworth et al. [2008]; Foroozan et al. [2011].

The crystal-rich andesite produced by the 1995-1999 eruption includes mafic inclusions which show evidence of having been molten when incorporated into the host magma or a deep supply of basalt Annen and Sparks [2002]; Murphy et al. [1998]. The low temperature and high crystallinity of the erupted magma are thought to indicate a cool, highly crystalline magma body beneath the volcano. Hot mafic magma may underplate a less dense resident magma, and intrude into highly crystalline andesite Murphy et al. [1998]. Additional analysis suggests that magma contained a set of minerals that are stable at 115-130 MPa, equivalent to a minimum depth for a water-saturated magma chamber of 5-6 km depth Barclay et al. [1998]. Release of SO_2 gas from the volcano suggest that mafic intrusions recharged the sulphur content of a shallow magma system, further supporting a chamber at 5-7 km depth Edmonds et al. [2001]. Further petrological analysis has been interpreted as evidence of magma ponding at 10-12 km depth Devine et al. [2003]

Early seismicity in June 1995 occurred at mostly less than 7 km depth Aspinall et al. [1998]. While there were swarms of seismic events just before and after the lava extrusions, most were shallow and near the crater. Long-period and hybrid earthquakes were present before explosive activity, presumably when gas pressures were elevated Miller et al. [1998]. Watson notes that SO_2 emission rates, which may indicate basaltic magma ponding in the crust, before the 1997 dome collapse correlate with the amplitude of ground deformation cycles Watson et al. [2000]. Seismic data at Montserrat precedes volcanic activity and suggests ongoing activity throughout the 1995 eruption that continues to the present.

However, many of the existing observations only record shallow seismicity and are not well resolved.

2.4.5 Key characteristics

The Soufriere Hills Volcano erupted in several phases from 1995-2006, with different eruption rates for different extrusive events. The overall eruption rate, however, was constant.

Seismic data suggest ongoing activity at the volcano, and ground deformation data that correlate with extrusions and pauses suggests inflation and deflation of at least one magma chamber. The andesite crystal content suggests magma that pools at different depths in the crust.

The data from Soufriere Hills Volcano suggest further complexity in the magma plumbing system, including at least a magma chamber and deep source of magma recharge.

2.5 Mount St Helens

2.5.1 Abstract

Washington state's Mount St Helens 1980-86 eruption exhibits many of the same patterns as Soufriere Hills volcano - cycles of dome growth and collapse, evolving magma types, and seismic activity over a range of depths.

Mount St Helens began a series of eruptions in 1980 when a large landslide and powerful explosive eruption created a large crater. The following five years showed a series of lava extrusions and dome growth, punctuated by several smaller explosive events Brantley and Myers [2000]. The location of the volcano is shown in Figure 2.10, and a photo of the lava dome in 2007 is shown in Figure 2.11

After a large explosive eruption, Mount St Helens went into cycles of dome growth and collapse but the overall extrusion rate waned with time. In this section, we present data for the lava dome eruptions and illustrate the waning growth rate. We then provide more detail from the literature regarding seismic evidence for magma residing at depths of 7-14 km and changes in dacite composition and crystallinity one eruption to the next Blundy and Cashman [2001]; Gardner et al. [1995]; Scandone and Malone [1985]. We conclude with a brief discussion of literature which suggests different ways in which an eruption may be triggered Blake [1984]; Blundy and Cashman [2005]; Tait et al. [1989].

2.5.2 Background and timeline

At 8.32am PST on 18 May 1980, a magnitude 5.1 earthquake was recorded at Mount St Helens and, 15 to 20 seconds later, the bulging north flank and summit fell away in a landslide Brantley and Myers [2000]. This depressurised the volcano magma system and triggered an explosive eruption. This blast produced a column of ash and gas (eruption column) 24 km into the atmosphere. Less than an hour later, a second eruption column formed during an explosive eruption from the crater. Just after noon pyroclastic flows, or avalanches of hot ash, pumice, and gas, flowed from the crater at 80 to 130 km per hour. In the years that followed, there were periods of lava dome growth that gradually waned. The last period of growth in this sequence was recorded in 1986, although brief explosive events

were observed in 1989 and 1990 [GVP].

We present a timeline of the activity in the 1980-86 eruption. In the next section, we present data regarding the erupted volume and eruption rate.

Figure 2.10: Mount St Helens location in Washington State, USA

Figure 2.11: Close-up view of Mount St Helens lava dome in 2007.

2.5.2.1 Timeline of events in 1980-1986 eruptive series Brantley and Myers [2000]; Swanson and Holcomb [1989]

- Before I: 16 March 1980 to 17 May 1980
  - Increasing number of earthquakes in days leading up to 18 May explosion. Steam explosions and 150m bulge in volcano north flank. April shows major increase in seismic energy release Qamar et al. [1983]
- I: 18 May 1980 - Jan 1983
  - 18 May explosion: Magnitude 5.1 earthquake at 8.32am, then summit falls away in landslide. Explosive eruption of rock, ash, gas, and steam to the north sends eruption column 15 miles into atmosphere. Second eruption column builds during explosive column from crater. At noon, pyroclastic flows of hot ash, pumice, and gas are measured at 80 to 130 km per hour. Mineral content in the pumice indicates rapid ascent from reservoir, and some lava includes minerals representing "old" magma stored in conduit that is displaced by magma travelling from source to surface Eichelberger [1995].
  - 25 May - 16 Oct 1980: five smaller explosive episodes, eruption columns 12-15 km above sea level, each explosive event followed by aftershock-like series of earthquakes located 7 to 14 km beneath volcano Scandone and Malone [1985]. Lava extrusion begins to form lava dome.
  - 16 Oct 1980 - 21 Oct 1983: Lava dome building episodes, with minor explosive activity accompanying each episode. Each dome building episode adds 1 to 20 cubic km of new lava to the dome. By November 1980, electronic tiltmeter indicates net subsidence of 20-70cm (perhaps indicating deeper source of magma) Scandone and Malone [1985]
- II: Jan 1983 - May 1986
  - Four more dome building episodes show a slower rate of lava dome growth than in period I.
- III: May 1986 - Oct 1986

- Last dome growth building episode adds larger volume than previous slow growth rate apparent in period II.

- After III

  - Bursts of brief but intense seismic activity, lasting minutes to hours; accompanied by several small explosions with eruption columns from dome. After the 1980-1986 eruption series, dome growth ceased and Mount St Helens entered a period of dormancy. In 2004, a 20m diameter vent formed as a small explosion broke through a 150m thick glacier that had grown on the southern part of the crater since 1986. A dacite lava dome grew from 23 September 2004 to 31 December 2005 and exhibited sustained, near-equilibrium behaviour; the lava extruded in each episode was bubbly, and emitted volcanic gasses indicated the presence of magma with exsolved gas content lower than during the 1980s eruption Iverson et al. [2006].

2.5.3 Eruption data

The lava dome growth can be divided into three periods, delineated by the red lines in Figure 2.12. We include lava dome volume since 18 October 1980, as the eruption data from before 18 October contains both tephra deposits and lava dome in one figure, and lava domes between May and October were destroyed by subsequent explosive activity. The lava dome volume is measured by topographic maps (length, width, and depth) at the end of each extrusive episode, and each episode is represented by one point in the figure. The overall dome growth is divided into three periods: The extrusion rate increases rapidly at first (I) and becomes slower with time (II), and a final large dome growth event has a faster extrusion rate (III) and could be characterised as a separate event. Plotting the overall growth rate of the dome since 18 October 1980, we see that the rate decreases with time as shown in Figure 2.13. Significant explosive events occurred only in the first year of a multi-year eruptive sequence.

The duration of each extrusion remains fairly constant with the exception of the February 1983 event as shown in Figure 2.15, but the period between dome-building events increased with time as shown in Figure 2.13 Swanson and Holcomb [1989]. Additionally, explosive activity usually lasted hours while dome-building usually lasted days Swanson and Holcomb [1989].

In the next section we provide more detail about the Mount St Helens 1980-1986 eruption series.

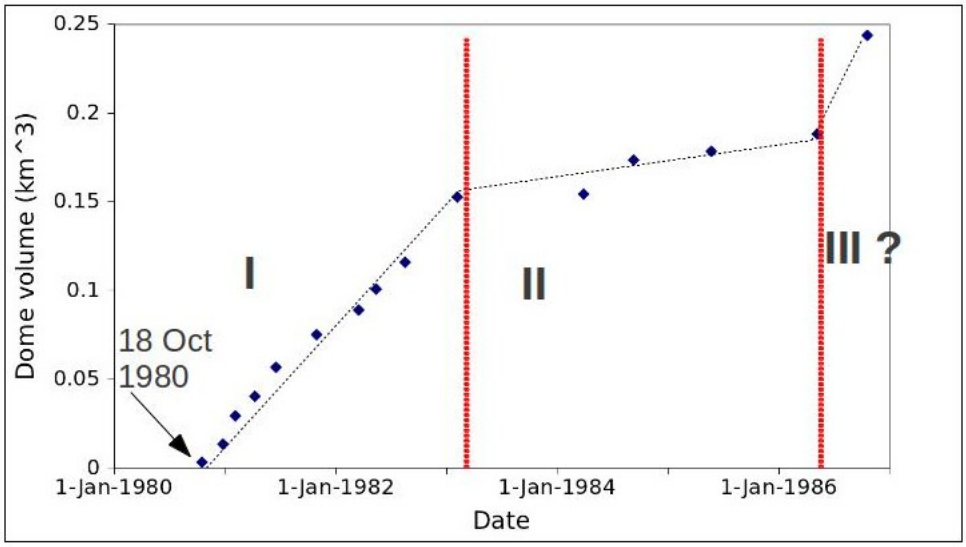

Figure 2.12: Mount St Helens lava dome growth, as measured by topographic maps (length, width, depth) at the end of each extrusive episode since 18 Oct 1980. Each point represents one episode. Information regarding lava dome volume before October 1980 does not separate tephra from lava dome, and domes between May and October were destroyed by subsequent explosive activity. The overall dome growth can be divided into three periods: Period I comprises a steady overall growth rate, period II is waning, and period III could be interpreted as a separate event. Pauses between events increase in duration as the eruptive sequence progresses, and dome growth stops after 1986 Swanson and Holcomb [1989].

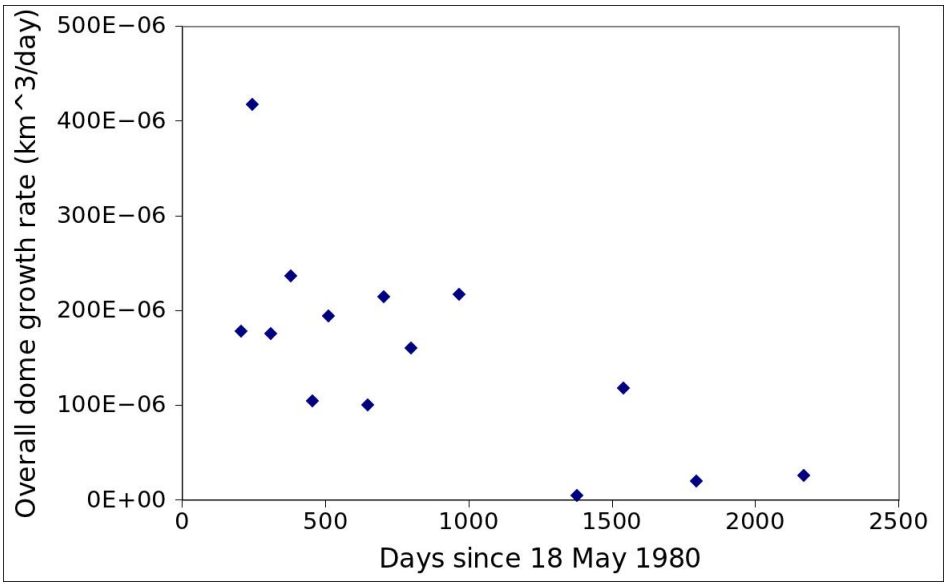

Figure 2.13: Mount St Helens lava dome growth rate wanes with time. This is a plot of the overall growth rate of the dome since 18 May 1980, using the dome growth data since 18 Oct 1980 Swanson and Holcomb [1989].

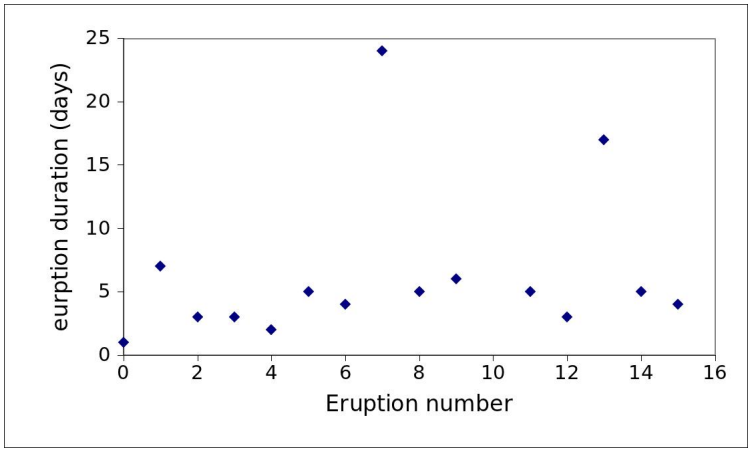

Figure 2.14: Durations of dome growth episodes remains fairly constant with the exception of two events including one in February 1983, which lasted for an entire year Swanson and Holcomb [1989]).

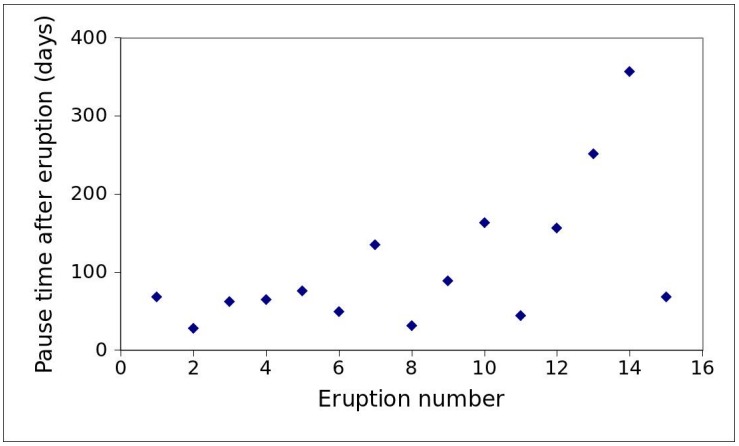

Figure 2.15: Period between dome growth events increases over time Swanson and Holcomb [1989].

2.5.4 Additional data and interpretation

The US Geological Survey has monitored erupted material and seismic data at Mount St Helens.

Earthquakes located 7-14 km beneath the volcano followed each explosive event in 1980, and the energy of each event was proportional to the corresponding volume of erupted magma Scandone and Malone [1985]. In later years, before an episode of dome growth, seismicity was typically low-frequency and situated in a vertically elongate volume at shallow depth beneath the soon-to-be-active vent Eichelberger [1995].

Mount St Helens' 1980 explosive events all erupted dacitic (silica content around 65 weight percent, and containing plagioclase feldsbar and hydrous minerals) magma, but these vary greatly in temperature, water content, crystallinity, and thus vicsosity. The erupted volume of dacite during explosive eruptions is correlated with the length of the preceding quiescent period Gardner et al. [1995]. There are compositional changes to more mafic and less hydrous lavas during explosive events of 1980 Scandone and Malone [1985]. Crystal content suggests that the explosive products from 18 May 1980 had crystallised at depths of >6 km Blundy and Cashman [2001].

The lava dome itself comprises dacitic magma with crystallinity that increased rapidly through 1980 then slowly through 1985; with silica content decreasing through 1981, then gradually increasing through 1986 Cashman [1992]; Murase et al. [1985]. And at least one mixed magma was recorded during the 18 May eruption Cashman [1992].

The literature has interpreted this information to suggest that a shallow intrusion fed the 18 May explosive eruption, and a deeper reservoir of silicic magma continued to supply the eruption after that Cashman [1992]. Additionally, Blake proposed and Tait further developed a mechanism by which the pressure in the reservoir does not require a deep source of recharge to trigger or sustain an eruption: rather, crystallisation of the magma causes it to become saturated with volatiles, leading to gas bubbles and thus pressure increase Blake [1984]; Tait et al. [1989]. Blundy and Cashman suggest this model is applicable to Mount St Helens based on crystal size and water content Blundy and Cashman [2005].

2.5.5 Key characteristics

After a large explosive eruption, Mount St Helens settled into cycles of dome growth and collapse but the overall extrusion rate waned with time. The short-term nature of the dome growth cycles (each extrusive event lasted for a roughly equal number of days) may be controlled by the conduit rather than a deep source, but we are interested in the long term effusion rate that wanes with time. Seismic activity and changes in dacite crystallinity and composition both suggest complex behaviour in the subsurface.

2.6 Mount Fugen, Unzen volcanic complex

2.6.1 Abstract

Mount Fugen of the Unzen volcanic complex in Japan included two main phases of eruption from 1990-95. The eruption comprised four episodes of dome growth that vary in rate (first fast, then slow, then fast, and finally slowing to nothing). Explosive events accompanied only the initial stages of dome growth.

The Unzen volcanic complex includes three large volcanoes on Japan's Shimabara Peninsula, east of Nagasaki, as shown in Figure 2.16. Seismic activity was detected at the volcano's flanks in the early stages of the eruption until it focused almost entirely beneath the summit crater. In this section, we present data showing the decreasing effusion rate, and a chart showing the positioning of seismic events during this time. We also discuss variations in magma composition that indicates new magma mingling with ponded old magma Nakada et al. [1999]; Nakamura [1995]. The eruption may indicate a chamber which is recharged from depth, with the end of the the eruption brought about by the recharge stopping.

Figure 2.16: Unzen volcano complex, on the Shimabara peninsula in southwest Japan

2.6.2 Background and timeline

In 1989, a swarm of earthquakes began below the western flank of Mount Fugen. After 198 years of dormancy (the most recent historical eruptions occurred in 1663 and 1792), an eruption started at the summit of the volcano Mount Fugen in November 1990. The ash cloud is shown in the top panel of Figure 2.17, and the lava dome after the eruption is shown in the bottom panel.

We present a timeline of the episodes of dome growth during the Mount Fugen 1990. In the next section, we present eruption and seismic data.

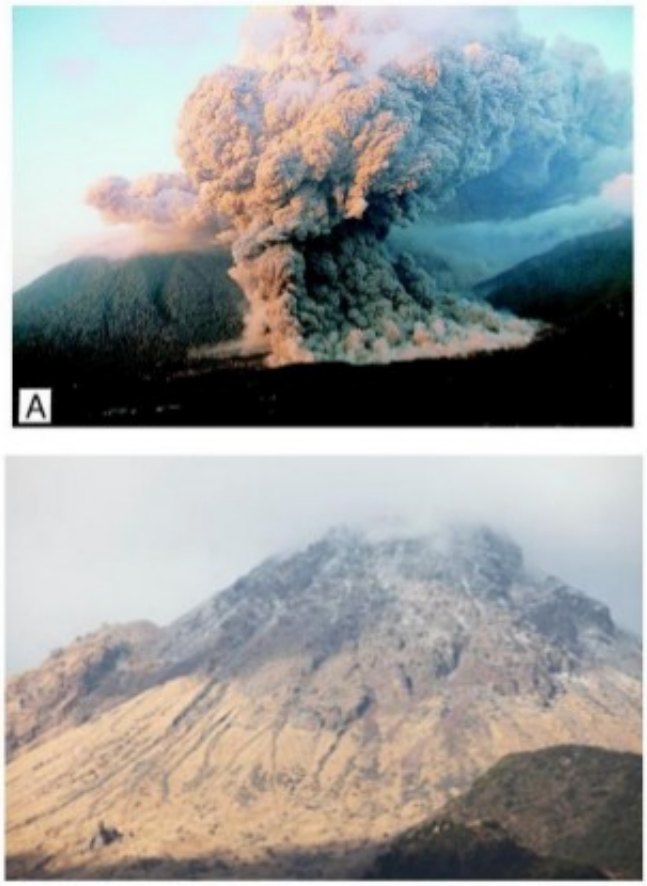

Figure 2.17: Ash cloud and pyroclastic flows on northeast flope of Mount Fugen at Unzen volcanic complex, 24 June 1993 (top), and the lava dome after the eruption (bottom) Nakada et al. [1999]

2.6.2.1 Timeline of events in 1990 - 1995 Nakada et al. [1999]

- I: November 1990 - December 1991
  - A phreatic eruption, preceded by earthquake swarms migrating toward the summit, begins in November 1990. Phreatic eruptions continue until May 1991 along with a first pulse of lava dome growth, and growth pauses for two weeks until later in May, at which point dome growth continues and pyroclastic flows and dome collapse begin to occur. Explosions occured in June 1991. In September 1991, the largest pyroclastic flow due to dome collapses releases up to $4{\times}10^6\ m^3$ of debris.
- II: December 1991 - October 1992
  - A very slow period of lava extrusion
- III: October 1992 - February 1993
  - Onset of a second pulse of lava extrusion in the form of a new lobe, and pyroclastic flows continue.
- IV: February 1993 - February 1995
  - Summit earthquakes continue and February 1995 sees the halt of lava effusion, followed by slow deformation of dome.
- After IV: The volcano has remained inactive since the 1995 activity.

2.6.3 Eruption data

Mount Fugen experienced explosive eruptions in its initial stages of dome growth during the 1990-95 eruption but was mostly a continuous effusion of magma. The cumulative volume for the lava dome growth, including volumes of dome-collapse pyroclastic flows, is shown in Figure 2.18 Nakada et al. [1999]. The total volume of lava erupted was 2.1×10^8 m^3, half of which remained as the summit lava dome. The data suggest four periods of dome growth I to IV, with rates 8.3, 2, 6.2, and 0.2×10^6 m^3 per month respectively. The periods of dome growth are delineated by dashed red lines, and the growth rates by dashed black lines. The overall growth rate of the lava dome (although these data are cumulative erupted volume, so also includes some pyroclastic material) is shown to wane with time in Figure 2.19.

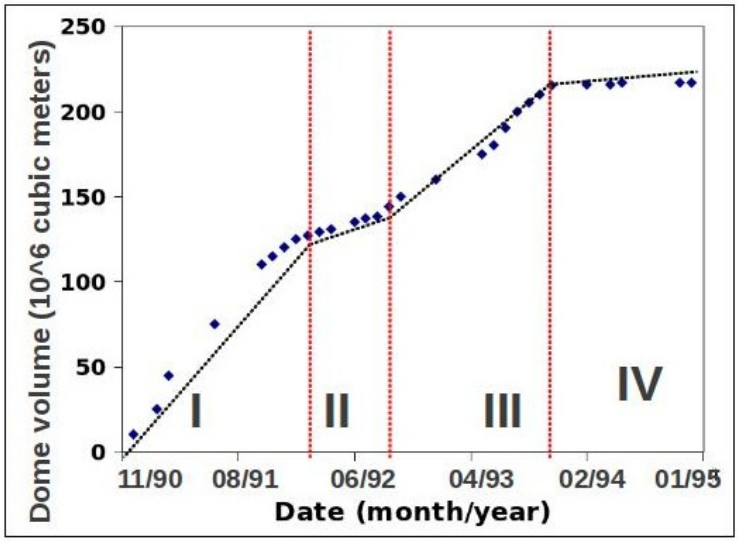

Figure 2.18: Mount Fugen, Unzen volcano complex, shows a gradually decreasing rate of effusion in 1990-95, and growth can be divided into episodes I-IV (red dashed lines) with four different eruption rates (black dashed lines). The individual data points do not corrrespond directly to pulses of growth; rather, they are cumulative dome volumes Nakada et al. [1999].

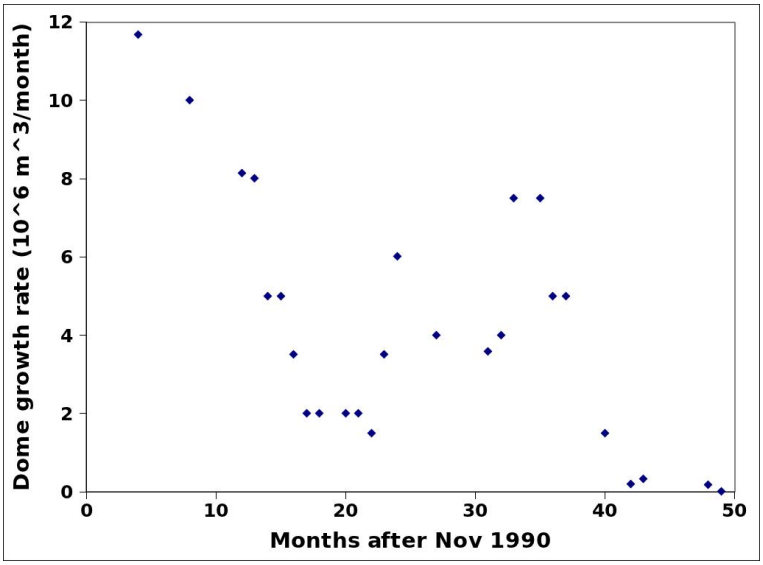

Figure 2.19: Mount Fugen, Unzen volcano complex, growth rate from November 1990 through 1995.

Earthquakes around the volcano indicate evolution of a subsurface system, or at least magma movement from east to west beneath the volcano. Seismic events shifted position from around the flanks to nearly directly beneath the summit as the eruptive sequence progressed. Figure 2.20 shows the change in epicenter positions over time. The top image provides a map of the area with dots indicating all the earthquakes during the 1990-95 eruption. The bottom image separates these events by date: the x-axis is the east-west position corresponding to the top image, and the y-axis shows the timing of events. Up until 1991, most earthquakes were located west of the summit. From 1991 to 1995, they were concentrated mostly underneath the summit. Low-frequency summit earthquakes coincide with emergence of a dome. We do not have detailed information regarding the depth of the earthquakes, although volcano-tectonic (V-T) earthquakes have been associated with 13 km depth [GVP] and the injection of magma into surrounding rock; and they became shallower as they migrated eastward Nakada et al. [1999].

In the next section, we present additional information regarding magma composition at Unzen.

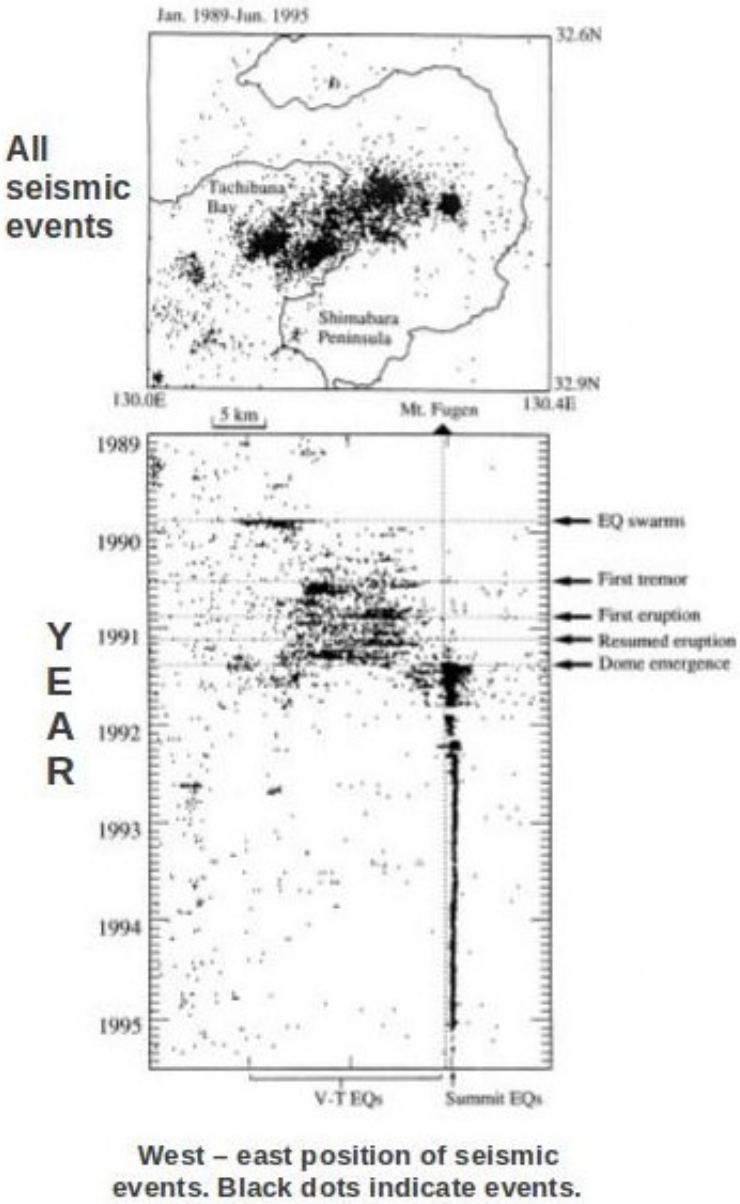

Figure 2.20: Unzen volcano complex change in position of earthquakes from 1989 - 1995. Top: map of all earthquakes during 1989-95 eruption. Bottom: earthquakes separated by date (y-axis) to show east-west position over time (x-axis). VT EQs = volcano-tectonic earthquakes, associated with deeper seismicity [GVP]. Summit EQs = mainly low-frequency earthquakes. Earthquakes shifted position from around the flanks to nearly directly beneath the summit Nakada et al. [1999]. V-T earthquakes are associated with 13 km depth [GVP] and are thought to be the result of injection of magma into surrounding rock.

2.6.4 Additional data and interpretation

Phases II and IV in Figure 2.18 show periods during which dome growth was very slow, indicating slow magma ascent and allowing for cooling and crystallisation. Variation in magma crystallinity also correlated to the lava effusion rate: lower effusion rate had higher crystallinity Nakada et al. [1999].

Ground deformation trends include old parts of the dome swelling and uplifting during periods II and IV, preceding the main pulses of activity, in November 1991 to December 1992 and February to March 1993 Nakada et al. [1999]. The dome began to deform slowly after magma effusion ceased in February 1995, and absence of surface deformation characterised the end of the eruption. Nakada et al. [1999].

The dome lava is dacite (silicic) with small but significant variations in composition, marked by mixing of high- and low-temperature magmas and the associated phenocryst (relatively large crystal) abundance Nakamura [1995]. Some enclaves ('blobs' containing two types of magma) in lavas further indicate mixing of new and old magmas during the eruption Nakada et al. [1999]; Nakamura [1995]. This follows from a chamber that contains old magma being replenished with new magma from depth (also indicated by deep seismicity).

2.6.5 Key characteristics

The 1990-95 eruption at Unzen is another example of a largely effusive eruption that decreased in rate. Seismic activity shifted from the flanks of the volcano in the early part of the eruption to beneath the summit in 1991, after which the lava dome kept growing. The dome growth was faster in phase I than in later phase III, and the dacite magma evolved compositionally and contained enclaves of basalt. These factors lead to a complex picture of a chamber which is recharged from a deep source or has been subjected to cooling and crystallisation of magma in order to build up the pressure required to exhibit two pulses of eruption.

2.7 Eyjafjallajokull

2.7.1 Abstract

The last volcano we discuss is Eyjafjallajokull. Eyjafjallajokull is an ice-covered stratovolcano on the south coast of Iceland as shown in Figure 2.21, just south of the mid-Atlantic Ridge, where the North American and Eurasian plates are moving apart. We discuss this volcano to provide context for a system whose seismic and magma composition data suggest magma that pools at multiple locations in Earth's crust.

Eyjafjallajokull erupted most recently in 2010. Its position at a divergent plate boundary means that it has a magma source derived from a rifting zone. We provide a compilation of seismic data that highlight specific areas of magma movement followed by a timeline describing the events of its 2010 eruption. We then discuss how these data has been interpreted to create a picture of multiple sills which erupt magma at different times, with the magma from a deeper sill bypassing the upper sills.

Figure 2.21: Location of Eyjafjallajokull

2.7.2 Background and timeline

The last historical eruption prior to 2010 was from December 1821 to January 1823 and produced intermediate-to-silicic tephra from the central caldera. Neighbouring Katla volcano historically erupts in the months after Eyjafjallajokull, producing basalt and dacite and rhyolite, which suggests a magma chamber complex with dykes and sills beneath Eyjafjallajokull and its neighbours. The 2010 eruption was preceded by deep-source ground inflation and deeper seismicity and consisted of both flank eruptions and explosive summit eruptions, one of which is pictured in Figure 2.22.

We provide a timeline of the activity during the 2010 eruption, and in the next section we provide seismic data showing the downward-propagating clusters of earthquakes during the eruption.

Figure 2.22: Eyjafjallajokull erupts in March 2010

2.7.2.1 Timeline of events: 2010 eruption series Sigmarsson et al. [2011]

- Dec 2009 - 20 March 2010: deep-source ground inflation begins, along with decreasing depth of seismicity. Thousands of microearthquakes detected under northeast flank Tarasewicz et al. [2012]

- 20 March 2010: Flank eruption produces olivine and plagioclase-phyric primitive and homogeneous mildly-alkaline basalt until 12 April; no ground deformation

- 14 April 2010: Explosive eruption from summit accompanied by seismicity at 5 km depth directly beneath summit. Suggests deflation of shallow magma chamber. Three types of basaltic, intermediate, and silicic magma compositions erupt until 19 April Sigmundsson et al. [2010]. Purely magmatic discharge from 21 - 27 April at rate of $10{\times}10^{6}$ kgs^{-1}

- Late April - early May: magmatic discharge 10^{4} to 10^{5} kgs^{-1}. Melting of 200m of overlying ice from summit region could reduce pressure on vent by 2 MPa Tarasewicz et al. [2012]. New injection of deep-derived basalt inferred by deep seismicity and the appearance of more primitive basalt (magnesium-rich olivine phenocrysts).

- 5 May 2010: Begin first of 3 explosive episodes, lasting 1-2 days each, preceded by seismicity at depths of 10-13 km, 19 km, and 24 km depth Tarasewicz et al. [2012]. Magmatic discharge increase to 10^{5} kgs^{-1}. Melt composition changes from less mafic to more silicic than first explosive phase.

- 6 May to late May: Decline in discharge until end of eruption.

2.7.3 Seismic data

The earthquakes during the Eyjafjallajokull 2010 eruption propagate downward through the crust. In Figure 2.23, red dots highlight 270 earthquakes deeper than 10 km, and blue dots show other earthquakes recorded in April and May during the summit eruption. The map in the top of the figure shows cross sections of the volcano subsurface along A-B and C-D, which describe where the earthquakes occur Tarasewicz et al. [2012]. Earthquakes are clustered at distinct depths.

The 2010 eruption effused $1.4{\times}10^7$ m^3 of lava and exploded $1.4{\times}10^8$ m^3 of tephra. In the next section, we explore information about the types of magma erupted and how this information has been used to build a picture of a multi-sill magma plumbing system.

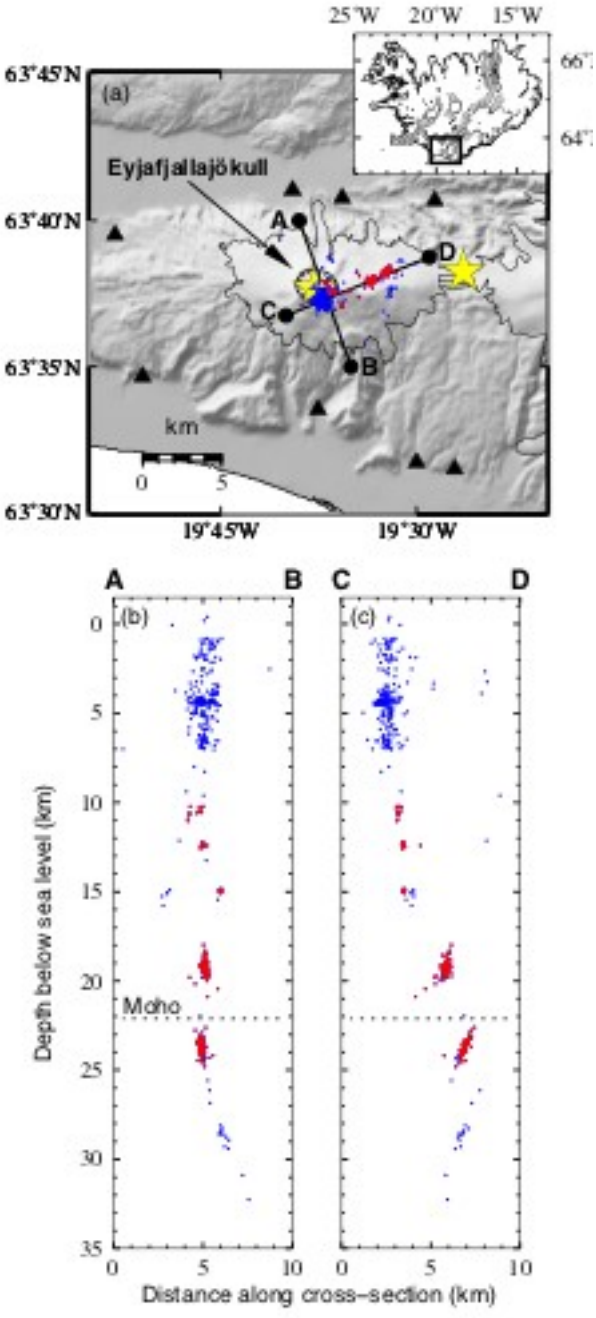

Figure 2.23: Epicenters of 502 microearthquakes (blue and red dots) recorded from 13 April to 17 May 2010 during the summit eruption. Red dots highlight earthquakes above 10 *km* depth that form a downward-propagating series of clusters; blue dots show all other events during the period. In the map, black triangles are seismometer locations, thin black lines are extent of glaciers, and yellow stars are eruption sites Tarasewicz et al. [2012]. The discrete clusters of events suggest areas in which magma movement occurs.

2.7.4 Additional data and interpretation

Eyjafjallajokull is composed of a combination of basaltic and andesitic lavas Sigmundsson et al. [2010]. Presence in the tephra record of basaltic, intermediate, and silicic compositions suggests magma mingling without homogenisation. Over time the mafic component became more primitive but formed a smaller proportion of the melt, and the silicic component became less evolved but formed a larger proportion of the melt Sigmarsson et al. [2011]. Rapid compositional changes in products suggest that basalt mixing with silicic magma occurs on a timescale of a few hours to days, while the interval between first detected magma injection (indicated by volcano-tectonic earthquakes) and eruption was several months Sigmarsson et al. [2011].

Ground deformatio n was rapid but negligible before the first eruption (0.5 mm per day) Sigmundsson et al. [2010]. The lack of surface deformation during the eruption indicates that the amount of magma drained from shallow depth was small; rather, magma flowed from considerable depth Sigmundsson et al. [2010]. One interpretation is that mafic magma either bypassed the shallow magma chamber or counterbalanced the erupted volume with inflow of fresh magma Tarasewicz et al. [2012].

As shown in Figure 2.23, many of the 270 earthquakes at Eyjafjallajokull deeper than 10 km occurred in clusters at 24 km and 15 km depth separated in time, indicating that there may be a response of each sill to the draining of another Tarasewicz et al. [2012]. The progressive deepening of seismic activity can be likened to a decompression wave propagating downward through the crust and causing sequential depressurisation of vertically stacked magma chambers as melt is mobilised and moved Tarasewicz et al. [2012].

2.7.5 Key characteristics

Eyjafjallajokull is a stratovolcano situated near a rift zone. It erupted explosively alongside an extrusive flank eruption in 2010, and changing magma composition over the course of the eruption has been interpreted as evidence of multiple sills from which magma may at times mingle but also bypass each other. Seismic evidence indicates a downward-propagating sequence in which chambers erupt successively. This provides context for a highly complex system of chambers at multiple locations in Earth's crust.

2.8 Discussion and conclusions

In this chapter, we have discussed the activity from five volcanoes which have experienced long-lived effusive eruptions with cycles of activity and repose. Features in the eruption style, magma composition, and seismic activity at these volcanoes are important indicators of processes that may be controlled by a deep plumbing system.

The long-term eruption rate of these effusive eruptions is either constant (Soufriere Hills Volcano and Mount Etna) or waning (Mount St Helens and Unzen). However, the eruption rates vary from one cycle to the next at each volcano. A constant eruption rate suggests a magma plumbing system that comprises at least a chamber and a deep source magma recharge.

Magma composition changes in time and sometimes involves two types of magma at the same volcano. Changes in crystal content and chemistry suggest the depth at which the magma pools in the crust, as crystal fractionation can be linked to certain pressures. Eruption of multiple magma types, or magmas that have evolved as mixing of multiple types over time, suggest a deep source injection of new magma into older, evolved magma.

Seismic activity is detected at different depths in the crust as well as different horizontal positions relative to the main eruptions, and these positions and depths change over the course of an eruption. This, along with ground deformation data in the vicinity of the volcano that shows inflation and deflation in conjunction with eruptive activity, suggests complex behaviour of magma in the subsurface.

Mount Etna has been used in one of the early examples of a single chamber magma plumbing system model, built by Wadge, which provides a framework in which to think about magma plumbing systems. Similarly, Eyjafjallajokull provides context for a model of multiple chambers that evolve over time.

We need to understand how a deep magma system controls the evolution of these eruptions and will generate a simple theoretical model to do so. In the next chapter, we begin with a model of a single chamber with and without recharge from a deep mantle source.

Chapter 3

A single chamber model

3.1 Abstract

The purpose of this chapter is to explore how the long-term trends of eruptions discussed in the previous chapter are controlled by a deep magma plumbing system. We build on the Wadge single chamber model to include the following components involved in establishing a long-term eruption trend: an elastic magma chamber and the relationship between chamber pressure and magma outflow volume; the rate of eruption from chamber to surface; the rate of recharge of magma into the chamber; and critical chamber overpressures at which the eruption starts and stops.

We refer to the literature models that focus on both chamber and conduit and focus on effusive eruptions as the type of event which is responsible for the majority of lava output in a multi-year eruptive cycle. We provide a model of a waning eruption and include a magma recharge to the chamber. We calculate eruption and pause duration for an eruptive series that experiences multiple episodes of effusion. We impose a critical value of overpressure for which the eruption starts and stops, which is a key element of our model. We conduct a parameter study in which we investigate the effects of conduit resistance, critical pressure at which an eruption starts and stops, and chamber volume on the efflux rate and volume. Changing the recharge rate allows for changes in eruption and pause durations from one cycle to the next.

A key result of this chapter is the application of the model to data from Mount St Helens and Unzen, whose eruptions wane with time, to calculate an effective conduit radius at these volcanoes. We also apply the recharge model to surface deformation and efflux data from the Soufriere Hills Volcano to calculate a magma recharge rate during the 1996-2007 eruption. We discuss these applications in the context of Stasiuk's model of an exponentially decaying eruption rate and eruption data from La Soufriere de St Vincent and Lonquimay.

3.2 Effusive eruption model, single chamber

We recall from the introduction that the literature refers to several models of a volcano in which the dynamics of a magma chamber control the onset and termination of an eruption, as well as the volume of magma which is released. If the system becomes sufficiently pressurised, magma may erupt to the surface; but if the degasses and crystallises rapidly, it may solidify in the crust.

We are interested in modeling slow effusive flow. Over the course of a lava extrusion, dome collapse generates pyroclastic flow, but chamber pressure is the main mechanism for the effusive eruption itself. In an effusive eruption, a slow viscous flow of lava erupts slowly, as gas escapes from the magma. The eruption rate needs to be slow enough for bubbles to escape by gas loss through permeable magma and conduit walls Jaupart and Allègre [1991]; Melnik and Sparks [1999].

Blake provides a model of a magma chamber in which inflow of material to the chamber from below leads to magma pressure P which exceeds lithostatic pressure P_L by an amount greater than the tensile strength of the chamber walls Blake [1981]. The rate of pressurisation of the magma reservoir as new magma is injected depends on the compressibility of the magma and the elasticity of the surrounding crust Bower and Woods [1997]; Huppert and Woods [2002]. The volume V of a liquid magma with bulk modulus κ changes with pressure P as

$$\frac{dV}{dP} = \frac{V}{\kappa} \tag{3.1}$$

Blake [1981]; Druitt and Sparks [1984].

3.2.1 Understanding a model of slow effusive flow

We consider a low Reynolds number flow driven by a pressure gradient G through a pipe that is described by Poiseuille flow relations Melnik and Sparks [2006]; Wilson and Head III [1981]

$$G = \frac{8\mu Q}{\pi r^4} \tag{3.2}$$

for a pipe of radius r, effective magma viscosity μ, and volume flux Q.

Magma ascending a conduit of length L goes from a chamber at pressure P_{CH} to a surface pressure P_S. At depth, it also has the weight of the magma column adding to the pressure. Thus

$$\frac{P_{CH} - P_S - \rho g L}{L} = \frac{8\mu Q}{\pi r^4} \tag{3.3}$$

for effective magma density ρ. In equilibrium, we suppose that

$$P_{CH} = P_S + \rho g L \tag{3.4}$$

If the chamber is overpressured by ΔP then

$$Q = \frac{\pi r^4 \Delta P}{8\mu} \tag{3.5}$$

This leads us to the flow law

$$Q_{er}(t) = F \Delta P(t) \tag{3.6}$$

where $1/F$ is representative of the resistance to flow within the conduit.

Figure 3.1 gives a diagram of the model components. The magma chamber has volume V_c, pressure P, and the resistance factor in the conduit connecting the chamber to the surface due to viscosity, crystallisation, and friction is $1/F$. Eruption rate to the surface is Q_{er}, and a recharge rate of magma from a deep source is Q_{in}; though we do not consider recharge in this example, we include this for future reference.

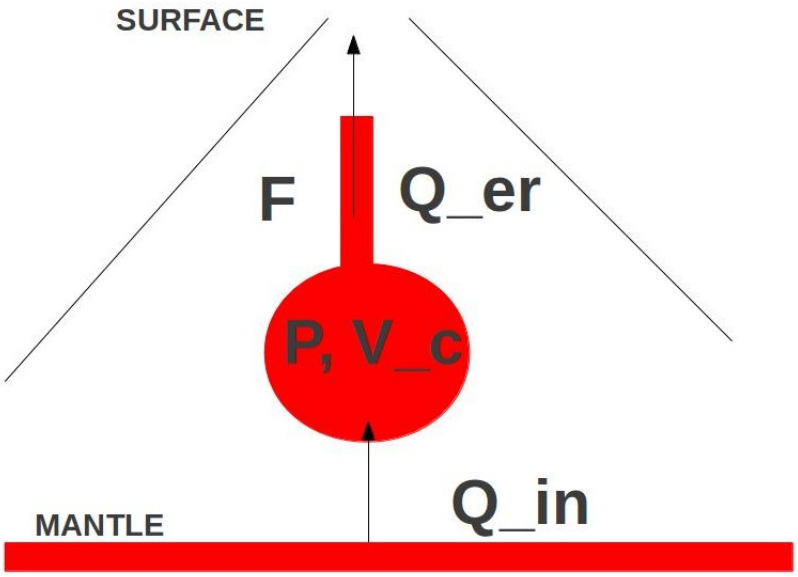

Figure 3.1: Diagram of single chamber model: volume V_c, pressure P, resistance in conduit connecting chamber to surface $1/F$, eruption rate to surface Q_{er}, and recharge rate of magma from deep source Q_{in}

The pressure change in the chamber associated with the flow in Equation 3.6 is

$$\frac{d\Delta P}{dt} = \frac{-F\Delta P(t)}{\beta V_c} \tag{3.7}$$

for chamber volume V_c, magma bulk compressibility β (inverse of bulk modulus κ from Equation 3.1), and conduit resistance $1/F$. Solving this equation leads to a chamber overpressure that evolves as simple exponential decay

$$\Delta P = \Delta P(0) exp(-\frac{Ft}{\beta V_c}) \tag{3.8}$$

for initial chamber overpressure $\Delta P(0)$.

The volume efflux Q_{er} also follows exponential decay

$$Q_{er} = \frac{dV}{dt} = F\Delta P(0) exp(\frac{-Ft}{\beta V_c}) \tag{3.9}$$

Equation 3.9 shows that the flow rate scales as $F\Delta P(0)$ and the time of eruption scales as $\beta V_c/F$ as shown in dimensionless plot Figure 3.2.

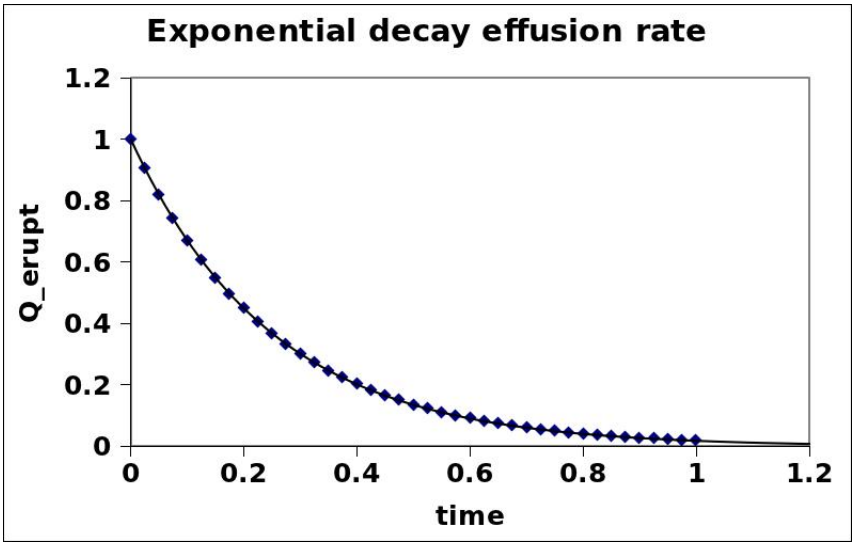

Figure 3.2: Efflux rate Q_{er} decays exponentially with time in a single depressurising chamber.

3.2.2 Applying the model

We solve Equation 3.9 for the erupted volume $V(t)$

$$V(t) = \beta V_c \Delta P(0)(1 - exp(-\frac{Ft}{\beta V_c})) \tag{3.10}$$

Equation 3.10 shows that the total erupted volume V_{tot} after a large time t is

$$V_{tot} = \beta V_c \Delta P(0) \tag{3.11}$$

and

$$ln(1 - \frac{V(t)}{V_{tot}}) = \frac{-Ft}{\beta V_c} \tag{3.12}$$

To compare data from real volcanoes with this model, we begin by comparing measurements of erupted volume $V(t)$ at a series of times t. We plot ln(1-V(t)/V_{tot}) as a function of time. The purpose of this exercise is to find a value for V_{tot} that makes the relationship in Equation 3.12 linear, and thus consistent with an exponential decay rate. Once we have this value, we can gain some insight into other parameters in the righthand side of Equation 3.12.

The significance of V_{tot} is as follows. From the data for $V(t)$ at a volcano we want to estimate the total volume V_{tot} that would erupt if the chamber depressurises completely, and the timescale over which it erupts. If we assume that the eruption stops smoothly and has erupted the entire available volume due to chamber pressure change, we can estimate the maximum value of $V(t)$ as V_{tot}. Then we can calculate the time constant of the eruption.

From Equation 3.12, once we verify a value for V_{tot}, we can also estimate $F/\beta V_c$, which is the slope of a plot of ln(1-V(t)/V_{tot}) versus time. However, we choose estimated values of magma bulk compressibility β and initial chamber overpressure $\Delta P(0)$, and use these, based on Equation 3.11, to estimate the size of the chamber V_c. Thus we only gain knowledge of F in relation to several broadly defined parameters (variability discussed in next section).

Using V_{tot} and estimated values of $\Delta P(0)$, β, and V_c allows us to find a range of effective values for F for a given eruption. If we know magma viscosity μ, we can then get a range of effective conduit radius from Equations 3.5 and 3.6.

Next we apply the model as described above to various eruptions, beginning with finding values of V_{tot} for La Soufriere de St Vincent and Paricutin to demonstrate their behaviour as exponentially decaying eruptions, and showing a range of chamber volumes and overpressures associated with these values.

3.2.3 Application of model to St Vincent and Paricutin

First we look at the 1979 eruption of La Soufriere de St Vincent in the Windward Islands of the Caribbean. This data was collected by plots of the lava dome in time, assuming an edge angle of 30 degrees and a flat top, which leads to error of at least 10% Huppert et al. [1982]. In Figure 3.3, we plot

$$ln(1 - \frac{V(t)}{V_{tot}}) \tag{3.13}$$

as a function of time. Recall from the previous section that, according to Equation 3.12, this relationship will be linear for exponential decay. The purpose of this plot is to find a value of V_{tot}.

We estimate V_{tot} to be $4.8{\times}10^7$ m^3, which is the volume that was erupted by the end of the data set. At the end of the eruption, if the estimate of V_{tot} is incorrect, the effective error is amplified, which may explain the apparent deviation in the last point. However, as shown in Figure 3.4, our model provides a good fit to the St Vincent erupted volume data. We selected V_{tot} to minimise the root square error of volume compared to the data points. Although this is the best fit, V_{tot} between 46 and $50{\times}10^6$ m^3 gives a least squares correlation in excess of 0.99.

We also argue that the eruption really started after the first seven days of monitoring. In the original data set, there was uncertainty regarding when the eruption began. Our model shows it started in earnest on Day 7, and the erupted volume before this was negligible.

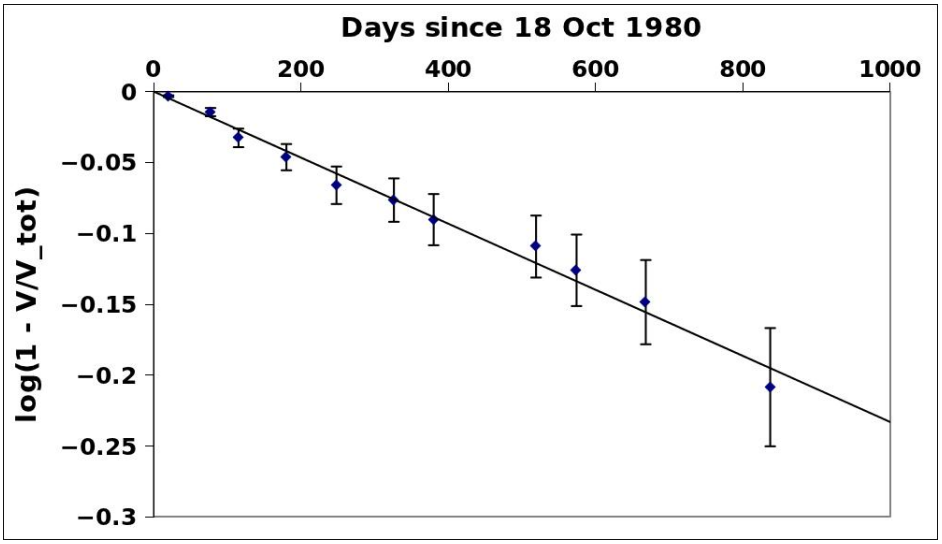

Figure 3.3: Application of exponential decay model to La Soufriere de St Vincent 1979 eruption. Plot of ln(1-V/Vtot) for V_{tot} equal to the maximum observed lava dome volume is linear (slope is $-F/\beta V_c$), showing a good exponential fit for V_{tot}=48×10^6 m^3. Data is from Huppert et al. [1982]

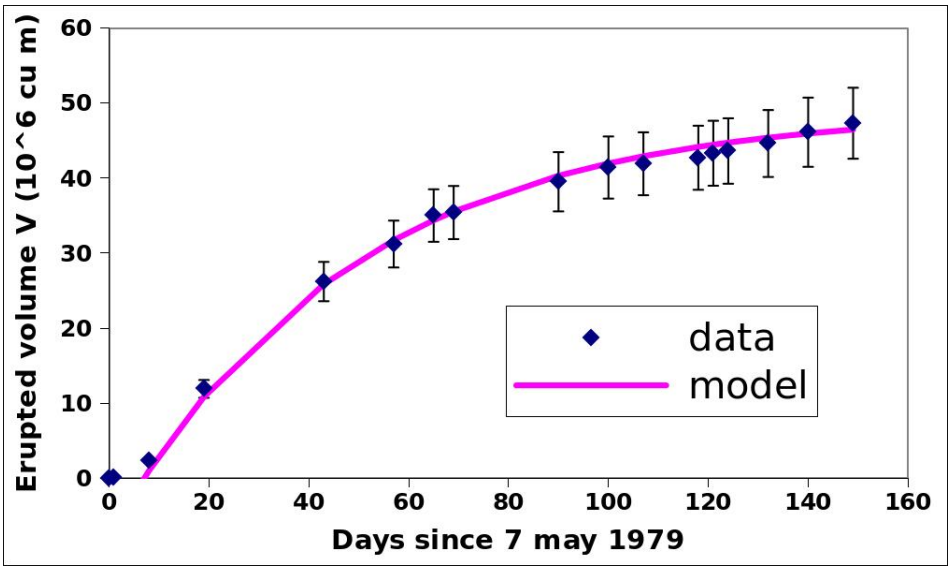

Figure 3.4: Application of exponential decay model to La Soufriere de St Vincent 1979 eruption data. Erupted volume shows good fit to exponential decay with the time constant from our model, and shows that eruption started at t=7 days. Data is from Huppert et al. [1982]

Mexico's Paricutin volcano began erupting in 1943 and stopped 1952, after erupting 1.385×10^9 m^3 of magma Fries [1990] as presented in Stasiuk et al. [1993]. Stasiuk showed an exponential fit of the data but according to our model, the erupted volume V_{tot} should have been larger at 1.475×10^9 m^3. We show our model using this value of V_{tot} in Figure 3.5. We argue that it only actually erupted 1385×10^6 m^3 because other conduit dynamics caused it to stop although the chamber was still overpressured. Although the errors associated with lava dome measurements are not known, we plot error bars of 10%.

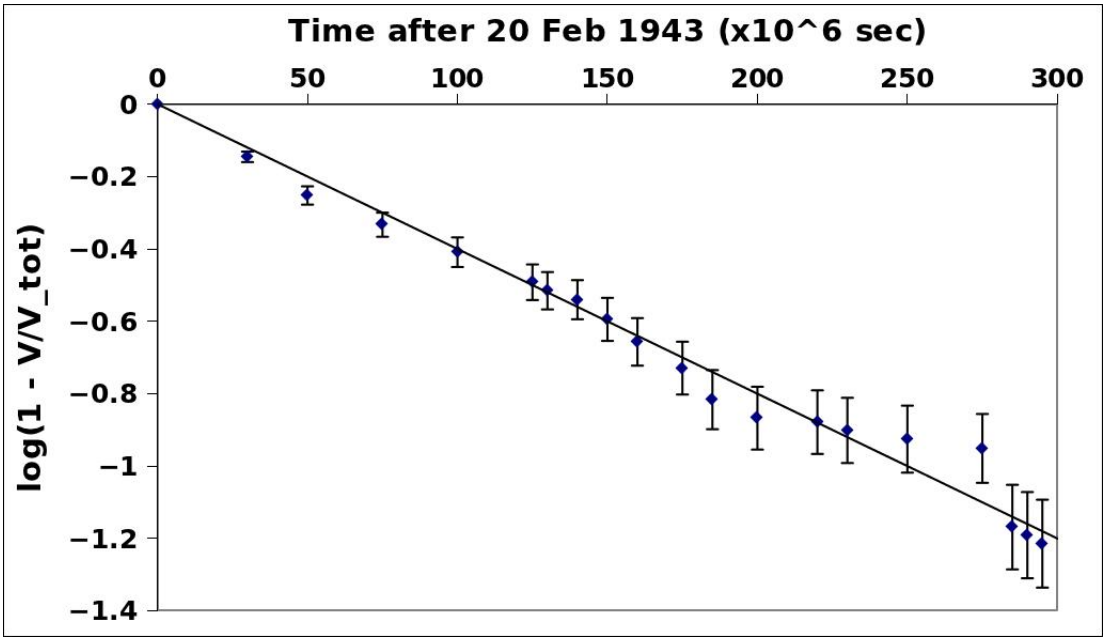

Figure 3.5: Application of exponential decay model to Paricutin 1943 eruption. Plot of ln(1-V/Vtot) for V_{tot} equal to the maximum observed lava dome volume is linear (slope is $-F/\beta V_c$), showing a good exponential fit for V_{tot}=1475×10^6 m^3. Data is from Fries [1990] as presented in Stasiuk et al. [1993].

The likely range of chamber overpressures at volcanoes such as La Soufriere de St Vincent and Paricutin is 10^6 to 10^7 Pa Bower and Woods [1998]; Huppert and Woods [2002]; Sparks [1978]. Choosing V_{tot} for each volcano, and magma bulk compressibility β=10^{-9} Pa^{-1} for a degassed magma Huppert and Woods [2002], allows us to show the chamber overpressure as a function of chamber volume V_c based on Equation 3.11. In Figure 3.6 we show the initial chamber overpressure $\Delta P(0)$ as a function of chamber volume V_c for overpressures from 1 to 10 MPa. The consequence is that the chamber volumes fall within a huge range between 147 and 1475 km^3 at Paricutin (top) and 5 and 50 km^3 at St Vincent (bottom). However, the value of V_{tot} is nonetheless important for evaluating time dependency of the eruption, and showing behaviour associated with a single chamber model.

Initial chamber overpressure $\Delta P(0)$ is a value sufficient to fracture the country rock Bower and Woods [1998]; Druitt and Sparks [1984]. This must be above the magma reservoir lithostatic pressure, and whether the walls adjust elastically or not contributes to the variability in overpressure Scandone [1996]. Effect of pressure variations with depth in the chamber are small and thus neglected Druitt and Sparks [1984]. The precise value of overpressure may depend on regional stress field, local stratigraphy, and chamber size and geometry, and may vary significantly from one volcano to the next Bower and Woods [1998].

Bulk compressibility β depends on detailed properties of the magma, particularly rheology and crystallisation sequence, and this varies from case to case and is not fully understood Huppert and Woods [2002]. One standard assumption for slow effusive eruptions is that bubbles and crystals remain well mixed within the magma layer in which they form. Bulk compressibilities are assumed to be the same for basaltic and silicic magmas, and throughout the country rock, but precise values depend on specific locations and rock properties. Bulk magma density and hence compressibility varies with pressure, exsolved volatile content, and crystal content, and thus with depth Bower and Woods [1997]. The model values of β are a representative average. This leads to variability in input parameters.

We acknowledge that estimates with one order of magnitude variation are problematic. The more useful implication is that of time dependencies of volume efflux rate on chamber pressure and volume. A summary of different time

dependencies for different model configurations is provided in Chapter 7.

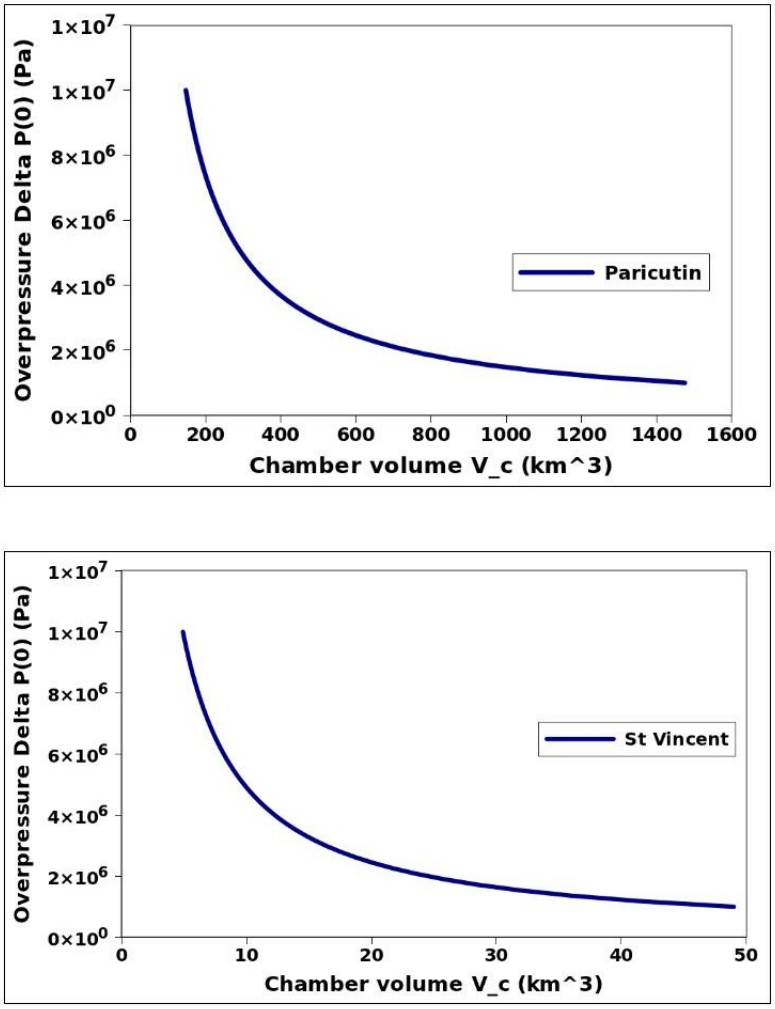

Figure 3.6: Initial chamber overpressures $\Delta P(0)$ from 1 to 10 MPa imply values of chamber volume V_c from 147 to 1475 km^3 at Paricutin (top) and 5 to 50 km^3 at La Soufriere de St Vincent (bottom).

3.2.4 Application of model to Mount St Helens

Next we use the model to find a V_{tot} value for Mount St Helens. The volcano appears to erupt until the end of Phase I as shown in Figure 3.7, followed by a period of much reduced eruption in Phase II. Phase III seemed to increase in eruption rate. We will model Phase I of the Mount St Helens 1980-86 eruption, after which the eruption appears to have slowed but has not reached an asymptote. Volumes are topographic images of dome height, width, and length, which are likely to provide an upper bound on actual volume.

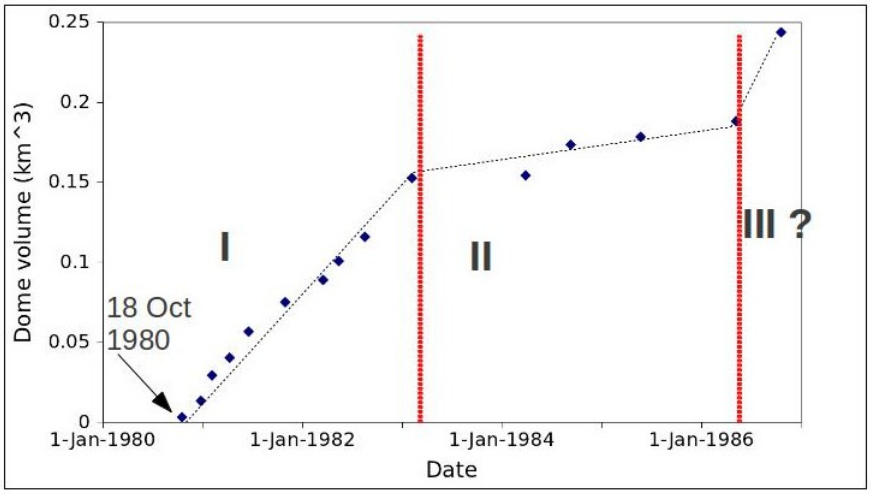

Figure 3.7: Mount St Helens lava dome growth, as measured by topographic maps (length, width, depth) at the end of each extrusive episode since 18 Oct 1980 Swanson and Holcomb [1989]. We will model Phase I as a single depressurising chamber. Reprinted from Chapter 2.

We estimate the effective V_{tot} which corresponds to the volume that would have erupted had there not been some other control on the eruption which brought about the end of the phase. The volume erupted as shown in Figure 3.7 is a lower bound on V_{tot}.

We take the erupted volume data for Phase I (the first 800 days of eruption since measurements of ongoing dome growth began on 18 May 1980) and fit the curve in which we estimate $\beta V_c \Delta P(0)$ and the best fit slope. This provides V_{tot} between 0.3 and 0.5 km^3 with a least squares correlation factor of at least 0.99. These values give slopes $F/\beta V_c$ from 1.5 to $3\times\ 10^{-4}s^{-1}$. In Figure 3.8 we show the plot of ln(1-V/V_{tot}) vs time for V_{tot}=0.4 km^3. The volume measurements have some uncertainty which we do not know, but we assume the value is an upper bound and suggest that a 7% error in each dimension leads to error bars of at least 20%.

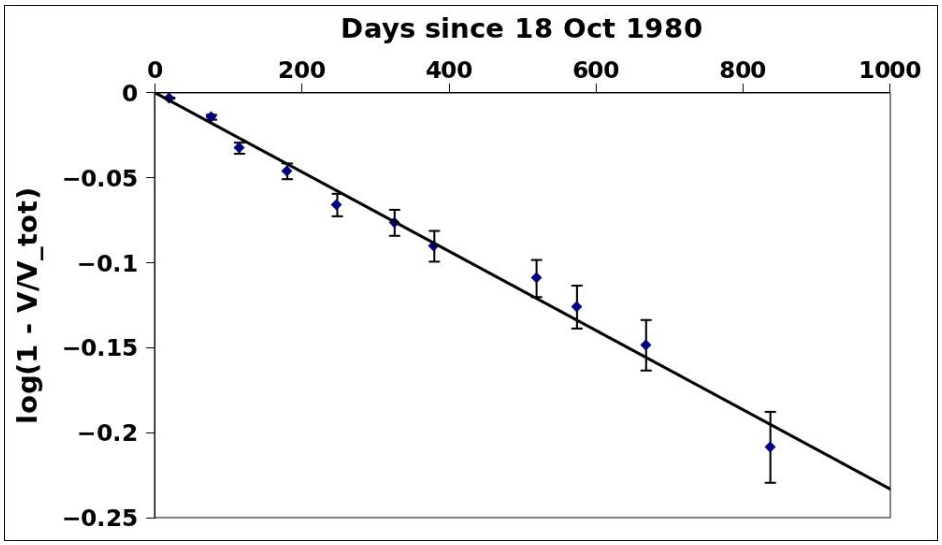

Figure 3.8: The first 800 days of the Mount St Helens 1980 eruption (Phase I) fit our exponential decay single chamber model: Plot of ln(1-V/V_{tot}) is linear for V_{tot}=0.4 km^3.

Chamber overpressure $\Delta P(0)$ is expected to lie within the range 10^6 to 10^7 Pa Bower and Woods [1998]; Huppert and Woods [2002]; Sparks [1978]. For V_{tot}=0.4km^3 and magma bulk compressibility β=10^{-9} Pa^{-1} for a degassed magma, we show the chamber overpressure as a function of chamber volume V_c based on Equation 3.11. In Figure 3.9 we show the initial chamber overpressure $\Delta P(0)$ as a function of chamber volume V_c for overpressures from 1 to 10 MPa. This suggests a chamber volume V_c between 20 and 400 km^3, which is a huge range and requires further constraint.

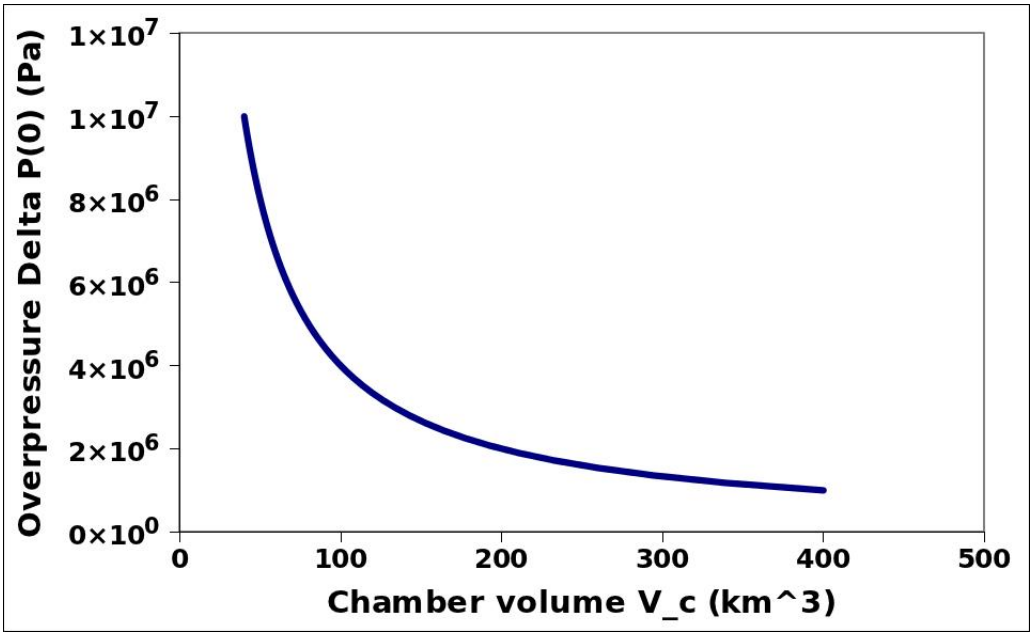

Figure 3.9: Initial chamber overpressure $\Delta P(0)$ from 1 to 10 MPa suggests a chamber volume V_c between 20 and 400 km^3 at Mount St Helens.

Mount St Helens can be difficult to interpret in terms of an eruption rate because, as shown in Chapter 2, it comprises a series of discrete lava dome eruptions. This means that Figure 3.8 is a rate of volume change at the surface rather than an overall eruption rate and suggests that nonlinear dynamics in the shallow conduit may regulate eruption at the surface. However, the overall magma flow rate is waning. The model points to a chamber decompressing even though the surface displays discrete eruptions. We will return to this in Chapter 4.

3.2.5 Application of model to Unzen

We investigate the eruption of Mount Fugen of the Unzen volcano complex 1990-95 eruption in a similar way using data to evaluate a value of V_{tot} appropriate for a single chamber system. Unzen's magma efflux nearly stops in Phases II and IV, as shown in Figure 3.10. This requires an explanation for the re-starting of the eruption, such as re-pressurisation of the chamber by a magma recharge. However, it is interesting to understand whether the first phase can be interpreted in the context of a single chamber decompressing.

Phases I and II of the eruption decreased in rate, but there was a discrete change at the end of Phase II with the formation of a new lobe of the lava dome. This might have arisen from a deep magma supply becoming active. Noting the caveat that a deep supply may cause the eruption rate to increase, we will model Phases I and II as a single chamber erupting without the influence of another source of magma.

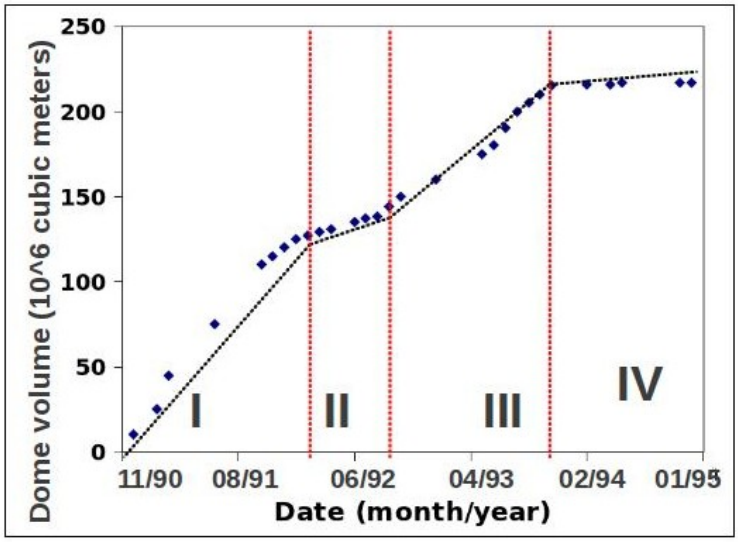

Figure 3.10: Mount Fugen, Unzen volcano complex, lava dome volume in 1990-95 eruption, re-printed from Chapter 2 Nakada et al. [1999].

We take the erupted volume data for Phases I and II and find a value of V_{tot}=1.50×10^7 m^3 that gives a good fit for a plot of ln(1-V/V_{tot}) vs time as shown in Figure 3.11. Values of V_{tot} from 1.48 to 1.52×10^7 m^3 give a least squares correlation factor of at least 0.99. A single decompressing chamber seems to be a good model of the first 23 months of the Unzen eruption. We do not know error associated with lava dome measurements, but we plot error bars of 10%.

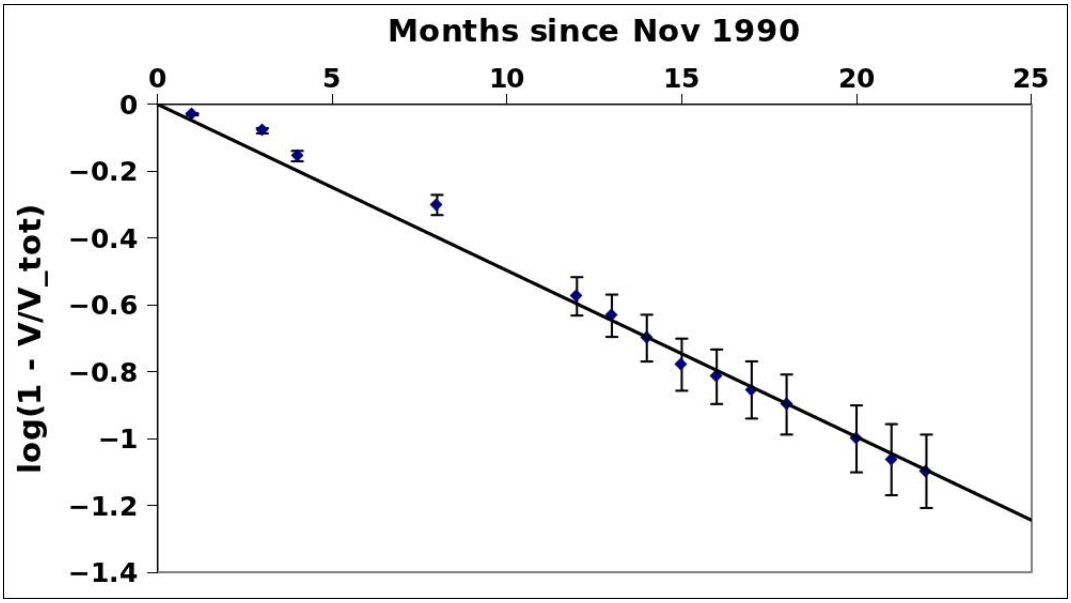

Figure 3.11: The first 23 months of the Unzen 1990 eruption (Phases I and II) fit our exponential decay single chamber model: Plot of ln(1-V/V_{tot}) is linear for V_{tot}=150×10^6 m^3.

For V_{tot}=1.50×10^7 m^3 and magma bulk compressibility β=10^{-9} Pa^{-1} for a degassed magma, we can again show the chamber overpressure as a function of chamber volume V_c based on Equation 3.11. In Figure 3.12 we show the initial chamber overpressure $\Delta P(0)$ as a function of chamber volume V_c for overpressures from 1 to 10 MPa. This suggests a chamber volume V_c between 15 and 150 km^3.

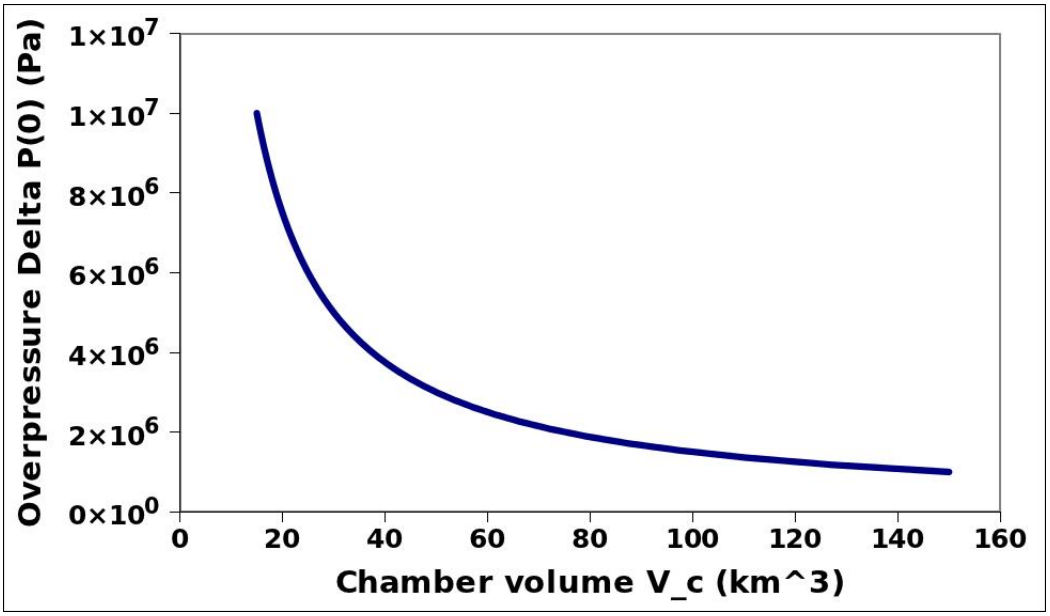

Figure 3.12: Initial chamber overpressure $\Delta P(0)$ from 1 to 10 MPa suggests a chamber volume V_c between 15 and 150 km^3 at Unzen.

Finally, we can estimate a conduit radius at Unzen for a range of effective magma viscosities by combining Equations 3.5 and 3.12, where F is obtained from the model in Figure 3.11: slopes $F/\beta V_c$ range from 2.8×10^{-6} to 3×10^{-7} s^{-1} so F is calculated for a selected combination of β, V_c, and V_{tot}.

We choose several chamber volumes V_c from Figure 3.12, conduit length or chamber depth $L = 10km$, bulk compressibility β=$10^{-9}Pa^{-1}$, and a range of effective viscosities μ from 10^5 to 10^7 Pas which have been proposed at other volcanoes, and used here as a constraint on values at Unzen Bower and Woods [1998]; Gardner et al. [1995]; Scandone and Malone [1985]. In Figure 3.13, we plot the effective conduit radius for this range of viscosities.

This analysis suggests that the first 23 months of the Unzen eruption behave as a single decompressing chamber. After this, in Phases III and IV from Figure 3.10, the eruption rate appears to increase. This requires further complexity than can be explained by a single chamber, and may suggest the presence of a second chamber or recharge to the original chamber.

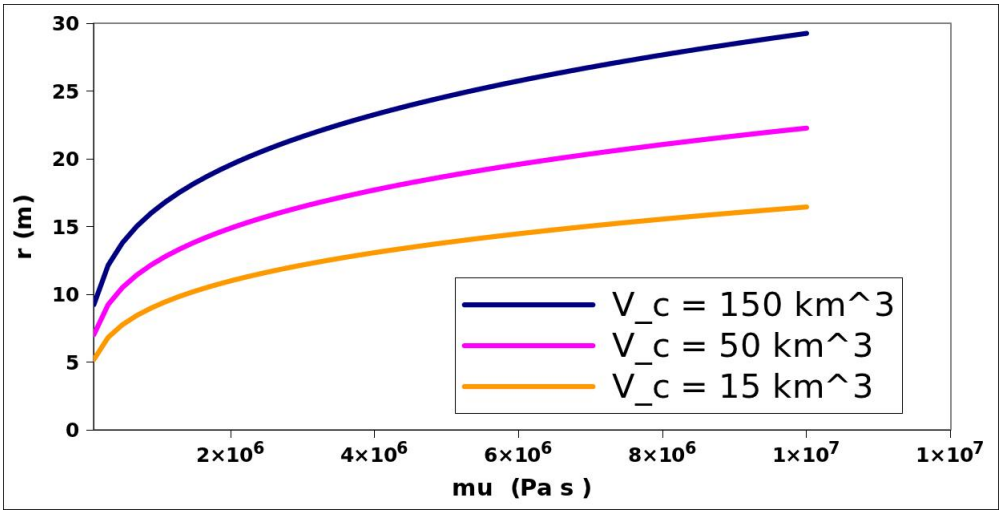

Figure 3.13: Unzen effective conduit radius for magma viscosities μ from 10^5 to 10^7 Pas and chamber volumes 15, 50, and 150 km^3.

3.2.6 A more complex system

Finally, we discuss the 1988-1990 eruption of Lonquimay volcano in Chile, which we presented in Chapter 1. The erupted volume since 25 December 1988 is shown to deviate from an exponential decay in Figure 3.14 which Stasiuk interprets as a result of conduit erosion and changing magma Stasiuk et al. [1993]. It appears to have a fast efflux rate until 75 days, then a slower efflux rate for the remainder of the eruption. We will consider the interpretation of this data in terms of a more complex magma chamber system.

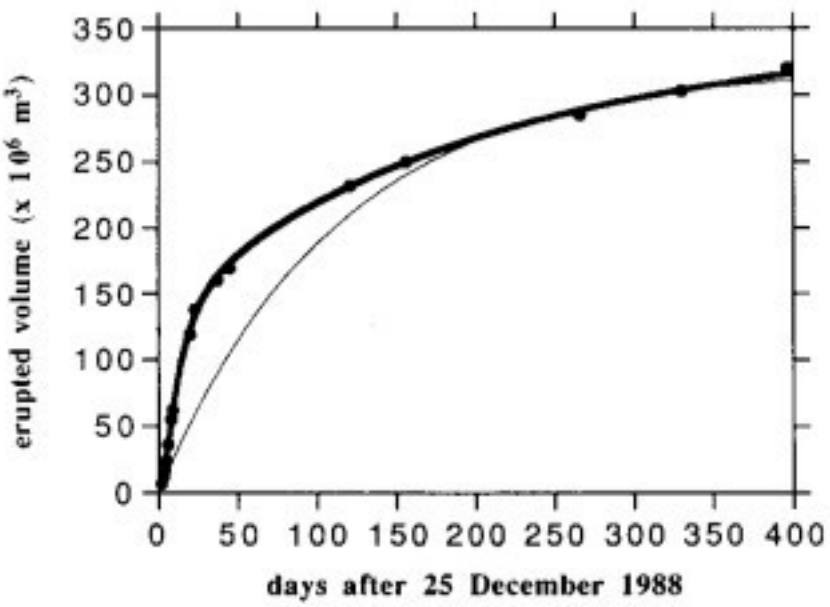

Figure 3.14: Erupted volume at Lonquimay in 1998-1990. The light curve is an exponential fit to the erupted volume data shown by dots and fitted with the thick black least-squares curve Stasiuk et al. [1993]. The data deviate from exponential decay, and appears to erupt rapidly until 75 days and then slow down.

Using a curve fit for the erupted volume data as shown in Figure 3.14, Stasiuk calculated a dimensionless eruption rate Q^* and plotted this as a function of erupted volume $1 - V^*$, as shown by the light curve shown in Figure 3.15. The dark lines show two nearly linear sections A and B with A the first 100 days of eruption and B the last 125 days. This suggests two phases of eruption, each of which demostrates a linear relationship between eruption rate and volume erupted.

The model of the eruption from a single closed chamber suggests a linear relationship between erupted volume and eruption rate as described in Equations 3.9 and 3.10. The observation that Lonquimay can be broken into two such straight line curves suggests that there might have been one chamber which initially controlled the eruption. Once this decompressed, a second chamber with a longer time constant, perhaps situated deeper in the Earth's crust, became the source of overpressure driving the eruption.

The fact that the early phase of the eruption appears to behave as a closed single chamber until it decompressed is consistent with the picture of Unzen. However, subsequent evolution of these two eruptions are different: At Unzen, the eruption rate subsequently increased, whereas at Lonquimay, the rate decreased.

This introduces the concept of a recharge of magma to the system, which is the topic of the next section. In Chapter 4, we will introduce the concept of a second chamber that feeds the erupting chamber, as a possible method by which this recharge is added.

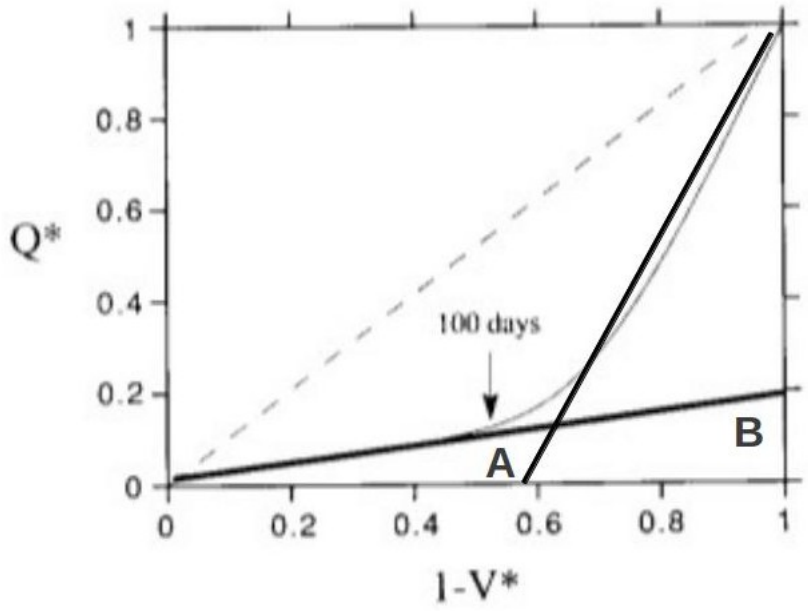

Figure 3.15: Eruption rate at Lonquimay in 1998-1990. Dimensionless eruption rate Q^* (light curve) calculated by Stasiuk Stasiuk et al. [1993]. The dark lines show two nearly linear sections A and B with A the first 100 days of eruption and B the last 125 days. This shows two phases of eruption, each of which seems to display a linear relationship between eruption rate and mass erupted.

3.3 Effusive eruption model, single chamber with recharge

The single chamber model in the previous section shows how an effusive eruption efflux rate may decay exponentially. The model does not explain how an eruption starts and stops nor how the eruption rate could deviate from exponential.

In this section, we allow for a constant rate of magma recharge to the chamber. This can lead to an increase in chamber overpressure, so we introduce a critical overpressure at which an eruption starts. Since an eruption leads to a decrease in chamber overpressure, we introduce a second lower pressure at which we assume an eruption ceases and a plug forms in the volcanic conduit. The mechanism for this may be associated with crystallisation of magma following decompression and exsolution of volatiles, which can occur on a timescale faster than the flow for sufficiently small overpressures Melnik and Sparks [2005].

The end of the eruptive event implies a slow flow that has had time to cool or crystallise, and forms an immobile plug in the conduit. The subsequent influx of magma builds up sufficient pressure to remobilise the plug and start the new eruption. Alternatively, the critical pressure which is no longer sufficient to drive the plug from the conduit can be interpreted as a yield stress condition, a non-Newtonian magma stops flowing as long as it reaches the yield stress before it reaches the pressure required to pump it out Denlinger and Hoblitt [1999]; McBirney and Murase [1984].

For simplicity, in the present model we continue to assume that flow rate is linearly proportional to chamber overpressure. We account for nonlinearity by requiring chamber overpressure to increase to a maximum value prior to the resumption of an eruption once a conduit plug has been formed.

We build on the exponential decay model in the previous section by adding a magma input to the chamber, Q_{in}, and modifying Equation 3.7 for pressure change to be

$$\beta V_c \frac{d\Delta P}{dt} = Q_{in} - F\Delta P(t) \tag{3.14}$$

for chamber overpressure $\Delta P(t)$, chamber volume V_c, magma bulk compressibility

β, and conduit resistance $1/F$. Solving for the chamber overpressure ΔP

$$\Delta P = exp(\frac{-Ft}{V_c\beta})(\Delta P(0) - \frac{Q_{in}}{F}) \tag{3.15}$$

For an eruption that starts at time $t = 0$ and ends at time $t = t^*$, the pressure change proceeds as exponential decay. We write the overpressures at which an eruption starts and stops as

$$\Delta P(0) = \Delta P_{START} \tag{3.16}$$

and

$$\Delta P(t^*) = \Delta P_{STOP} \tag{3.17}$$

The time it takes for an effusive eruption to re-start again once the chamber has been sufficiently repressurised due to magma recharge is $t = t^{**}$. The recharge duration t^{**} is

$$t^{**} = \frac{\beta V_c}{Q_{in}}(\Delta P_{START} - \Delta P_{STOP}) \tag{3.18}$$

Once this time has ellapsed, the next effusive event begins. Then cycles proceed with eruptions lasting time t^* and pauses t^{**}. These cycle durations are a key feature of our model.

Combining the recharge time expression with the ΔP expression gives

$$exp(\frac{-Ft^*}{\beta V_c}) = \frac{\Delta P_{STOP} - \frac{Q_{IN}}{F}}{\Delta P_{START} - \frac{Q_{IN}}{F}} \tag{3.19}$$

so the eruption duration t^* and condition for stopping the eruption are

$$t^* = \frac{\beta V_c}{F} ln \frac{\Delta P_{STOP} - \frac{Q_{IN}}{F}}{\Delta P_{START} - \frac{Q_{IN}}{F}} \tag{3.20}$$

$$P_{STOP} > \frac{Q_{IN}}{F} \tag{3.21}$$

Our model allows an investigation of how recharge rate, chamber volume, and conduit resistance affect duration of eruption t^* and duration of recharge t^{**}. Both scale linearly with chamber volume and bulk modulus; thus different

chamber volumes change the duration but not the characteristics of the eruption. Eruption duration depends on magma input rate Q_{in}, conduit resistance F, and pressures ΔP_{STOP} and ΔP_{START}. Recharge duration depends only on recharge rate Q_{in} and both pressures.

In the next section, we provide examples of how these factors affect effusion cycle duration and rate. Each example in the following section is initiated at chamber overpressure ΔP_{START}.

3.3.1 Parameter study

We imagine a magma recharge that supplies the chamber for a time period of 1 unit. For each subset of the parameter study, we look at a time interval scaled to give three cycles for the 'middle' chamber size used in the study when all other parameters are held the same, so time t is scaled as t/τ, where τ is the time it takes for the 'middle' chamber to erupt three cycles and corresponds to the ratio $\beta V/F$ with compressibility β contained in volume parameter V. The erupted volume is normalised to the total volume supplied to the chamber for this case expressed as flux Q, so volume V is scaled as $V/Q\tau$.

3.3.1.1 Chamber volume

A smaller chamber has a shorter eruption duration and releases less magma than a larger chamber because there is a smaller amount of magma in the system overall. Figure 3.16 shows the effect of different chamber volumes on eruption volume and duration. The 'large' chamber (orange) is 1.5 times the size of the 'small' chamber (blue). The recharge period t^{**} is longer for the largest chamber than for the smallest chamber (0.3 and 0.2 respectively), and the eruption period t^{*} is also longer for the largest chamber than for the smallest chamber (0.2 and 0.1 respectively). Thus a larger chamber would be expected to have a smaller number of eruptive events in the same time that a smaller chamber would have a larger number of events, and a larger volume output would be expected from a larger chamber.

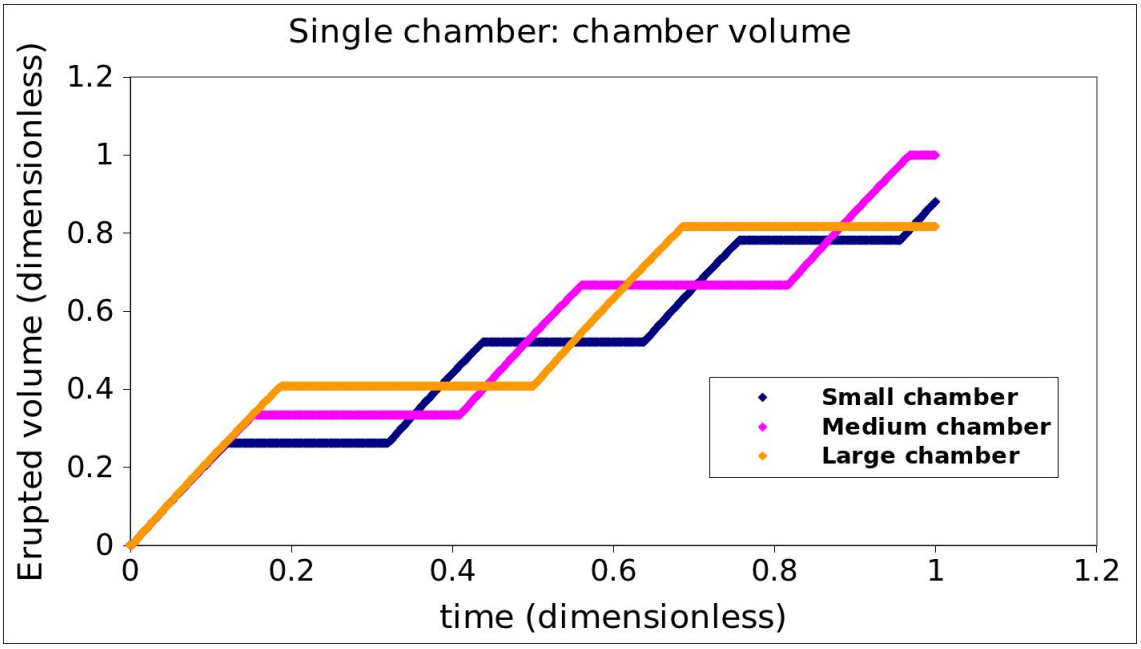

Figure 3.16: Single chamber: Larger chamber volumes give longer eruption duration t^{*}, longer recharge duration t^{**}, and larger output volumes in each effusion. 'Large' chamber (orange) is 1.5 times the volume of 'small' chamber (blue).

3.3.1.2 Recharge rate Q_{in}

It takes more time for a slower magma recharge rate to pressurise the chamber sufficiently to restart the eruption. Figure 3.17 shows the effect of different magma input rates on eruption volume and duration. The fastest Q_{in} (orange) is twice as fast as the slowest Q_{in} (blue). The recharge period t^{**} is shorter for the fastest Q_{in} than for the slowest (0.15 and 0.5 respectively), and the eruption period t^{*} is longer for the fastest Q_{in} than the slowest (0.2 and 0.1 respectively).

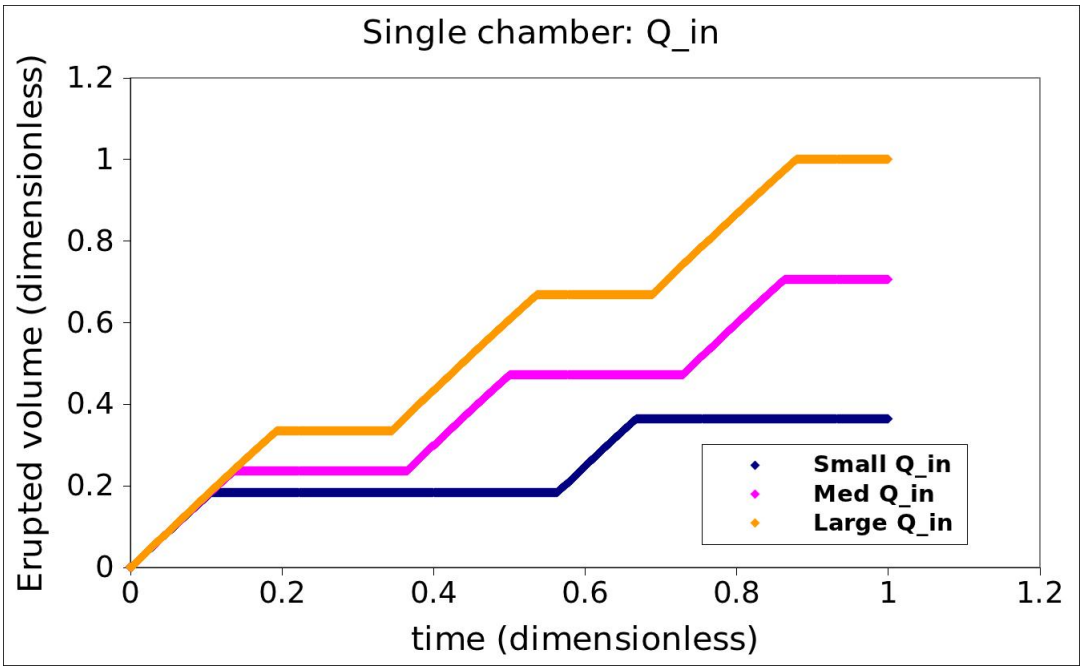

Figure 3.17: Single chamber: Faster recharge rate gives longer eruption duration t^{*} and shorter recharge duration t^{**}; slower recharge rate gives shorter eruption duration and longer recharge duration. 'Large' Q_{in} (orange) is twice as fast as 'small' Q_{in} (blue).

3.3.1.3 Conduit resistance

The resistance in the conduit connecting the magma chamber to the surface comprises magma viscosity and restrictive conduit walls, all of which impede the magma's ability to flow freely. Figure 3.18 shows the effect of changing the conduit resistance. The recharge period t^{**} is the same for all resistances (0.2), because no material is erupting and thus the conduit resistance has no effect. The eruption period t^{*} is longer for the largest resistance than the smallest (0.3 and 0.1 respectively), as it is more difficult for the magma to move through the conduit and thus takes longer to reach ΔP_{STOP}.

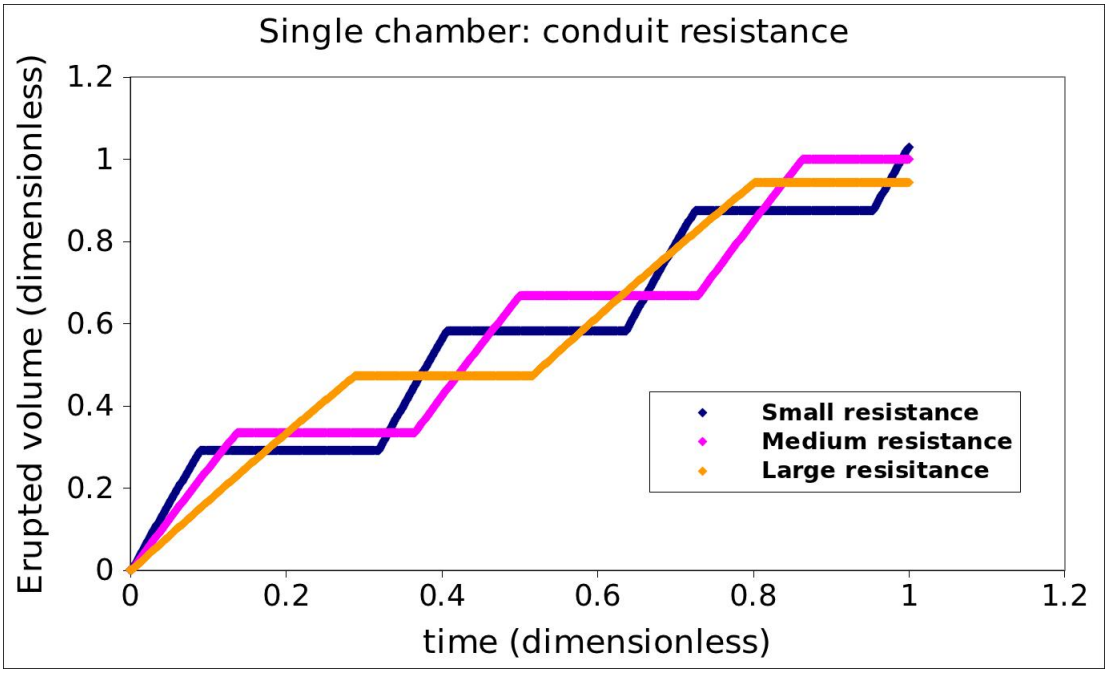

Figure 3.18: Single chamber: Larger conduit resistance gives longer period of eruption but has no effect on period of recharge. 'Large' resistance (orange, F=1) is twice as large as 'small' resistance (blue, F=0.5). Medium resistance is pink (F=0.67), resistance values dimensionless

3.3.1.4 Stopping overpressure ΔP_{STOP}

The overpressure that the chamber must reach for the eruptive event to stop determines how long an eruption can continue. Figure 3.19 shows the effect of changing the value of this overpressure, ΔP_{STOP}. The largest value of ΔP_{STOP} (orange) is 1.2 times the smallest (blue). The recharge period t^{**} is longer for the smaller ΔP_{STOP} than for the larger (0.5 and 0.2 respectively), and the eruption period t^{*} is also longer for the smaller ΔP_{STOP} than the larger (0.3 and 0.1 respectively). The volume output is thus larger for a smaller stopping overpressure as more magma must be removed before a smaller ΔP_{STOP} is reached.

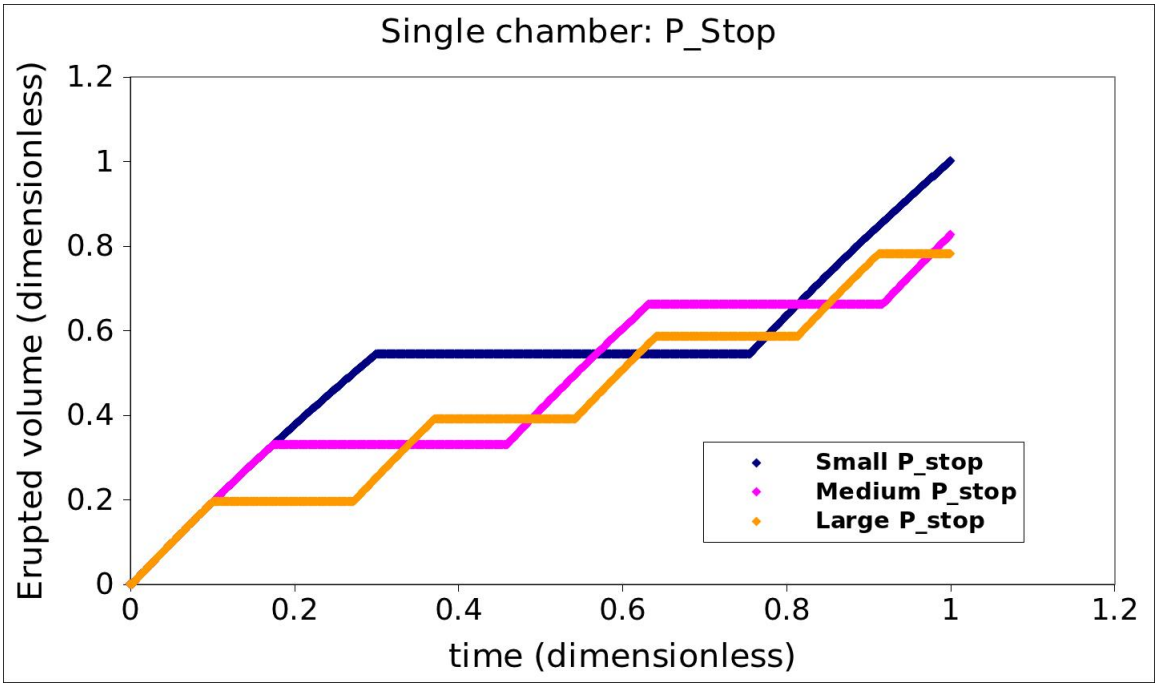

Figure 3.19: Single chamber: smaller ΔP_{STOP} values give longer periods of both eruption and recharge, and larger output volumes. 'Large' ΔP_{STOP} (orange) is 1.2 times as large as 'small' ΔP_{STOP} (blue).

3.3.1.5 Starting pressure ΔP_{START}

The overpressure that the chamber must reach for a new eruptive event to begin determines how long the chamber will recharge. Figure 3.20 shows the effect of changing the value of this overpressure, ΔP_{START}. The largest value of ΔP_{START} (orange) is 1.2 times the smallest (blue). The recharge period t^{**} is longer for the largest ΔP_{START} than for the smallest (0.45 and 0.15 respectively), and the eruption period t^{*} is also longer for largest ΔP_{START} than for the smallest (0.25 and 0.05 respectively). The volume output during one event is thus larger for a larger starting overpressure as more magma must be removed before a smaller ΔP_{START} is reached.

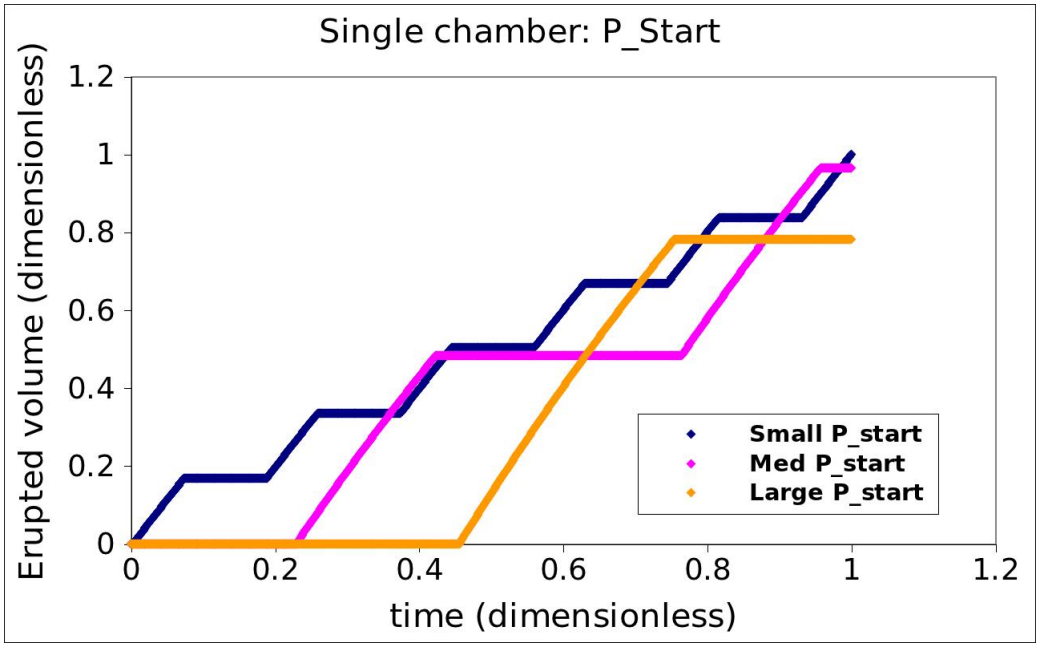

Figure 3.20: Single chamber: larger ΔP_{START} values give longer periods of both pause and eruption, and larger output volumes. 'Large' ΔP_{START} (orange) is 1.2 times as large as 'small' ΔP_{START} (blue).

3.3.2 Varying recharge rate Q_{in}

One question arising from this study is what it is that regulates both the individual cycles and the long-term eruption trend. The volcanoes discussed in Chapter 2 show complex cycles of eruption that have not reached steady state. The Soufriere Hills volcano and Mount Etna long-term eruptions appear to progress at a constant rate, but the cycles of eruption do not have the same rate each time. Mount St Helens and Unzen eruption rates wane with time.

We can model different eruption duration with a variable recharge rate. Changing the recharge rate Q_{in} allows for changes in eruption and pause durations. We consider the effects if the recharge rate changes over time, as shown in Figure 3.21.

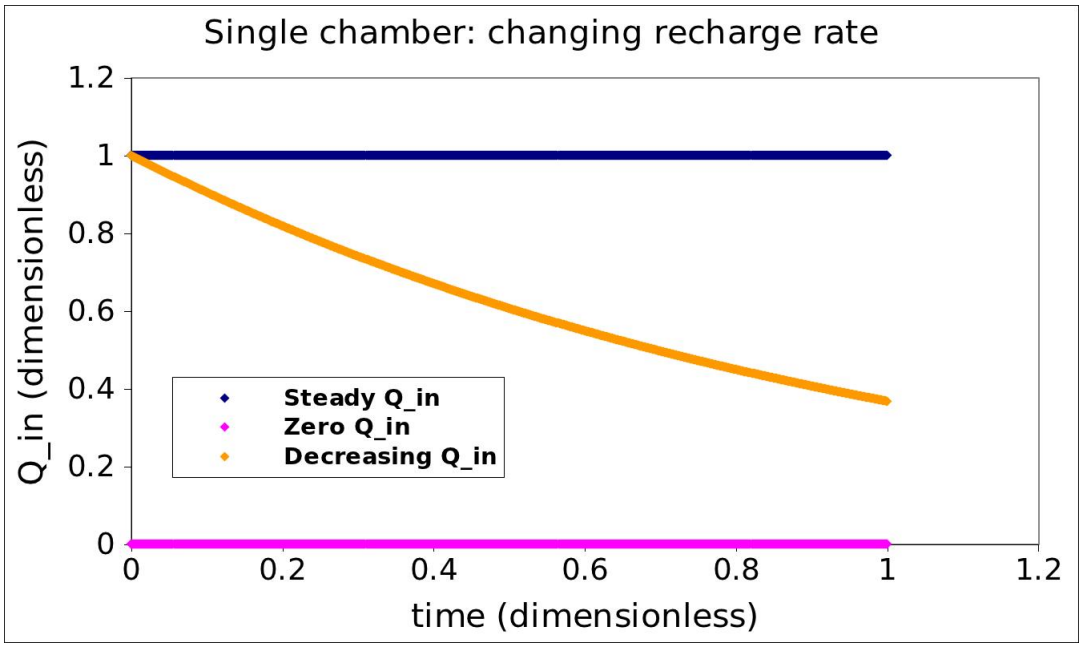

Figure 3.21: Single chamber: Recharge rate Q_{in} does not have to be a constant value (blue). A zero recharge rate (pink) will cause an eruption to cease once the initial overpressure drops. A decreasing recharge rate (orange, Q_{in}=exp(-t)) will decrease the eruption duration t^* and increase the recharge duration t^{**} from one cycle to the next.

Varying Q_{in} allows us to model cycles in which eruption duration t^* and recharge duration t^{**} change from one cycle to the next, as shown in Figure 3.22. A constant Q_{in} (blue) gives constant t^* and t^{**} for each cycle and will carry on this way until another factor (conduit resistance or start/stop overpressure) changes. A zero Q_{in} (pink) provides no mechanism to restart an eruption, and the eruption ceases once the critical overpressure has been reached. A decreasing Q_{in} (orange) gives shorter eruption durations and longer recharge durations. Eventually, as Q_{in} approaches 0, the eruption duration will reach 0 and the eruptive sequence will stop. However, the question still remains of what causes a change in recharge rate.

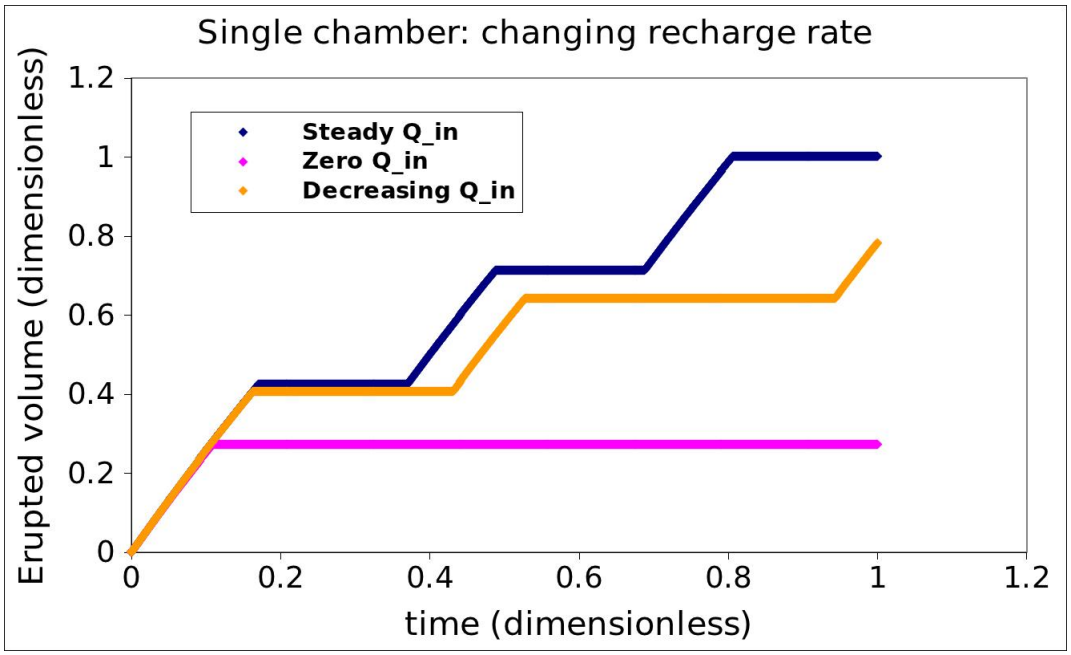

Figure 3.22: Single chamber: Steady recharge rate (blue) gives constant eruption and pause durations from one cycle to the next; zero recharge rate (pink) provides no mechanism to restart an eruption so the eruption ceases once the critical overpressure has been reached; and a decreasing recharge rate (orange) gives shorter eruption and longer recharge durations.

3.4 Application to Soufriere Hills Volcano

While we do not know what controls the recharge rate, we can use our model to provide an estimate of the recharge rate at the Soufriere Hills Volcano.

The rate of chamber volume change dV/dt is simply the difference between magma input Q_{in} and magma erupted Q_{er}

$$\frac{dV}{dt} = Q_{in} - Q_{er} \tag{3.22}$$

The chamber volume inflates when magma flows into the chamber, and deflates when magma flows out of the chamber. Therefore at some point during each eruption and pause, the chamber volume will go back to a reference '0' value.

We refer back to our discussion of the Soufriere Hills Volcano in Chapter 2 and note that ground surface deformation measured by GPS units around the volcano accompanies each phase of eruption and repose. This surface deformation is proportional to the chamber volume change Elsworth et al. [2008]; Mattioli et al. [1998]; Mogi [1958]. When the surface deformation is 0 relative to some reference point, the rate of chamber volume change is also 0. Because we know the eruption rate during each cycle of eruption at Soufriere Hills Volcano, we can calculate a reasonable Q_{in} during each cycle as well as for the overall eruption.

First we present more detail on the surface deformation that we referred to in Chapter 2. In Figure 3.23, we present vertical surface deformation (residual) data from four GPS stations around Montserrat, along with mass efflux data. Mattioli notes that 'episode duration is not uniform and that these bounds are closely, although not exactly, aligned in time with initiation and cessation of lava efflux at SHV' Mattioli et al. [2010]; Sparks et al. [1998]; Wadge et al. [2010].

Each red dot represents a 24 hour average absolute point position estimate relative to the Earth's centre of mass. Three dome growth periods are represented by gray shading (subsidence), while unshaded periods (uplift) are periods with minimal surface lava efflux. We sketch an average value with black lines. Dashed horizontal black lines show the 0 reference point, bisecting the Pause 2 period at t3, which we choose as the point at which chamber volume is not changing. This occurs in December 2005, blue 't3' in the figure.

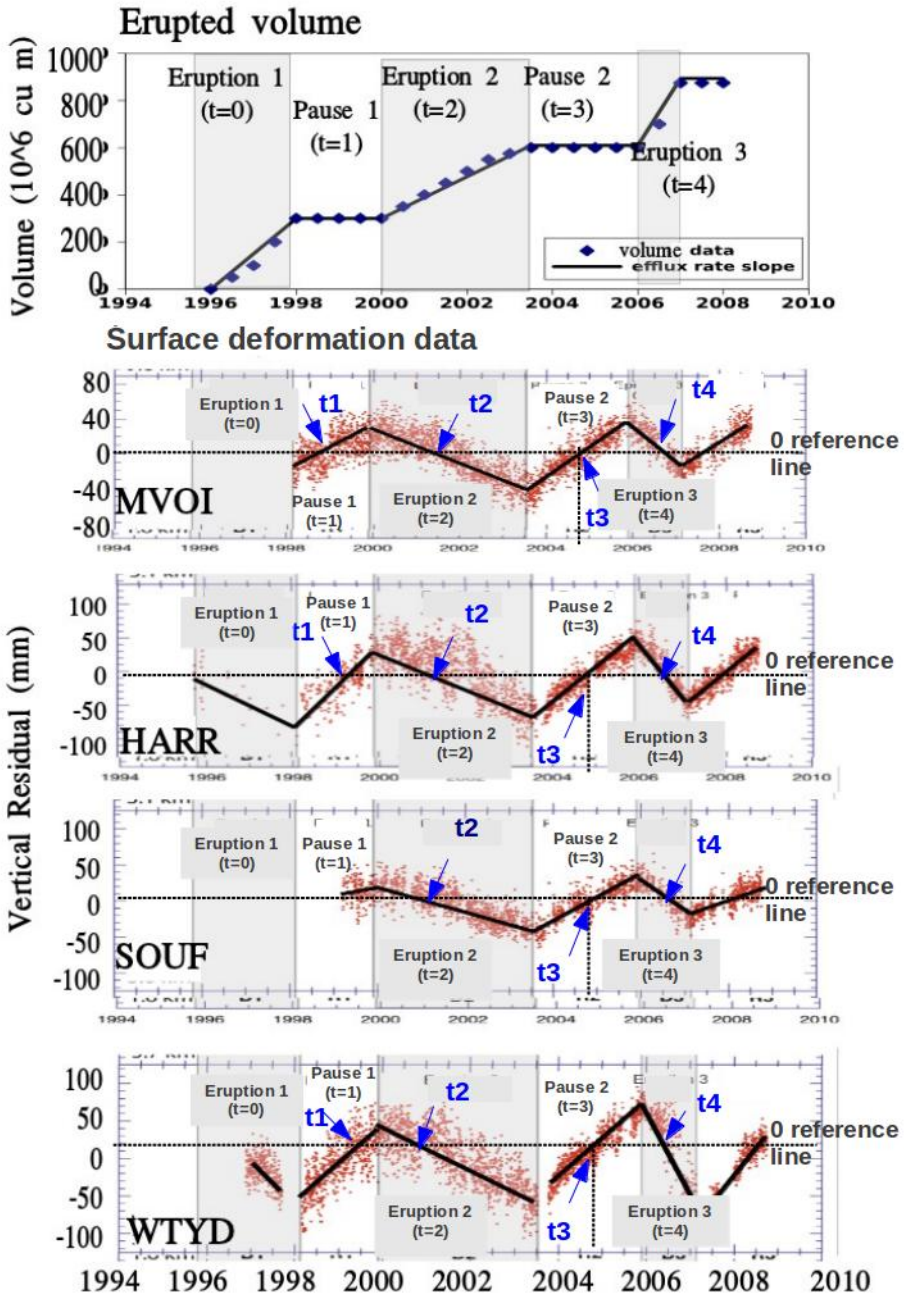

Figure 3.23: Erupted volume (top panel) and vertical surface deformation at four GPS stations around Soufriere Hills Volcano Mattioli et al. [1998]. Average surface deformation values have been sketched by hand (black lines). Horizontal black lines show reference point, bisecting Pause 2 period, at which surface deformation is 0. Average surface deformation is 0 at the times indicated by blue arrows.

We then note the time at which the average surface deformation crosses the 0 reference line in each episode from Pause 1 through Eruption 3 (1998-2007), indicated by red arrows in Figure 3.24. Surface deformation data for Eruption 1 (1996-1998) is incomplete so we disregard it. These are the points at which volume change crosses 0. We find the value at each station and take the average time $t1^*$ through $t4^*$ over all the stations. Then we choose an input flux value Q_{in} and, using Equation 3.22, calculate the chamber volume change during each episode for the eruption rate Q_{er} indicated by the eruptions in the top panel of Figure 3.23.

We choose 14 values of Q_{in} and calculate chamber volume change for each of them. This chamber volume change, relative to a reference volume, from 1998 through 2006 is shown in Figure 3.24, with different colour lines indicating different Q_{in} values. The chamber volume change crosses 0 at times $t1$ through $t4$ for each pause and erupt event. We calculate the error associated with each of these points with respect to the average values from the data, $t1^*$ through $t4^*$. From the error calculations, shown in Figure 3.25, we determine that the best fit value of magma recharge rate Q_{in} is $5.4{\times}10^6\ m^3/month$.

In Figure 3.26, we show the chamber volume change associated with this Q_{in} and times t^* from the Mattioli data at which surface deformation and thus chamber volume change are 0 relative to reference time in late 2004. For this best fit model, there is some variation in crossing time (orange ticks). This points to some of the additional complexity associated with a magma plumbing system, which we discuss in Chapter 4.

This analysis has allowed us to approximate a magma recharge rate to a single chamber. This recharge rate rationalises the surface deformation and efflux data, and provides a tool that can be applied to other volcanoes for which similar data exist.

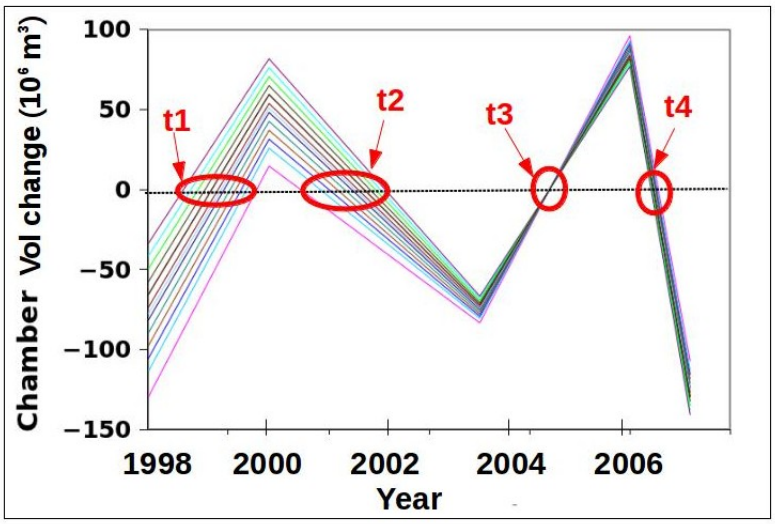

Figure 3.24: Chamber volume change calculated for each of 14 values of recharge rate Q_{in} (shown in different colours). We note the times $t1$ through $t4$ at which the chamber volume is 0 relative to reference time and volume in late 2004. The chamber volume increase and decrease correspond to the pauses and eruptions shown in Figure 3.23.

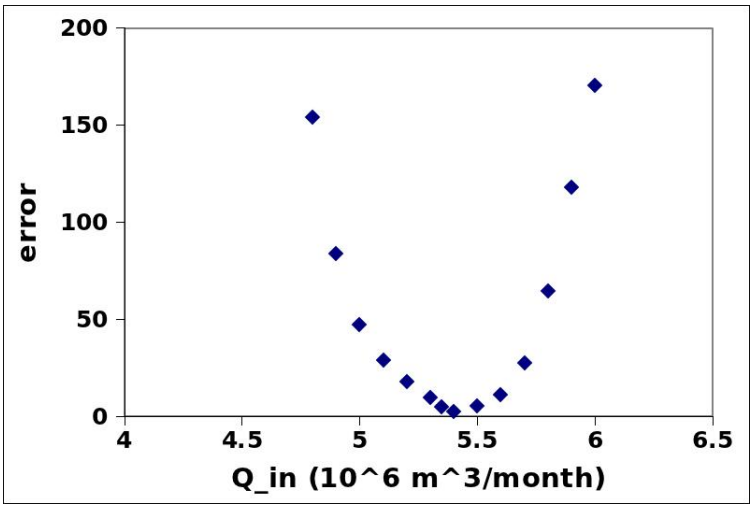

Figure 3.25: Error associated with volume change $dV = 0$ points in model from Figure 3.24 compared with Mattioli data.

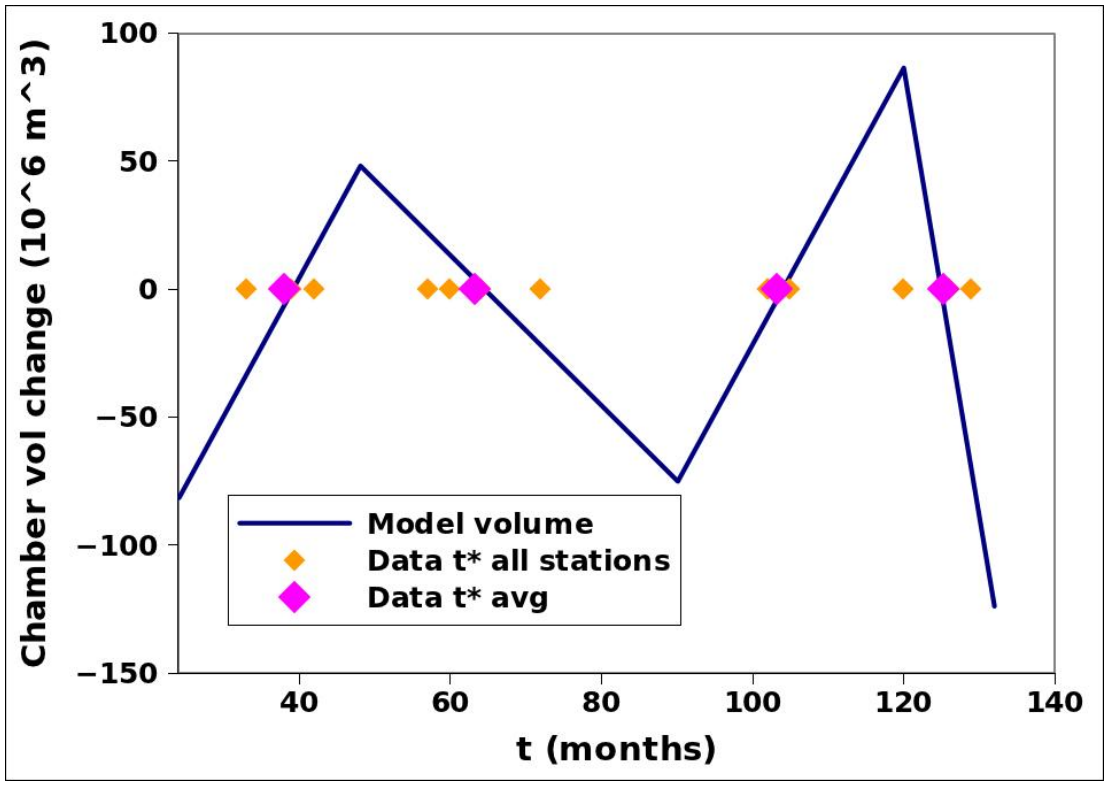

Figure 3.26: Chamber volume change calculated for $Q_{in} = 5.4{\times}10^6\ m^3/month$, and times t^* from the Mattioli data at which surface deformation and thus chamber volume change are 0 relative to reference time and volume in late 2004 Mattioli et al. [1998].

3.5 Discussion and conclusions

In this chapter we have developed a model of a single closed chamber system and interpreted data from La Soufriere de St Vincent, Paracutin, Mount St Helens, and Unzen in the context of this model. We have analysed data from Lonquimay and used this, along with patterns at Unzen, as motivation to add a recharge to the chamber. We developed a single open chamber model to allow for magma recharge and nonlinearity of a plug in the conduit which leads to cycles of eruption that start and stop such as at the Soufriere Hills Volcano.

A key result of this chapter is our application of the closed single chamber model to Mount St Helens and Unzen to provide an estimate for the chamber volume and effective conduit radius at these two volcanoes. We combined the recharged single chamber model with surface deformation data from the Soufriere Hills Volcano to provide an estimate of the recharge rate to the magma chamber. We also noted that Unzen and Lonquimay seem to indicate two timescales of eruption: Unzen erupted and waned then suddenly increased eruption rate in a new phase, while Lonquimay erupted and waned, then became much slower as though a second source took control of the eruption. In both cases, the first phase could be controlled by a single chamber erupting, then a second source may begin to take control.

3.5.1 Motivation for further work

The current model does not explain what controls the recharge rate of the chamber, nor what dictates the pressure at which an eruption starts and stops. In the next chapter, we develop the model to include a second chamber, which may act as a buffer to the recharge rate by storing and releasing magma over time.

Multiple magma types and changing magma type over time at Mount St Helens, Unzen, Soufriere Hills Volcano, and Eyjafjallajokull also suggest multiple chambers that interact with each other. The ground deformation data at Soufriere Hills volcano demonstrates complex cycles which correlate to the stopping and starting of an eruption, and thus to chamber overpressures ΔP_{START} and ΔP_{STOP}, and has been interpreted in the context of multiple magma chambers Elsworth et al. [2008]. Seismic events that change location and intensity

preceding and during an eruption also suggest a magma plumbing system that is more extensive than a single point source.

Drawing on work in the literature, in the next chapter we expand our version of the recharged single chamber model to incorporate a second chamber. In Chapter 5 we combine this with a Mogi model which uses the dual chamber model to predict surface deformation trends. This will expand our understanding of a deep chamber as the main mechanism by which an effusive eruption produces large amounts of magma. The focus of the next chapters will be to develop this model and investigate how it predicts flow rate and surface deformation patterns.

Chapter 4

A two chamber model

4.1 Abstract

In the previous chapter, we explored a closed single chamber system, and then investigated how a steady recharge of magma from below can lead to cycles of chamber inflation and deflation. In this chapter, we will develop a series of models to explore how such a supply of magma may be regulated by a deeper chamber, and investigate the long-term control of a deep source. These models are motivated partly by evidence of magma ponding at multiple depths in the Soufriere Hills Volcano, and we return to data from Mount St Helens to show that the building blocks of the model are able to provide a framework in which to interpret the data.

We present a quantitative two chamber model and derive an analytical solution which relates the surface eruption rate to the evolution of the chamber pressures. The two chambers' pressures evolve on different timescales. Typically, the upper chamber evolves more rapidly, and the lower chamber evolves on a longer timescale. We explore the effects of chamber size and conduit resistance on the timescales of pressure change and eruption rate. We present a solution for a closed two chamber system, and then explore the effects of recharge in an open system.

By introducing a critical pressure in the upper chamber at which the eruption starts and stops, we show that magma recharge can lead to nonlinear cycles of

eruption. The transient evolution may involve series of eruption-repose cycles which are controlled by the deep chamber.

We interpret data on the evolution of eruption rate at various volcanoes in the context of this model. Lonquimay volcano in Chile shows two phases of eruption, which we interpret as being controlled first by a shallow chamber and then by a deeper chamber. At Unzen, the initial waning phase of eruption appears to be similarly controlled by an overpressurised shallow chamber, and then the eruption rate increases as the result of a deeper source of magma. If recharge to the shallow chamber decreases in rate, the period between cycles of inflation and deflation can become longer, which is reminiscent of Mount St Helens where intervals between successive dome-building events increase over time.

4.2 Introduction

Erupted magma at the Soufriere Hills Volcano contains minerals that are stable at 115-130MPa, suggesting that the magma has spent time at a depth of 5-6km beneath the Earth's crust Barclay et al. [1998]. This has led to the hypothesis of a magma reservoir situated at 5-6 km depth. Further, there is evidence that new basalt which triggered the eruption reached this magma chamber, due to the presence of mafic inclusions in erupted material and SO2 gas emitted from the volcano which is derived from new mafic magma Edmonds et al. [2001]; Murphy et al. [1998]. However, the majority of the erupted material at the Soufriere Hills Volcano 1995-1999 eruption is crystal-rich andesite.

In addition, it has been hypothesised based on fractionation of mafic inclusions that the new mafic magma formed a second reservoir or intrusion at a depth of 10-12 km in the Earth's crust as it ascended Devine et al. [2003]. This motivates the development of a more complex model in which two connected reservoirs are situated in the crust. The lower chamber is supplied by a deeper source of mafic magma, but it also supplies the shallow chamber while the shallow chamber erupts andesite to the surface. This more complex picture of multiple sills or reservoirs is consistent with an emerging view of magma genesis and fractionation Annen and Sparks [2002].

Observations of eruptions at other volcanic systems such as Unzen and Lonquimay also suggest a magma plumbing system that is more complex than the single chamber model in Chapter 3, as evidenced by continuing activity after the first phase of eruption which we interpreted to behave as a closed single chamber system. At Unzen in 1990-95, the eruption waned in the first phase and then increased in rate, suggesting a rapid recharge from a high pressure source. At Lonquimay in 1988, the eruption waned after the first phase, then continued at a slower rate as though a deeper reservoir had taken control of the eruption.

We also note that at Mount St Helens, our analysis showed that the whole system could appear as a closed single chamber system, but details at the surface suggest a shallow system that regulates surface eruptions. We interpret these episodes of lava dome growth in terms of a shallow elastic magma reservoir that responds to the decompression of a deeper source reservoir at 7-10 km.

4.3 General model

We develop a two chamber model with which to explore the dynamics of a magma system and investigate the differences from a single chamber system.

Figure 4.1 is a diagram of the 2-chamber model. The lower and upper chambers have volumes V_2 and V_1, overpressures ΔP_2 and ΔP_1, and the resistance to magma flow in the conduit connecting lower to upper chamber is $1/F_2$ and shallow to surface is $1/F_1$. Additionally, the upper and lower chambers have bulk compressibility β_1 and β_2, respectively. As in the single chamber model, we treat β as a constant in order to focus on the simplest dynamics. The volume eruption rate to the surface is Q_{er}, and the lower chamber is recharged from a deep mantle source at rate Q_{in}. The transfer of magma between chambers occurs at rate $Q_{2,1}$. We assume that

$$Q_{er} = F_1 \Delta P_1 \tag{4.1}$$

and

$$Q_{2,1} = F_2(\Delta P_2 - \Delta P_1) \tag{4.2}$$

This leads to the rate of pressure change $d\Delta P_2/dt$ in the lower chamber is

$$\frac{d\Delta P_2}{dt} = \frac{1}{\beta_2 V_2} Q_{in} - \frac{F_2}{\beta_2 V_2}(\Delta P_2 - \Delta P_1) \tag{4.3}$$

for magma recharge to lower chamber Q_{in}, resistance between chambers $1/F_2$, and elastic modulus β_2. The pressure change in the upper chamber is similarly

$$\frac{d\Delta P_1}{dt} = \frac{F_2}{\beta_1 V_1}(\Delta P_2 - \Delta P_1) - \frac{F_1}{\beta_1 V_1}\Delta P_1 \tag{4.4}$$

for conduit resistance $1/F_1$, and compressibility β_1.

At equilibrium, the chamber pressures are constant and given by

$$\Delta P_1(eq) = \frac{Q_{in}}{F_1} \tag{4.5}$$

and

$$\Delta P_2(eq) = (\frac{1}{F_1} + \frac{1}{F_2})Q_{in} \tag{4.6}$$

In the next sections, we will explore the model and show what it predicts regarding chamber pressure evolution and how the chambers interact with each other.

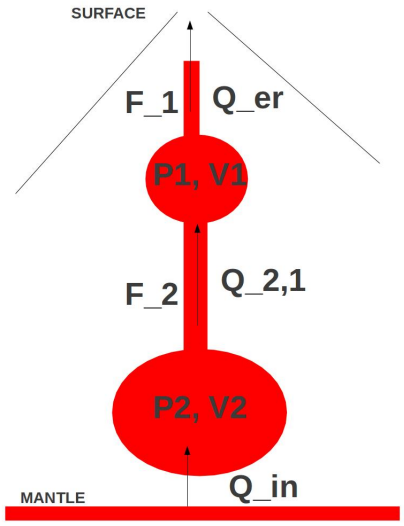

Figure 4.1: Diagram of two chamber model: lower and upper chamber volumes are V_2 and V_1, pressures are P_2 and P_1; resistance in conduit connecting lower to upper chamber is $1/F_2$ and upper to surface is $1/F_1$. Eruption rate to surface is Q_{er}; recharge rate from deep mantle source is Q_{in}; transfer of magma between chambers is at rate $Q_{2,1}$.

4.4 Analytical solution

In this section, we derive a series of solutions for the evolution of eruption rate and chamber overpressures in the system described in section 4.3, and consider a two-chamber magma system with a constant recharge to the lower chamber. We then describe how the system evolves to the steady state described in Equations 4.5 and 4.6. In the next section, we extend the model further to allow for a critical overpressure ΔP_{crit} at which the eruption continues and show that for a constant magma recharge, this leads to a series of eruption cycles analagous to but different in detail from those in Chapter 3. We also describe the transient evolution in which there is no recharge, but a deep chamber continues to pressurise the shallow chamber leading to a series of eruption episodes with progressively longer time intervals between eruptions.

4.4.1 Solution

First we look at the adjustment to steady state. The lower and upper chamber pressures are expressed in the pressure change equations 4.3 and 4.4, rewritten below, with equlibrium components described in equations 4.5 and 4.6.

$$\frac{d\Delta P_2}{dt} = -\frac{F_2}{\beta_2 V_2}(\Delta P_2 - \Delta P_1) + \frac{1}{\beta_2 V_2} Q_{in} \tag{4.7}$$

$$\frac{d\Delta P_1}{dt} = \frac{F_2}{\beta_1 V_1}(\Delta P_2) - \frac{1}{\beta_1 V_1}(F_2 + F_1)\Delta P_1 \tag{4.8}$$

We rewrite the pressure rate change equations as a matrix M

$$\frac{d}{dt}\begin{pmatrix} \Delta P_2 \\ \Delta P_1 \end{pmatrix} = M = \begin{pmatrix} \frac{-F_2}{\beta_2 V_2} & \frac{F_2}{\beta_2 V_2} \\ \frac{F_2}{\beta_1 V_1} & \frac{-1}{\beta_1 V_1}(F_2 + F_1) \end{pmatrix} \begin{pmatrix} \Delta P_2 \\ \Delta P_1 \end{pmatrix} + \begin{pmatrix} \frac{Q_{in}}{\beta_2 V_2} \\ 0 \end{pmatrix} \tag{4.9}$$

The solution to Equation 4.9 has the form

$$\begin{pmatrix} \Delta P_2 \\ \Delta P_1 \end{pmatrix} = \begin{pmatrix} a \\ b \end{pmatrix} exp(-\lambda_{\pm} t) + \gamma \tag{4.10}$$

where a, b, and γ are constants, and λ satisfies

$$0 = \begin{vmatrix} \lambda - \frac{F_2}{\beta_2 V_2} & \frac{F_2}{\beta_2 V_2} \\ \frac{F_2}{\beta_1 V_1} & \lambda - \frac{1}{\beta_1 V_1}(F_2 + F_1) \end{vmatrix} \tag{4.11}$$

To simplify the notation, we introduce some dimensionless parameters for compressibility constants β, resistance constants F, and volumes V, as

$$F = \frac{F_2}{F_1} \tag{4.12}$$

$$B = \frac{\beta_2}{\beta_1} \tag{4.13}$$

$$V = \frac{V_2}{V_1} \tag{4.14}$$

$$G = \frac{BF}{V} \tag{4.15}$$

and we express λ in terms of ω and upper chamber constants

$$\lambda = \omega \frac{F_1}{\beta_1 V_1} \tag{4.16}$$

Equation 4.16 means that ω is the eruption rate scaled to the upper chamber timescale, which is $F_1/\beta_1 V_1$ as indicated by Equation 3.15. Further, G in Equation 4.15 represents the ratio of timescales for upper and lower chamber overpressure changes, which depend on the same parameters for the respective chambers. A small G corresponds to a lower chamber that quickly settles into a steady decay, and a large G corresponds to an upper chamber that responds quickly.

We can expand and rewrite equation 4.11 as

$$\omega^2 - [F + 1 + G]\omega + G = 0 \tag{4.17}$$

and solving for ω

$$\omega_{\pm} = \frac{F + 1 + G \pm \sqrt{(F + 1 + G)^2 - 4G}}{2} \tag{4.18}$$

This is the scaled decay rate, relative to the upper chamber, of overpressures ΔP_1 and ΔP_2 in the upper and lower chambers. Items to note about decay rate ω from Equation 4.18 include

- ω>0 so the chamber pressures always decrease to equilibrium
- ω is real and positive

We next apply boundary conditions in order to show values for ΔP_1 and ΔP_2 during the transition to steady state for the general solution

$$\begin{pmatrix} \Delta P_2 \\ \Delta P_1 \end{pmatrix} = \alpha \begin{pmatrix} a_+ \\ b_+ \end{pmatrix} exp(-\lambda_+ t) + \beta \begin{pmatrix} a_- \\ b_- \end{pmatrix} exp(-\lambda_- t) + \begin{pmatrix} \gamma_a \\ \gamma_b \end{pmatrix} \tag{4.19}$$

where α and β are unknown, γ is $\Delta P(eq)$ from Equations 4.5 and 4.6, and $(a_+ b_+)'$ and $(a_- b_-)'$ are eigenvectors of M. We need to find the eigenvectors and apply the boundary conditions at time $t = 0$ to find α and β.

We choose initial values at time $t = 0$ for lower and upper chamber pressures

$$\begin{pmatrix} \Delta P_2(0) \\ \Delta P_1(0) \end{pmatrix} \tag{4.20}$$

and put these into the general solution at time $t = 0$

$$\Delta P_2(0) - \gamma_a = \alpha a_+ + \beta a_- \tag{4.21}$$

$$\Delta P_1(0) - \gamma_b = \alpha b_+ + \beta b_- \tag{4.22}$$

The eigenvectors of the original matrix M, assuming that M has real eigenvalues, are

$$-\lambda_+ \begin{pmatrix} a_+ \\ b_+ \end{pmatrix} = M \begin{pmatrix} a_+ \\ b_+ \end{pmatrix} \tag{4.23}$$

$$-\lambda_- \begin{pmatrix} a_- \\ b_- \end{pmatrix} = M \begin{pmatrix} a_- \\ b_- \end{pmatrix} \tag{4.24}$$

Using the substitutions for ω and dimensionless values in equations 4.12

through to 4.16, the root λ_+ can be expressed as

$$-\omega_+ \begin{pmatrix} a_+ \\ b_+ \end{pmatrix} = \begin{pmatrix} -G & G \\ F & -(1+F) \end{pmatrix} \begin{pmatrix} a_+ \\ b_+ \end{pmatrix} \tag{4.25}$$

or

$$-\omega_+ a_+ = -Ga_+ + Gb_+ \tag{4.26}$$

and

$$-\omega_+ b_+ = Fa_+ - (1+F)b_+ \tag{4.27}$$

$$b_+ = \frac{G-\omega_+}{G} a_+ \tag{4.28}$$

so the eigenvectors are

$$\begin{pmatrix} a_+ \\ b_+ \end{pmatrix} = \begin{pmatrix} G \\ G-\omega_+ \end{pmatrix} \tag{4.29}$$

and, similarly for λ_-

$$\begin{pmatrix} a_- \\ b_- \end{pmatrix} = \begin{pmatrix} G \\ G-\omega_- \end{pmatrix} \tag{4.30}$$

Returning to equations 4.21 and 4.22 for initial pressures, we can now solve for α and β

$$\Delta P_2(0) - \gamma_a = \alpha G + \beta G \tag{4.31}$$

$$\Delta P_1(0) - \gamma_b = \alpha(G-\omega_+) + \beta(G-\omega_-) \tag{4.32}$$

Solving for α and β leads to

$$\beta = \frac{(\Delta P_2(0) - \gamma_a)(G-\omega_+) - (\Delta P_1(0) - \gamma_b)G}{G(\omega_- - \omega_+)} \tag{4.33}$$

$$\alpha = \frac{\Delta P_2(0) - \gamma_a - G\beta}{G} \tag{4.34}$$

The complete solution for the rate of change of overpressures ΔP_1 and ΔP_2 in the upper and lower chambers is

$$\Delta P_1(t) = \alpha(G-\omega_+)e^{-\lambda_+ t} + \beta(G-\omega_-)e^{-\lambda_- t} + \frac{Q_{in}}{F_1} \tag{4.35}$$

$$\Delta P_2(t) = \alpha G e^{-\lambda_+ t} + \beta G e^{-\lambda_- t} + \frac{(1+F)Q_{in}}{F_2} \tag{4.36}$$

In the limit as t approaches infinity, Equations 4.35 and 4.36 go to equilibrium values in Equations 4.5 and 4.6.

4.4.2 Transition to steady state

The eruption rate is directly related to the upper chamber overpressure. In this section, we investigate how the rate of pressure decay in both chambers depends on different properties of the system.

We investigate how different properties of the system affect the decay rates and pressure changes. The ratio of lower to upper chamber volumes V could range from 1 to 100, with the latter case corresponding to a relatively small upper chamber. The ratio of lower to upper chamber compressibilities B is around 1, because there should not be a vast difference in the properties of the rock in which the two chambers are situated. The resistance in the deep and shallow conduits, F, could vary with conduit size and magma viscosity, which is related to magma pressure Blundy and Cashman [2005]; Woods and Koyaguchi [1994]. We consider values from 1 to 100. This means that G, which is the ratio of upper chamber to lower chamber timescale ($G = BF/V$), ranges from 0.01 to 100. A small G corresponds to a lower chamber that responds quickly, and a large G corresponds to an upper chamber that responds quickly. We imagine that magma recharge rate $Q_{in} = 0$, to illustrate the principle of overpressurised chambers transitioning to equilibrium.

4.4.2.1 Chamber volume

First we show the effect of chamber volume ratio on decay rate, and set $B = 1$, $F = 1$, and V from 1 to 100. The upper chamber decay rate ω_+ (pink) approaches a value of 2 (pink dashed) for the limit of large V, as shown in Figure 4.2. This corresponds to the early time decompression rate of the upper chamber, before the lower chamber's effect is apparent. The lower chamber decay rate ω_- (blue) approaches a value of $G/2$ (blue dashed), corresponding to the recharge from

lower chamber and thus to the ratio of upper to lower chamber timescales. This corresponds to a slow evolution which is controlled by the lower chamber. Both V and ω are displayed on a log scale. Decay rates are dimensionless.

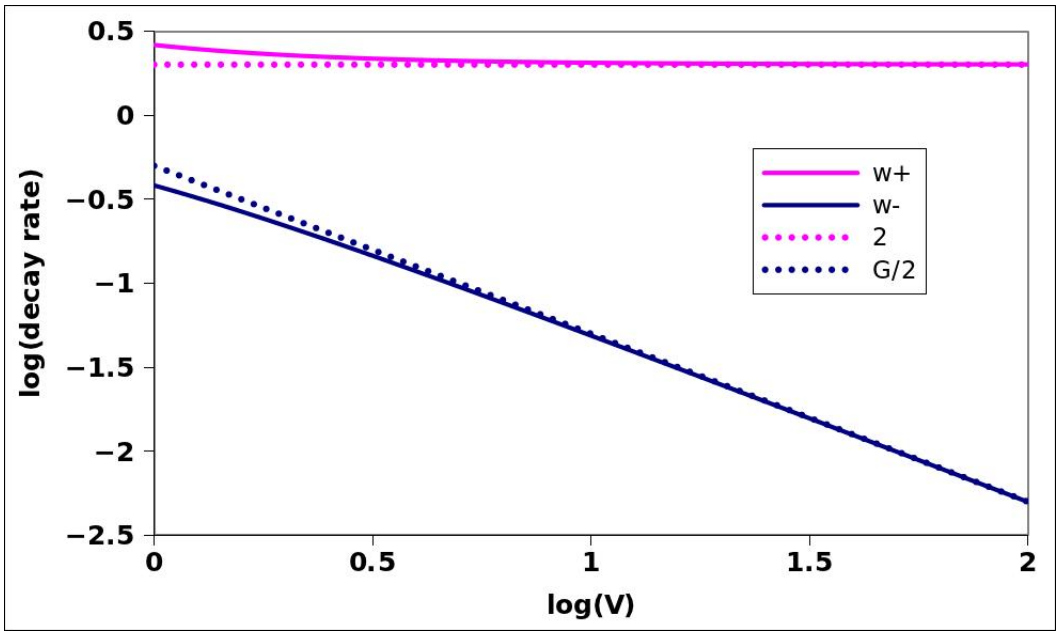

Figure 4.2: Decay rate vs chamber volume ratio. Upper chamber decay rate ω_+ (pink) approaches value of 2 (pink dashed) for large value of V. Lower chamber decay rate ω_- (blue) approaches a value of $G/2$ (blue dashed), corresponding to the recharge from lower chamber, for large value of V. Decay rates are scaled to the timescale of the upper chamber.

To illustrate how the system behaves for the limit $V = 100$ (large lower chamber), we look at how the upper and lower chamber pressures change over time. In Figure 4.3, both pressures decay to 0, but the lower chamber (blue) decays more gradually and consistently for the entire time. The upper chamber (pink) decays rapidly at first, then settles into a gradual decay alongside the lower chamber. The inset chart highlights the first 5 time units of upper chamber decay, to show that it is a smooth curve. The study of large V, indicating a tiny upper chamber and huge lower chamber, indicates a rapidly adjusting upper chamber decay rate (ω_+) and a slowly adjusting lower chamber decay rate (ω_-). While both chamber pressures decay to 0, the large lower chamber controls the long term evolution. Decay rates are dimensionless.

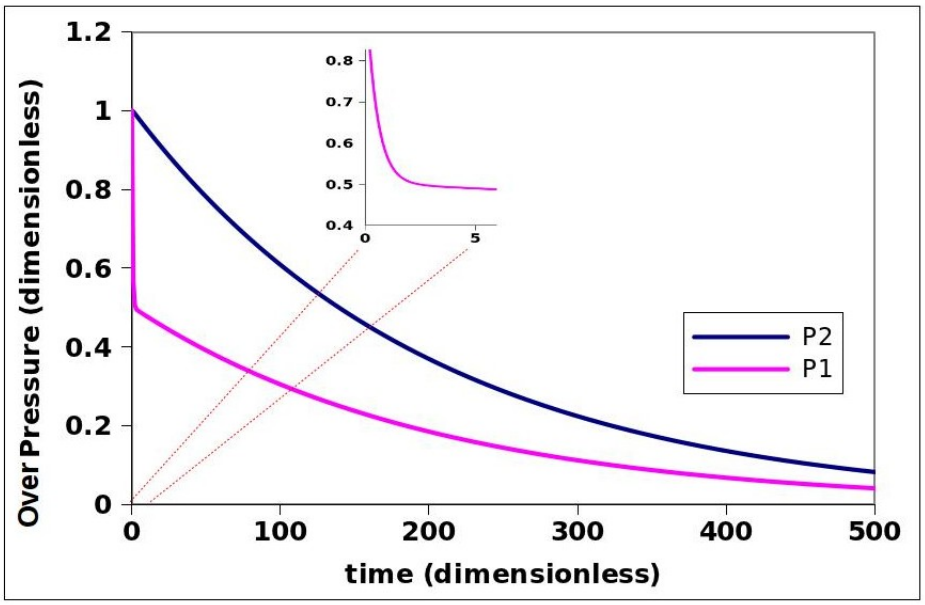

Figure 4.3: Chamber pressures for lower:upper chamber ratio 100. Both chamber pressures decay to 0. Lower chamber (blue) decays gradually and consistantly. Upper chamber (pink) decays rapidly at first, then settles into gradual decay. Inset chart highlights initial upper chamber decay, which is also a smooth curve. Decay rates are dimensionless.

To illustrate how the system behaves for the limit $V = 1$ (equal size chambers), we look at how the upper and lower chamber pressures change over time for equal size chambers. In Figure 4.4, the upper chamber (pink) decays rapidly at first, then settles into a gradual decay alongside the lower chamber. The lower chamber (blue) decays more gradually. The study of small V indicates similar pressure decay rates in both chambers at later times.

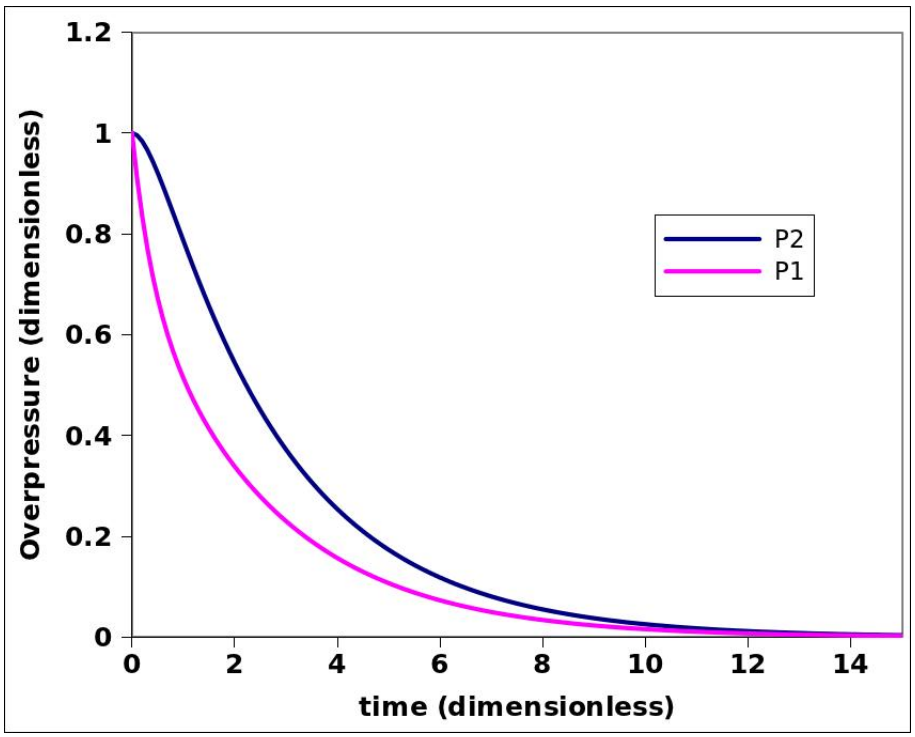

Figure 4.4: Chamber pressures for lower:upper chamber ratio 1. Both chamber pressures decay to 0 at similar rates. Lower chamber (blue) decays gradually and consistantly. Upper chamber (pink) decays somewhat more rapidly at first, then settles into gradual decay. Decay rates are dimensionless.

Finally, we look at the case for $V = 0.1$, indicating an upper chamber larger than a lower chamber. In Figure 4.5, the chambers decay at similar rates, with upper chamber (pink) decaying slightly more rapidly than lower chamber (blue) at first. A larger upper chamber dominates pressure change effects such that the system behaves as a single draining chamber, similarly as for chambers with minimal resistance between them (large F as in Figure 4.7). Reducing the ratio further to $V = 0.01$ leads to yet smaller difference in the two chambers' pressure change rates.

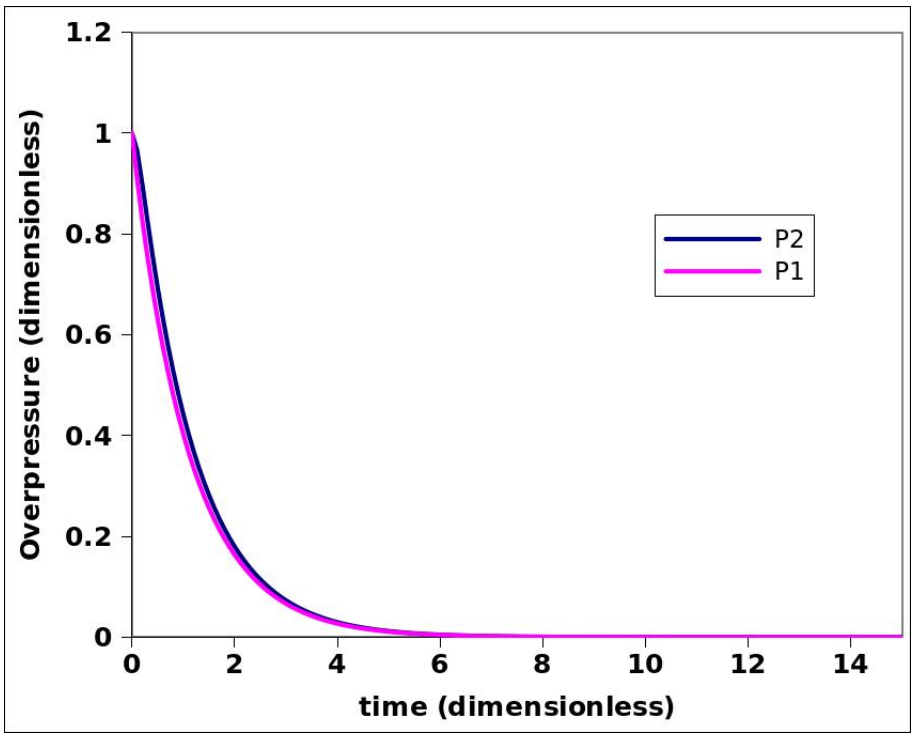

Figure 4.5: Chamber pressures for lower:upper chamber ratio 0.1. Both chamber pressures (upper, pink; lower, blue) decay to 0 at similar rates, with upper chamber decaying more rapidly at first. Decay rates are dimensionless.

4.4.2.2 Conduit resistance

Next we illustrate how a system behaves for different F. Recall that $1/F_2$ is the resistance value and that F is F_2/F_1, so a large F corresponds to a low resistance between the two chambers. We choose $B = 1$ and $V = 1$, and F can range from 0.01 to 100. A small F corresponds to a situation in which magma cannot move easily from the lower to upper chamber, and the lower chamber catches up with the upper chamber. A large F corresponds to a situation in which magma flows relatively freely between the two chambers.

We show how the decay rates evolve for different F in Figure 4.6. Lower chamber decay rate ω_+ (blue) is 0 for small F and approaches a value of $2G$ (blue dashed), indicating the timescale ratio of upper to lower chambers, for large F. Upper chamber decay rate ω_- (pink) is small for small F, as the two chambers are not in communication, then increases to a value of $1/2$ (pink dashed) for large F when the chambers are in good communication and decay together. The lower chamber takes longer to adjust for small F, and the upper chamber keeps erupting. Decay rates are dimensionless.

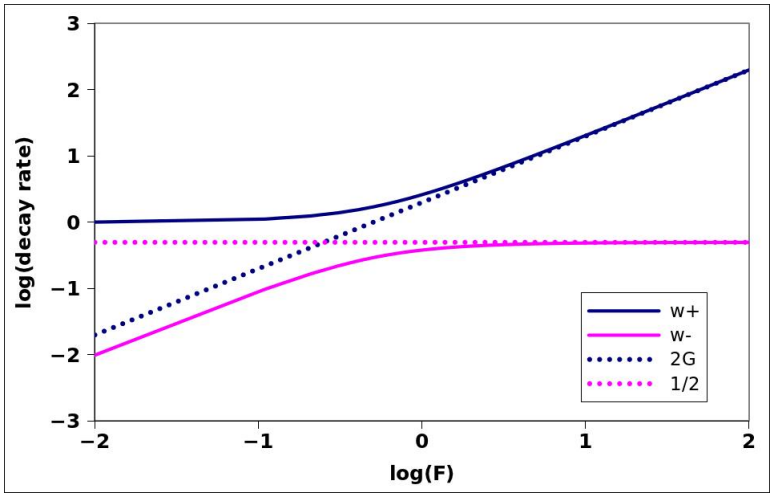

Figure 4.6: Decay rate vs resistance ratio F expressed on log scale. Lower chamber decay rate ω_+ (blue) is 0 for small F and approaches value of $2G$ (blue dashed), indicating timescale ratio of chambers, for large F. Upper chamber decay rate ω_- (pink) is small for small F, increases to value of $1/2$ (pink dashed) for large F when chambers are in good communication. Decay rates are dimensionless.

To illustrate how the system behaves for the limit $F = 100$, we look at how the upper and lower chamber pressures change when the two chambers are in good communication. Figure 4.7 shows that both upper (pink) and lower (blue) decay to 0, gradually and consistantly, at a similar rate. The two chambers effectively act as a single chamber, as there is minimal inhibition to flow between the two. The inset shows that lower chamber pressure (blue) initially decays more slowly than upper chamber (pink) at early times, but it is only in very early times that this difference is apparent.

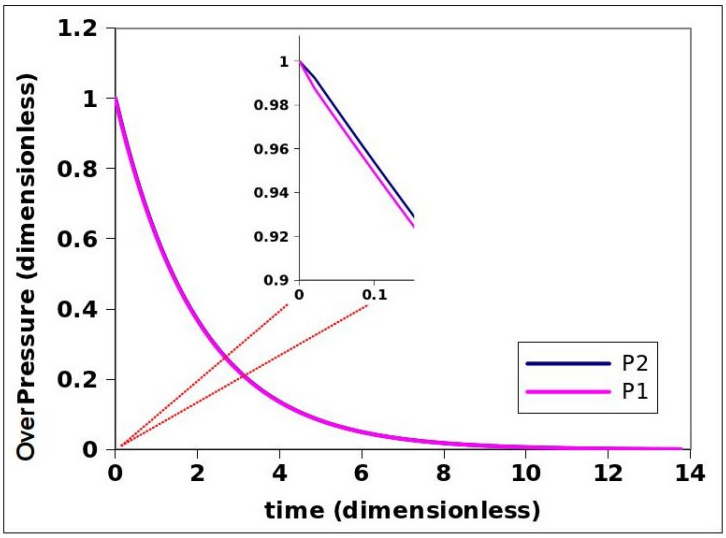

Figure 4.7: Chamber pressures for lower:upper resistance ratio $F = 100$. Upper (pink) and lower (blue) chamber pressures decay at similar rate. Inset shows that lower chamber pressure (blue) decays more slowly than upper chamber (pink) for early times. The two chambers effectively act as a single chamber.

Finally, we illustrate how the system behaves for the limit of small $F = 0.1$, corresponding to a situation in which magma cannot move easily from the lower to upper chamber. Figure 4.8 shows that both upper (pink) and lower (blue) decay to 0, but the upper chamber decays rapidly at first while the lower chamber takes time to catch up. That is, the lower chamber pressure lags behind upper chamber pressure.

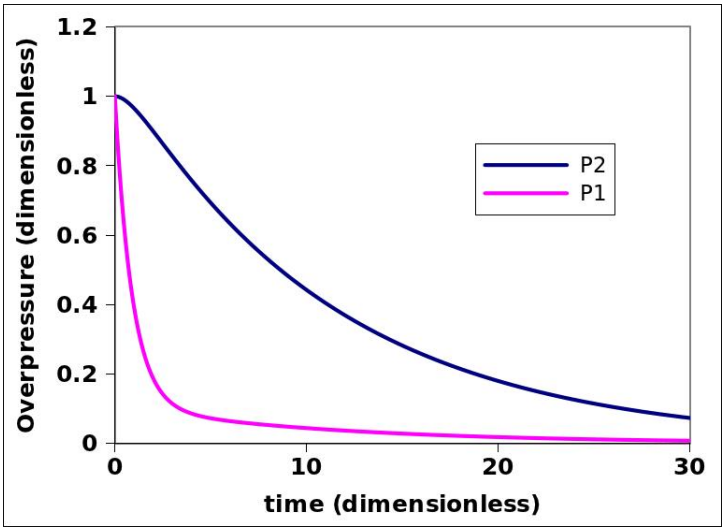

Figure 4.8: Chamber pressures for lower:upper resistance ratio $F = 0.1$. Upper (pink) decays rapidly at first while lower (blue) decays steadily, taking time to catch up and lagging behind the upper chamber. Decay rates are dimensionless.

In this section, we have investigated how different properties of the system affect the decay rates and pressure changes. Pressure changes are directly correlated to eruption rate, so we have provided insight to how a dual chamber magma system behaves when there is no magma recharge.

4.4.3 Application to Lonquimay 1988 eruption

In Chapter 3, we noted that Lonquimay volcano appeared to progress in two phases, with a rapid phase followed by a slow phase, as shown in Stasiuk's model in Figure 3.14. Figure 4.8 is reminiscent of this pattern, as the efflux rate is proportional to the top chamber pressure (Equation 4.1). This corresponds to the change in pressure in Figure 4.8 at around $t = 4$, going from a rapid eruption rate to a gradual eruption rate. There is error associated with the lava dome measurements, but we do not have an idea of what value such error takes.

In a comparison to the Lonquimay eruption, we assume the initial overpressure in each chamber to be the same. Then the shallow chamber controls the eruption, as it evolves on a rapid timescale. The change in character of the eruption occurs after around 0.45 of the volume has been erupted. We fit the Lonquimay data with equal chamber volumes of 12.5 km^3, bulk compressibility $10^{-9}Pa^{-1}$, initial chamber overpressure 10^6 Pa, and lower conduit resistance larger than that of the upper conduit (small $F = 0.1$).

Figure 4.9 is a plot of this model scaled on the timescale of the erupting shallow chamber. This is not a unique solution: we have assumed the two chambers are the same size, and allow for a shorter timescale for the upper and a longer timescale for the lower chamber, which constrain F. We choose comparable chamber volumes V_c because both phases of eruption produce roughly the same amount of magma. Time is scaled as $V_c\beta/F$, so the solution is non-unique.

From this application we get two time constants and a chamber volume linked to elastic modulus and initial overpressure as $\beta V_c \Delta P(0)$. The V_c is obtained by assuming β and $\Delta P(0)$ as stated above. This provides a good fit, but if we had more information we could get different values for V_c.

The eruption stops because there is no recharge to maintain chamber pressure. In the next section, we investigate cycles that could occur if the lower chamber is repressurised.

This interpretation uses a two chamber model with resistance from deep to shallow chamber much larger than resistance from conduit to surface. This is consistent with our earlier picture of an intrusion of magma that has cooled and evolved, and is more viscous when it starts to feed the shallow chamber.

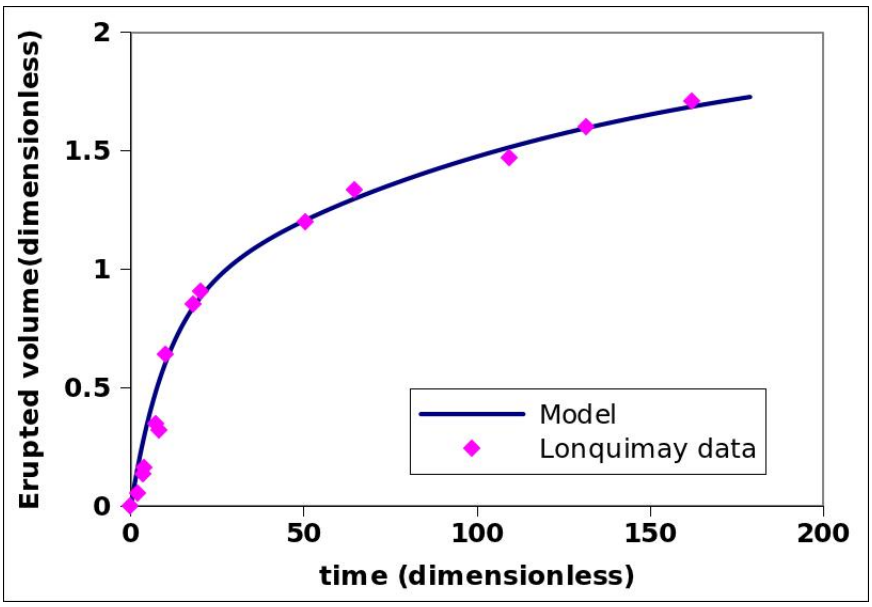

Figure 4.9: Erupted volume at Lonquimay volcano 1988 eruption, and model of two chambers with small F (magma cannot move easily from lower to upper chamber). The eruption progresses rapidly at first and then slowly after time = 25, as the eruption rate transitions to a second regime. Model has equal chamber volumes 12.5 km^3, bulk compressibility $10^{-9}Pa^{-1}$, initial chamber overpressure 10^6 Pa, and lower conduit resistance larger than that of the upper conduit (small $F = 0.1$).

4.5 Eruption cycles

4.5.1 Start/stop pressure model

In the previous section, we modeled a two chamber system that had no magma recharge rate ($Q_{in} = 0$) and no control on when an eruption starts or stops. This meant that both upper and lower chamber pressures decreased to 0.

Now we draw on Chapter 3 and say that the chamber must reach a critical overpressure ΔP_{START} to begin an eruption and decrease to overpressure ΔP_{STOP} before an eruption stops. As magma decompresses, it becomes more viscous and forms a plug in the shallow system. The critical start/stop overpressures in the shallow chamber relate to the formation of the plug, and the pressure buildup to remove the plug. We imagine that the critical overpressure occurs in the shallow chamber, because this is where crystallisation occurs. We couple the shallow chamber to a deep chamber which repressurises the shallow chamber. This gives a control on the recharge rate to the shallow chamber in terms of the dynamics of a second chamber.

We provide a diagram showing the influence of recharge on eruption rate and chamber overpressure. In Figure 4.10 we show how an eruption can increase or decrease to a steady state depending on recharge rate. We first sketch an eruption rate Q_{er} that is proportional to upper chamber overpressure ΔP (black). As long as the upper chamber overpressure is above ΔP_{STOP} the system will erupt. When the upper chamber overpressure is ΔP_{START}, the eruption can either build up or decay to steady state, depending on the recharge from the deep chamber.

For an eruption that begins at ΔP_{START} and has no recharge $Q_{in} = 0$ (pink), the chamber overpressure decays from ΔP_{START} at point A until it reaches ΔP_{STOP} and the eruption ceases. For an eruption that begins at ΔP_{START} and is supplied by critical recharge rate Q^*_{in} (blue), the chamber overpressure decays from ΔP_{START} at point A until overpressure $\Delta P(B)$ which is just larger than ΔP_{STOP}, and the eruption continues at steady state as described by Equations 4.5 and 4.6 which requires that $Q_{in} = Q_{er}$. This critical recharge rate sustains the eruption and maintains chamber overpressure larger than ΔP_{STOP}. For an eruption that begins at ΔP_{START} and is supplied by 'large' recharge rate

Q_{in}^{**} (red), the chamber overpressure increases from ΔP_{START} at point A until overpressure $\Delta P(C)$ and the eruption continues at steady state.

However, if recharge rate $Q_{in,cycle}$ is between Q_{in}^{*} and Q_{in}^{**} (green), as long as overpressure is not larger than $\Delta P(A)$, the lower chamber still builds up pressure and feeds magma into the upper chamber. The upper chamber overpressure builds up until it reaches ΔP_{START}. The sudden increase to eruption rate at point A upon reaching ΔP_{START} at point D could be due to sufficient pressure building up to remove a plug that has formed in the conduit. At this point the chamber erupts from point A until upper chamber pressure reaches ΔP_{STOP}. Then the overpressure builds back up until it reaches ΔP_{START} at point D again, leading to a series of cycles between ΔP_{START} and ΔP_{STOP}.

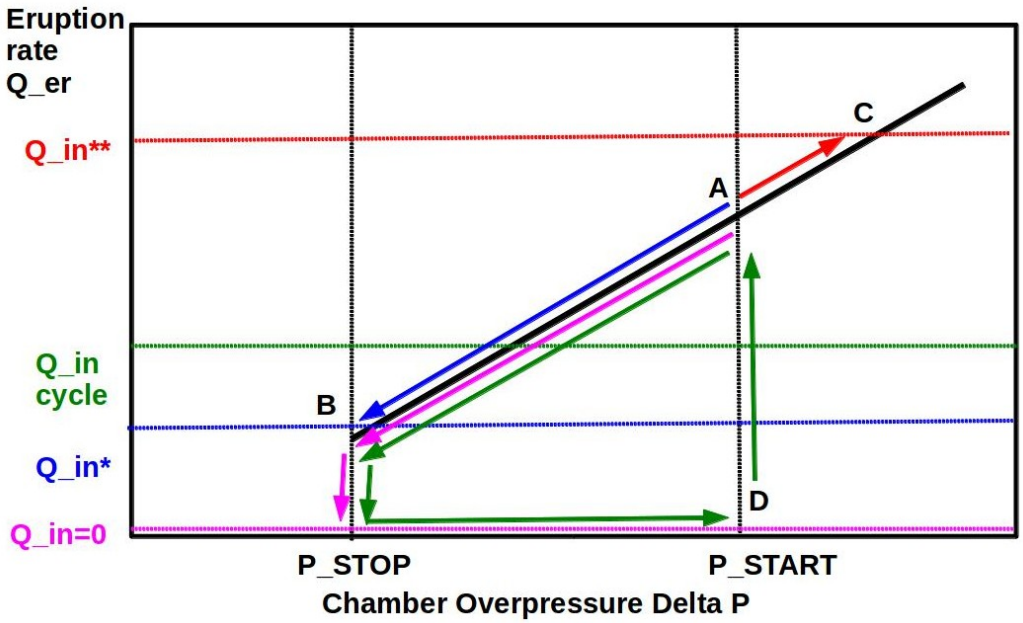

Figure 4.10: Diagram showing the influence of recharge on eruption rate for sketch of eruption rate proportional to upper chamber overpressure (black). Eruption that begins at ΔP_{START} and has no magma recharge $Q_{in} = 0$ (pink) decays and ceases at ΔP_{STOP}. Critical recharge rate Q_{in}^{*} (blue) sustains chamber overpressure decays from A until $\Delta P(B)$ which is slightly larger than ΔP_{STOP} and eruption continues at steady state as described by Equations 4.5 and 4.6. Large recharge rate Q_{in}^{**} (red) leads to increase in chamber overpressure and eruption at higher steady state C. Recharge rate between Q_{in}^{*} and Q_{in}^{**} (green) leads to cycles in chamber overpressure.

Modification of the equations in Section 4.3 leads to a model that shows cycles of chamber overpressure and eruption rate with time. Combined with the rate of pressure change in lower chamber from Equation 4.3 and magma transfer between chambers as in Equation 4.2, the following equations give the cycles in chamber overpressure and eruption rate for a system in which an eruption starts and stops at a critical upper chamber overpressure.

Upper chamber overpressure ΔP_1 is initiated at value ΔP_{START}. While

$$\Delta P_{STOP} \leq \Delta P_1 \leq \Delta P_{START} \tag{4.37}$$

and eruption rate Q_{er} takes a positive value as in Equation 4.1 (which corresponds to the last term in Equation 4.4/4.41) the rate of pressure change in the upper chamber takes a negative value as chamber pressure drops during an eruption:

$$\frac{d\Delta P_1}{dt} = \frac{F_2}{\beta_1 V_1}(\Delta P_2 - \Delta P_1) - \frac{F_1}{\beta_1 V_1}\Delta P_1 \tag{4.38}$$

This case is identical to that in Equation 4.4. However, when the upper chamber overpressure drops to $\Delta P_1 = \Delta P_{STOP}$, the eruption rate Q_{er} ceases so

$$Q_{er} = 0 \tag{4.39}$$

As long as $Q_{er} = 0$ and

$$\Delta P_{START} > \Delta P_1 > \Delta P_{STOP} \tag{4.40}$$

the rate of pressure change in the upper chamber becomes

$$\frac{d\Delta P_1}{dt} = \frac{F_2}{\beta_1 V_1}(\Delta P_2 - \Delta P_1) \tag{4.41}$$

which takes a positive value, with the upper chamber overpressure building up until $\Delta P_1 = \Delta P_{START}$ and an eruption begins again.

The cycles between ΔP_{START} and ΔP_{STOP} from the above discussion are depicted in Figure 4.11. This indicates cycles in eruption rate. The lower chamber pressure also oscillates, as the lower chamber still builds up pressure and feeds

magma into the upper chamber. The recharge rate indicates when an eruption proceeds in cycles and when it adjusts to steady state without cycles, as shown by the different cases in Figure 4.10. We next show this cyclic behaviour using a numerical simulation of the solution to the pressure change equations from Section 4.4.

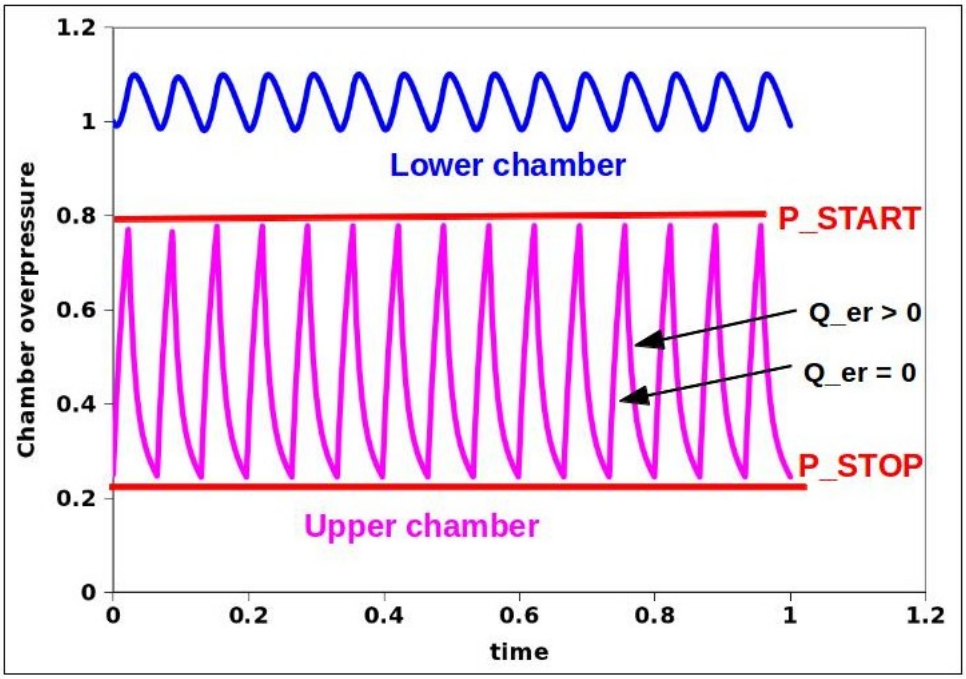

Figure 4.11: Steady state cycles of changing pressure in upper chamber. Depending on whether recharge rate is sufficient to sustain an eruption, the upper chamber cycles between ΔP_{START} and ΔP_{STOP}. When the chamber is repressurising until an eruption can begin at ΔP_{START}, the eruption rate $Q_{er} = 0$. When the pressure is dropping, the chamber is erupting and $Q_{er} > 0$.

4.5.2 Cycles at equilibrium

We conduct a brief parameter study to explore the effects of chamber volume and conduit resistance on the equilibrium pressure cycles' timescales. Referring again to values in equations 4.12 through to 4.15, we investigate the effects of increasing lower to upper chamber volume ratio V and increasing resistance between the two chambers F. Recall that upper conduit resistance is $1/F_1$ and resistance between chambers is $1/F_2$, so a large F_1 or F_2 corresponds to a small resistance. Thus a larger F, brought about by increasing F_2 or decreasing F_1, corresponds to a larger resistance in the upper conduit and a lower resistance between the two chambers.

In Figure 4.12 we set chamber volumes equal ($V = 1$) and explore the chamber pressure effects of $F = 1, 10$, and 50. Dashed lines represent lower chamber overpressure ΔP_2, solid lines represent upper chamber overpressure ΔP_1. Both chambers are initiated below the overpressure required to start an eruption, ΔP_{START}.

In all cases in this study, we use stepwise Euler integration to numerically solve Equations 4.37 through 4.41 in Microsoft Excel. The initial overpressure in each chamber is specified as halfway between critical starting pressure P_{START} and P_{STOP}, with eruption rate $Q_{er} = 0$ so the chamber overpressure is initially increasing and the outflux is paused. The rate of overpressure change ΔP in each chamber is calculated at time t, multiplied by the timestep dt, and added to the overpressure at time $t - 1$. We perform resolution checks for double the number of timesteps in the original figures from Sections 4.5.2.1 to 4.5.2.3, with examples shown at the end of this section (section 4.5.2.4).

4.5.2.1 Equal chamber volumes $V = 1$

For equal resistances $F = 1$ (blue), the lower chamber settles into steady cycles of overpressure (from $t = 10$), while the upper chamber oscillates between $\Delta P_{START} = 1$ and $\Delta P_{STOP} = 2$. The upper chamber loses pressure as fast as F_1 allows it to drain, and the lower chamber cannot refill it fast enough to maintain pressure. Thus the upper and lower chambers act separately, with upper conduit resistance controlling the upper chamber pressure change and recharge rate Q_{in} controlling the lower chamber pressure change. When the eruption stops ($t = 4$), the upper chamber increases pressure rapidly and the lower chamber continues to

lose pressure at first, because it has to fill the upper chamber, then it follows the upper chamber rate of change. Thus as long as the eruption rate and recharge rate occur on similar timescales, the cycles are steady and rapid compared to those for larger F.

Increasing F to 10 (orange) means that the two chambers are in better communication with each other and the resistance from upper chamber to surface is larger than the resistance between the two chambers. The upper and lower chambers behave similarly; both oscillating between $\Delta P_{START} = 1$ and $\Delta P_{STOP} = 2$ with slightly longer cycles than for $F = 1$. The timescale of cycles is slower than for $F = 1$. The lower chamber overpressure lags behind the upper chamber during an eruption as the upper chamber loses its volume first, but they soon lose pressure at the same rate. The upper chamber overpressure lags behind the lower chamber during recharge as the lower chamber first needs to feed the upper chamber, but they are soon both fed by Q_{in} at the same rate. Thus the pressure buildup during recharge is slower than for $F = 1$ and cycles are longer overall.

Further increasing F to 50 (pink) gives a case in which the two chambers have such little resistance between them that they act effectively as a single chamber, and follow identical pressure patterns controlled by the resistance from upper chamber to surface. The timescale of cycles is faster than for $F = 10$ because there is negligible lag between upper and lower chamber pressure change. During recharge, Q_{in} reaches both chambers simultaneously; during eruption, F_1 slows both chambers simultaneously. Thus the cycles are those of a single large chamber without the delay that occurs for $F = 10$.

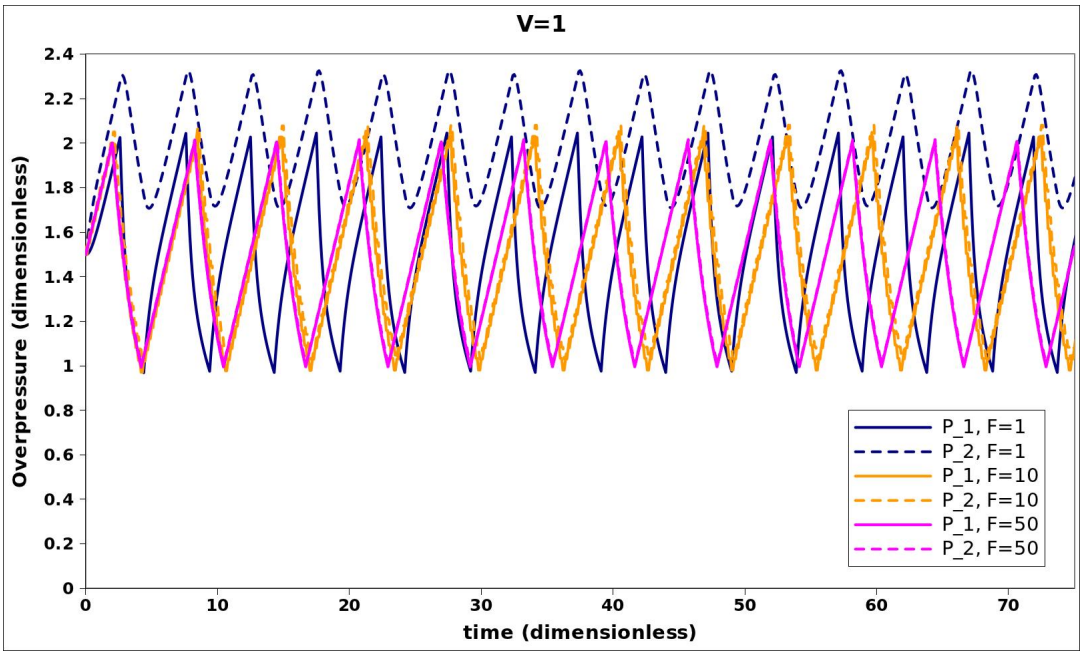

Figure 4.12: Steady state overpressure cycles (from $t = 10$) for equal chamber volumes $V = 1$. Dashed lines represent lower chamber overpressure ΔP_2, solid lines represent upper chamber overpressure ΔP_1. For equal resistances $F = 1$ (blue), the lower chamber settles into steady cycles of overpressure. The upper chamber has rapid pressure change cycles controlled by upper conduit resistance $1/F_1$ while recharge rate Q_{in} controls the lower chamber pressure change. For $F = 10$ (orange), resistance from upper chamber to surface is larger than resistance between the two chambers so both behave similarly. For $F = 50$ (pink), the two chambers have minimal resistance between them and act as a single chamber, following an identical pressure pattern. The timescale of cycles is faster for $F = 100$ than $F = 10$ because coupling between the chambers occurs more rapidly and there is no delay recharge Q_{in} reaches both at the same time. The timescale of cycles for $F = 1$ is faster because there is sufficiently high resistance that the lower chamber never loses a significant amount of pressure, thus overpressure change happens faster.

In Figure 4.13, we plot the erupted volume V associated with these overpressures. Recall that eruption rate is

$$Q_{er} = F_1 \Delta P_1 \tag{4.42}$$

so erupted volume is simply the integral of the rate. As in the overpressure plot, erupted volume is shown for equal resistances between conduits ($F = 1$, blue); resistance from upper chamber to surface larger than resistance between two chambers ($F = 10$, orange); and minimal resistance between two chambers ($F = 50$, pink). All erupt a similar amount of magma, with shorter recharge durations for $F = 1$.

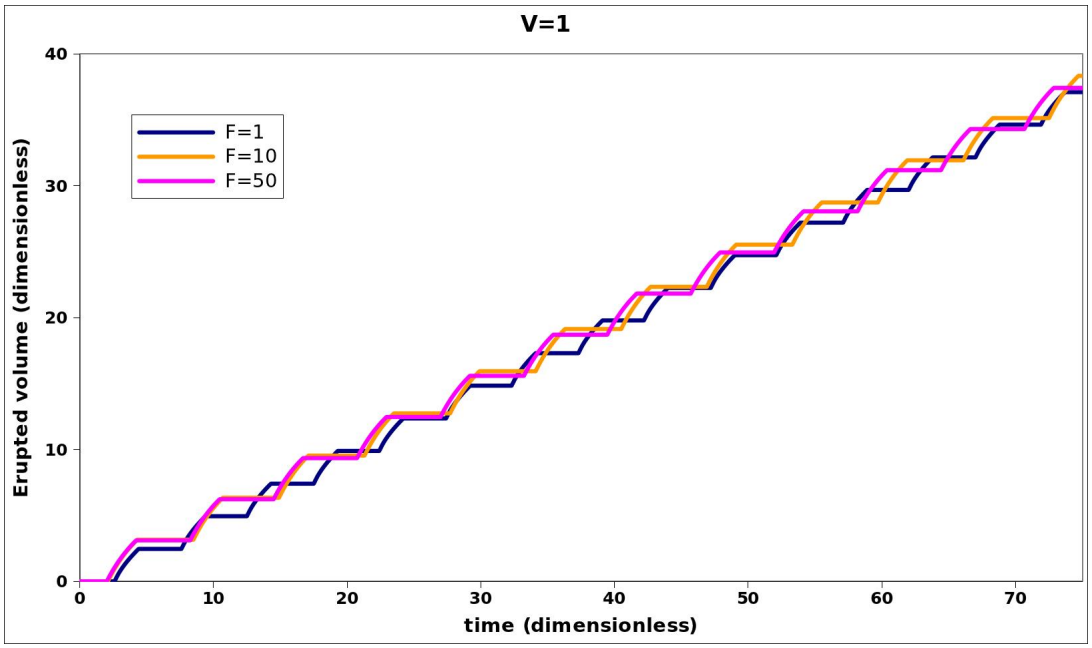

Figure 4.13: Steady state erupted volume cycles (from $t = 15$) for equal chamber volumes $V = 1$. Each example shows a similar erupted volume over time. Shown for equal resistances between conduits ($F = 1$, blue); resistance from upper chamber to surface larger than resistance between two chambers ($F = 10$, orange); and minimal resistance between two chambers ($F = 50$, pink).

4.5.2.2 Lower chamber larger than upper chamber $V = 10$

In Figure 4.14 we increase the lower chamber volume ($V = 10$) and explore the chamber pressure effects of $F = 1, 10$, and 50. Dashed lines represent lower chamber overpressure ΔP_2, solid lines represent upper chamber overpressure ΔP_1. Both chambers are initiated below the overpressure required to start an eruption, ΔP_{START}. Until time $t = 10$, both chambers are building up to ΔP_{START}, which takes more time than for $V = 1$ because of the lower chamber's larger volume.

For equal resistances $F = 1$ (blue), the lower chamber settles into steady cycles of overpressure at about $t = 20$, while the upper chamber oscillates between $\Delta P_{START} = 1$ and $\Delta P_{STOP} = 2$. The variation in lower chamber pressure (blue dashed) is small because the large volume responds less to the recharge Q_{in}. The resistance between the two chambers is sufficient that the upper chamber pressure (blue solid) changes rapidly and does not see the minimal pressure loss in the lower chamber.

As before, increasing F to 10 (orange) means that the two chambers are in better communication with each other and the resistance from upper chamber to surface is larger than the resistance between the two chambers. Once the upper chamber reaches $\Delta P_{START} = 2$, just after $t = 10$, its pressure drops rapidly as the small upper chamber erupts its magma and then decreases gradually alongside the deep chamber. When the upper chamber reaches $\Delta P_{STOP} = 1$, at $t = 23$, its overpressure increases rapidly for less than one time unit and then increases gradually alongside the deep chamber. The lower chamber overpressure lags behind the upper chamber during an eruption as the upper chamber loses its volume first, but the upper chamber lags behind the lower chamber during recharge as Q_{in} needs time to reach both chambers. This lag is very small for $V = 10$. The lower chamber controls the eruption rate when it is much larger than the upper chamber, because the time it takes for the small upper chamber to fill and empty is very small compared to the ovearll timescale of the cycles.

Further increasing F to 50 (pink) means that the two chambers have such little resistance between them that they act effectively as a single chamber, and follow an identical pressure pattern controlled by the resistance from upper chamber to surface. As with $F = 10$ (orange), there is a very brief rapid drop in upper

chamber overpressure at the beginning and end of an eruption as it empties and fills, then couples to the large lower chamber which takes more time to change pressure. However, the lag is negligible compared to $F = 10$, so the controlling factor is the large lower chamber and the cycles are slower than for $F = 10$ because the chambers couple more rapidly. It takes longer for Q_{in} to cause a pressure change in the larger volume.

The lower chamber controls the eruption rate when it is much larger than the upper chamber, as the time it takes for the small upper chamber to fill and empty is very small compared to the overall timescale of the cycles. The largest F (pink) has the longest timescales because it takes longer for Q_{in} to create a pressure change in what is effectively one large chamber than it does for the chambers to achieve the coupled state as was the case in $V = 1$.

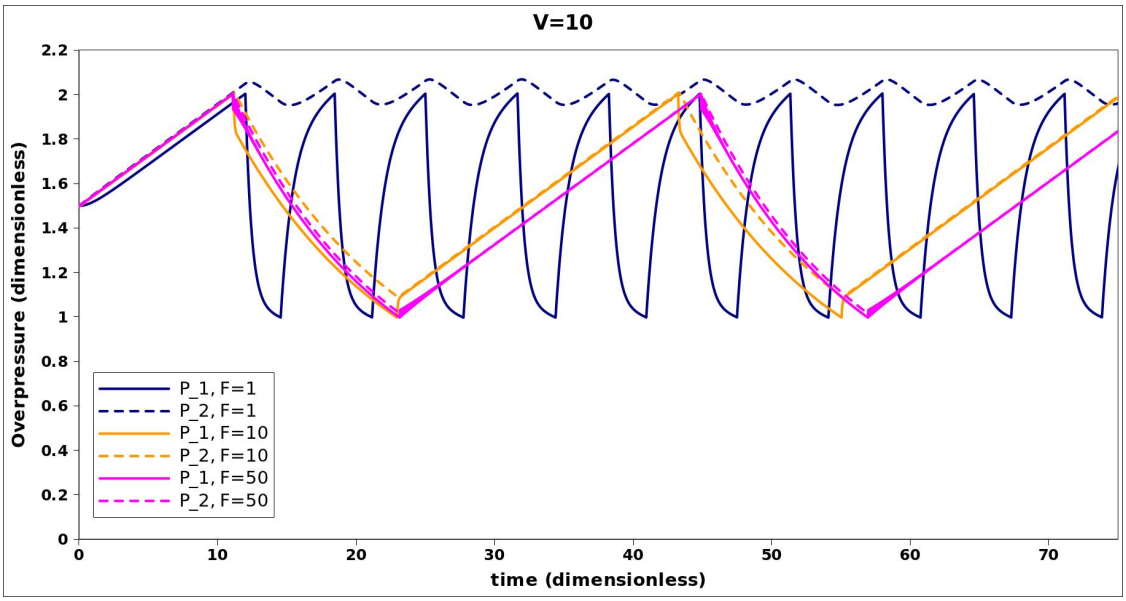

Figure 4.14: Steady state (from $t = 23 - 58$ shows a complete cycle) overpressure cycles for large lower chamber $V = 10$: cycles are slower than for equal chamber volumes. Dashed lines represent lower chamber overpressure ΔP_2, solid lines represent upper chamber overpressure ΔP_1. For equal resistances $F = 1$ (blue), the lower chamber settles into steady cycles of slight overpressure while the upper chamber undergoes large pressure changes as it drains and fills. For $F = 10$ (orange), resistance from upper chamber to surface is larger than resistance between the two chambers so both behave similarly after a rapid initial change in upper chamber pressure while it fills or empties ($t = 10, 23$). For $F = 50$ (pink), the two chambers have minimal resistance between them and act as a single chamber, following an identical pressure pattern, and the rapid initial change in upper chamber pressure ($t = 10, 23$) is less pronounced. The largest F (pink) has the longest timescales because it takes longer for Q_{in} to create a pressure change in what is effectively one large chamber than it does for the chambers to achieve a coupled state.

In Figure 4.15, we plot the erupted volume V associated with these overpressures. As in the pressure plot, erupted volume is shown for equal resistances between conduits ($F = 1$, blue); resistance from upper chamber to surface larger than resistance between two chambers ($F = 10$, orange); and minimal resistance between two chambers ($F = 50$, pink). The volume erupted is largest for minimal resistance (pink).

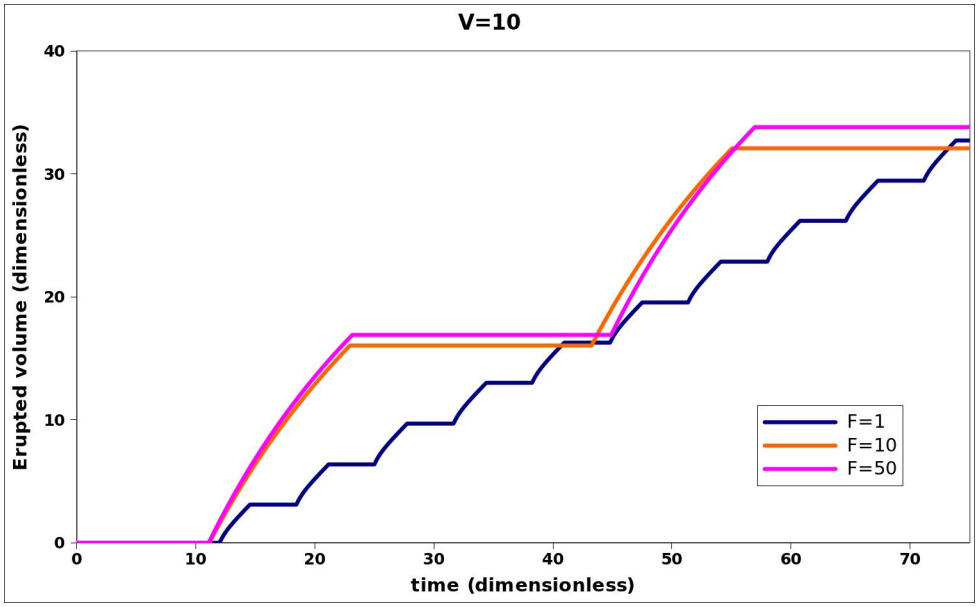

Figure 4.15: Steady state erupted volume cycles (from $t = 23 - 58$ shows a complete cycle) for chamber volume ratio $V = 10$. The erupted volume at a given time is largest for minimal resistance between chambers (pink). Shown for equal resistances between conduits ($F = 1$, blue); resistance from upper chamber to surface larger than resistance between two chambers ($F = 10$, orange); and minimal resistance between two chambers ($F = 50$, pink).

In Figure 4.16, we also explore cases for F between 1 and 10, adding plots of $F = 1.5$ (red), $F = 2$ (black), and $F = 5$ (turquoise) to the original plot of $F = 1$ (blue). We note that $F = 5$ behaves similarly to $F = 10$ (orange in Figure 4.14) but on a shorter timescale, so for ease of visualisation, we leave out $F = 10$ and $F = 50$ in this figure.

As before, increasing F means that the two chambers are in better communication with each other and the resistance from upper chamber to surface is larger than the resistance between the two chambers. Once the upper chamber reaches ΔP_{START}, its pressure drops rapidly as it erupts its magma and then decreases gradually alongside the deep chamber. When the upper chamber reaches ΔP_{STOP}, its overpressure increases rapidly at first and then increases gradually alongside the deep chamber. This leads to two apparent phases of eruption rate, with shift from fast to slow pressure drop in the upper chamber occuring more rapidly for increasing values of F, from $F = 1.5$ (red) to $F = 2$ (black) to $F = 5$ (turquoise). For extremely large values of F, the shift becomes less apparent as the chambers couple rapidly (illustrated by pink in Figure 4.14). The lower chamber overpressure lags behind the upper chamber during an eruption as the upper chamber loses its volume first, but the upper chamber lags behind the lower chamber during recharge as Q_{in} needs time to reach both chambers. The largest F (turquoise) has the longest cycles because it takes longer for Q_{in} to create a pressure change in what is effectively one large chamber than it does for the chambers to achieve the coupled state as was the case in $V = 1$.

In Figure 4.17, we plot the erupted volume associated with these overpressures. As in the pressure plot, erupted volume is shown for equal resistances between conduits ($F = 1$, blue); resistance from upper chamber to surface larger than resistance between two chambers ($F = 1.5$, red; $F = 2$, black; $F = 5$, turquoise; $F = 10$, orange); and minimal resistance between two chambers ($F = 50$, pink). The erupted volume in a single cycle is largest for minimal resistance between chambers (pink). Although not shown here, we note that for $V = 1$, values of F between 1 and 10 cause small shifts in pressure change cycle durations; for $V = 100$, trends are similar to the cases shown here for $V = 10$ but occur on a longer timescale.

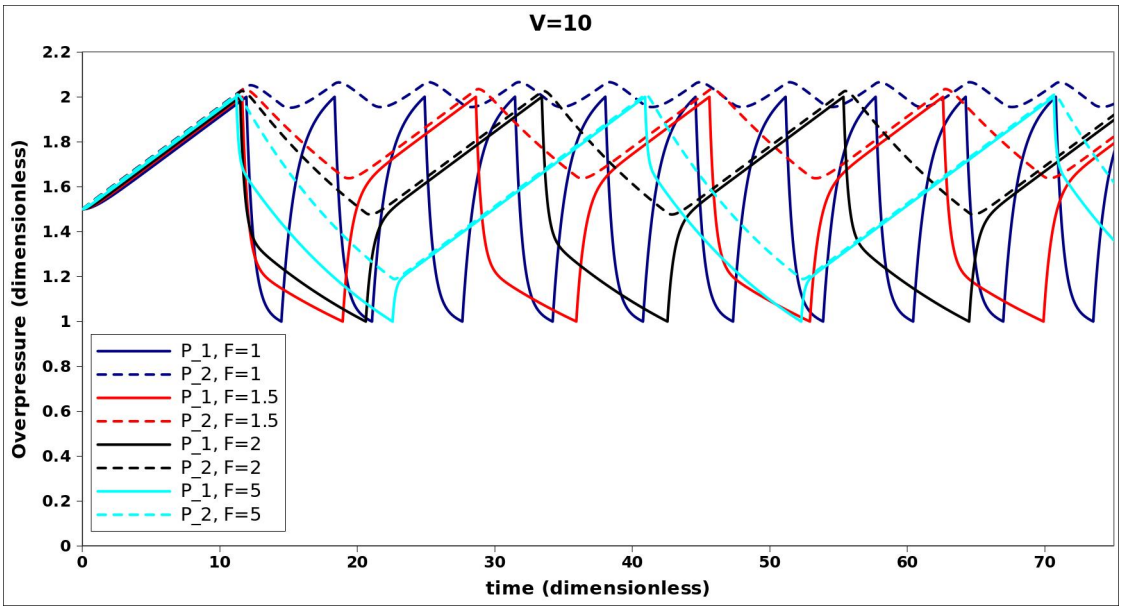

Figure 4.16: Steady state pressure cycles including F between 1 and 5 for chamber volume ratio $V = 10$. Dashed lines represent lower chamber overpressure ΔP_2, solid lines represent upper chamber overpressure ΔP_1. For equal resistances $F = 1$ (blue), the lower chamber settles into steady cycles of slight overpressure while the upper chamber undergoes large pressure changes as it drains and fills. For $F = 5$ (turquoise), resistance from upper chamber to surface is larger than resistance between the two chambers so both behave similarly after a rapid initial change in upper chamber pressure while it fills or empties. This shift from fast to slow pressure drop in the upper chamber occurs more rapidly for increasing values of F, from $F = 1.5$ (red) to $F = 2$ (black) to $F = 5$ (turquoise). The largest F (turquoise) has the longest timescales because it takes longer for Q_{in} to create a pressure change in what is effectively one large chamber than it does for the chambers to achieve a coupled state.

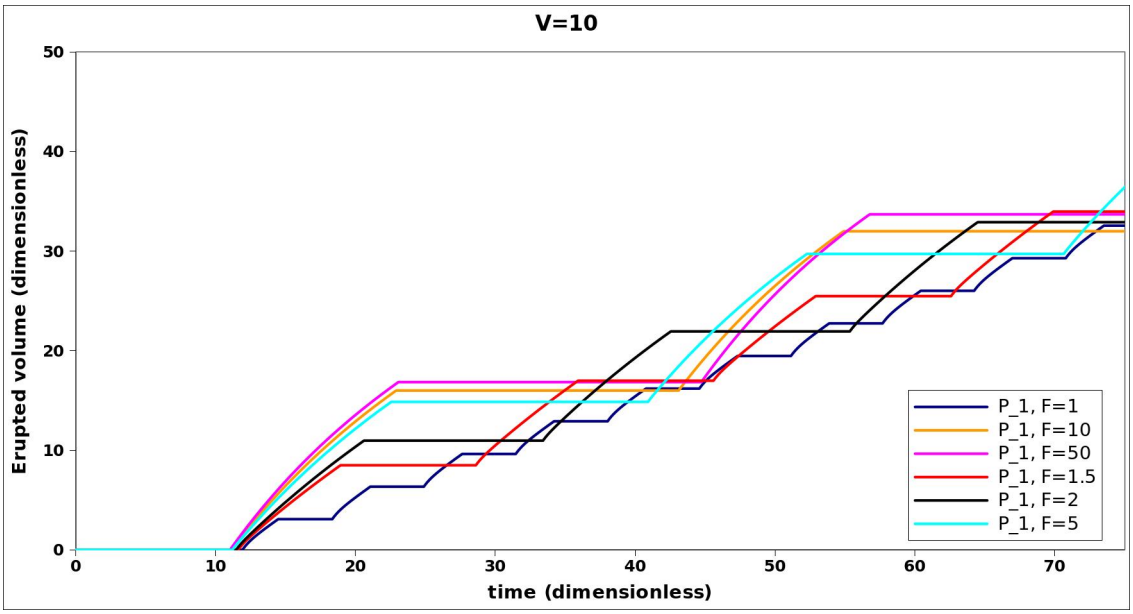

Figure 4.17: Steady state erupted volume cycles for more values of F, and chamber volume ratio $V = 10$. The erupted volume in a single cycle is largest for minimal resistance between chambers (pink). Shown for equal resistances between conduits ($F = 1$, blue); resistance from upper chamber to surface larger than resistance between two chambers ($F = 1.5$, red; $F = 1.5$, black; $F = 5$, turquoise; $F = 10$, orange); and minimal resistance between two chambers ($F = 50$, pink).

4.5.2.3 Lower chamber much larger than upper chamber $V = 100$

In Figure 4.14 we increase the lower chamber volume ($V = 100$) and explore the chamber overpressure effects of $F = 1, 10$, and 50. Dashed lines represent lower chamber overpressure ΔP_2, solid lines represent upper chamber overpressure ΔP_1. Both chambers are initiated below the overpressure required to start an eruption, ΔP_{START}. Until time $t = 100$, both chambers require more time to build up to ΔP_{START} because of the lower chamber's larger volume.

The behaviour of each chamber pair for the extremely large V is the same as for $V = 10$ but the timescale for pressure buildup in each cycle is significantly longer. A massive lower chamber requires more magma input to build up to ΔP_{START} and, similarly, to drain to ΔP_{STOP}. When $F = 1$, the lower chamber overpressure (blue dashed) undergoes minimal change in each cycle because the upper chamber erupts and refills rapidly without coupling to the deep chamber. For larger F, with the exception of the immediate initial filling or emptying, the upper chamber has minimal effect on the overall eruption pattern and merely acts as a tiny extension of the lower chamber. The timescale of cycles for $F = 10$ and $F = 50$ are indistinguishable because any lag due to the upper chamber is dampened by the coupling to the huge lower chamber.

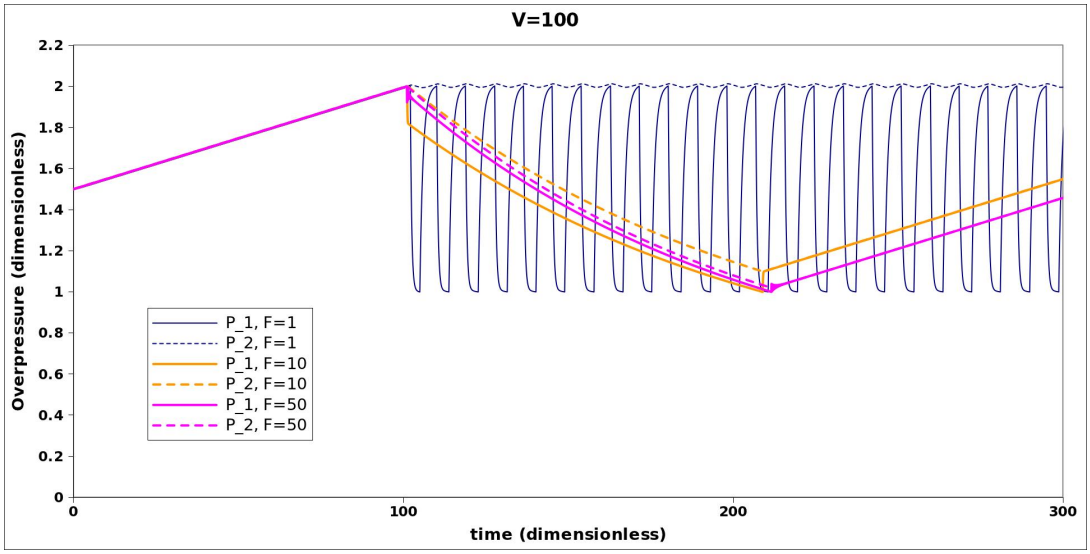

Figure 4.18: Steady state overpressure cycles for large lower chamber $V = 100$: cycles are slower than for $V = 1$ or $V = 10$. Dashed lines represent lower chamber overpressure ΔP_2, solid lines represent upper chamber overpressure ΔP_1. For equal resistances $F = 1$ (blue),the lower chamber overpressure (blue dashed) undergoes minimal change in each cycle because the upper chamber erupts and refills rapidly without coupling to the deep chamber. For $F = 10$ (orange), resistance from upper chamber to surface is larger than resistance between the two chambers so both behave similarly after a rapid initial change in upper chamber overpressure while it fills or empties ($t = 10$ and $t = 210$). For $F = 50$ (pink), the two chambers have minimal resistance between them and act as a single chamber, following an identical pressure pattern, and the rapid initial change in upper chamber overpressure ($t = 100$ and $t = 210$) is less pronounced. The timescale of cycles for $F = 10$ and $F = 50$ are indistinguishable because any lag due to the upper chamber is dampened by the coupling to the huge lower chamber.

In Figure 4.15, we plot the erupted volume V associated with these pressures. As in the pressure plot, erupted volume is shown for equal resistances between conduits ($F = 1$, blue); resistance from upper chamber to surface larger than resistance between two chambers ($F = 10$, orange); and minimal resistance between two chambers ($F = 50$, pink). The behaviour for the extremely large V is the same as for $V = 10$ but the timescale is significantly longer.

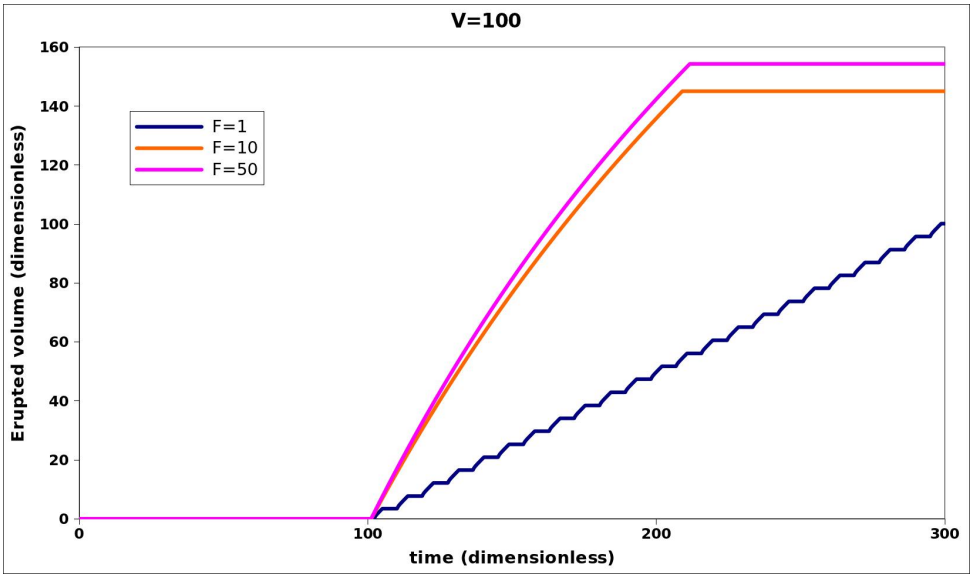

Figure 4.19: Steady state erupted volume cycles for equal chamber volumes $V = 1$. The erupted volume at a given time is largest for minimal resistance between chambers (pink). Shown for equal resistances between conduits ($F = 1$, blue); resistance from upper chamber to surface larger than resistance between two chambers ($F = 10$, orange); and minimal resistance between two chambers ($F = 50$, pink).

4.5.2.4 Resolution checks

To check the resolution of the timescale used in the pressure cycle diagrams, we replot Figures 4.12, 4.14, and 4.18, with a timestep $dt = 0.01$. This is at least double the number of timesteps and at most five times the number of timesteps in the original figures, as not all the cases in the original figures had the same timesteps.

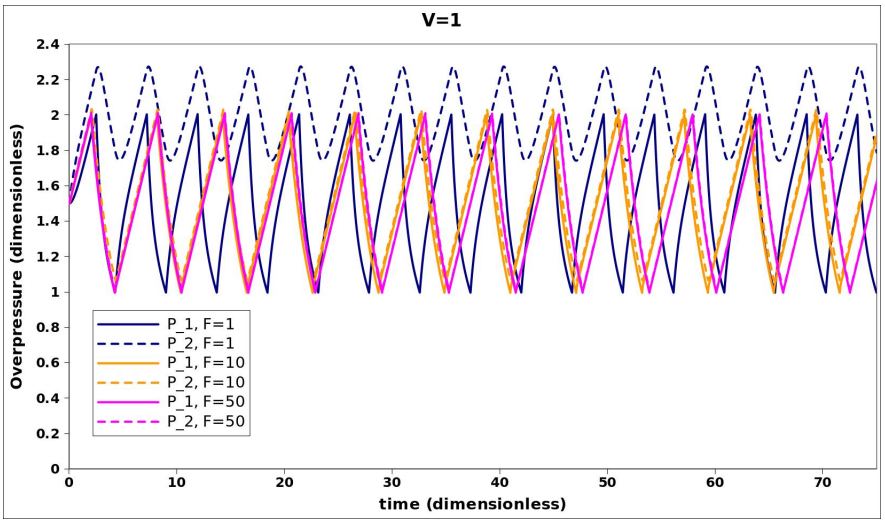

Figure 4.20: Resolution check: overpressure cycles for equal chamber volumes $V = 1$. See Figure 4.12 for detailed discussion of cycles.

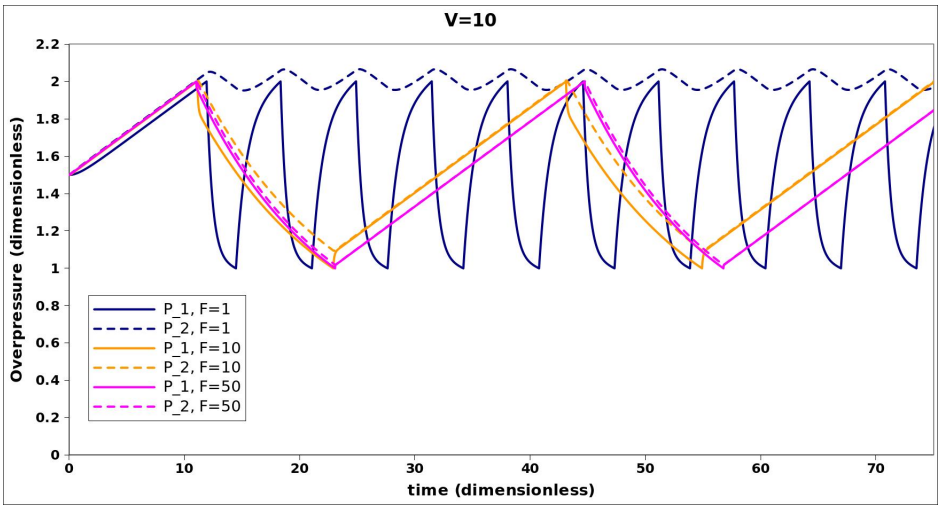

Figure 4.21: Resolution check: overpressure cycles for larger lower chamber $V = 10$, doubling the number of timesteps from the original figure. See Figure 4.14 for detailed discussion of cycles.

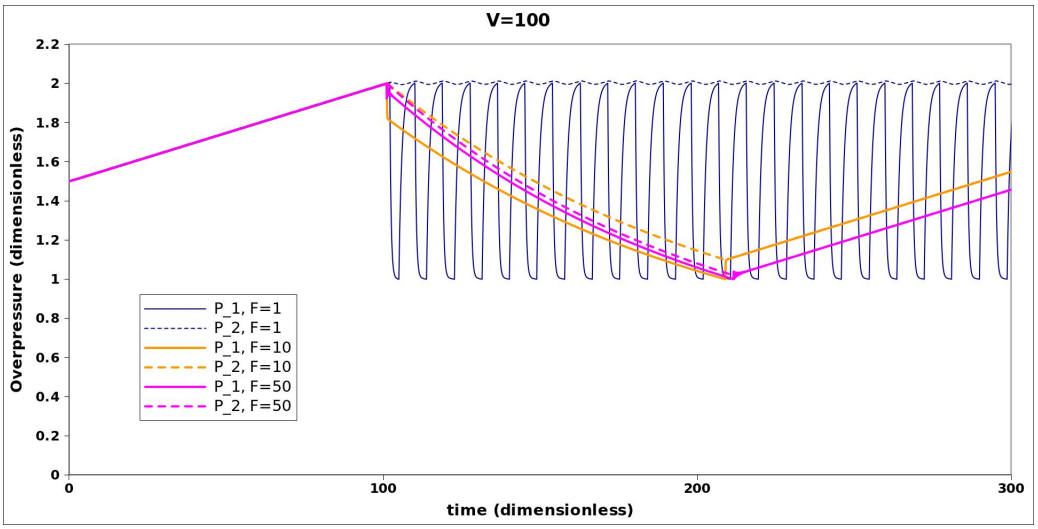

Figure 4.22: Resolution check: overpressure cycles for largest lower chamber $V = 100$, doubling the number of timesteps from the original figure. See Figure 4.18 for detailed description of cycles.

4.5.3 Steady state cycles accounting for magma density

In all of our calculations until now, we have neglected the effect of magma weight in the conduit on the pressure in the lower chamber: a column of fluid above the chamber will increase the chamber pressure. The effective magma density is the difference in density between the density of the magma, ρ_{magma} and the density of the crust ρ_{crust}, so effective magma density $\Delta\rho$ is

$$\Delta\rho = \rho_{magma} - \rho_{crust} \tag{4.43}$$

This adds a term to the eruption rate Q_{er} and flux $Q_{2,1}$ between the two chambers:

$$Q_{er} = F_1(\Delta P_1 - \Delta\rho g h_1) \tag{4.44}$$

$$Q_{2,1} = F_2(\Delta P_2 - \Delta\rho g h_2 - \Delta P_1) \tag{4.45}$$

for resistances $1/F_1$ and $1/F_2$, and conduit lengths h_1 and h_2. This means that overpressure change equations 4.3 and 4.4 become

$$\frac{d\Delta P_2}{dt} = \frac{1}{\beta_2 V_2} Q_{in} - \frac{F_2}{\beta_2 V_2}(\Delta P_2 - \Delta P_1 - \Delta\rho g h_2) \tag{4.46}$$

and

$$\frac{d\Delta P_1}{dt} = \frac{F_2}{\beta_1 V_1}(\Delta P_2 - \Delta P_1 - \Delta\rho g h_2) - \frac{F_1}{\beta_1 V_1}(\Delta P_1 - \Delta\rho g h_1) \tag{4.47}$$

The effect of adding this density is to shift the chamber overpressures to higher values. As an example, we consider a lower chamber which contains magma of higher density than the surrounding crust. This denser magma is injected to the upper chamber, which contains magma of comparable density to that of the crust. An analagous situation happens if the shallow chamber contains a denser magma.

We recalculate the equilibrium overpressure cycles shown in Figure 4.12, for equal chamber volumes and equal resistance both between chambers and from upper chamber to surface, in Figure 4.23. We show both the overpressure cycles without this added magma pressure (blue), and the new calculation (pink). The

lower chamber (dashed) has a higher pressure than it did without the added magma density. The upper chamber (solid) has smaller fluctuations relative to the absolute overpressure in the deep chamber. This will be important to our analysis of surface deformation data in later chapters.

In the next section, we investigate how an over- or under-pressured lower chamber adjusts to the steady state cycles described in this section.

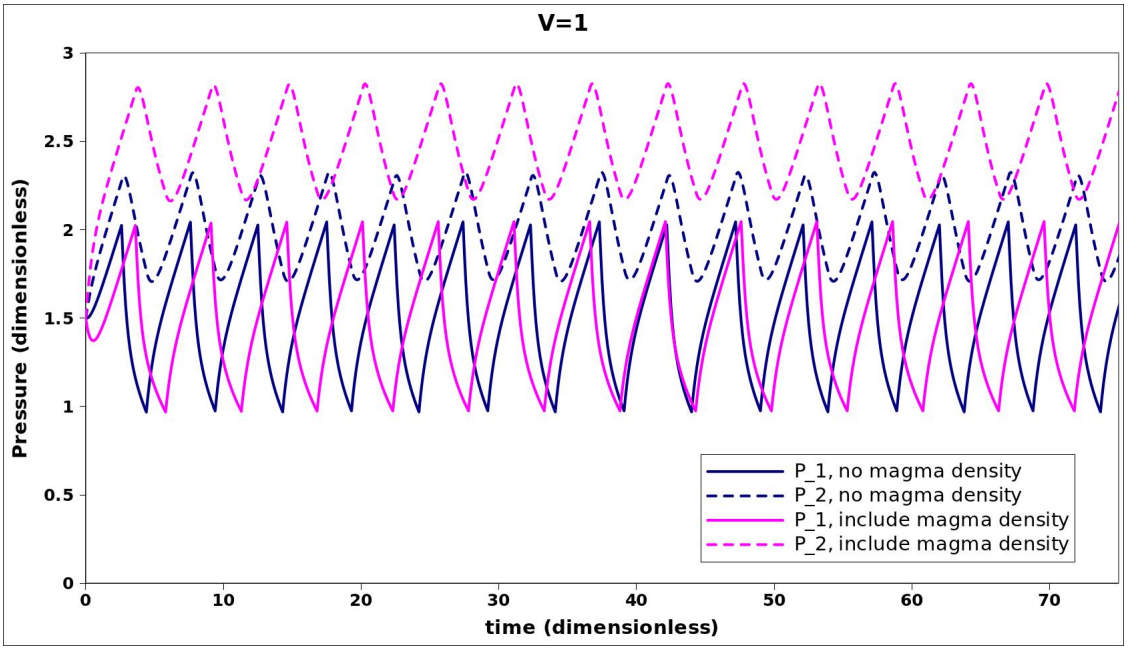

Figure 4.23: Steady state pressure cycles for equal chamber volumes ($V = 1$) and equal resistance between chambers and to surface ($F = 1$). Calculations ignoring the density of magma adding to the overpressure in the lower chamber are shown in blue; including the density of magma are shown in pink. The upper chamber (solid) has smaller fluctuations relative to absolute overpressure in the deep chamber (dashed) when the density is included.

4.5.4 Impact of different initial overpressure in chambers

Until now, our calculations have assumed that both chambers begin their eruption cycle at P_{START}. Now we investigate what happens if the chambers do not start at equilibrium: in the following calculations, we initiate the upper and lower chambers at over- and underpressures.

Figure 4.24 shows the evolution of lower chamber pressure for several cases. If the initial lower chamber overpressure $\Delta P_2(0)$ is the pressure required to start an eruption ($\Delta P_2(0) = \Delta P_{START}$, blue), the lower chamber pressure immediately synchronises to equilibrium cycles of equal period. If the lower chamber is overpressured by a small amount ($\Delta P_2(0) > \Delta P_{START}$, orange), it may undergo a few shorter cycles before adjusting to steady state. These could appear as a steady state system in the early time of an ongoing eruption. If the lower chamber pressure overpressured by a large amount ($\Delta P_2(0) >> \Delta P_{START}$, green), it may take an entire cycle to adjust. This could appear as a waning eruption without recharge. If the lower chamber is underpressured ($\Delta P_2(0) < \Delta P_{START}$, pink), it may also take an entire cycle to adjust. The corresponding cycles in the upper chamber are shown in Figure 4.25.

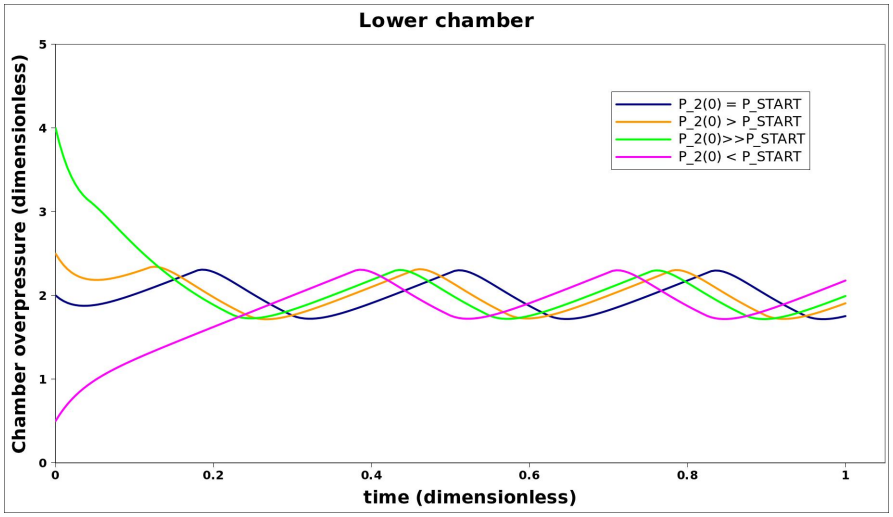

Figure 4.24: Over- and underpressured lower chamber (ΔP_2) adjustment to steady state cycles: Slightly overpressured lower chamber (orange) undergoes a small number of shorter cycles. Significantly overpressured chamber (green) takes a full cycle to adjust. Underpressured chamber (pink) takes at least a full cycle to adjust. For early times of an ongoing eruption, these adjustment periods could be interpreted as a different steady state or waning or constantly increasing eruption.

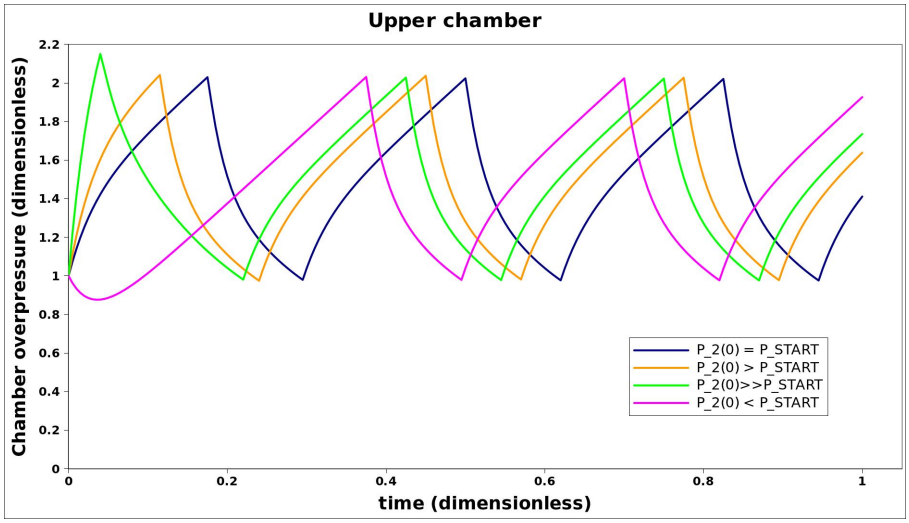

Figure 4.25: Over- and underpressured lower chamber (ΔP_2) adjustment to steady state cycles: corresponding upper chamber pressures (ΔP_1).

4.5.5 Application to Mount St Helens

We have provided an interpretation of how Lonquimay volcano erupts, with a second chamber beginning to erupt after a first chamber is depleted. More complex data exists for the Soufriere Hills Volcano and Mount St Helens. The Soufriere Hills Volcano is complicated because its cycles of eruption and pauses and surface deformation are not periodic and the eruption involves different magma types. In Chapter 3 we calculated a magma recharge rate for this volcano, but the non-periodic cycles of surface deformation make it difficult to provide a unique interpretation in terms of a two-chamber model.

Mount St Helens is interesting because it showed an overall waning rate of eruption, but the eruption is comprised of sixteen discrete episodes with increasing periods between events, as shown in Figure 4.26 (reprinted from Chapter 2). In Chapter 3 we showed that Phase I can be modelled by an exponential decay rate. Now we propose that the discrete eruptive events can be accounted for by the cycles shown in our two-chamber model, with a slow recharge from deep to shallow chamber which rebuilds the critical pressure necessary for an eruption to resume.

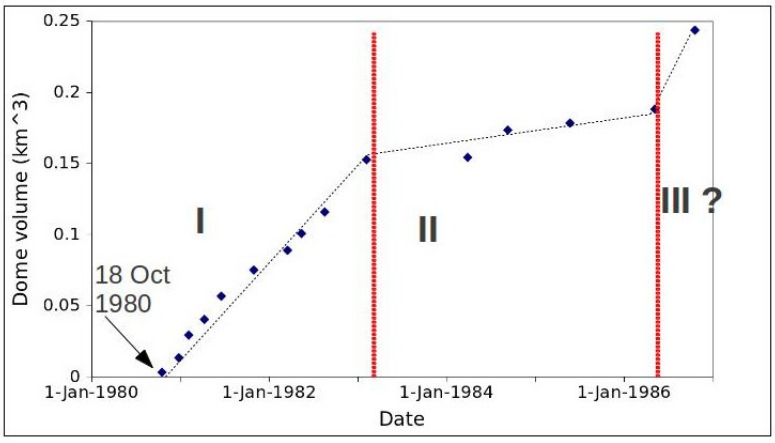

Figure 4.26: Mount St Helens lava dome growth, as measured by topographic maps (length, width, depth) at the end of each extrusive episode since 18 Oct 1980 Swanson and Holcomb [1989]. Each data point represents a discrete eruptive episode. Re-printed from Chapter 2.

We choose chamber volumes, conduit resistances, and critical starting and stopping pressures to model these cycles and demonstrate an increase in period between eruptions. For a larger lower chamber and a greater resistance between the chambers than from upper chamber to surface, we calculate chamber pressures and erupted volume when the recharge to the deep chamber is 0. Figure 4.27 shows the deep chamber (dashed) and shallow chamber (solid) pressures over time as predicted by the model. The deep chamber pressure decays exponentially, while the shallow chamber pressure carries on in cycles with increasing time between eruptions.

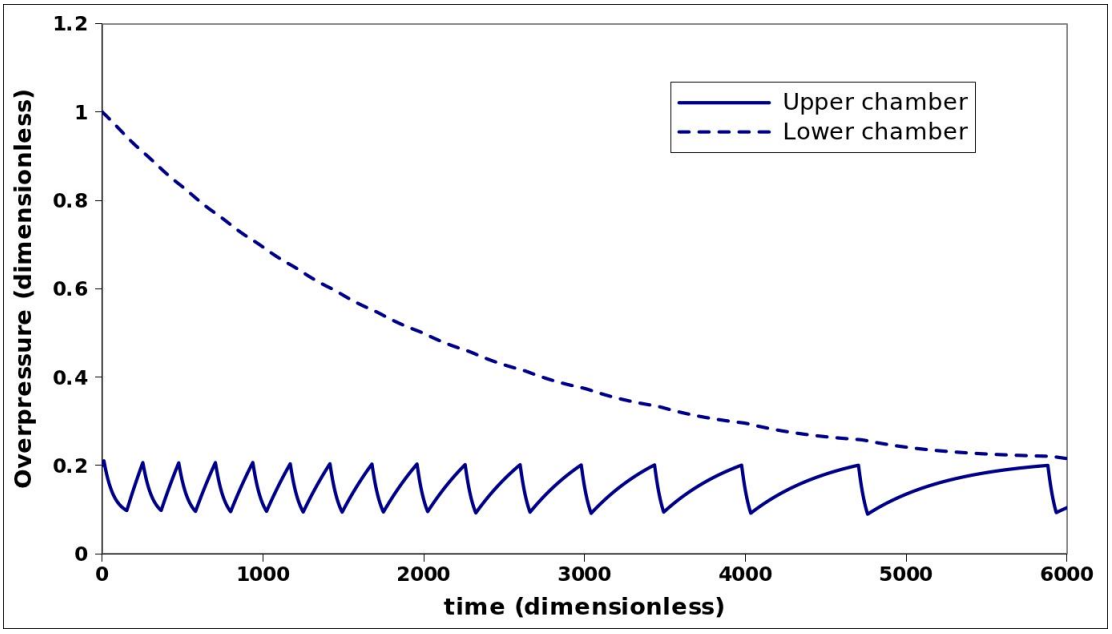

Figure 4.27: Two-chamber model with parameters chosen to give increasing periods between eruptions: deep chamber pressure (dashed) decays exponentially, while shallow chamber pressure (solid) carries on in cycles.

The model prediction of the period between eruptions is shown in Figure 4.28, and the time between eruptive events increases. Mount St Helens data is shown in pink on the plot. The data fits the model for upper conduit resistance 10^5 Pas/m^3 and lower conduit resistance 10^8 Pas/m^3 (based on timescales); bulk magma compressibility 10^{-9} Pa^{-1}; upper chamber volume 3 km^3 and lower chamber 50 km^3. We scale times t to the lower chamber: dimensionless time $\tau{=}\beta_2 V_2/F_2$ for upper chamber volume V_2, compressibility β_2, and conduit resistance factor $1/F_2$.

Finally, Figure 4.29 shows the erupted volume predicted by the model (blue), and Mount St Helens data (pink). Times are scaled to the lower chamber. The initial lower chamber overpressure $\Delta P(0)$ is 10 MPa, while the upper chamber stops and starts at overpressures 2 and 1 MPa. This is not a perfect fit, but assuming 20% error in lava dome measurement, is consistent with the model for an eruption that produces 0.25 to 0.3 km^3 of magma. It indicates the principle that the deep chamber pressure is much stronger than the resistance in the upper conduit. Once this resistance is overcome, there is low resistance to eruption and the eruption will progress in cycles.

This model shows that a gradually waning deep chamber that feeds a shallow chamber which erupts in cycles can rationalise lava dome building episodes observed at Mount St Helens.

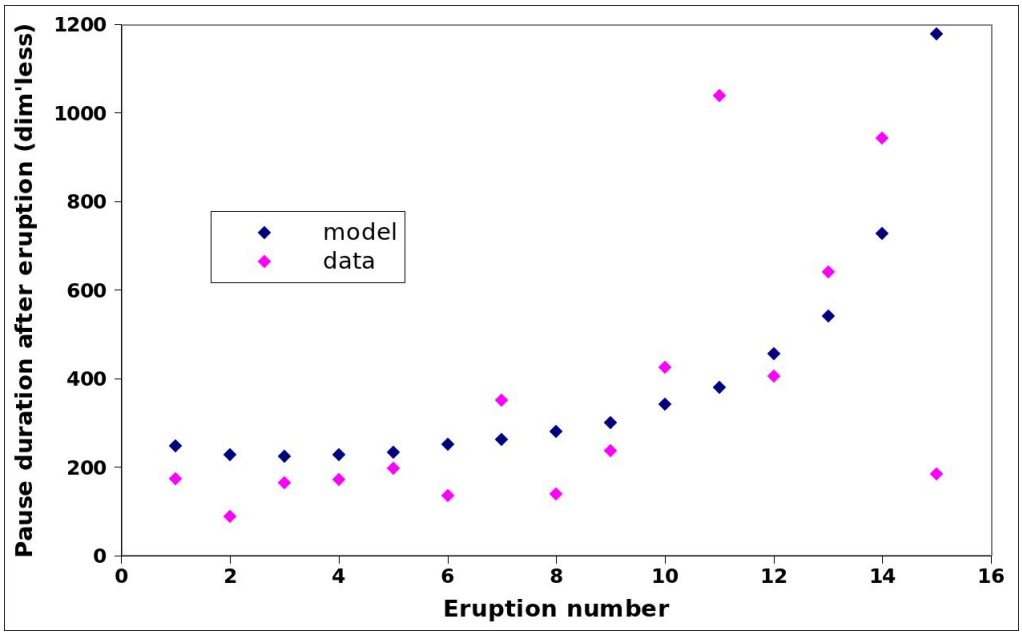

Figure 4.28: Two-chamber model with deep chamber pressure decaying exponentially and shallow chamber pressure cycling: period between eruptions increases for model (blue) and Mount St Helens lava dome growth data (pink). Data from Swanson and Holcomb [1989]. Scaled to lower chamber timescale.

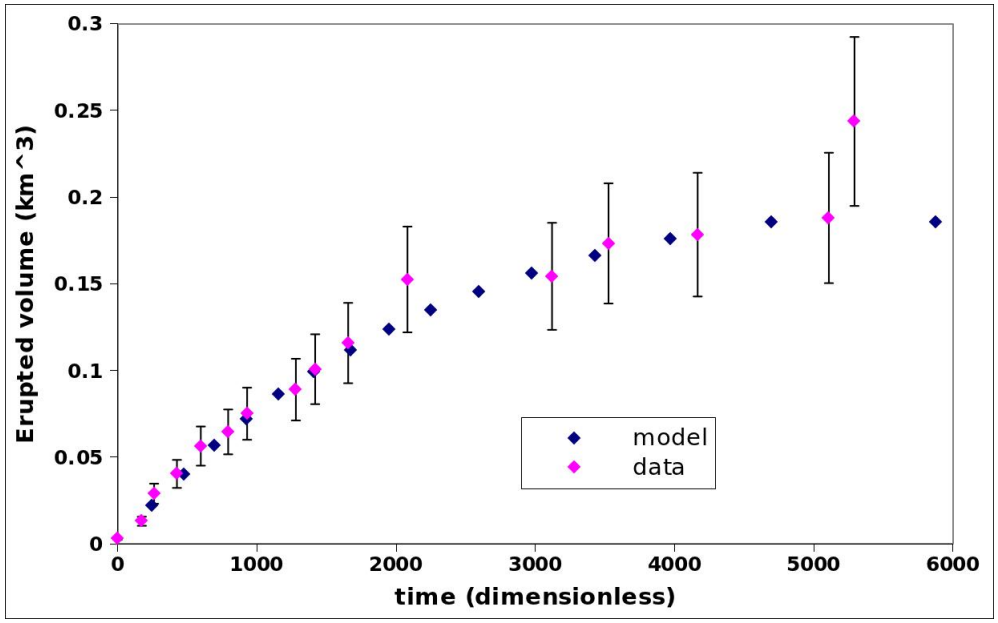

Figure 4.29: Erupted volume at Mount St Helens volcano. Time 0 indicates 18 May 1980. Suggests exponential decay of deep chamber.

4.6 Discussion and conclusions

In this chapter, we presented a model of a dual chamber magma system and derived an analytical solution for chamber overpressures during an erupting system's transition to steady state. We provided a simulation for the cycles of eruptions that occur during steady state.

We identify two timescales for the pressure changes during transition to steady state, with recharge rate $Q_{in} = 0$ corresponding to a situation in which both chamber overpressures decay to 0. If the lower chamber is much larger than the upper chamber, the upper chamber overpressure drops rapidly and then settles into gradual decay alongside the lower chamber. If the resistance between chambers is small during transition to steady state, the two chambers act as one large chamber and both decay gradually. If the resistance between chambers makes it difficult for magma to transfer from lower to upper chamber, the upper chamber pressure drops rapidly and the lower chamber pressure lags behind. The Lonquimay volcano eruption in 1988 provides an example which can be interpreted by a two chamber system with large resistance between chambers.

Supplying the lower chamber with a constant magma recharge $Q_{in} > 0$ allows the steady state pressure to cycle between two critical values, resulting in cycles of eruption and pause. Increasing the lower chamber volume leads to longer duration cycles, while changing conduit resistance ratio F adds complex effects on the cycle duration. Including the density of magma in the conduit as contributing to the chamber overpressure means that the upper chamber has smaller fluctuations relative to the absolute overpressure in the deep chamber.

It is possible for cycles to occur during the transient adjustment period before steady state cycles are reached. Whether these occur, and their timescale, is controlled by whether the lower chamber is over or underpressured.

We have shown how a large deep chamber decaying exponentially can control the overall rate of an eruption such as Mount St Helens, while the eruption rate at the surface is rapid compared to the deep chamber evolution. Lonquimay and Mount St Helens both show examples of an eruption in which a deep chamber input to a shallow chamber occurs more slowly than the shallow chamber eruption to the surface. This is due to a higher resistance between deep and shallow

chambers.

In the next chapter, we use the Soufriere Hills Volcano surface deformation rate to illustrate that a single chamber may be too simple to describe this volcano because the surface deformation shape changes in time. We will illustrate how surface deformation data is interpreted by a two-chamber system.

Chapter 5

Surface deformation model and application to Soufriere Hills Volcano

5.1 Abstract

In this chapter, we combine our magma chamber model with a Mogi model to understand the effects of magma chamber dynamics on the Earth's surface Mogi [1958]. We calculate profiles of ground deformation in the vicinity of the volcano during an eruptive event as described by the decaying pressure solution in Chapter 4, thus investigating the surface deformation change in both space and time that correlates to a magma effusion.

First we present a single chamber Mogi model Mogi [1958], and show that the profile of the deformation over a horizontal cross section changes only in amplitude. We then present a double chamber Mogi model, and show that the effect of a second equally pressurised chamber is to change the surface deformation rate. For two chambers that depressurise at different rates, as shown by our model in Chapter 4, the shape of the surface deformation over a horizontal cross section changes in time. Finally, we show that if two chambers are offset horizontally, the surface deformation profile is asymmetric on either side of the volcano vent.

We analyse surface deformation data from the Soufriere Hills volcano and

observe a spatial change in surface deformation over time, as indicated by our model of a dual chamber system with different pressurisations. The fact that these deformations do not change the same amount from one station to the next suggest asymmetry in a profile of the surface deformation and thus a horizontal offset between magma chambers.

We conclude that inverting a surface deformation data set to gain detailed information about the magma chamber system can become very complex.

5.2 Introduction

Since the early 1990s, Global Positioning System (GPS) geodesy has become common in volcano monitoring because of its high precision, relatively low cost, and ease of use. As discussed in Chapter 4, inversions of surface deformation data from the Soufriere Hills volcano has led to models of multiple magma chambers whose inflation and deflation translates to deformation of the ground.

Elsworth Elsworth et al. [2008] proposes a model for the Soufriere Hills volcano of two stacked magma reservoirs at depths of 6 and 12 km, connected from surface to deep crust and mantle by vertical conduits. The model co-inverts surface efflux and GPS data to recover rates of crustal magma transfer throughout the eruption.

Mattioli Mattioli et al. [2010] did a series of best-fit solutions of Soufriere Hills surface deformation data for different shapes of a single chamber, and showed that any number of plausible geometries fit the data equally well. They conclude that the Soufriere Hills magma plumbing system cannot be uniquely defined based solely on surface deformation data. Voight suggested a 'magma sponge hypothesis' in which magma transferred into or out of a crustal reservoir could be accommodated by compression or decompression of stored reservoir magma, and erupted magma is approximately balanced by deep influx Voight et al. [2010].

These models acknowledge that it is not possible to assess the geometry of the Soufriere Hills Volcano plumbing system nor the inferred volume changes in great detail Foroozan et al. [2010]. Numerical simulations suggest that the shallow chamber may control periodic behaviour for a system with 5 and 19 km depth chambers Foroozan et al. [2011], with efflux resuming when the shallow chamber reinflates to its initial threshold pre-eruptive volume and ceases when it loses some amount of its volume. The Foroozan numerical model searches a full parameter space of potential chamber depths.

Many inversions of surface deformation data for volcanic systems assume a homogeneous crust. But homogeneous elastic crustal models underestimate both the depth and excess pressure of the deformation source. Use of an elastic crust in reservoir models is justified based on observation of constant rates of surface deformation and comparisons of erupted volume to ground deformation adjusted for surface load Voight et al. [2010]. However, crustal layering should be taken

into acccount when inverting ground deformation data Crescentini and Amoruso [2007]. Considering a heterogeneous crust by varying the elastic modulus with depth leads to model predictions of a deeper pressure source than inferred by a homogenous elastic model Foroozan et al. [2010]. Further, in a dual reservoir model within a nonhomogeneous crust, the deeper chamber undergoes volume changes an order of magnitude larger than the shallow chamber Foroozan et al. [2010]. And while a homogeneous elastic model has led to the conclusion that a precise geometry of the subsurface cannot be inferred Mattioli et al. [2010], accounting for crustal heterogeneity can provide some further insight. Models incorporating a heterogeneous crust show that horizontal deformation is amplified for a spherical source geometry; maximum horizontal deformation at the free surface is closer to the source; radial extent to which vertical surface deformation occurs is smaller; and differences from a homogeneous model are more pronounced for certain chamber geometries Hautmann et al. [2010].

It may be even more than two magma reservoirs driving an eruption. Tryggvason suggested several magma reservoirs feeding magma toward a shallow reservoir situated beneath the center of Iceland's Krafla volcano caldera Tryggvason [1986]. This is based on seismic discontinuities in several regions, and speculation on the timing at which each reservoir contributed to the flow. At Eyjafjallajokull in 2010, changes in magma chemistry suggest a complex chamber system and systematic downward propagation of seismicity through the crust occurred in a series of steps Tarasewicz et al. [2012]. They suggest that the magma release came from elastic sills 1 to 10 km^3 in size.

We now explore how patterns of surface deformation might evolve with a dual chamber magma system. A system with two chambers that pressurise at different rates shows surface effects different from two chambers that pressurise at the same rate. The unique feature of our model is that it shows how the surface deformation profile around a volcano will evolve in time for different combinations of magma chambers.

5.3 Single chamber Mogi model

To calculate surface deformation based on the volume change of a subsurface chamber, we use the Mogi model presented by Elsworth Elsworth et al. [2008]. As shown in Figure 5.1, R is the hypotenuse of the triangle made by the GPS station at distance r from the center of the volcano, and the chamber at depth z with volume V. If the volume undergoes change, via pressurisation from a magma recharge or depressurisation from an eruption, the change is translated to the surface as radial deformation rates $\dot{r_1}$ and $\dot{r_2}$ and vertical deformation rate $\dot{z_1}$ and $\dot{z_2}$ at stations 1 and 2.

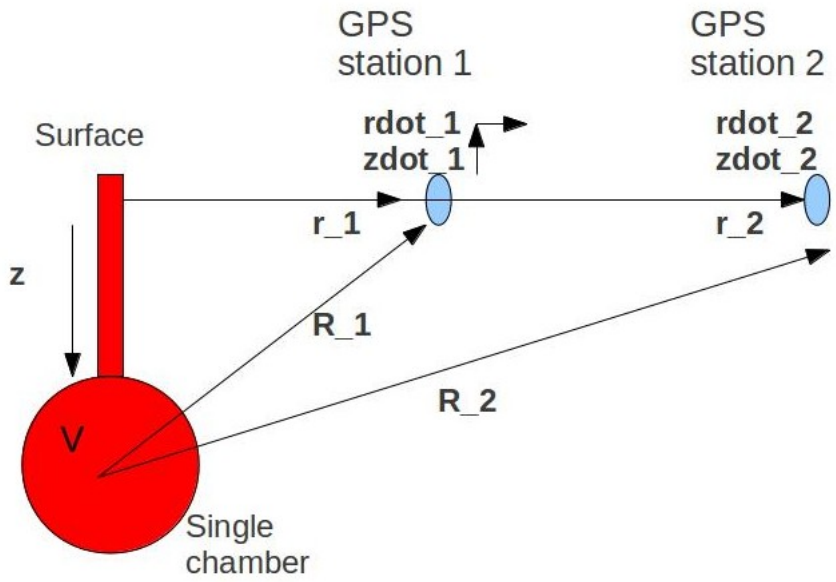

Figure 5.1: Diagram of Mogi model application to single chamber magma system. Chamber is depth z beneath the surface, volume V, and GPS stations are located at positions r_1 and r_2. An inflation or deflation in chamber volume due to magma recharge or eruption translates to the surface as radial deformation rates $\dot{r_1}$ and $\dot{r_2}$ and vertical deformation rate $\dot{z_1}$ and $\dot{z_2}$ at stations 1 and 2.

The resulting radial surface deformation rate at stations r_1 and r_2 for a chamber volume change dV are

$$\dot{r}_1 = a_1 dV \tag{5.1}$$

$$\dot{r}_2 = a_2 dV \tag{5.2}$$

with coefficients

$$a_1 = \frac{3}{4\pi} \frac{r_1}{(R_1)^3} \tag{5.3}$$

$$a_2 = \frac{3}{4\pi} \frac{r_2}{(R_2)^3} \tag{5.4}$$

The vertical surface deformation at stations r_1 and r_2 for a chamber volume change dV are

$$\dot{z}_1 = b_1 dV \tag{5.5}$$

$$\dot{z}_2 = b_2 dV \tag{5.6}$$

with strain nucleus coefficients

$$b_1 = \frac{-3}{4\pi} \frac{z}{(R_1)^3} \tag{5.7}$$

$$b_2 = \frac{-3}{4\pi} \frac{z}{(R_2)^3} \tag{5.8}$$

This represents the effect of an inflating chamber collapsed to a point within a homogeneous elastic half-space bounded by a horizontal surface, and for a Poisson ratio of 0.25 Elsworth et al. [2008].

The chamber volume change dV is related to pressure change dP by the chamber volume V and the bulk compressibility in the chamber β Blake [1981].

$$dV = V dP \beta \tag{5.9}$$

Using the Mogi model, we calculate the radial and vertical surface deformation rates $\dot{r}$ and $\dot{z}$ for a range of positions r in the vicinity of a volcano brought about by a single deflationg chamber at depth $z = 10\ km$ (Figure 5.2). Deformation rates are normalised: actual deformation decreases relative to a reference value during an eruption as chambers depressurise. We choose dP early in the eruption

to be twice the value of dP later in the eruption, and show profiles of the surface deformation 60km on either side of the volcano (the chamber is situated below the volcano vent at $r = 0$, and positions to the left of centre are negative). We provide curves for the deflation rate early in the eruption (blue) and the deflation rate later in the eruption (pink).

The radial displacement rate (top panel) is zero immediately over the chamber, and increases until $r = z$. Then it decreases until it is not detectable at larger r. The vertical displacement (bottom panel) is maximised at the volcano vent $r = 0$ and decreases further away from the volcano.

The key point of the single chamber Mogi model is that the surface deformation profile over a horizontal cross section changes only in magnitude: the ratio of deformation rate at any two times is the same at all r; that is, $\dot{r}(early)/\dot{r}(late)$ and $\dot{z}(early)/\dot{z}(late)$ always take the same value. Only the magnitude of the deformation rate changes in time.

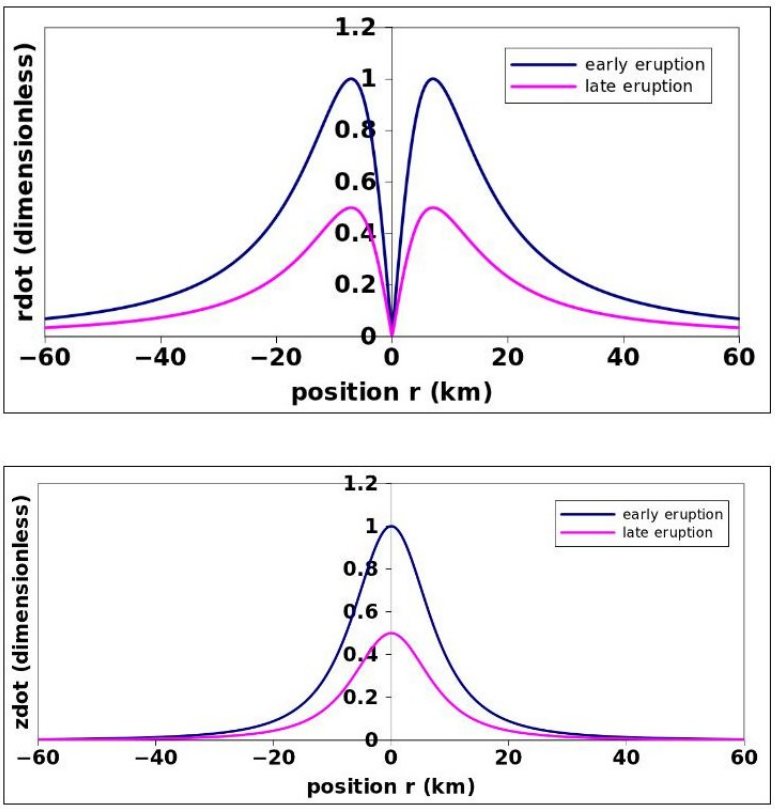

Figure 5.2: Single chamber eruption: profile of radial ($\dot{r}$, top) and vertical ($\dot{z}$, bottom) surface deformation rates for 60 km to the left and right of a volcano with central vent at $r = 0$ and single chamber at depth $z = 10$ km. Deformation rates are normalised: actual deformation decreases relative to reference value during an eruption. The profile early in an eruption (blue), with a high pressure change rate, has a higher magnitude surface deformation rate than at the end of an eruption (pink). Only the magnitude of deformation changes in time.

5.4 Double chamber Mogi model

To calculate surface deformation based on the volume change of a subsurface chamber, we use the Mogi model extended to two point sources. The effect of multiple reservoirs may be accommodated by superposition of inflation velocities, and Elsworth assumes the two chambers are pressurised the same amount Elsworth et al. [2008]. This requires an understanding of the volume changes in upper and lower chambers dV_1 and dV_2. Our model predicts these volume changes, as they are directly proportional to pressure changes dP_1 and dP_2. To calculate surface deformation rate from two chambers, the signal from two chambers are added.

As shown in Figure 5.3, R_1^i and R_2^i are the hypotenuses of the triangles made by GPS stations at distances r_1 and r_2 from the center of the volcano to the upper chamber of volume V_1 at depth z_1, as shown in Figure 5.3. Similar coefficients exist for the lower chamber of volume V_2 at depth z_2 chambers, designated as R_1^{ii} and R_2^{ii}. If the upper chamber undergoes a volume change dV_1, via pressurisation from a magma recharge or depressurisation from an eruption, the change is translated to the surface as radial deformation rates $\dot{r_1^i}$ and $\dot{r_2^i}$ and horizontal deformation rate $\dot{z_1^i}$ and $\dot{z_2^i}$ at stations 1 and 2. Similar deformation rates exist in response to volume change dV_2 in the lower chamber.

Other potential effects in the dual chamber system include changes in the lower chamber and conduit which may influence the upper chamber: as the signal from a subsurface chamber is transmitted through the crust to the surface, so could the signal from a lower chamber be transmitted through the crust to the upper chamber. However, the further the two chambers are separated, the less the effect will be. Models treat chamber pressurisation as independent of source volumes, thus neglecting interactions within the crust besides the pressure changes within the chambers themselves Hautmann et al. [2012]. The effect of topographic relief, or variations in pressure due to surface mass, increases for sources at shallower depths Hautmann et al. [2010], so the influence of the lower chamber on the upper may be less noticeable due to buffering by the mass of crust separating the two chambers. Shear stress along the shallow conduit wall could also generate surface deformation Green et al. [2006] but it would not be enough to influence

strain records, and the connection between the two chambers would not generate any surface deformation Hautmann et al. [2012]. Further, a cylindrical conduit as assumed in the model would not be able to explain deformation variations recorded in the tangential direction Hautmann et al. [2009].

Additionally, we assume the free surface to be flat at $z = 0$ Hautmann et al. [2010]. This is justified by the fact that effect of topography on the deformation pattern decreases with increasing depth of the pressure source Cayol and Cornet [1998]; Hautmann et al. [2012]. However, the volcanic edifice has an effect on chamber pressures and thus surface deformation, as the pressure imposed on each point extending radially from centre varies with edifice shapes from shield volcanoes with gentle slopes to stratovolcanoes with deeper flanks. For example, an edifice situated directly above the centre of a magma chamber means that the maximum stress is reach ed at the top of the chamber Pinel and Jaupart [2003]. Further justification is provided by surface deformation patterns that remained robust during a dome collapse at the Soufriere Hills Volcano Widiwijayanti et al. [2005].

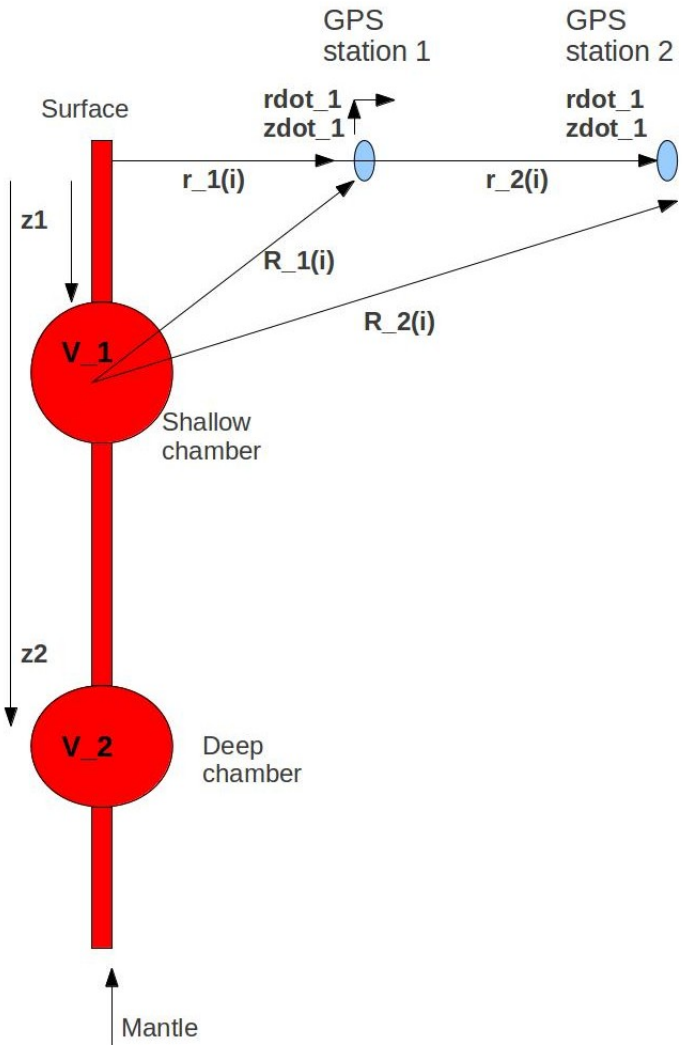

Figure 5.3: Diagram of Mogi model application to 2-chamber magma system. Upper chamber is volume V_1 at depth z_1, lower chamber is volume V_2 at depth z_2. GPS stations are distances r_1 and r_2 from the center of the volcano. An inflation or deflation in upper chamber volume dV_1 due to pressurisation or magma release translates to the surface as radial deformation rate $\dot{r_1^i}$ and $\dot{r_2^i}$ and horizontal deformation rate $\dot{z_1^i}$ and $\dot{z_2^i}$ at stations 1 and 2. Similar deformation rates exist in response to lower chamber volume change dV_2.

The radial deformation rates $\dot{r_n}$ at points r_n from the volcano, using the dimensions indicated in the diagram and chamber volume changes dV, are found by superposing the effects from the two chambers:

$$\dot{r}_n = a_n^i dV_1 + a_n^{ii} dV_2 \tag{5.10}$$

with strain nucleus coefficients for upper and lower chambers respectively

$$a_n^i = \frac{3}{4\pi} \frac{r_n}{(R_n^i)^3} \tag{5.11}$$

$$a_n^{ii} = \frac{3}{4\pi} \frac{r_n}{(R_n^{ii})^3} \tag{5.12}$$

The vertical deformation rates $\dot{z_n}$ at points r_n are similarly:

$$\dot{z}_n = b_n^i dV_1 + b_n^{ii} dV_2 \tag{5.13}$$

with strain nucleus coefficients for upper and lower chambers respectively

$$b_n^i = \frac{-3}{4\pi} \frac{z_n}{(R_n^i)^3} \tag{5.14}$$

$$b_n^{ii} = \frac{-3}{4\pi} \frac{z_n}{(R_n^{ii})^3} \tag{5.15}$$

These represent the effect of an inflating chamber collapsed to a point within a homogeneous elastic half-space bounded by a horizontal surface, and for a Poisson ratio of 0.25 Elsworth et al. [2008].

5.4.1 Surface profile: adding a second chamber

Next we explore the pressure decay model from Chapter 4 for two chambers at different depths. Adding a second chamber changes the surface deformation rate, as the GPS units detect effects from the lower chamber as well.

Initially, we suppose that both chambers depressurise at equal rates during an eruption so $dP_1 = dP_2$ and $dV_1 = dV_2$. In Figure 5.4, we plot the radial (top panel) and vertical (bottom panel) surface deformation rate profiles from 40km to the left and right of a volcano with central vent at $r = 0$. Deformation rates are normalised: actual deformation decreases relative to a reference value during an eruption as chambers depressurise. The upper chamber is $z_1 = 5\ km$ depth, and the lower chamber is $z_2 = 10\ km$ depth. For the lower chamber alone (pink), surface deformation rate is minimal. The upper chamber alone (blue) shows a significant surface effect: maximum ratio of deformation rate of upper chamber alone to lower chamber alone is 4:1. The two chambers superposed (orange) show the maximum surface deformation ratio: both chambers combined to lower chamber alone is 5:1.

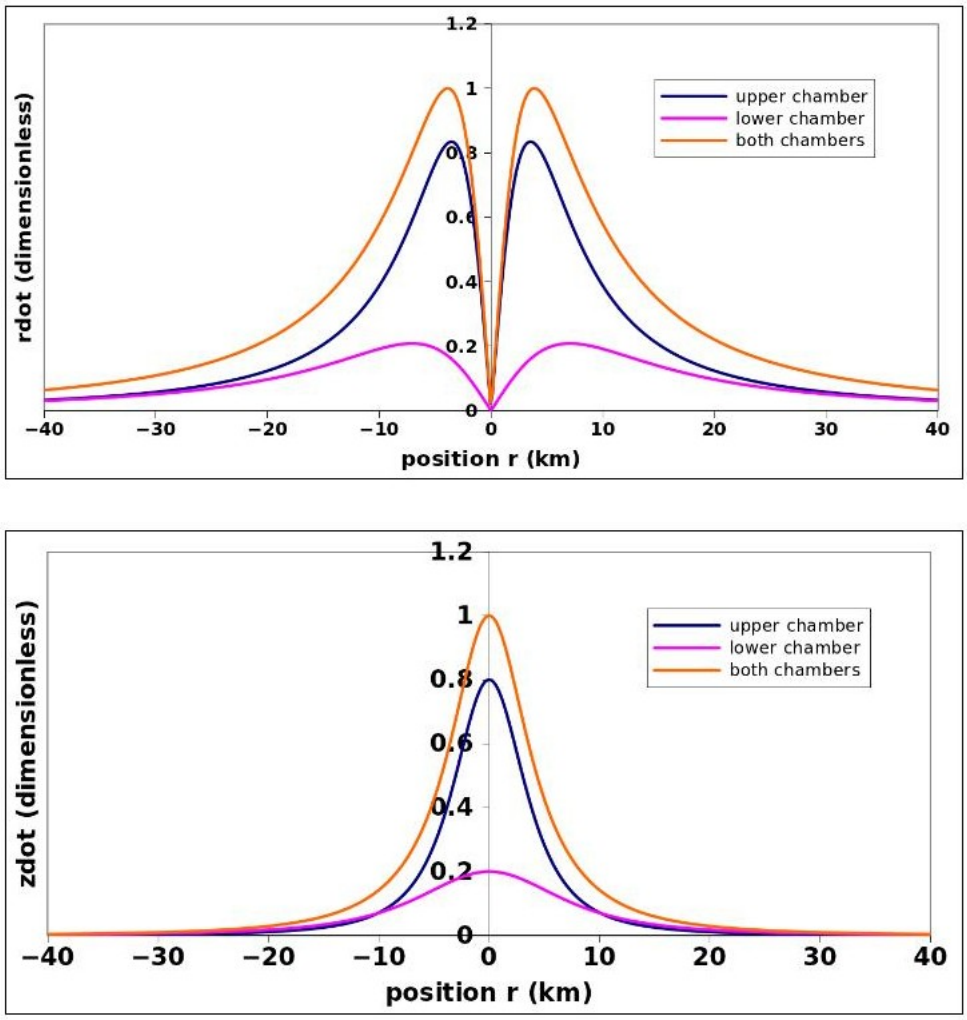

Figure 5.4: Upper chamber at depth $z_1 = 5\ km$, lower chamber at depth $z_2 = 10\ km$: profile of radial ($\dot{r}$, top) and vertical ($\dot{z}$, bottom) surface deformation rates for 40 km to the left and right of a volcano with central vent at $r = 0$. Deformation rates are normalised: actual deformation decreases relative to reference value during an eruption. Lower chamber alone (pink) shows minimal surface effect; upper chamber alone (blue) shows larger surface effect; two chambers superposed (orange) show maximum surface effect. Maximum ratio of upper chamber alone to lower chamber alone is 4:1; of both chambers combined to lower chamber alone is 5:1.

Figures 5.5 and 5.6 show surface deformation rates for deeper second chambers ($z_2 = 15\ km$ and $z_2 = 20\ km$ respectively). Again, deformation rates are normalised: actual deformation decreases relative to a reference value during an eruption as chambers depressurise. Increasing the chamber's depth reduces its independent expression at the surface (pink), and the deformation due to the lower chamber alone eventually becomes barely noticeable. The deformation profile from a single upper chamber (blue) and superposed upper and lower (orange) become more similar for a deep lower chamber: as the lower chamber becomes deeper, the upper chamber will be the only one whose effect is detectable at the surface.

Adding a lower chamber to the magma system changes the surface deformation rate. How deep the chamber is determines how much it impacts the deformation. In this section we have investigated the effect of two chambers that are pressurised equally at a given time, but a situation in which the two chambers are pressurised at different rates will affect how much the effect of each is seen at the surface.

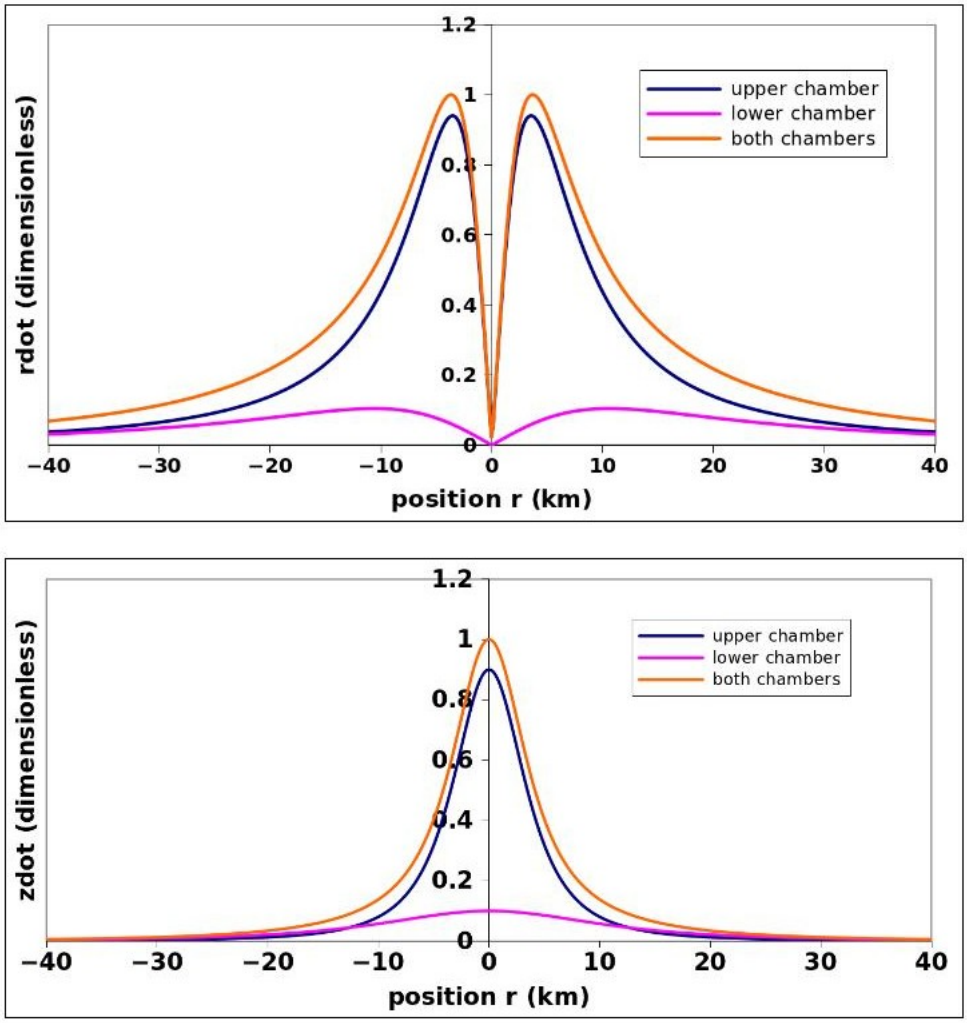

Figure 5.5: Upper chamber at depth $z_1 = 5\ km$, lower chamber at depth $z_2 = 15\ km$: profile of radial ($\dot{r}$, top) and vertical ($\dot{z}$, bottom) surface deformation rates. Deformation rates are normalised: actual deformation decreases relative to reference value during an eruption. Deeper lower chamber alone (pink) becomes less noticeable at the surface, and has less contribution to combined effect with upper chamber (orange and blue are more similar than in Figure 5.4). Maximum ratio of upper chamber alone to lower chamber alone is 9:1; of both chambers combined to lower chamber alone is 10:1.

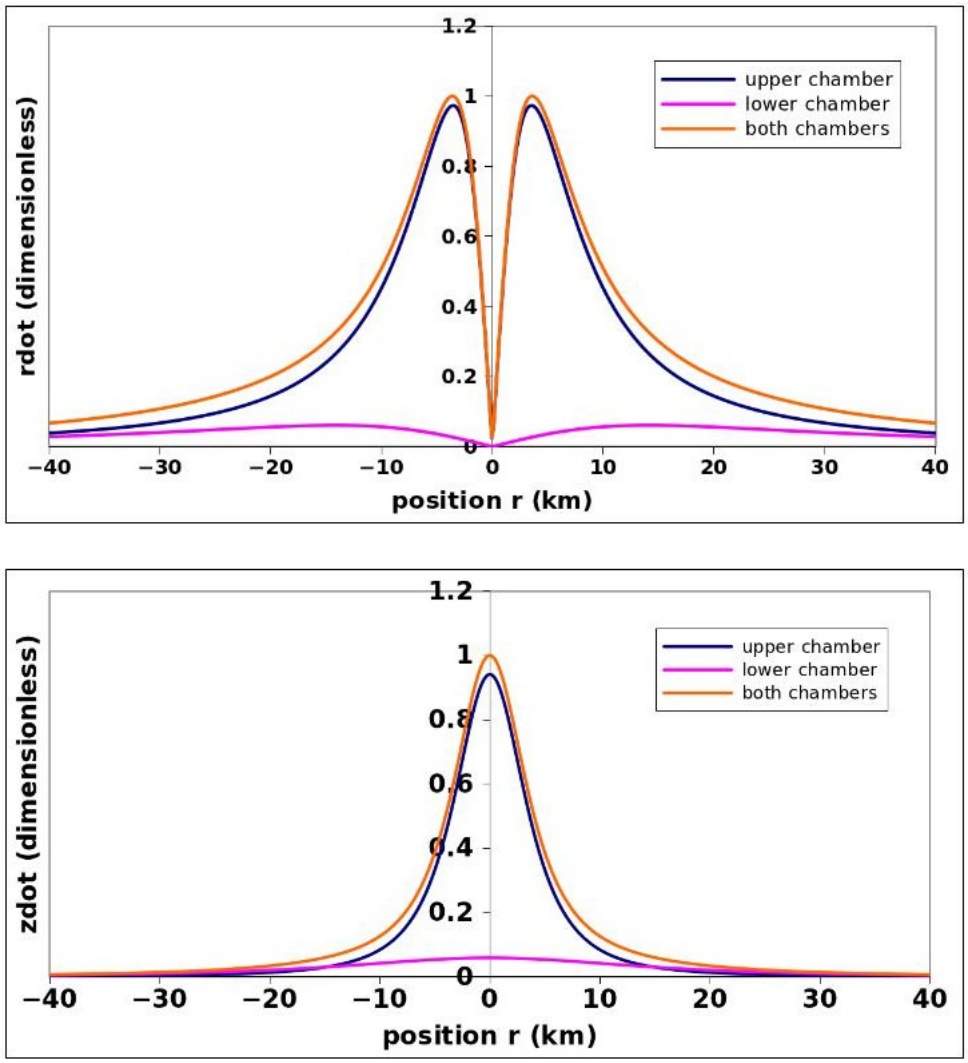

Figure 5.6: Upper chamber at depth $z_1 = 5\ km$, lower chamber at depth $z_2 = 20\ km$: profile of radial ($\dot{r}$, top) and vertical ($\dot{z}$, bottom) surface deformation rates. Deformation rates are normalised: actual deformation decreases relative to reference value during an eruption. Very deep lower chamber alone (pink) is barely noticeable at the surface, and entire surface effect is due to upper chamber (blue and orange are less distinguishable than for shallower deep chamber). Maximum ratio of upper chamber alone to lower chamber alone is 19:1; of both chambers to lower chamber alone is 20:1.

5.4.2 Surface profile: shape change over time

In the previous section, we showed that a deep chamber enhances surface deformation when it is not too deep to be seen by the GPS unit. The deep chamber changed the magnitude of surface deformation at a given time when the rate of depressurisation in the two chambers dP_1 and dP_2 were equal. In our dual magma chamber model from Chapter 4, there is evidence that dP_1 and dP_2 are different at different times. If dP_1 is not equal to dP_2, this changes how much the effect of the each chamber is translated to the surface deformation.

Recall from Chapter 4 the solution for chamber pressures P_1 and P_2, equations 4.35 and 4.36. For a single eruption, we are interested in the surface deformation rate at times t_1 through t_7 in Figure 5.7. The rates of pressure change dP_1 and dP_2 are different at each of these times.

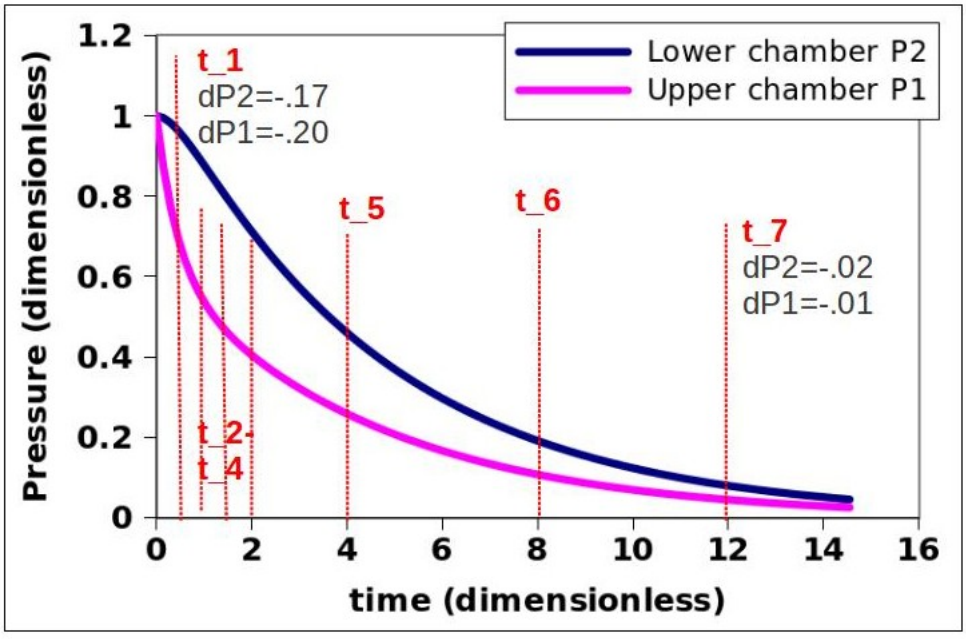

Figure 5.7: For a waning eruption, we provide a profile of surface deformation (negative values indicate deflation during eruption) at times t_1 through t_7 as shown in the plot of upper and lower chamber pressures. The rates of pressure changes dP_1 and dP_2 take different values at each of these times.

In Figure 5.8, we plot the radial (top panel) and vertical (bottom panel) surface deformation from 40 km to the left (negative value) and right of a volcano with central vent at $r = 0$. We calculate the actual deformation, rather than deformation rate, simply by integrating deformation rates $\dot{r}$ and $\dot{z}$ over the time interval:

$$r(t) = \int \dot{r} dt \tag{5.16}$$

$$z(t) = \int \dot{z} dt \tag{5.17}$$

Deformation values are normalised to the value at time t_1: actual deformation decreases relative to reference value during an eruption. The upper chamber is at $z_1 = 5$ km depth, and the lower chamber is at $z_2 = 10$ km depth.

In Figure 5.9, we re-plot the surface profile scaling each time to have maximum deformation value 1. This highlights the different shape of deformation profile over time, which is much more pronounced for radial deformation (top) than vertical deformation (bottom). Note that the radial distance r from the volcano is critical for observing how different the deformation is from one time to the next.

The key point is that for chambers that pressurise at unequal rates, the shape of the surface deformation changes over time.

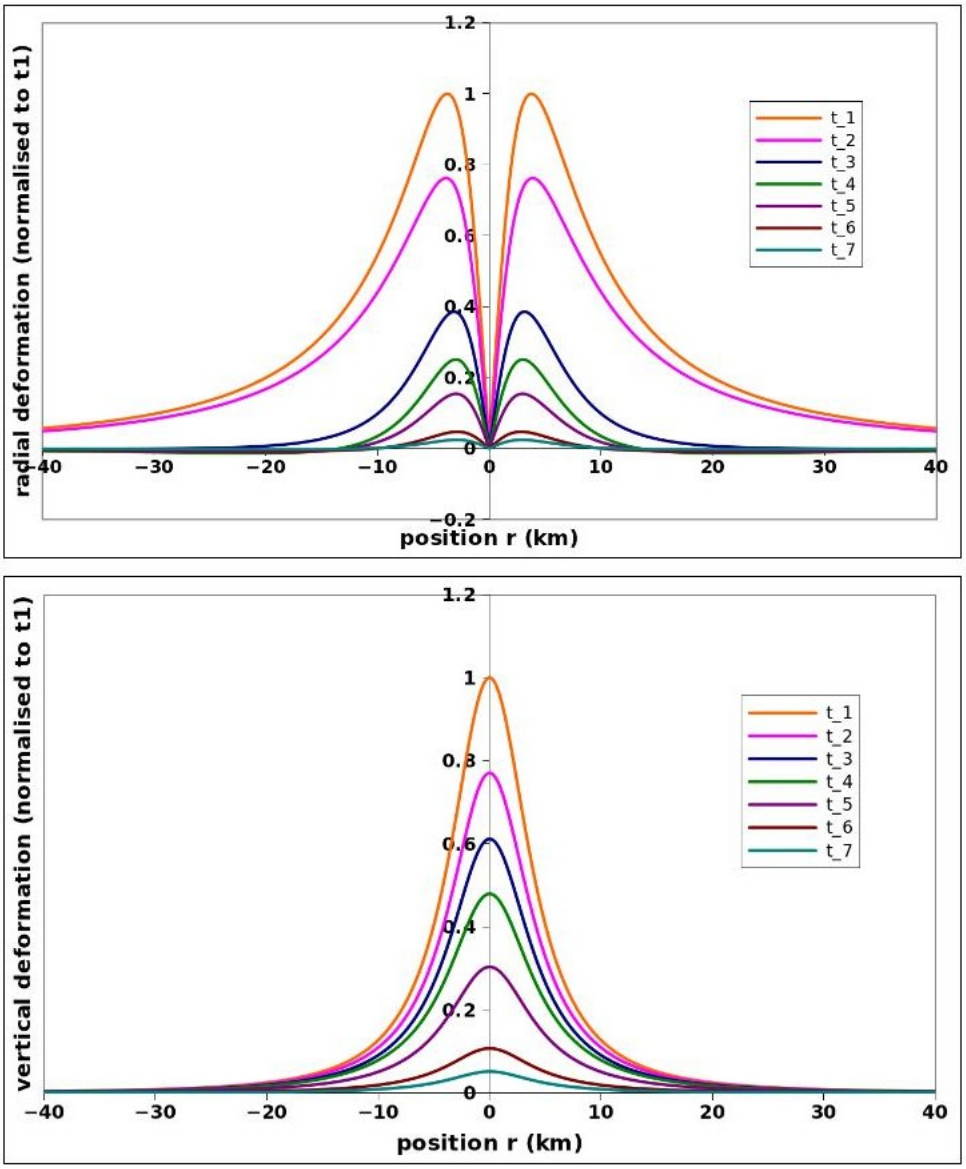

Figure 5.8: Profile of radial (top) and vertical (bottom) surface deformation for 40 km to the left and right of a volcano with central vent at $r = 0$. Two pressurised chambers whose pressures decay at different rates during an eruption for times t_1 (orange) through t_7 (turquoise). Deformation values are normalised to value at t_1: actual deformation decreases relative to reference value during eruption. The profile of surface deformation changes shape over time.

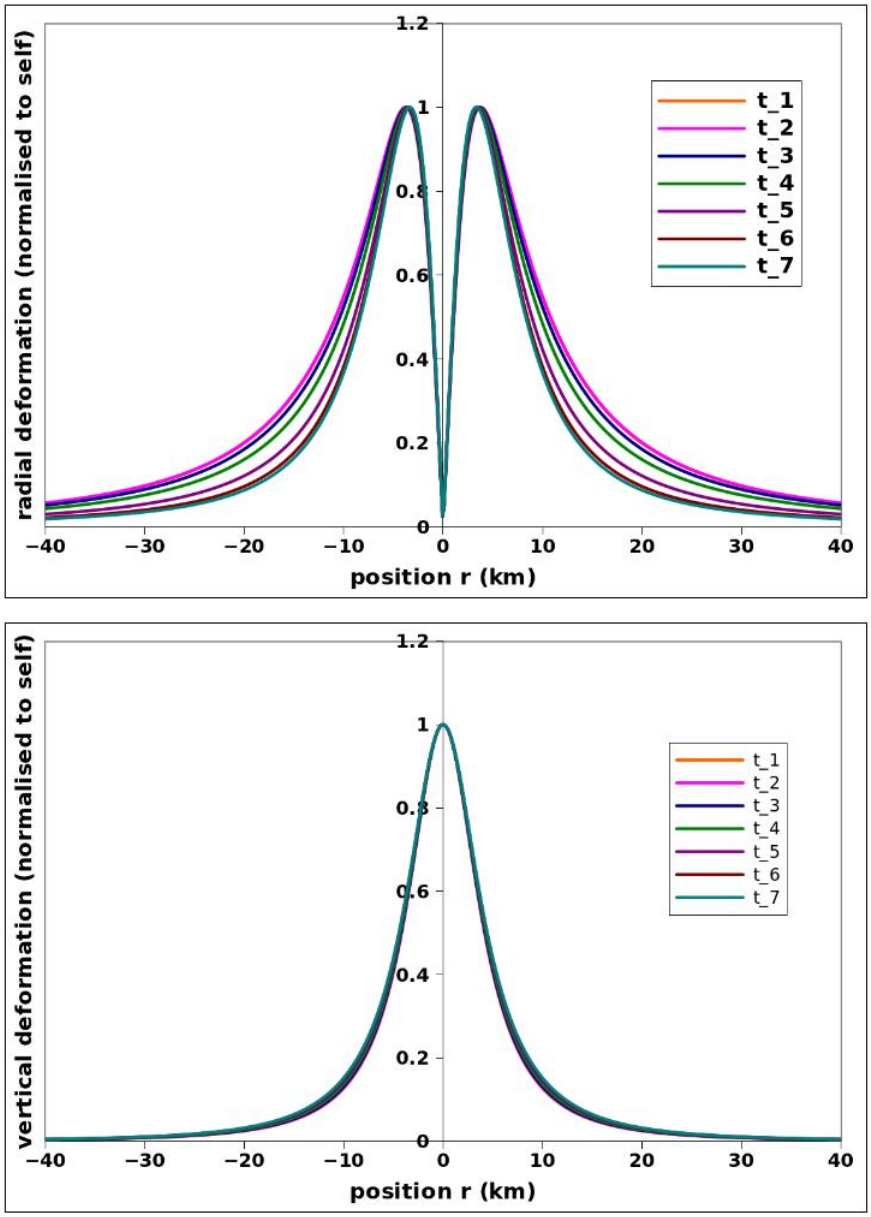

Figure 5.9: Profile of radial (top) and vertical (bottom) surface deformation for 40 km to the left and right of a volcano with central vent at $r = 0$, normalised to maximum value at each time. This highlights the change in deformation profile over time.

5.4.3 Horizontally offset chambers

Finally, we investigate the surface deformation rates if the two magma chambers are offset horizontally. If the two chambers are situated beneath each other to the left and right of the central vent, as shown in Figure 5.10, it is reasonable to expect the surface deformation at different positions r to behave differently. Points A and B will respond more to the shallow chamber, while the deep chamber will have more effect on points C and D. This adds an extra layer of complexity to inverting surface deformation data to get information about the subsurface.

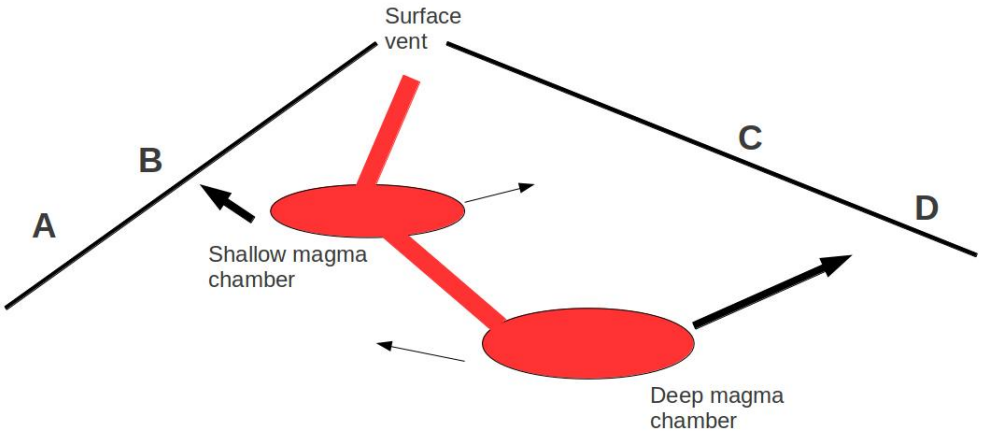

Figure 5.10: Horizontally offset magma chambers. Points A and B will respond more to the shallow chamber, while the deep chamber will have more effect on points C and D.

In Figure 5.11, we show surface deformation for horizontally offset chambers, adjusting the Mogi model calculations to account for the shift. We plot the radial (top panel) and vertical (bottom panel) surface deformation from 40 km to the left (negative value) and right of a volcano with central vent at $r = 0$ for times t_1 through t_7 as marked in Figure 5.7. We calculate the actual deformation, rather than deformation rate, simply by integrating deformation rates. Deformation values are normalised to the value at t_1: actual deformation decreases relative to reference value during eruption. The profile of surface deformation changes shape over time. The two chambers are situated at 5 km and 10 km depth, and we show surface deformation rate from 30 km to the left (negative) to 30 km to the right (positive) of the central volcanic vent. The upper chamber is shifted 1 km to the left of center, and the lower chamber is shifted 1km to the right of center. The key point is that horizontally offset chambers lead to an asymmetric surface deformation profile.

In Figure 5.12, we re-plot the surface profile scaling each time to have maximum deformation value 1. This highlights the different shape of deformation profile over time, which is much more pronounced for radial deformation (top) than vertical deformation (bottom). Note that the radial distance r from the volcano is critical for observing how different the deformation is from one time to the next.

In the next section, we will look at how the surface profile of the Soufriere Hills Volcano changes in time.

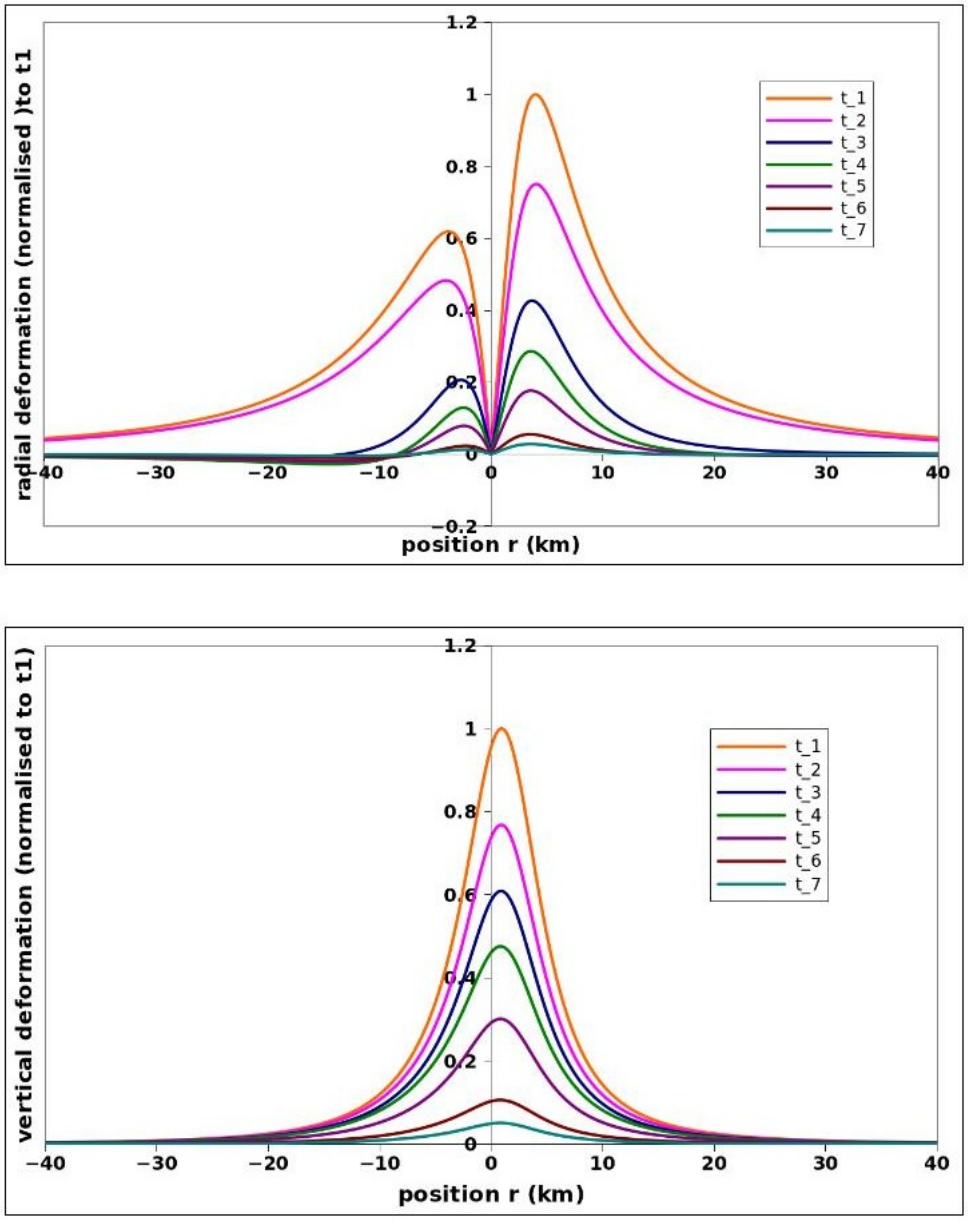

Figure 5.11: Horizontally offset magma chambers surface deformation radial (top panel) and vertical (lower panel). Chambers at 5 km and 10 km depth, upper chamber shifted 1km to the left of center, lower chamber shifted 1 km to the right. Two pressurised chambers whose pressures decay at different rates during an eruption for times t_1 (orange) through t_7 (turquoise). Deformation values are normalised to value at t_1: actual deformation decreases relative to reference value during eruption. The profile of surface deformation is asymmetric.

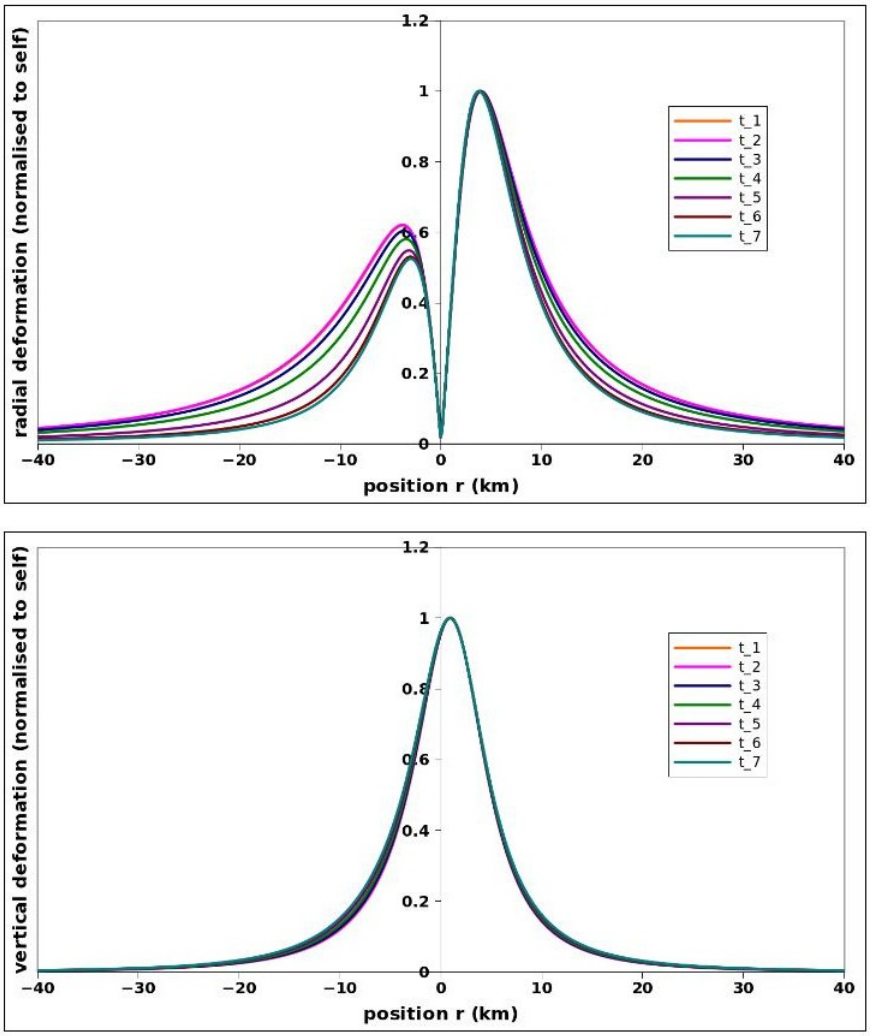

Figure 5.12: Profile of radial (top) and vertical (bottom) surface deformation for offset chambers, 40 km to the left and right of a volcano with central vent at $r = 0$, normalised to maximum value at each time. This highlights the change in deformation profile over time.

5.5 Application to Soufriere Hills Volcano

5.5.1 Data

Our model may help to explain some of the differences in surface deformation profiles brought about by a single magma chamber, two uniformly pressurised chambers, two nonuniformly pressurised chambers, and horizontally offset chambers. In this section, we refer back to surface deformation data from the GPS stations at the Soufriere Hills volcano that we presented in Figure 3.23 and explain it in the context of our model.

Mattioli 2010 Mattioli et al. [2010] reports on GPS data collected over the period 1995 to 2009 at the Soufrire Hills Volcano (SHV), Montserrat, West Indies. Foroozan provide surface deformation rates for ten sites around the volcano by inverting the Mattioli data for dual Mogi sources at 5 km and 19 km depth Foroozan et al. [2011]. The Foroozan data are interesting but we save these for a later study, as they do not include the detailed raw data provided by Mattioli. In this study, we are interested in the profile of surface deformation in the vicinity of a volcano. We look to the most complete raw vertical surface deformation data provided by Mattioli and discuss what can be learned from their relative temporal and spatial changes.

Figure 5.13 shows the locations of four GPS stations of interest to us based on the completeness of their data sets, each identified by a four-letter label and a red triangle, around the volcano.

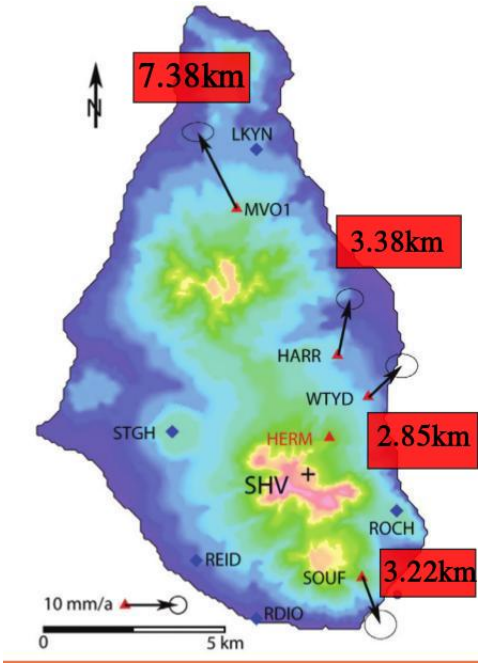

Figure 5.13: GPS stations around Soufriere Hills Volcano. Numbers in red boxes are horizontal distance from central vent. Central vent is marked '+' labelled 'SHV'. Black arrows and ellipses are observed site velocities and errors as given by Mattioli Mattioli et al. [2010]

Elsworth 2008 Elsworth et al. [2008] provides average surface deformation rates (vertical and horizontal) for two phases of eruption and two phases of recharge. In Figure 5.14, we sketch these values through the Mattioli vertical surface deformation data at four stations to come up with a different set of numbers than those provided by Elsworth. We will refer to our average values as the 'new model,' though we acknowledge that there are many possible values that could be used. To plot the Elsworth vertical data ($\dot{z}$) which is given as mm/year rate of surface deformation, we took the given $\dot{z}$ for an episode, multiplied it by the time period for that episode, and added this to the end value of the previous episode to plot the next point on the graph.

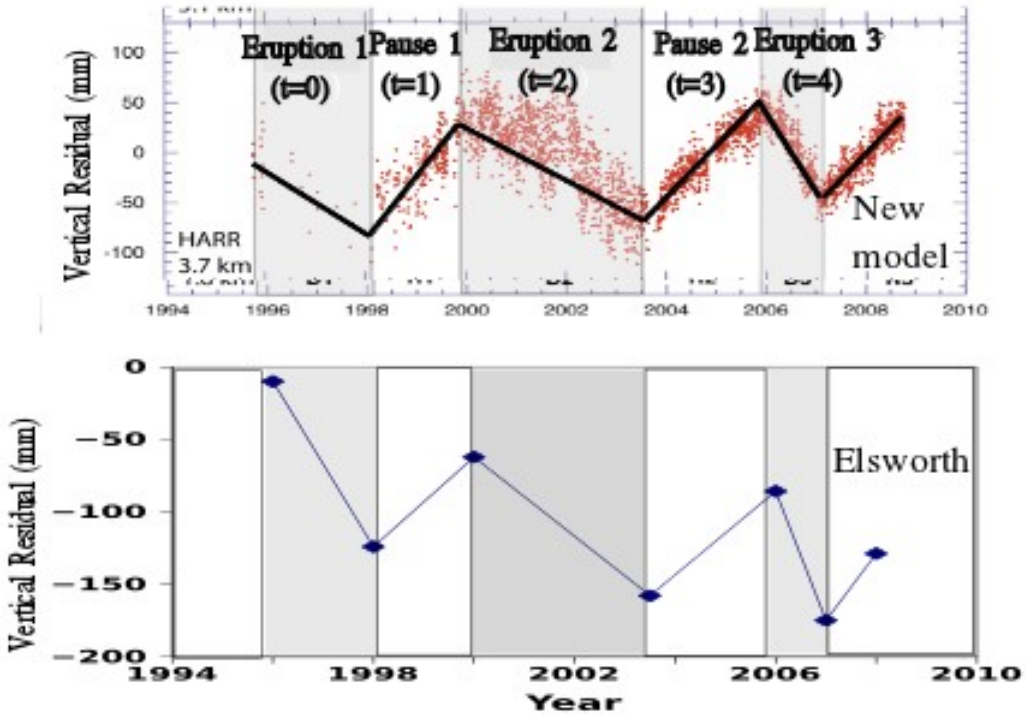

Figure 5.14: Mean tilt values from Elsworth at GPS station 'HARR' (bottom), interpreted as mm/yr Elsworth et al. [2008]. The values do not coincide with the 'new model' we draw on top of the raw data from Mattioli (top): note that the values at the end of each eruption (grey-shaded region) decrease in Elsworth but increase in New Model.

The values given by Elsworth for $\dot{z}$ might also be interpreted as change in surface deformation z over the time in that episode, not per year as is indicated. Taking that to be the case, we sketch the Elsworth values over the Mattioli data alongside our 'new model' values in Figure 5.15. These exercises justify the use of our 'new model' values.

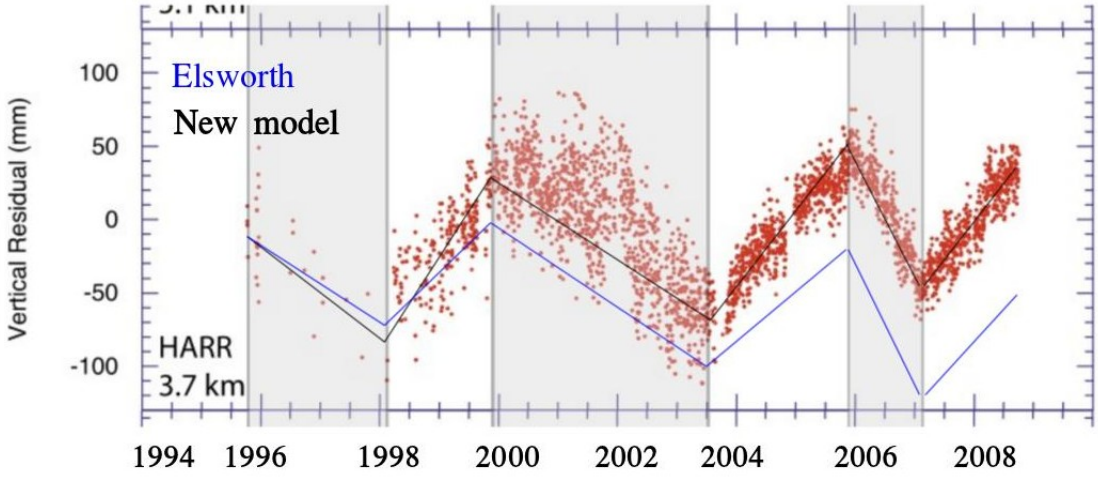

Figure 5.15: Another interpretation of Elsworth data at GPS station 'HARR' (blue), supposing that the given values are the total surface deformation change during the duration of the episode, rather than deformation rate. The values do not coincide with the 'new model' we draw on top of the raw data from Mattioli (red dots, black line average).

We re-print the Soufriere Hills Volcano surface deformation data from the four stations around Montserrat, along with mass efflux data, in Figure 5.16, and draw average values of surface deformation within each episode. We assume that the erupted volume suggests a correlation to the tilt end/erupt phases. The key observation is that deformation rates are different at different stations around the volcano.

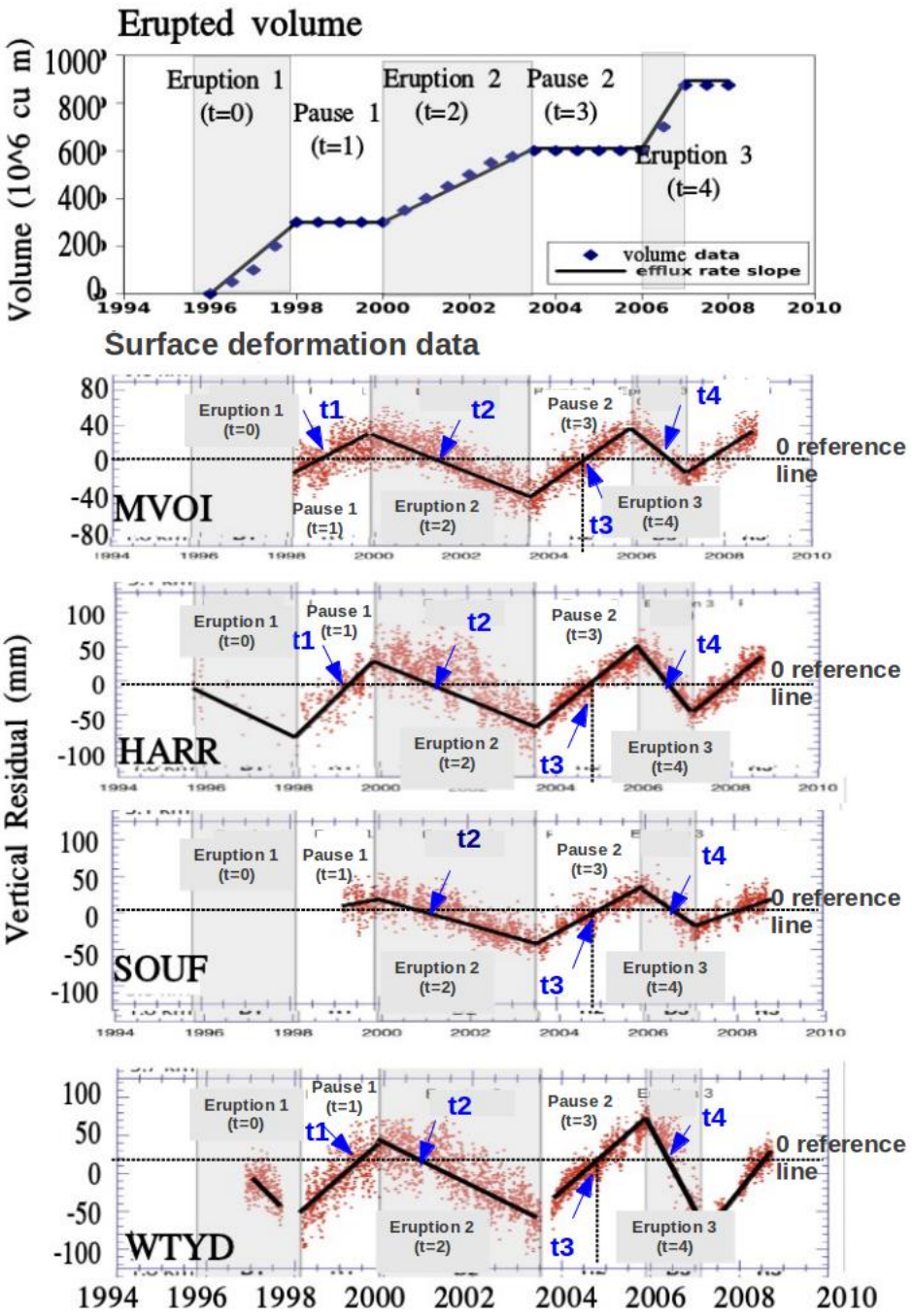

Figure 5.16: Erupted volume and vertical surface deformation at four GPS stations around Soufriere Hills Volcano Mattioli et al. [1998]. New model average surface deformation values have been sketched as solid black lines.

5.5.2 Surface deformation comparison

In our general Mogi model for a dual chamber system, we compared surface deformation rates over a range of locations. Data at the Soufriere Hills volcano exists for up to ten different locations, and we only have the complete raw data for four different locations, so it is not practical to compare the overall profile of surface deformation rate. Instead, we take the value of surface deformation at the end of each pause and each eruption. Comparison of these values provide a summary view of the surface deformation changes in time and space.

The top panel of Figure 5.17 shows the vertical surface deformation at the end of two pauses and two eruptions from the Soufriere Hills volcano. The data show different values at different times and places. At the end of the pauses (dark blue and yellow), the values are similar at SOUF and MVOI, but there is a big difference at WTYD and HARR. At the end of eruptions (pink and light blue), the values are similar at stations SOUF and MVOI but different at WTYD and HARR. These observations suggest a spatial change in surface deformation rates over time, as indicated by our model of a dual chamber system with differently pressurised chambers. Further, the surface deformation at WTYD at the end of eruption $t2$ is less than at the end of eruption $t1$. For all other stations, the deformation at the end of eruption $t2$ is larger than at the end of eruption $t1$.

In the bottom panel of Figure 5.17, we assign station SOUF a value 1 at all times and normalise the deformation at all other locations relative to this location. The scatter is smaller than implied by the raw data in the top panel. This shows the importance of reference location for drawing information from surface deformation data.

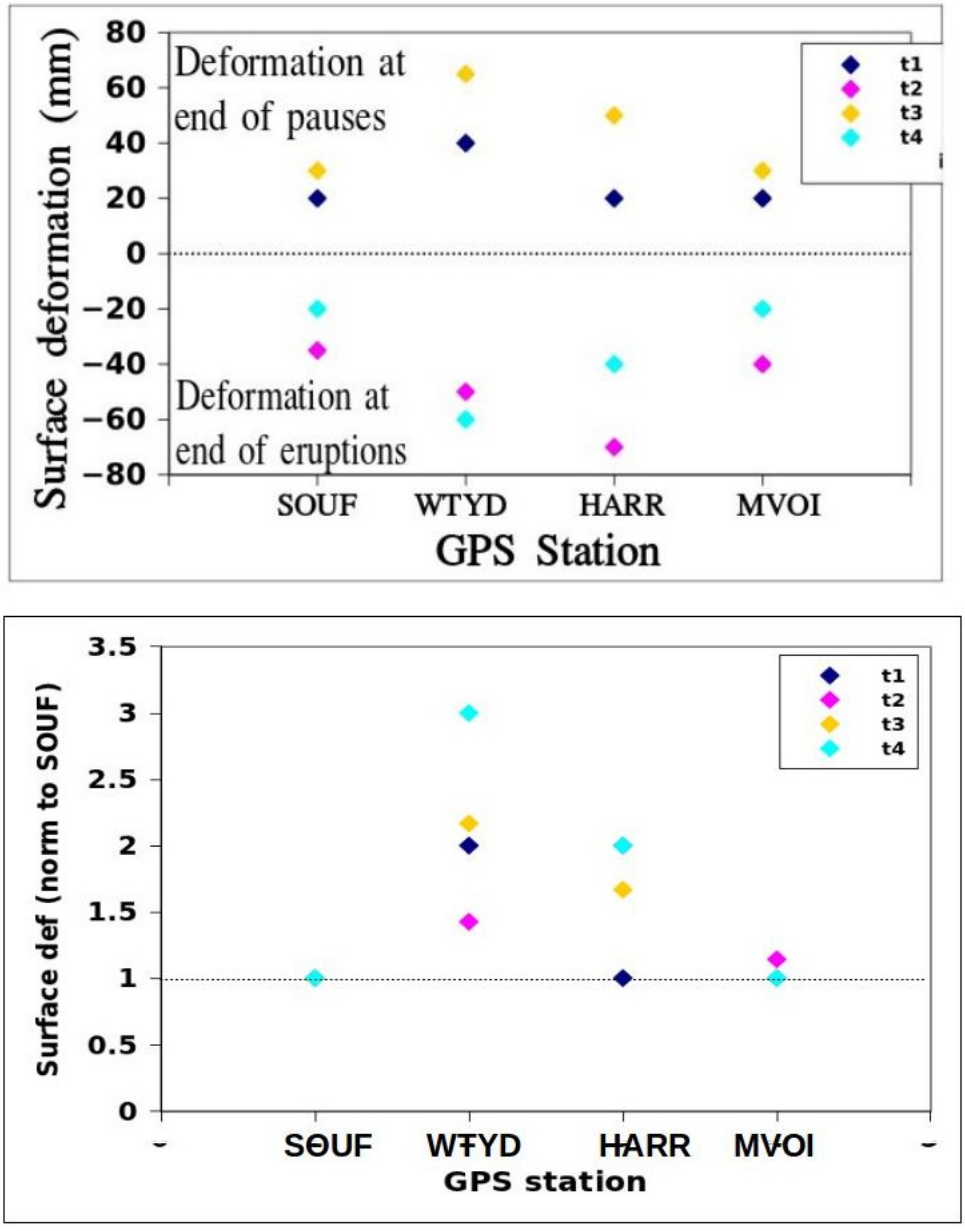

Figure 5.17: Top: Surface deformation at Soufriere Hills volcano at end of each pause (dark blue and yellow) and of each eruption (light blue and pink). Stations are arranged in order from south to north about the central volcano vent, going anticlockwise. The data show different magnitudes of surface deformation at different times and places, suggesting a spatial change in surface deformation over time. Bottom: Surface deformation at Soufriere Hills volcano at end of each pause and of each eruption normalised to value at location SOUF.

In Figure 5.18, we plot the ratio of vertical surface deformation at the end of eruptions 1 and 2 (purple, time $t2$ and time $t4$), and at the end of pauses 1 and 2 (blue, time $t1$ and time $t3$). The ratio of deformation at the end of each eruption (purple) is not the same from one station to the next: It nearly doubles from the end of the first to the end of the second eruption at three stations, but reduces to about 75% at station WTYD. The ratio of vertical deformation at the end of the first pause to the end of the second pause (blue) varies from 0.3 to 0.6.

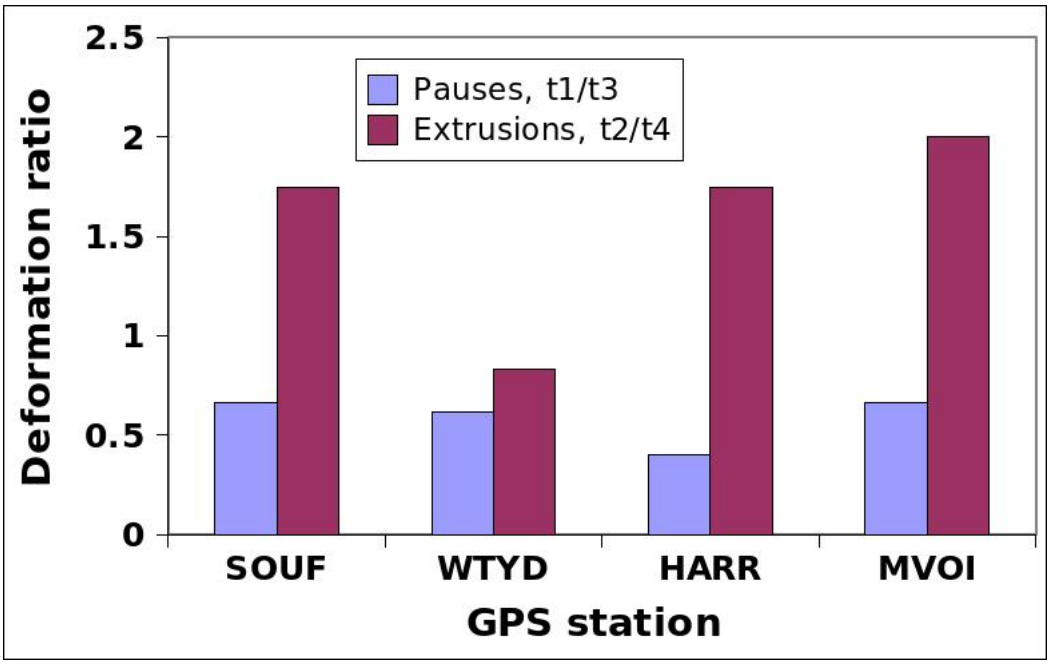

Figure 5.18: Ratio of surface deformation at end of each pause (blue) and each eruption (purple). Stations are arranged in order from south to north about the central volcano vent, going anticlockwise. These observations suggest a spatial change in surface deformation rates over time, as well as asymmetry from one location to the next.

Our interpretation that two reservoirs at different depths and pressures evolve at different rates helps to rationalise observations of changing surface deformation shape at the surface.

Our model includes several parameters, including relative chamber volume, relative chamber depth, and horizontal offset between chambers. The surface deformation data set from Soufriere Hills Volcano is sparse spatially, with GPS units monitoring a limited area. This makes the problem non-unique to invert. However, while it is very difficult to invert the data, we rationalise why there might be changes in surface deformation from one location to the next.

Different variables lead to similar magnitudes in surface deformation signal. The Soufriere Hills Volcano deformation data to which we have access are only collected within a 7 km radius of the volcano, yet the chambers are thought to be situated at a depth of 6-12 km. Our model shows that there is variation in the near-field data for small variations of the properties.

It is difficult to get helpful bounds on the surface deformation given that the data set is so sparse. The chamber depth, aspect ratio, and horizontal positions are all unknown. With further seismic studies it may be possible to constrain these parameters better.

5.6 Discussion and Conclusions

5.6.1 Summary of results

In this chapter, we presented a Mogi model for single and dual magma chamber systems and explored the effects of pressure change as predicted by our magma chamber model on surface deformation. We demonstrate the difficulty of modeling the complexity of surface deformation data.

We showed that the horizontal profile of surface deformation due to a single chamber has a spatially correlated shape for different locations in the vicinity of a volcano, and only the magnitude changes with time: thus a single chamber does not suffice to explain surface deformation that changes spatially in time. We then investigated how a dual chamber system affects surface deformation. We showed how the effect of a second lower chamber changes the surface deformation, while the depth of the chamber determines how much impact it has. If the two chambers pressurise at different rates, the shape of the tilt changes in time. Offsetting the two chambers horizontally leads to an asymmetrical surface deformation profile. The upper and lower chambers have different effects at different points on the surface.

We use our model to show that the Soufriere Hills Volcano surface deformation data is consistent with more than one chamber whose pressures evolve differently. Inverting this data set to gain detailed information about the subsurface magma system can become very complicated.

This chapter has shown some principles and challenges regarding surface deformation associated with volcanic eruptions.

Chapter 6

Experiments

6.1 Abstract

In this chapter we develop an analogue experimental model of the dual-chamber volcanic plumbing system. After discussing some laboratory analogues of magma chambers from the literature, we explain the experimental regimes that we will address. Then we describe the development of the experimental apparatus and how we measure the laboratory analogues of eruption rate and chamber pressure.

We present experimental results for steady state experiments, in which the laboratory system represents a volcano erupting at an equilibrium rate. We also present results for transient experiments in which opening the valve in a plastic tube corresponds to breaking a plug in a volcanic conduit, after which the eruption can continue to steady state. This represents an eruption that either increases or decreases to steady state, as shown by the model in Chapter 4.

Finally, we consider an overturn of magma types within the lower chamber of a volcanic system, and demonstrate the flow rate and pressure change with an experiment. We modify the dual chamber magma system model developed in Chapter 4 for application to the experimental system, and relate the experiment to the 1988 Lonquimay eruption which is fast at first and then decreases to steady state.

6.2 Introduction

We present a set of experiments to provide a laboratory analogue of the two-chamber volcanic system that we modeled in the previous chapter, in which a large lower chamber feeds into a shallow upper chamber which erupts material to the surface.

6.2.1 Magma chamber laboratory experiments in the literature

Magma chamber models in the literature handle non-linear valves and chamber overturn.

Whitehead and Helfrich modeled periodic flow from a chamber through a conduit with a non-linear valve. They did an experiment in which syrup flowed from a reservoir, which received a constant influx of syrup, through a pipe placed in a cooled bath to an exit hole Whitehead and Helfrich [1991]. Flow was steady or periodic depending on the temperature of the bath and the flow rate into the reservoir. Cold syrup resists flow more than warm syrup, so if the reservoir pressure is not sufficient, the syrup stops flowing as it cools. When the reservoir pressure increases sufficiently due to influx, the syrup flows again. This creates periodic cycles in the flow rate.

Eruptions like the Soufriere Hills Volcano include elements of two magmas, indicating that the underlying magma chamber has hosted at least two different magmas. In some cases, two distinct layers of magma are erupted in sequence, such as during the AD79 eruption of Mount Vesuvius: grey pumice erupted followed by a transition to white pumice, leading to a layered fall deposit.

Such layering may be established when a pulse of new mafic magma is injected beneath a more evolved silicic magma in the base of a chamber. The hot mafic magma cools, with crystals and bubbles growing in the melt. If their production rate exceeds their rate of separation from the mixture, the magma decreases in density. The density of this lower layer of basaltic magma may decrease sufficiently that it leads to an overturn of layers during the eruption Phillips and Woods [2002]; Woods and Cowan [2009]. This overturn is accompanied by a

change in pressure of the system resulting from the change in temperature of the two magma layers and the associated change in exsolved volatile mass Phillips and Woods [2002].

Cowan and Woods created a laboratory model in which two stratified layers of polymer-laden water, the lower of which is volatile-rich and contains 5 wt% salt, are decompressed using a vacuum pump such that gas comes out of solution and causes the lower layer to reduce in density. The timescale of decompression is sufficiently rapid that a large scale overturn of the layers ensues Woods and Cowan [2009]. Phillips and Woods create a laboratory model in which the density of the lower layer in a stratified tank decreases due to gas release via electrolysis. If the lower layer fluid has sufficient viscosity, created by addition of a polymer, a large-scale overturn occurs Phillips and Woods [2002].

Thomas' experiments investigate how gas bubbles from an underlying mafic magma layer in a chamber migrate into the more viscous upper silicic layer Thomas et al. [1993]. Gas bubbles injected to a viscosity stratified system are allowed to rise through the fluid. The experiments show two regimes, in which the bubbles either move individually across the interface and entrain a small amount of lower layer fluid; or they formed a foam layer at the interface which becomes unstable and causes a coarse mixture of the layers.

While laboratory models of magma chambers in the literature investigate overturn and mixing, gas release, and conduit effects, the development of further laboratory analogues to explore eruptions from pressurised chambers and the interaction amongst multiple chambers will greatly enhance this body of work.

6.2.2 Experimental concept

Figure 6.1 shows how we translate a two chamber volcanic system into a laboratory analogue. The lower chamber (2) is represented by an open-top gravity feed tank filled with glycerol, representative of 'magma' (red in the diagram). The gravity feed tank is constantly topped up with glycerol to maintain its pressure, indicating either a very large chamber volume (V_2) or a constant recharge to the chamber.

The 'lower chamber' is connected by a flexible plastic pipe (2a) to an upper chamber (1), which is represented by a sealed-top tank filled partly with air and partly with glycerol. The tank is situated beneath the gravity feed, so it represents an upper chamber fed from the lower chamber due to pressure direction although the actual position is reversed. The compressibility of the magma and elasticity of the chamber is represented by the contracting and expanding of the air layer.

The conduit connecting the upper chamber to the surface (1a) is also represented by a flexible plastic pipe extending from (1) to a collection bucket. This system represents the pressure gradient in a volcano, in which a deeper subsurface chamber has a higher pressure and the surface is effectively at atmospheric pressure. In the actual volcano, both conduits have some degree of elasticity. In our laboratory analogue, they are rigid.

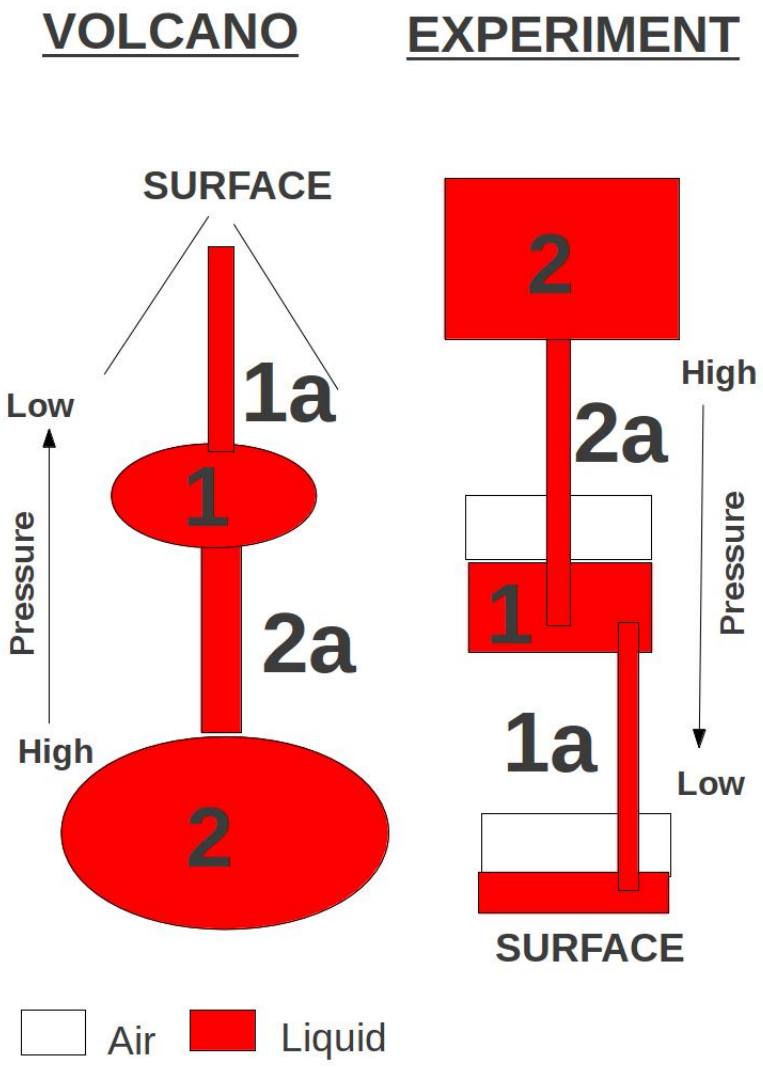

Figure 6.1: Diagram of laboratory analogue volcano experiment. Lower chamber (2) is represented as a gravity feed filled with glycerol ('magma,' red) which feeds into a sealed-top tank that represents an upper chamber (1) by a plastic pipe (2a). This represents the pressure gradient in a volcano, in which a deeper subsurface chamber has a higher pressure and the surface is effectively at atmospheric pressure. The upper chamber is compressible, which is represented by an air layer that expands and contracts according to the ideal gas law. Liquid is released from the upper chamber to a collection bucket, representing the surface, via another plastic pipe (1a).

6.2.3 Conditions of experiment

Key elements of our experiment include the upper chamber having a large impact in modulating the eruption rate, and acting as a buffer to pressure change in the lower chamber. That is, the upper chamber has a larger pressure change per unit time than does the lower chamber. This requires that the lower chamber volume V_2 is much larger than the upper chamber

$$V_2 \gg V_1 \tag{6.1}$$

so the lower chamber volume is much larger than the volume erupted at rate Q_{er},

$$V_2 \gg \int Q_{er} dt \tag{6.2}$$

While the lower chamber pressure change P_2 is constant, upper chamber pressure P_1 changes in time. This is further explained by noting that, for lower chamber volume V_2 with compressibility β_2 and upper chamber volume V_1 with compressibility β_1, the pressure changes in upper and lower chambers are related to volume change as, respectively,

$$dP_2 = \frac{1}{\beta_2 V_2} dV_2 \tag{6.3}$$

$$dP_1 = \frac{1}{\beta_1 V_1} dV_1 \tag{6.4}$$

We also note that compressibility β collectively describes compressible magma and chamber wall elasticity (of the country rock). In order to model the pressure response of a volcanic system we must account for liquid magma, crystals, exsolved bubbles, and compressibility of the wall rock Woods and Huppert [2003]. Our model incorporates all compressibility elements into one component. Additionally, experiments are not scaled to a real volcanic system, but rather incorporate dimensions that are convenient given the available materials in the laboratory.

6.3 Eruption regimes to model

In the experiments we investigate steady state flow, transient flows, and a flow triggered by a sudden pressure change due to magma overturn.

In the first situation we investigate steady state flows. The Soufriere Hills volcano underwent periods of steady state eruption, at which magma efflux rate was constant over periods of 2 - 3 years (t0, t2, and t4 in Figure 2.8). The steady state flow experiment investigates the relationship between deep and shallow chamber pressures at steady state.

A system in which lower chamber pressure P_2 is initially higher than upper chamber pressure P_1 adjusts to a steady outflux rate Q_{out}. The short timescale is controlled by the upper chamber, but the long timescale at equilibrium is controlled by the lower chamber. We show how the constantly recharged lower chamber controls the equilibrium flow rate.

In the second situation, we investigate transient flows as they transition to equilibrium. The Soufriere Hills volcano, Mount St Helens, the Unzen volcanic complex, and Mount Etna all undergo cycles of eruption and pause. The start and stop of an eruption could be caused by conditions in the conduit, which may either inhibit an eruption starting or make it easy for an eruption to start.

This can be conceptualised by, respectively, a strong or a weak plug in the upper conduit. If there is a strong plug, the upper chamber pressure will build up to a high pressure to remove the plug, then run down to equilibrium as the eruption progresses. The Mount Etna 1950-51 eruption in Figure 2.4 is one example of a single eruptive run-down event. If there is a weak plug, the upper chamber pressure will increase rapidly at first but then slow to equilibrium as recharge from the lower chamber is countered by gradual outflow. Our experiments demonstrate both of these cases.

We also investigate a chamber in which magma overturn leads to a sudden pressure drop and eruption of two layers of magma, as is indicated by Mount Vesuvius' two types of tephra.

In the next section, we explain the development of the experimental design. We then present the results, data, and a model to explore the relationship between lower and upper chambers and conduit resistance for these regimes.

6.4 Development of experimental design

In this section we explain the development of the experimental design. The basic principle is that glycerol flows through the dual chamber system from the gravity feed ('lower chamber') through a pipe to the sealed-top tank ('upper chamber'), and out of another pipe to a collection bucket that sits on a scale. This outflux rate, Q_{out}, represents the volcano eruption rate.

In the experiments, we measure outflux Q_{out} as well as the rate of pressure change in the elastic upper chamber. The chamber overpressurises if influx rate from the gravity feed is greater than the outflux rate to the collection box. The pressure change is of key interest: it depends on the initial conditions of the lower chamber gravity feed. The experiments involve varying the initial conditions and observing the result on outflux rate and upper chamber pressure.

Figure 6.2 shows the structure of the experimental system, and Table 6.4.1 details the dimensions and materials. The lower chamber, an open-lid Perspex tank, is placed height H above the scale on which the collection bucket sits. It imposes pressure P_2 above the collection bucket and is filled with glycerol. The glycerol level is maintained in this tank throughout the experiment, such that the pressure does not change. A flexible plastic tube connects the gravity feed to the upper chamber and has conduit resistance $1/F_2$ (see Section 6.6). A valve allows flow through the tube to be started and stopped.

A sealed Perspex chamber placed 1 m above the collection bucket represents the upper magma chamber and has height dimension h_{max} and pressure P_1. It is filled to level h with glycerol. The remaining volume in the tank is comprised of air volume V_{air} and is analogous to the pressurisation of a magma chamber: its compression and decompression with pressure change due to influx from the gravity feed and outflux to the collection bucket represents the expansion and contraction of an elastic chamber. A flexible plastic tube connects the 'upper chamber' to the collection bucket and has resistance $1/F_1$ (see Section 6.6). A valve allows the flow through the tube to be started and stopped.

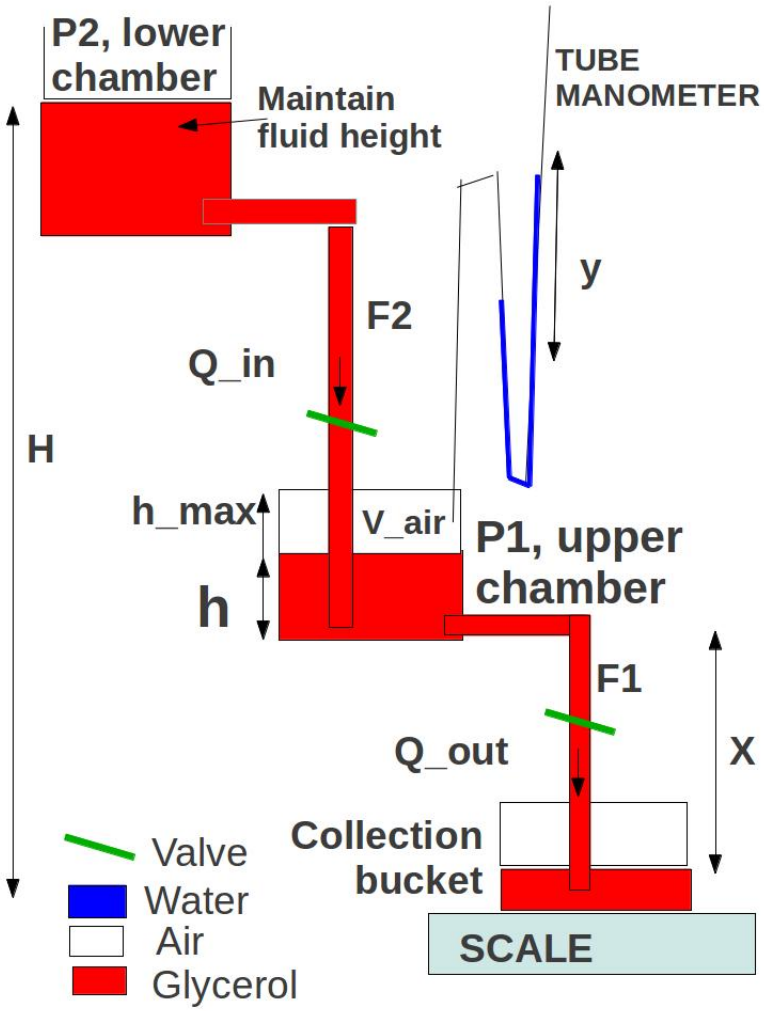

Figure 6.2: Diagram of laboratory analogue volcano experiment. The lower chamber (pressure P_2), an open-lid Perspex tank, is height H above collection bucket. Plastic tube connects gravity feed to the air-tight 'upper chamber', with conduit resistance $1/F_2$. Valves allow flow through pipes to be started and stopped. Air-tight Perspex chamber 1 m above collection bucket represents upper magma chamber (pressure P_1, height dimension h_{max}) filled to height h with glycerol. The remaining air layer in the box has volume V_{air}. Compression and decompression of air layer due to influx from gravity feed and outflux to collection bucket represents pressurisation of magma chamber. Tube manometer measures pressure in 'upper chamber', scale measures mass outflux Q_{out} to open-top collection bucket X below the sealed tank.

Table 6.4.1 gives the dimensions and detailed properties of each element of the design pictured in Figure 6.2. The glycerol 'magma' is vegetable glycerin purchased from Univar UK, and diluted to 70% in our experiments. Height differences between tanks are achieved by positioning tanks on assortment of tabletops and boxes available in the lab. In the table, we refer to 'lower chamber' designated by pressure $P2$ in Figure 6.2 as Tank 2, and 'upper chamber' designated by pressure $P1$ as Tank 1.

Sources of error specific to the experimental design include potential air leakage in the sealed 'upper chamber', or Tank 1, and at joinings between plastic tubing and tanks. The entire system is tested for air tight quality by filling each chamber and pipe which will see pressure changes during the experiment to the specified starting fluid level, sealing the valves, and allowing the system to sit, sealed, overnight. The fluid levels in each chamber and in the manometer are measured before and after a 24 hour period to confirm that no leakage occurs. As a precautionary measure, all pipe attachments and the lid to the 'upper chamber' are coated in silicon grease.

Sources of measurement error in the experiments include fluid level in the collection bucket (measured to within $+/-3x10^{-3}m$, and used to adjust pressure calculations involving X); fluid level in the 'deep chamber' (held constant to within $+/-2x10^{-2}m$); fluid level in the manometer (measured to within $+/-2x10^{-3}m$); and mass outflux measured in the collection bucket (+/-5 grams).

6.4.1 Step by step procedures

In this section, we provide a step-by-step procedure of the general process by which an experiment is set up and run. The 'Procedure' list is for filling the tanks with fluids and running the experiment once the setup is achieved as described in Figure 6.2 and Table 6.4.1. Specifics in the context of steady state and transient cases (changing the value of H) are elaborated on in Section 6.5.

DIMENSION	VALUE (metres)	DETAIL
Glycerol level in Tank 2 'lower chamber'	0.15 to 0.17	Tank 2 is plastic beaker 0.15m diameter
H (Figure 6.2)	1.05 to 1.07	Tank 2 placed on boxes reaching 0.58m above bench top
Pipe diameter ($F2$)	$9x10^{-3}$	Tygon flexible plastic tubing
Pipe length ($F2$)	1.45	Tygon flexible plastic tubing attached to plastic joiner drilled to $\leq$1cm above bottom of Tank 2. Pipe connects to lid of Tank 1 and extends below lid in separate unit to $\leq 0.5cm$ above base of Tank 1.
h (Figure 6.2)	0.12	Glycerol, unpressurised system
h_{max} (Figure 6.2, Tank 1 'upper chamber' vertical dimension)	0.25	2cm thick Perspex tank
Tank 1 horizontal dimension	0.2	2cm thick Perspex tank
Pipe diameter ($F1$)	$7x10^{-3}$	Tygon flexible plastic tubing
Pipe length ($F1$)	0.5	Tygon flexible plastic tubing attached to plastic joiner drilled to 0.04m above bottom of Tank 1
Bottom of Tank 1 above outlet in collection bucket, X (Figure 6.2)	0.37	Adjust value of X for changing fluid heights during experiment
Collection bucket diameter	0.15m	Plastic beaker
Bottom of manometer loop from ground	0.23	Tygon flexible tubing attached to plastic stand
Manomter tube diameter	$2x10^{-3}$	Tygon flexible tubing attached to plastic joiner drilled on top of Tank 1
Manometer fluid above bottom of loop, ($y = 0$)	0.517	Dyed water, unpressurised system

Procedure

- Drill and leave open a small connector joint on top of the Tank 1 lid for use in connecting manometer (Section 6.4.2).
- Remove lid on 'upper chamber' Tank 1 and pour in glycerol to height h while valve on outflux pipe $F2$ is shut.
- Replace and seal lid on Tank 1, so portion of influx pipe $F2$ on underside of lid is immersed in Tank 1 glycerol.
- Using Peristaltic pump, fill influx pipe $F2$ from glycerol stock, thus raising glycerol level in Tank 1.
- Attach influx pipe $F2$ to connector joint at bottom of Tank 2, and fill Tank 2 to 0.15m depth, while Tank 2 is placed below the level of fluid in Tank 1. Allows any air bubbles in connector valve to pipe $F2$to be removed.
- Seal valve on influx pipe $F2$ and replace Tank 2 to desired pressure head at height H.
- Open valve on outflux pipe $F1$, allowing glycerol to flow from Tank 1 into Collection Bucket until outflux pipe is filled with glycerol and free of air bubbles, and glycerol level in Tank 1 is back to h. Re-seal valve.
- Remove excess glycerol from Collection Bucket using syringe or cup, such that end of outflux pipe is just submerged.
- Collection bucket should already be placed on mass balance, which in turn is connected to computer.
- Attach free end of tube manometer to small connector joint on top of Tank 1 (see Section 6.4.2). Ensure water level in manometer is at equilibrium.
- To begin experiment, turn on data logger for mass balance. Open both influx and outflux valves (second pair of hands useful).
- While glycerol is flowing between tanks, record time, water level in tube manomter (see Section 6.4.2) and mass in Collection Bucket (via computer).

6.4.2 Manometer tests

We connect a tube manometer to the upper chamber tank in order to estimate the pressure in this tank while glycerol is flowing. We run a trial steady state experiment to show that it works. To test the tube manometer, we maintain the gravity feed at a constant height and pressurise the sealed chamber by opening the valve connecting the two. Once equilibrium is reached between sealed chamber and gravity feed, meaning that the glycerol height in the sealed chamber is not changing, we confirm that the pressure measured by height of water in the manometer tube is equal to the height difference between gravity feed head and fluid level in the sealed chamber. We then calculate chamber pressure in the following ways, and repeat the test for five different gravity feed heights. Their agreement, and thus the robustness of the manometer, is apparent in Figure 6.3.

1. We measure the air level corresponding to glycerol level h inside the sealed chamber before and after pressurisation ($h(0)$ and $h(t)$ respectively), and calculate pressure change from the ideal gas law. The ideal gas law says that, assuming constant temperature and number of gas molecules, the product PV of air pressure and volume is the same at all times. We calculate the pressure increase dP relative to original atmospheric pressure P_{atm} (gas law, blue in Figure 6.3):

$$dP = \frac{P_{atm}h(0)}{h(t)} \tag{6.5}$$

2. The pressure change ΔP according to fluid level rise Δy in the manometer is calculated for water density ρ (yellow).

$$\Delta P = \rho g \Delta y \tag{6.6}$$

$$dP = \frac{P_{atm} + \Delta P}{P_{atm}} \tag{6.7}$$

3. We acquire a pressure gague for temporary use while we are testing the manometer. Its value is noted before and after steady state is reached (pink).

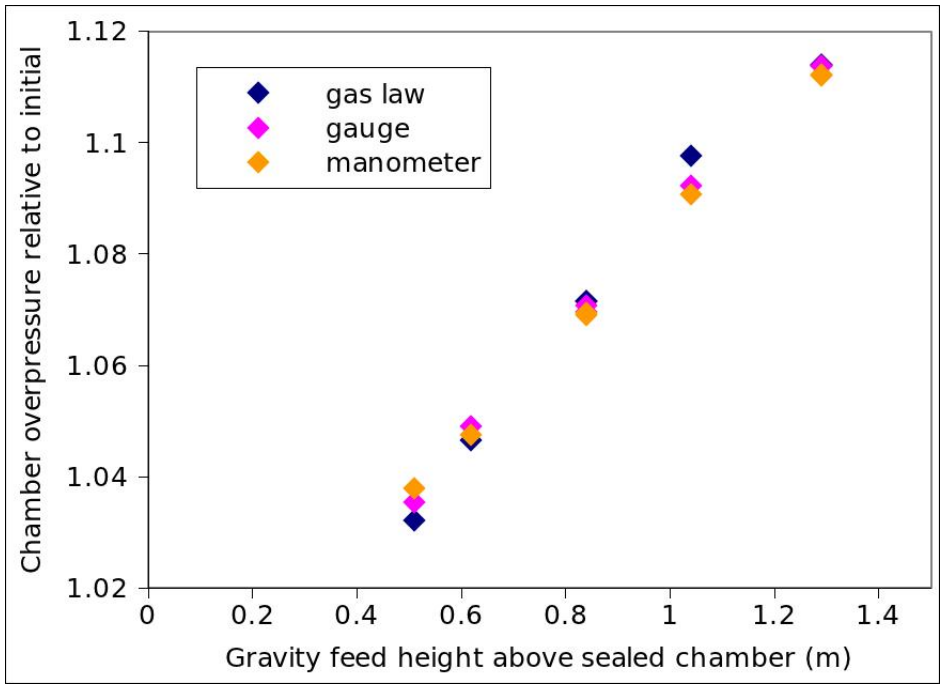

Figure 6.3: Testing tube manometer via pressurisation of the sealed chamber. Overpressure measured by the fluid height in the box and ideal gas law (blue), a digital pressure gauge (pink; loaned to us for temporary use while developing the experimental design), and a tube manometer (yellow) fall on a straight line and comfirm the robustness of the tube manometer for tracking pressure change over time. Horizontal axis is gravity feed height above base of sealed 'upper' chamber.

6.5 Results and interpretation

6.5.1 Steady state experiments

In the first set of experiments, we measure the steady state flow rate from upper chamber to collection bucket, and the upper chamber pressure for a series of gravity feed pressures.

A system in which lower chamber overpressure ΔP_2 is in communication with upper chamber overpressure ΔP_1 adjusts to a steady outflux rate Q_{out}. The short timescale of adjustment is controlled by the upper chamber, but the long timescale at equilibrium is controlled by the lower chamber. We show how the constantly recharged lower chamber controls the equilibrium flow rate.

In the experiment, both valves are initially shut. The sealed tank upper chamber is filled to level h with glycerol, and the gravity feed lower chamber is filled to a level H with glycerol. Both valves are opened and the glycerol is allowed to flow through both chambers, with the gravity feed being maintained to a constant level (within +/-0.5 cm). The outflux and chamber pressure adjust to a steady state value. At steady state, we measure the pressure in the upper chamber using the manometer and the outflux rate to the collection bucket using the scale. We run the steady state experiment for several different gravity feed heights.

Figure 6.4 shows data from the steady state experiments. The volume outflux rate Q_{out} scales linearly with lower chamber overpressure. The lower chamber overpressure is expressed as overpressure due to glycerol mass height above collection bucket. This indicates that a higher overpressure from the lower chamber of a dual-chamber system drives a faster eruption rate. The pressure imposed by the gravity feed chamber is expressed in Pa above atmospheric pressure.

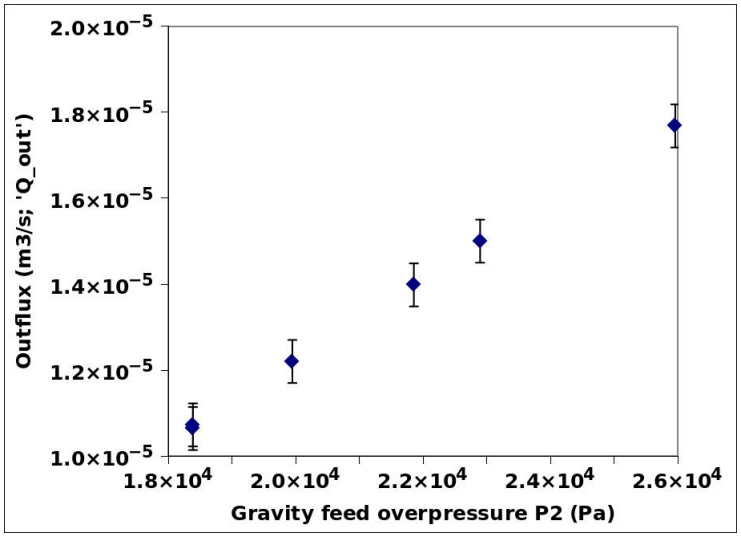

Figure 6.4: Steady state experiment: outflux vs lower chamber overpressure (P_2) at equilibrium. Each data point is a separate steady state experiment. Volume outflux rate Q_{out} at steady state sales linearly with lower chamber overpressure. The overpressure imposed by the gravity feed chamber is expressed in Pa above atmospheric pressure. This indicates that a higher overpressure due to the lower chamber of a dual-chamber system drives a faster steady state eruption rate.

Figure 6.5 shows that the upper chamber overpressure ΔP_1 scales linearly with lower chamber overpressure ΔP_2. Both are expressed as overpressure due to glycerol mass height above collection bucket, with units Pa above atmospheric pressure. This indicates that a higher overpressure from the lower chamber of a dual-chamber system leads to a higher overpressure in the upper chamber. Our model from the previous chapters suggest that this pressurised shallow chamber controls the short term trends of the eruption, but the deep chamber controls the long term steady state eruption rate. The steady state experiments demonstrate only the long term trend, which is that the lower chamber directly controls both efflux rate and upper chamber pressure.

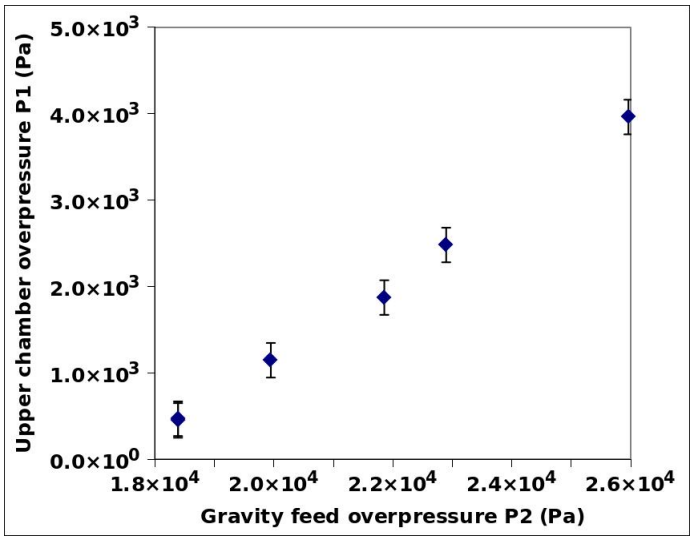

Figure 6.5: Steady state experiment: upper vs lower chamber overpressure at equilibrium. Each data point is a separate steady state experiment. Upper chamber overpressure P_1 scales linearly with lower chamber overpressure P_2. Both are expressed as overpressure due to glycerol mass height above collection bucket, with units Pa above atmospheric pressure.

6.5.2 Transient experiments

We investigate an eruption that either increases or decreases to steady state and show that the transition phase is controlled by the upper chamber pressure, as shown by the model in Chapter 4.

In each experiment, we begin by setting up a steady state experiment as discussed in the previous section. This allows the system to adjust to a steady flow. Then we impose a sudden pressure change by either increasing or decreasing the gravity feed head H. This simply involves moving the gravity feed tank to a different height. We measure the outflux rate Q_{out} and the upper chamber tank overpressure ΔP_1 during the transition to steady state from the new initial conditions.

First we investigate a decrease in deep chamber overpressure. The deep chamber gravity feed is moved from a higher to a lower H. Figure 6.6 shows the outflux rate Q_{out} (top panel, converted to volume flux) and manometer height (bottom panel, directly proportional to upper chamber pressure and the value we later use in a model). Both decrease rapidly at first but then slow to a steady state. The raw data show the transition from the newly imposed intial conditions (decreased gravity feed pressure) to the steady state. This may correspond to a strong plug in a volcanic conduit, in which there is significant resistance to an eruption beginning. The upper chamber pressure must build up to remove the plug, then will run down to equilibrium as the eruption progresses.

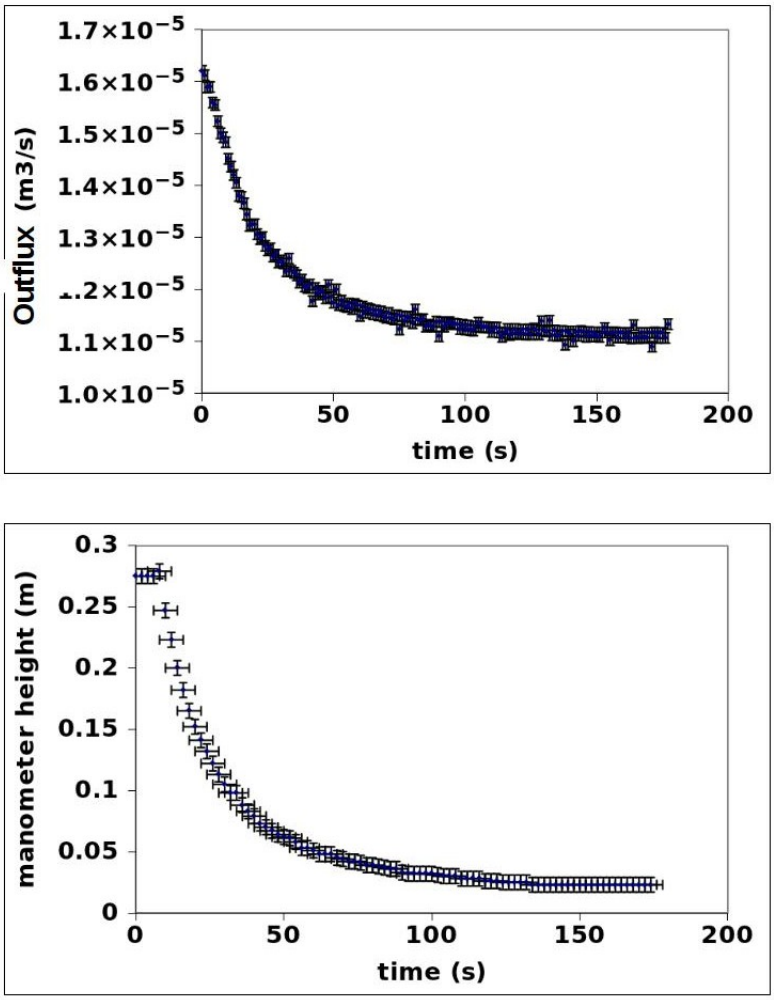

Figure 6.6: Transition to lower deep chamber overpressure (raw data). Deep chamber gravity feed is moved from a higher to a lower H. Outflux rate Q_{out} (top panel) and manometer height (bottom panel, directly proportional to upper chamber pressure) both decrease rapidly at first but then slow to a new steady state.

Next we investigate an increase in deep chamber overpressure. The deep chamber gravity feed is moved from a lower to a higher H. Figure 6.7 shows the outflux rate Q_{out} (top panel, converted to volume flux) and manometer height (bottom panel, directly proportional to upper chamber pressure and the value we later use in a model). Both increase rapidly at first but then slow to a new steady state as recharge from the lower chamber is countered by gradual outflow. The raw data show the transition from the newly imposed intial conditions (increased gravity feed pressure) to the new steady state. This may correspond to a weak plug in a volcanic conduit, in which there is little resistance to an eruption beginning. The upper chamber pressure will increase rapidly at first but then slow to equilibrium as recharge from the lower chamber is countered by gradual outflow. Such increase could not occur in a single chamber system.

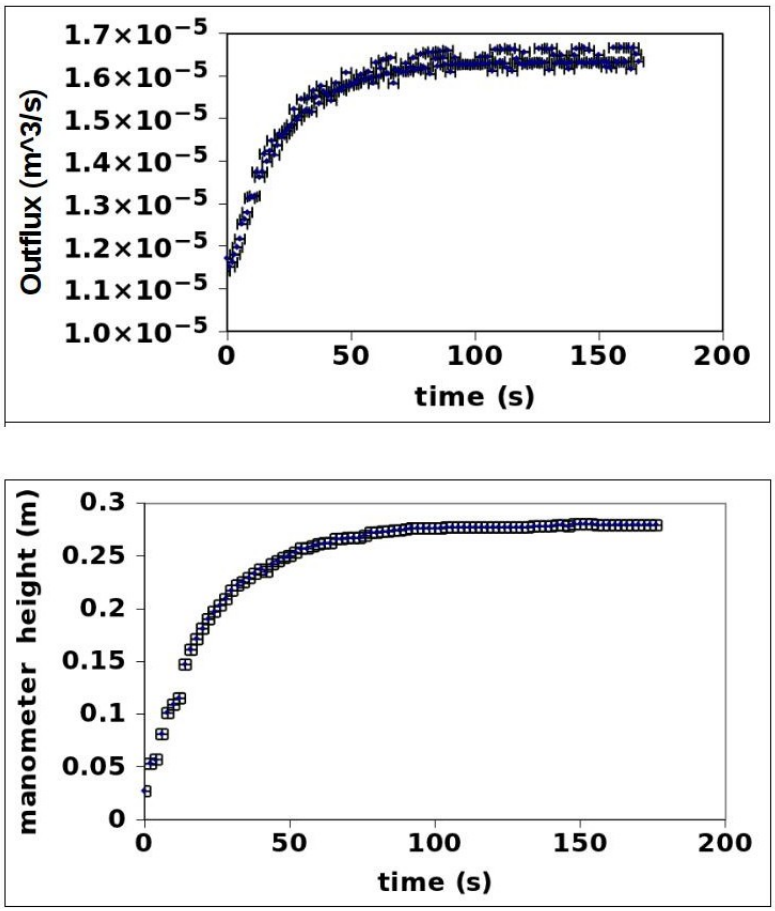

Figure 6.7: Transition to higher deep chamber overpressure (raw data). Deep chamber gravity feed is moved from a lower to a higher H. Outflux rate Q_{out} (top panel) and manometer height (bottom panel, directly proportional to upper chamber pressure) both increase rapidly at first then slow to steady state.

6.5.3 Overturn experiments: another interpretation of results

In the previous section, we presented the transient experimental results and interpreted them as an eruption in which the upper chamber overpressure changes due to input from the lower chamber. This is a model of an eruption increasing or decreasing to steady state as shown in Chapter 4. However, a sudden increase in lower chamber pressure could also be indicative of an overturn of magma in the chamber Phillips and Woods [2002].

We represent this phenomenon with our apparatus by first setting up a steady state experiment, allowing the outflux and upper chamber pressure to settle into an equilibrium value. Then we impose a sudden pressure increase by raising the gravity feed head H to twice its original value at time $t = 75\ s$. Figure 6.8 shows the transition to faster flow rate Q_{out} (top panel) and higher chamber pressure (bottom panel, indicated by manometer fluid height). Such a transition could not occur with a single chamber alone. The second chamber increase to a higher overpressure causes an increase in eruption rate. This could be attributed to the magma overturn.

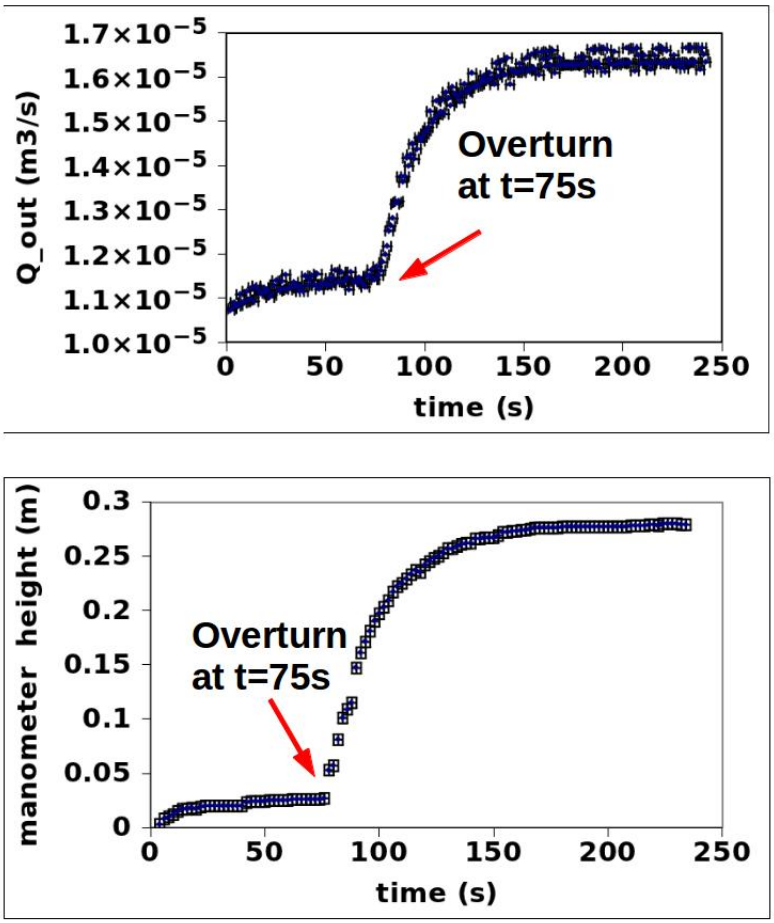

Figure 6.8: Lower chamber overturn (raw data). Outflux and pressure reach steady state, then deep chamber gravity feed is moved from a lower to a higher H at time $t = 75\ s$. Outflux rate Q_{out} (top panel) and manometer height (bottom panel, directly proportional upper chamber pressure) both increase rapidly at first then slow to new steady state.

6.6 Model

In this section we apply the two-chamber model developed in Chapter 4 to the laboratory setting, and show that it fits both the steady state and transient data. The entire model is a simplified version of that presented and solved in Chapter 4. Experiment dimensions referred to in the model are depicted in Figure 6.2.

The volume influx from the gravity feed chamber (referred to as lower chamber) to the sealed tank (referred to as upper chamber) is referred to as Q_{in} and is driven by the pressure drop between the lower chamber (P_2) and the upper (P_1) chamber, with resistance factor $1/F_1$:

$$Q_{in} = F_1(P_2 - P_1(t)) \tag{6.8}$$

The outflux is the difference between chamber pressure and external pressure, which is atmospheric pressure P_a plus the weight of the glycerol W_{gly} above the outflow pipe, with resistance factor F_2

$$Q_{out} = F_2(P_1(t) - P_a + W_{gly}) \tag{6.9}$$

Note that in all cases, Q_{out} is measured as a mass flux dM/dt and converted to volume flux of glycerol density ρ_g as

$$Q_{out} = \frac{1}{\rho_g}\frac{dM}{dt} \tag{6.10}$$

The pressure in the upper chamber is measured using the tube manometer. As the upper chamber pressure changes due to influx of glycerol from the gravity feed and outflux of gylcerol to the collection box, the water in the tube manometer rises height y from equilibrium. Thus the upper chamber pressure P_1 is

$$P_1(t) = P_a + \rho_w g y(t) \tag{6.11}$$

for atmospheric pressure P_a, while the pressure in the lower chamber, for gravity head height H, remains at

$$P_2 = P_a + \rho_g g H \tag{6.12}$$

6.6.1 Steady state solution

For glycerol height in the outflux bucket X, we have steady state solutions for volume flux between lower and upper chambers Q_{in} and outflux from upper chamber Q_{out} in terms of measurable quantities

$$Q_{in} = F_2(\rho_g g H - \rho_w g y) \tag{6.13}$$

$$Q_{out} = F_1(\rho_w g y + \rho g X) \tag{6.14}$$

At steady state, flux into the upper chamber equals flux out of the upper chamber

$$Q_{in} = Q_{out} \tag{6.15}$$

We use the steady state solutions to determine pipe resistance factors F_1 and F_2. Running steady state experiments for five different lower chamber pressures P_2 - that is, maintaining a gravity feed at constant H and allowing y and Q_{out} to reach equilibrium - we measure y and Q_{out} for each overpressure. From this, we calculate F_2 and F_1. Figures 6.9 and 6.10 show F_2 and F_1 for different equilibrium values of Q_{out}. They both take a value of $2{\times}10^{-9}$ m^3/Pas in each steady state experiment.

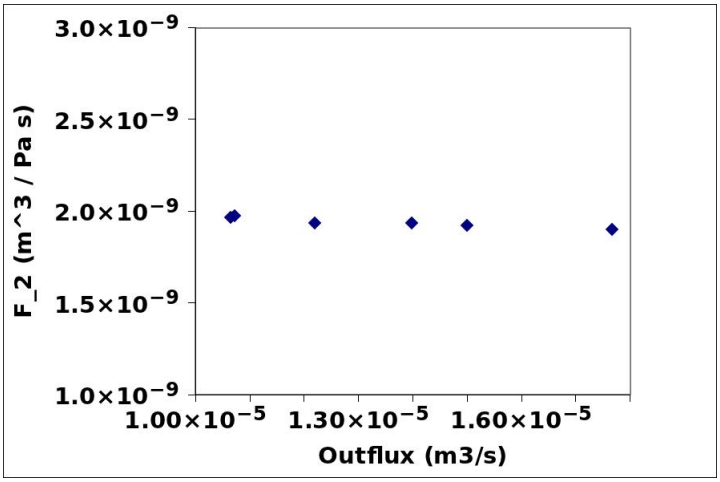

Figure 6.9: Steady state in 2-chamber experiment, resistance constant F_2 (m^3/Pas) for influx to upper chamber calculated for several different steady state outfluxes Q_{out}. $1/F_2$ is the resistance in the pipe connecting connecting the upper and lower chambers

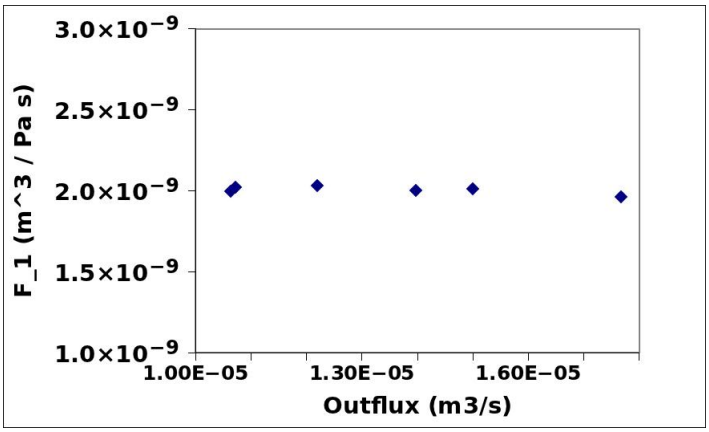

Figure 6.10: Steady state in 2-chamber experiment, resistance constant F_1 $(m^3/Pas)$for upper chamber to surface calculated for several different steady state outfluxes Q_{out}. $1/F_1$ is the resistance in the pipe connecting the upper chamber to the surface.

6.6.2 Transient model and ideal gas law

We invoke the ideal gas law to test our model's use of an air layer as the upper chamber elasticity. From this we confirm the measured manometer height y and outflux Q_{out} based on fluid levels within the chamber. A complete analytical solution for the two chamber model is provided in Chapter 4. The following analysis is a basic application of this model to demonstrate the suitability of our experiment. Dimensions in the model are noted in Figure 6.2.

The pressure P_1 in the upper chamber and thus the glycerol level $h(t)$ and volume of air V_{air} inside the chamber of height h_{max} and area A are given by the ideal gas law. The volume of air in the upper chamber changes over time as glycerol enters and leaves the box, changing the pressure by amount dP.

$$P_1(t)V_{air}(t) = P_1(0)V_{air}(0) \tag{6.16}$$

$$P_1(t) = P_a + dP(t) \tag{6.17}$$

$$dP(t) = \rho_w g y(t) \tag{6.18}$$

$$V_{air} = (h_{max} - h(t))A \tag{6.19}$$

This means that the glycerol level in the chamber is

$$h(t) = \frac{P_1(0)(h_{max} - h(0))}{P_a + \Delta P} = \frac{P_1(0)(h_{max} - h(0))}{P_a + \rho_w g y(t)} \tag{6.20}$$

Then the water level in the manometer is

$$y(t) = \frac{1}{\rho_w g}(\frac{P_1(0)(h_{max} - h(0))}{(h_{max} - h(t))} - P_a) \tag{6.21}$$

To evaluate the model, we measure $y(t)$ and use the gas law to estimate the glycerol level $h(t)$ in the upper chamber using the above equation. From the $y(t)$ value we calculate

$$Q_{in}(t) = F_2(\rho_g g H - \rho_w g y(t)) \tag{6.22}$$

and

$$Q_{out}(t) = F_1(\rho_w g y(t) + \rho g X(t)) \tag{6.23}$$

using the steady state solutions (Equations 6.13 and 6.14) for F_2 and F_1. The total volume rate of change in the upper chamber Q is

$$Q(t) = Q_{in}(t) - Q_{out}(t) \tag{6.24}$$

We know the chamber area so for a time interval dt we can calculate the glyerol level change $dh(t)$ in the chamber

$$dh(t) = \frac{Q_{in}(t)dt}{A} \tag{6.25}$$

We confirm that the gas law-derived $h(t)$ compares with the manometer height $y(t)$.

Figures 6.11 through 6.14 show the agreement of two transient experiments with the gas law-based model. In each experiment, blue markers show the experimental data with error bars and pink line shows the model. Figures 6.11 and 6.12 show the outflux and chamber pressure (manometer height y) in which the gravity head is lowered so the pressure head decreases to steady state. Figures 6.13 and 6.14 show the outflux and chamber pressure (manometer height y) in which the gravity head is raised so the pressure head increases to steady state.

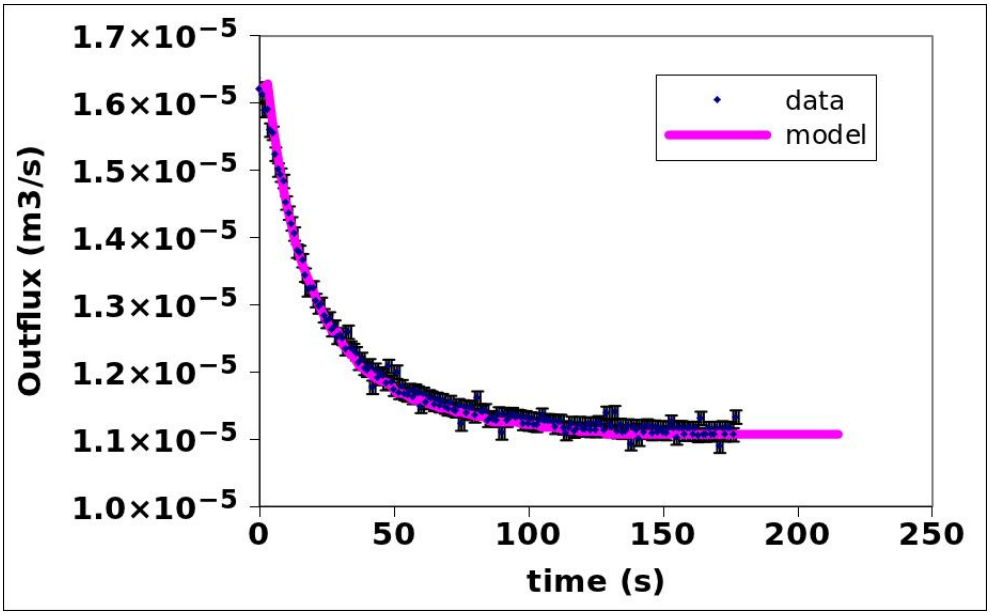

Figure 6.11: Transient experiment: Outflux when gravity head is lowered so the upper chamber pressure decreases to steady state.

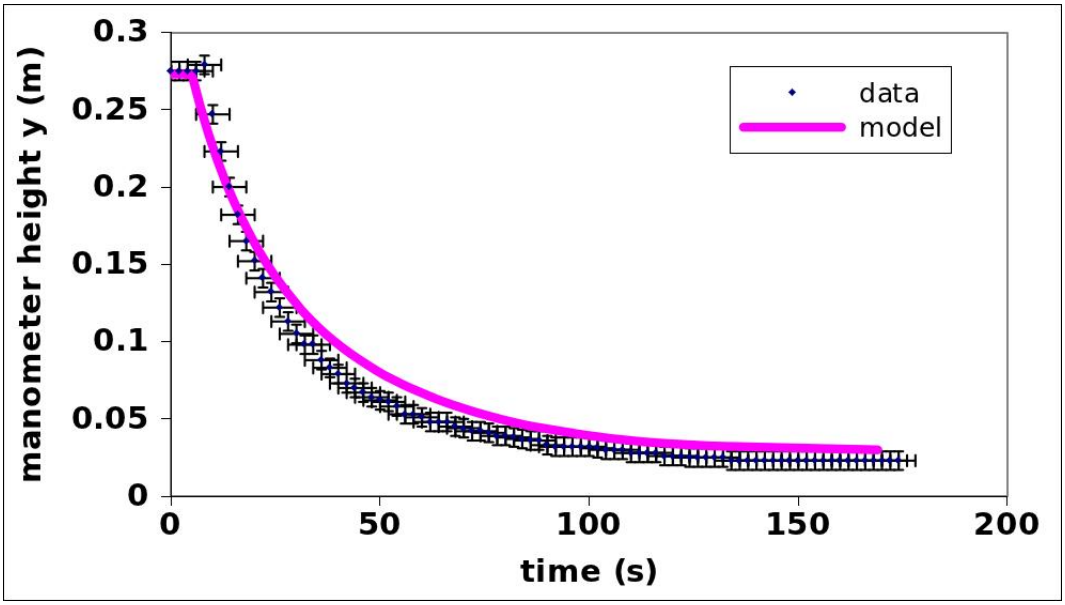

Figure 6.12: Transient experiment: Manometer height (upper chamber pressure) when gravity head is lowered so the upper chamber pressure decreases to steady state.

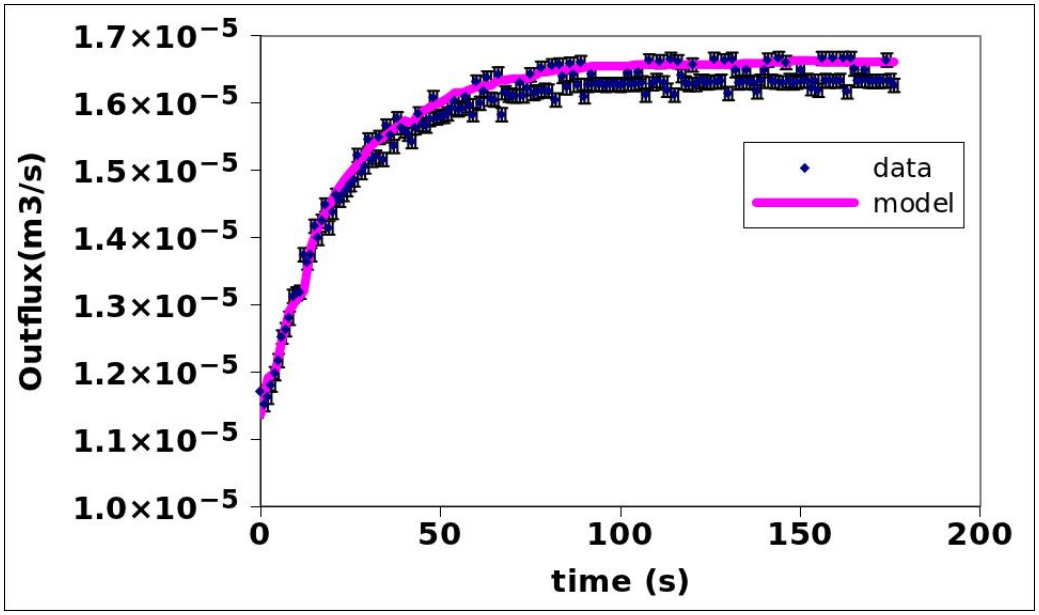

Figure 6.13: Transient experiment: Outflux when gravity head is raised so the upper chamber pressure increases to steady state.

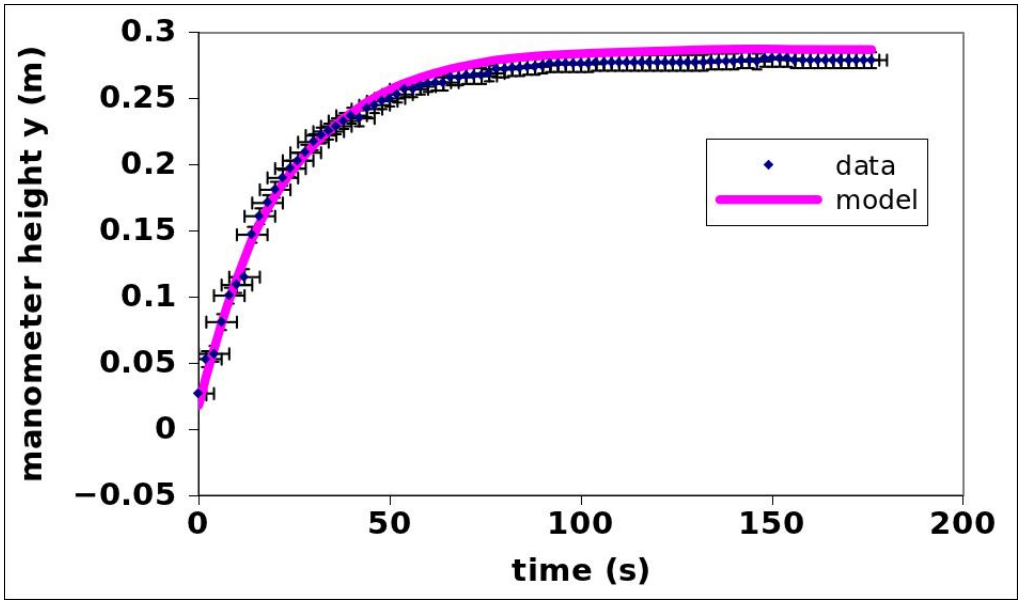

Figure 6.14: Manometer height (upper chamber pressure) when gravity head is raised so the upper chamber pressure increases to steady state.

6.6.3 Application to Lonquimay 1988 eruption

The example shown in Figure 6.11 of an experiment with an initially rapid outflux that slows to steady state, as in the case of an eruption with a strong conduit plug that resists an eruption beginning. The upper chamber pressure must build up to remove the plug. The efflux rate is reminiscent of the two-chamber model that we used to interpret the Lonquimay 1988 eruption in Chapter 4.

In Figure 6.15, we show the erupted volume, along with the fit from our two-chamber model. The experiments show a similar effect: at time $t = 25$ in the Lonquimay model, the flow rate transitions from fast to slow, as it does around time $t = 50$ s in the experiment in Figure 6.11. This provides experimental support for the principles of a two-chamber system, in which the deep chamber is maintained at constant pressure from a magma recharge. The adjustment of an eruption from overpressure to steady state is one way to explain Lonquimay volcano's deviation from a simple exponential decay of eruption rate.

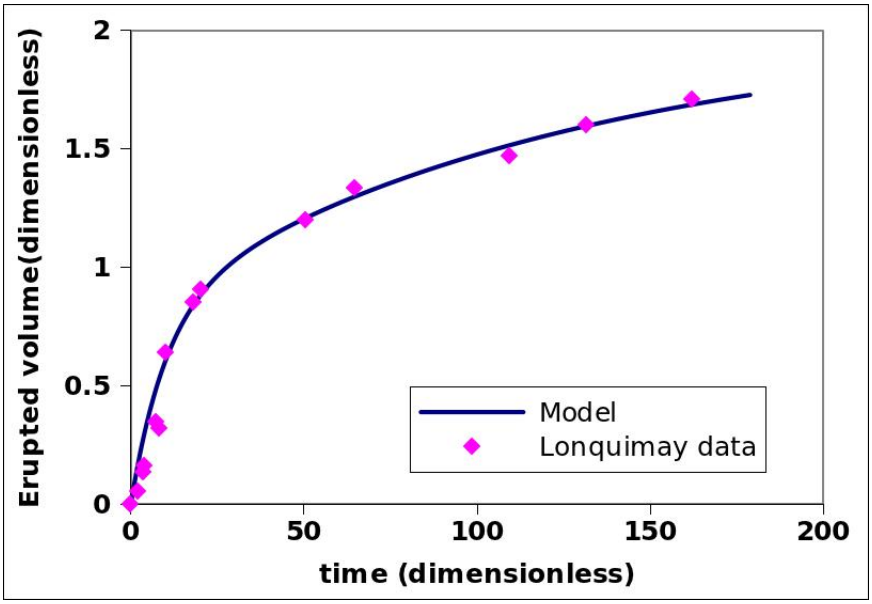

Figure 6.15: Erupted volume for Lonquimay 1988-1990 eruption (pink), with our 2-chamber model (blue). The flow rate slows to steady state from overpressure, reminiscent of the transient experiments in Figure 6.11.

6.7 Discussion and conclusions

In this chapter, we presented a set of experiments in support of the two chamber eruption model presented in Chapter 4. We applied the model to a situation in which an air layer in a sealed tank represents a pressurised elastic upper chamber, and verify that this is a suitable laboratory analogue.

A system in which lower chamber pressure P_2 is initially higher than upper chamber pressure P_1 adjusts to a steady outflux rate Q_{out}. The short timescale of transition is controlled by the upper chamber, but the long timescale at equilibrium is controlled by the lower chamber. The constantly recharged lower chamber controls the equilibrium flow rate. Our experiments demonstrate two cases of an eruption that transitions to a steady state flow. The conditions in the conduit from upper chamber to surface may inhibit an eruption starting, or they may make it easy for an eruption to start. This can be conceptualised by, respectively, a strong or a weak plug in the upper conduit. If there is a strong plug, the upper chamber pressure will build up to a high pressure to remove the plug, then run down to equilibrium as the eruption progresses. This is reminiscent of the efflux rate at Lonquimay, and our two-chamber model of the eruption. If there is a weak plug, the upper chamber pressure will increase rapidly at first but then slow to equilibrium as recharge from the lower chamber is countered by gradual outflow. This is also reminiscent of the 1980-86 eruptive sequence of Mount St Helens which exhibits an overall waning eruption rate, erupting rapidly at first and slowing as it goes.

Finally, we provide an alternative interpretation of a sudden pressure increase in the lower chamber caused by an overturn of magma. This change takes a finite time to appear as outflux rate at the surface, and may be important to understanding an eruption that has periods of increased eruption rate such as Soufriere Hills volcano or two layers of eruption products such as at Mount Vesuvius.

Chapter 7

Conclusions and future work

7.1 Summary and conclusions

In this chapter, we summarise the main contributions of this thesis, the key elements of our model, and the scope for future work.

7.1.1 General summary

This thesis revisits observations from volcanic eruptions and builds a picture of the complexity of the long-term evolution of these eruptions, as well as a framework of how an eruption might be understood in terms of one or two coupled magma reservoirs. It has built support for the hypothesis that the deep plumbing system and interaction amongst magma chambers provide insight to the long-term pattern of eruption, and that the long-term observable trends respond to a magma reservoir. If a deep chamber wanes in pressure, the recharge to the shallow chamber decreases in rate.

The main content of this thesis is an investigation of long-term controls on volcanic events and the development of a model to explain these long-term trends and investigate the parameters that affect the evolution of an eruptive episode. We hypothesised that the long-term evolution rate of the eruption is controlled by a deep magma chamber, and the shorter cycling between events is controlled by the filling and emptying of a smaller shallow chamber. We applied the model to interpret various aspects of eruptions at Lonquimay, La Soufriere de St Vincent,

Mount St Helens, Unzen, and the Soufriere Hills Volcano. We did not simulate a volcanic eruption, but rather modeled aspects of processes controlled by a deep plumbing system.

We began the thesis by discussing the importance of studying volcanoes in terms of both hazard management and scientific interest, and identified features in the eruption style, magma composition, and seismic activity at these volcanoes that lead to a picture of multiple magma chambers. We discussed how these principles motivate new insights into a model of a magma plumbing system.

7.1.2 Key elements of models

We first developed a model of a closed single chamber system. A single chamber does not allow for all the complexity shown at real volcanoes; however, we interpret eruptions at Mount St Helens, Unzen, Paricutin, and La Soufriere de St Vincent in terms of a depressurising closed chamber.

The Lonquimay eruption in 1988 provides motivation for including a source of magma recharge to the chamber and developing a model of an open single chamber system. The cycles of eruption and ground inflation and deflation observed at Soufriere Hills Volcano provides motivation for assuming critical chamber overpressures at which an eruption starts and stops, thus allowing for periodic eruptions.

We rationalised surface deformation and eruption data in the context of an open single chamber system, and our analysis invited the concept of a second chamber in order to provide a source of magma recharge. We calculated a possible recharge rate for the Soufriere Hills Volcano. This led to a model with an analytical solution, although applying it to real data becomes complicated.

We then developed the model to explore how a recharge of magma may be regulated by a deeper chamber, and investigated the long-term control of a deep source. We presented a quantitative two chamber model and derived an analytical solution relating the surface eruption rate to the evolution of the chamber pressures. We showed that the two chambers' pressures evolve on different timescales, with the upper chamber typically evolving more rapidly.

We derived an analytical solution for the eruption rate of a closed two chamber

system and explored the effects of recharge in an open system. By introducing a critical pressure in the upper chamber at which the eruption starts and stops, we showed that magma recharge can lead to cycles of eruption. Lonquimay volcano in Chile shows two phases of eruption, which we interpreted in the context of a closed two-chamber system which is controlled first by a shallow chamber and then by a deeper chamber. For an open two chamber system, if recharge to the shallow chamber decreases in rate, the period between cycles of inflation and deflation can become longer, which is reminiscent of Mount St Helens where intervals between successive dome-building events increase over time.

Two chambers whose pressures evolve in different ways give a different surface deformation shape and magnitude than a single chamber, so we investigated how surface deformation profiles change over time.

Only the magnitude of surface deformation changes in time for a single chamber, while a second equally pressurised chamber has the effect of changing the shape. As for two chambers that depressurise at different rates, as shown by our model, the shape of the surface deformation over a horizontal cross section changes in time. Offsetting the chambers horizontally makes the profiles assymetric about the origin.

The Soufriere Hills Volcano deformation data changes in space and time, and our model shows that there is huge variation in the near-field data for small variations of properties on which there are few constraints. This makes it very difficult to uniquely invert surface deformation data; however, it is possible to rationalise why there might be changes in surface deformation from one location to the next.

Finally, we verified the model principles with a laboratory experiment, and presented results for steady state experiments which represent a volcano erupting at an equilibrium rate, as well as transient experiments which represent an eruption that either increases or decreases to steady state as shown by the two chamber model.

7.1.2.1 Time dependencies of model configurations

It is also worth noting that while many of the parameters used in the studies are not well defined (order of magnitude approximations for initial chamber overpressure and compressibility, for example), and thus the robustness of any model configuration's abilities to specify particular quantities is less important than their ability to provide information regarding different time dependencies. In that vein, Table 7.1.2.1 summarises the key traits of the model configurations from this thesis (F is conduit resistance, β is magma compressibility, V_c is chamber volume, ΔP_{START} and ΔP_{STOP} refer to critical pressure at which eruption starts and stops, F is the ratio of resistance in upper to lower conduits, and V is the ratio of lower to upper chamber volume). For further detail on effects of different parameters, refer back to Chapters 4 and 5.

MODEL	TIME DEPENDENCE	COMMENTS
Single chamber, no recharge	Exponential decay, time constant $F/\beta V_c$	Deviation from exponential decay may indicate more complex plumbing
Single chamber, recharge from depth	Phases of exponential decay, time constant $F/\beta V_c$; period between eruptions is $(\beta V_c/Q_{in})(\Delta P_{START} - \Delta P_{STOP})$	Decreasing recharge rate with time gives shorter eruption and longer period between eruptions
Double chamber, no recharge	Timescale of eruption rate is given by Equation 4.16	Noticeable surface effect is eruption that occurs on two different time scales before ceasing - fast then slow ($F = 0.1$ indicating magma that cannot move easily from lower to upper chamber; $V < 1$ indicating larger upper chamber than lower chamber), or fast then gradual ($V = 100$ indicating larger lower than upper chamber), or slow then fast ($V = 1$ indicating same size chambers); or in some cases gradual ($F = 100$, indicating chambers which are in good communication)
Double chamber, recharge from depth	Phases of eruption, timescale of rate for each cycle is given by Equation 4.16. Upper chamber cycles between ΔP_{START} and ΔP_{STOP}	Noticeable surface effect is eruption cycles each of which may occur on two different time scales before ceasing, depending on chamber volume ratio and conduit resistance ratio

7.1.3 What has been gained

From this study, we have gained a new model and a method by which to rationalise data from volcanoes that behave differently. Steady state cycles of effusive lava dome-building eruptions are complex, and this complexity extends to surface deformation observations. Our model demonstrates further understanding of the degree of complexity that exists and how it may arise, and we now have a broad framework in which to analyse different elements that contribute to the complexity. The literature presents a picture of a two chamber magma system, and we have presented a quantitative model that shows how such a system may behave.

We presented different types of data including eruption rate and surface deformation, and showed how some aspects of these data may be dominated by a deep or shallow chamber. We developed a framework for how a deeper source of magma in the crust could influence the eruption from a shallower chamber. The result of the work might help to identify which types of analysis are best for understanding the long-term evolution of an eruption, and which data types are most important to collect.

7.2 Future work

Our model provides a framework to which many more elements could be added in order to investigate how such elements contribute to the complexity of volcanic eruptions.

Tait describes an additional chamber pressurisation process by which crystallisation and volatile release in the chamber itself leads to pressurisation of the chamber Tait et al. [1989]. This second boiling may cause deviation from exponential decay. Cooling may occur on a longer timescale than the eruptions themselves, though this is not always the case if the magma reservoirs are thin sills or magma has small viscosity (faster convective cooling). In this thesis, we focus on higher viscosity andesite magma, though we cannot eliminate second boiling as a mechanism by which chamber pressure evolves. Developing our model to include this second boiling would provide new insights.

Magma compressibility and viscosity are complex properties that change with time, and it would enhance our model to include variation in magma density and viscosity based on magma ascent velocity and gas content Bower and Woods [1998]; Huppert and Woods [2002]. The depth at which the magma resides is also important to its volatile content and thus compressibility and viscosity.

Other items of interest are the critical overpressures ΔP at which an eruption starts and stops. Changing these values from one eruption cycle to the next would allow the model to account for changes in magma properties over time. Further investigation into the mechanisms of starting and stopping an eruption would also enhance the model and allow it to address further complexity.

We have also laid some groundwork for further investigation into what actually controls the magma supply rate to a chamber.

This thesis provides principles, a method by which to rationalise data from volcanoes, and a quantitative model that shows how a two chamber system may behave. More layers of complexity would enrich and enhance its descriptive ability.

References

P. Allard. Endogenous magma degassing and storage at Mount Etna. *Geophysical Research Letters*, 24(17):2219–2222, 1997. 27

C. Annen and RSJ Sparks. Effects of repetitive emplacement of basaltic intrusions on thermal evolution and melt generation in the crust. *Earth and Planetary Science Letters*, 203(3):937–955, 2002. 15, 28, 36, 105

WP Aspinall, AD Miller, LL Lynch, JL Latchman, and RC Stewart. Soufriere Hills eruption, Montserrat, 1995-1997: earthquake locations and fault plane solutions. *Geophysical Research Letters*, 25(18):3397–3400, 1998. 36

J. Barclay, MJ Rutherford, MR Carroll, MD Murphy, JD Devine, J. Gardner, and RSJ Sparks. Experimental phase equilibria constraints on pre-eruptive storage conditions of the Soufriere Hills magma. *Geophysical Research Letters*, 25(18):3437–3440, 1998. 15, 18, 29, 36, 105

A. Barmin, O. Melnik, and RSJ Sparks. Periodic behavior in lava dome eruptions. *Earth and Planetary Science Letters*, 199(1):173–184, 2002. 12, 14, 17

B. Behncke and M. Neri. Cycles and trends in the recent eruptive behaviour of Mount Etna (Italy). *Canadian Journal of Earth Sciences*, 40(10):1405–1411, 2003. iv, 20, 23, 24, 27

S. Blake. Volcanism and the dynamics of open magma chambers. *Nature*, 289: 783–785, 1981. 66, 157

S. Blake. Volatile oversaturation during the evolution of silicic magma chambers as an eruption trigger. *Journal of Geophysical Research*, 89(B10):8237–8244, 1984. 15, 38, 46

J. Blower. Factors controlling permeability-porosity relationships in magma. *Bulletin of volcanology*, 63(7):497–504, 2001. 9

JD Blower, HM Mader, and SDR Wilson. Coupling of viscous and diffusive controls on bubble growth during explosive volcanic eruptions. *Earth and Planetary Science Letters*, 193(1):47–56, 2001. 9

J. Blundy and K. Cashman. Ascent-driven crystallisation of dacite magmas at Mount St Helens, 1980-1986. *Contributions to Mineralogy and Petrology*, 140 (6):631–650, 2001. 15, 38, 46

J. Blundy and K. Cashman. Rapid decompression-driven crystallization recorded by melt inclusions from Mount St. Helens volcano. *Geology*, 33(10):793–796, 2005. 15, 38, 46, 112

S.M. Bower and A.W. Woods. Control of magma volatile content and chamber depth on the mass erupted during explosive volcanic eruptions. *Journal of Geophysical Research*, 102(B5):10273–10290, 1997. 13, 66, 74

S.M. Bower and A.W. Woods. On the influence of magma chambers in controlling the evolution of explosive volcanic eruptions. *Journal of Volcanology and Geothermal Research*, 86(1):67–78, 1998. 13, 74, 78, 82, 225

S. Brantley and B. Myers. Mount St. Helens from the 1980 eruption to 2000. *U.S. Geological Survey Fact Sheet 036-00*, http://pubs.usgs.gov/fs/2000/fs036-00/, 2000. v, 38, 40

K.V. Cashman. Groundmass crystallization of Mount St. Helens dacite, 1980–1986: a tool for interpreting shallow magmatic processes. *Contributions to Mineralogy and Petrology*, 109(4):431–449, 1992. 46

Valérie Cayol and François H Cornet. Effects of topography on the interpretation of the deformation field of prominent volcanoesapplication to etna. *Geophysical research letters*, 25(11):1979–1982, 1998. 161

E. Chassignet, C. Cenedese, and J. Verron. *Buoyancy-Driven Flows*. Cambridge University Press, 2012. 8

P. Cole, V. Bass, T. Christopher, C. Murrell, H. Odbert, P. Smith, R. Stewart, A. Stinton, R. Syers, and P. Williams. Montserrat volcano observatory scientific report for volcanic activity between 1 November 2010 and 30 April 2011. *Montserrat Volcano Observatory*, Open File Report(OFR 11-01), 2011. 33

L. Crescentini and A. Amoruso. Effects of crustal layering on the inversion of deformation and gravity data in volcanic areas: an application to the Campi Flegrei caldera, Italy. *Geophysical Research Letters*, 34(9), 2007. 155

G. Cumin. L'eruzione laterale etnea del novembre 1950 - dicembre 1951. *Istituto di Geografa e dell'Istituto di Vulcanologia dell'Universita di Catania*, 1954. 25, 26

R.P. Denlinger and R.P. Hoblitt. Cyclic eruptive behavior of silicic volcanoes. *Geology*, 27(5):459–462, 1999. 13, 86

JD Devine, MJ Rutherford, GE Norton, and SR Young. Magma storage region processes inferred from geochemistry of Fe–Ti oxides in andesitic magma, Soufriere Hills Volcano, Montserrat, WI. *Journal of Petrology*, 44(8):1375–1400, 2003. 18, 29, 36, 105

TH Druitt and RSJ Sparks. On the formation of calderas during ignimbrite eruptions. *Nature*, 310(5979):679–681, 1984. 12, 66, 74

M. Edmonds, D. Pyle, and C. Oppenheimer. A model for degassing at the Soufrière Hills Volcano, Montserrat, West Indies, based on geochemical data. *Earth and Planetary Science Letters*, 186(2):159–173, 2001. 18, 36, 105

J. Eichelberger. Silicic volcanism: ascent of viscous magmas from crustal reservoirs. *Annual Review of Earth and Planetary Sciences*, 23:41–64, 1995. 40, 46

D. Elsworth, G. Mattioli, J. Taron, B. Voight, and R. Herd. Implications of magma transfer between multiple reservoirs on eruption cycling. *Science*, 322 (5899):246–248, 2008. 30, 34, 36, 96, 101, 154, 156, 157, 160, 163, 179

R. Foroozan, D. Elsworth, B. Voight, and G.S. Mattioli. Dual reservoir structure at Soufrière Hills volcano inferred from continuous GPS observations and heterogeneous elastic modeling. *Geophysical Research Letters*, 37(19):L00E12, 2010. 154, 155

R. Foroozan, D. Elsworth, B. Voight, and G.S. Mattioli. Magmatic-metering controls the stopping and restarting of eruptions. *Geophysical Research Letters*, 38(5):L05306, 2011. 36, 154, 177

C Fries. Volumes and weights of pyroclastic material, lava and water erupted by Paricutin volcano, Michoacan, Mexico. *Transactions of the American Geophsyical Union*, 34:603–616, 1990. 73

J.E. Gardner, S. Carey, H. Sigurdsson, and M.J. Rutherford. Influence of magma composition on the eruptive activity of Mount St. Helens, Washington. *Geology*, 23(6):523–526, 1995. 38, 46, 82

D.N. Green, J. Neuberg, and V. Cayol. Shear stress along the conduit wall as a plausible source of tilt at Soufrière Hills Volcano, Montserrat. *Geophysical Research Letters*, 33(10), 2006. 160

A. Gudmundsson. How local stresses control magma-chamber ruptures, dyke injections, and eruptions in composite volcanoes. *Earth-Science Reviews*, 79 (1):1–31, 2006. 15

Smithsonian Institution GVP. Global Volcanism Program. *Department of Mineral Sciences*, http://www.volcano.si.edu/world/. 20, 27, 33, 39, 53, 54

S. Hautmann, J. Gottsmann, R.S.J. Sparks, A. Costa, O. Melnik, and B. Voight. Modelling ground deformation caused by oscillating overpressure in a dyke conduit at Soufrière Hills Volcano, Montserrat. *Tectonophysics*, 471(1):87–95, 2009. 161

Stefanie Hautmann, Joachim Gottsmann, R Stephen J Sparks, Glen S Mattioli, I Selwyn Sacks, and Michael H Strutt. Effect of mechanical heterogeneity in arc crust on volcano deformation with application to soufrière hills volcano,

montserrat, west indies. *Journal of Geophysical Research: Solid Earth (1978–2012)*, 115(B9), 2010. 155, 160, 161

Stefanie Hautmann, Dannie Hidayat, Nicolas Fournier, Alan T Linde, I Selwyn Sacks, and C Pyiko Williams. Pressure changes in the magmatic system during the december 2008/january 2009 extrusion event at Soufrière Hills Volcano, Montserrat (wi), derived from strain data analysis. *Journal of Volcanology and Geothermal Research*, 2012. 160, 161

H.E. Huppert and A.W. Woods. The role of volatiles in magma chamber dynamics. *Nature*, 420(6915):493–495, 2002. 13, 66, 74, 78, 225

H.E. Huppert, J.B. Shepherd, R. Haraldur Sigurdsson, and S.J. Sparks. On lava dome growth, with application to the 1979 lava extrusion of the Soufriere of St. Vincent. *Journal of Volcanology and Geothermal Research*, 14(3):199–222, 1982. 71, 72

R.M. Iverson, D. Dzurisin, C.A. Gardner, T.M. Gerlach, R.G. LaHusen, M. Lisowski, J.J. Major, S.D. Malone, J.A. Messerich, S.C. Moran, et al. Dynamics of seismogenic volcanic extrusion at Mount St Helens in 2004–05. *Nature*, 444(7118):439–443, 2006. 41

C. Jaupart and C.J. Allègre. Gas content, eruption rate and instabilities of eruption regime in silicic volcanoes. *Earth and Planetary Science Letters*, 102 (3):413–429, 1991. 10, 66

R. Luckett, B. Baptie, L. Ottemoller, and G. Thompson. Seismic Monitoring of the Soufriere Hills Volcano, Montserrat. *Seismological Research Letters*, 78(2): 192–200, 2007. 32

G.S. Mattioli, T.H. Dixon, F. Farina, E.S. Howell, P.E. Jansma, and A.L. Smith. GPS measurement of surface deformation around Soufriere Hills volcano, Montserrat from October 1995 to July 1996. *Geophysical Research Letters*, 25(18):3417–3420, 1998. 30, 96, 97, 100, 181

G.S. Mattioli, R.A. Herd, M.H. Strutt, G. Ryan, C. Widiwijayanti, and B. Voight. Long term surface deformation of Soufrière Hills Volcano, Montserrat from GPS

geodesy: Inferences from simple elastic inverse models. *Geophysical Research Letters*, 37(19):L00E13, 2010. 30, 35, 96, 154, 155, 177, 178

A.R. McBirney and T. Murase. Rheological properties of magmas. *Annual Review of Earth and Planetary Sciences*, 12:337, 1984. 86

O. Melnik and RSJ Sparks. Nonlinear dynamics of lava dome extrusion. *Nature*, 402(6757):37–41, 1999. 10, 66

O. Melnik and RSJ Sparks. Controls on conduit magma flow dynamics during lava dome building eruptions. *Journal of Geophysical Research*, 110(2):B02209, 2005. 12, 13, 17, 86

O. Melnik and S. Sparks. Transient models of conduit flows during volcanic eruptions. *Statistics in Volcanology*, pages 201–214, 2006. 67

AD Miller, RC Stewart, RA White, R. Luckett, BJ Baptie, WP Aspinall, JL Latchman, LL Lynch, and B. Voight. Seismicity associated with dome growth and collapse at the Soufriere Hills Volcano, Montserrat. *Geophysical Research Letters*, 25(18):3401–3404, 1998. 32, 36

K. Mogi. Relations between the eruptions of various volcanoes and the deformations of the ground surfaces around them. *University of Tokyo*, 1958. 96, 152

T. Murase, A.R. McBirney, and W.G. Melson. Viscosity of the dome of Mount St. Helens. *Journal of Volcanology and Geothermal Research*, 24(1):193–204, 1985. 46

MD Murphy, RSJ Sparks, J. Barclay, MR Carroll, A.M. Lejeune, TS Brewer, R. Macdonald, S. Black, and S. Young. The role of magma mixing in triggering the current eruption at the Soufriere Hills Volcano, Montserrat, West Indies. *Geophysical Research Letters*, 25(18):3433–3436, 1998. 36, 105

S. Nakada, H. Shimizu, and K. Ohta. Overview of the 1990–1995 eruption at Unzen Volcano. *Journal of Volcanology and Geothermal Research*, 89(1):1–22, 1999. v, 15, 48, 50, 51, 52, 53, 54, 55, 79

M. Nakamura. Continuous mixing of crystal mush and replenished magma in the ongoing Unzen eruption. *Geology*, 23(9):807–810, 1995. 48, 55

J.C. Phillips and A.W. Woods. Suppression of large-scale magma mixing by melt–volatile separation. *Earth and Planetary Science Letters*, 204(1):47–60, 2002. 188, 189, 208

Virginie Pinel and Claude Jaupart. Magma chamber behavior beneath a volcanic edifice. *Journal of Geophysical Research: Solid Earth (1978–2012)*, 108(B2), 2003. 161

A. Qamar, W.S. Lawrence, J.N. Moore, and G. Kendrick. Seismic signals preceding the explosive eruption of Mount St. Helens, Washington, on 18 May 1980. *Bulletin of the Seismological Society of America*, 73(6A):1797–1813, 1983. 40

R. Scandone. Factors controlling the temporal evolution of explosive eruptions. *Journal of Volcanology and Geothermal Research*, 72(1):71–83, 1996. 74

R. Scandone and S.D. Malone. Magma supply, magma discharge and readjustment of the feeding system of Mount St. Helens during 1980. *Journal of volcanology and geothermal research*, 23(3):239–262, 1985. 38, 40, 46, 82

P. Schiano, R. Clocchiatti, L. Ottolini, and T. Busà. Transition of Mount Etna lavas from a mantle-plume to an island-arc magmatic source. *Nature*, 412 (6850):900–904, 2001. 22

O. Sigmarsson, I. Vlastélic, R. Andreasen, I. Bindeman, JL Devidal, S. Moune, JK Keiding, G. Larsen, A. Höskuldsson, T. Thordarson, et al. Dynamic magma mixing revealed by the 2010 Eyjafjallajokull eruption. *Solid Earth Discuss*, 3: 591–613, 2011. v, 58, 61

F. Sigmundsson, S. Hreinsdóttir, A. Hooper, T. Árnadóttir, R. Pedersen, M.J. Roberts, N. Óskarsson, A. Auriac, J. Decriem, P. Einarsson, et al. Intrusion triggering of the 2010 Eyjafjallajokull explosive eruption. *Nature*, 468(7322): 426–430, 2010. 58, 61

RSJ Sparks. The dynamics of bubble formation and growth in magmas: a review and analysis. *Journal of Volcanology and Geothermal Research*, 3(1):1–37, 1978. 8, 9, 10, 74, 78

RSJ Sparks. Causes and consequences of pressurisation in lava dome eruptions. *Earth and Planetary Science Letters*, 150(3):177–189, 1997. 8, 15

RSJ Sparks, SR Young, J. Barclay, ES Calder, P. Cole, B. Darroux, MA Davies, TH Druitt, C. Harford, R. Herd, et al. Magma production and growth of the lava dome of the Soufrière Hills Volcano, Montserrat, West Indies: November 1995 to December 1997. *Geophysical Research Letters*, 25:3421–3424, 1998. 30, 96

M.V. Stasiuk, C. Jaupart, and R.S.J. Sparks. On the variations of flow rate in non-explosive lava eruptions. *Earth and Planetary Science Letters*, 114(4): 505–516, 1993. 3, 4, 12, 73, 83, 85

D.A. Swanson and R.T Holcomb. *Regularities in Growth of the Mount St. Helens Dacite Dome, 1980-1986: IN: IAVCEI Proceedings in Volcanology, Vol.2, Lava Flows and Domes*. Springer-Verlag, 1989. v, 40, 42, 43, 44, 45, 76, 146, 149

S. Tait, C. Jaupart, and S. Vergniolle. Pressure, gas content and eruption periodicity of a shallow, crystallising magma chamber. *Earth and Planetary Science Letters*, 92(1):107–123, 1989. 38, 46, 224

JC Tanguy. Tholeiitic basalt magmatism of Mount Etna and its relations with the alkaline series. *Contributions to Mineralogy and Petrology*, 66(1):51–67, 1978. 27, 28

J. Tarasewicz, R.S. White, A.W. Woods, B. Brandsdottir, and M Gudmundsson. Magma mobilization by downward-propagating decompression of the Eyjafjallajokull volcanic plumbing system. *Geophysical Research Letters*, Forthcoming, 2012. 15, 58, 59, 60, 61, 155

N. Thomas, S. Tait, and T. Koyaguchi. Mixing of stratified liquids by the motion of gas bubbles: application to magma mixing. *Earth and Planetary Science Letters*, 115(1):161–175, 1993. 189

E. Tryggvason. Multiple magma reservoirs in a rift zone volcano: ground deformation and magma transport during the September 1984 eruption of Krafla, Iceland. *Journal of Volcanology and Geothermal Research*, 28(1):1–44, 1986. 155

B. Voight, C. Widiwijayanti, G. Mattioli, D. Elsworth, D. Hidayat, and M. Strutt. Magma-sponge hypothesis and stratovolcanoes: Case for a compressible reservoir and quasi-steady deep influx at Soufrière Hills Volcano, Montserrat. *Geophysical Research Letters*, 37(19):L00E05, 2010. 154

G. Wadge. The storage and release of magma on Mount Etna. *Journal of Volcanology and Geothermal Research*, 2(4):361–384, 1977. 12, 20, 22, 25, 26, 27

G. Wadge and G.P.L. Walker. The output of the Etna volcano. *Nature*, 255: 385–387, 1975. 24

G. Wadge, R. Herd, G. Ryan, ES Calder, and J.C. Komorowski. Lava production at Soufrière Hills Volcano, Montserrat: 1995–2009. *Geophysical Research Letters*, 37(19):L00E03, 2010. v, 29, 30, 32, 34, 96

IM Watson, C. Oppenheimer, B. Voight, PW Francis, A. Clarke, J. Stix, A. Miller, DM Pyle, MR Burton, SR Young, et al. The relationship between degassing and ground deformation at Soufriere Hills Volcano, Montserrat. *Journal of Volcanology and Geothermal Research*, 98(1):117–126, 2000. 29, 36

JA Whitehead and K.R. Helfrich. Instability of flow with temperature-dependent viscosity: A model of magma dynamics. *Journal of Geophysical Research*, 96 (B3):4145–4155, 1991. 188

C. Widiwijayanti, A. Clarke, D. Elsworth, and B. Voight. Geodetic constraints on the shallow magma system at Soufrière Hills Volcano, Montserrat. *Geophysical Research Letters*, 32(11), 2005. 161

L. Wilson and J. Head III. Ascent and eruption of basaltic magma on the earth and moon. *Journal of Geophysical Research*, 86(B4):2971–3001, 1981. 8, 67

A.W. Woods and A. Cowan. Magma mixing triggered during volcanic eruptions. *Earth and Planetary Science Letters*, 288(1):132–137, 2009. 188, 189

A.W. Woods and H.E. Huppert. On magma chamber evolution during slow effusive eruptions. *Journal of Geophysical Research*, 108(B8):2403, 2003. 15, 16, 192

A.W. Woods and T. Koyaguchi. Transitions between explosive and effusive eruptions of silicic magmas. *Nature*, 370(6491):641–644, 1994. 10, 112

J.J. Wylie, B. Voight, and JA Whitehead. Instability of magma flow from volatile-dependent viscosity. *Science*, 285(5435):1883–1885, 1999. 5, 7, 29